©Copyright 2013
Cihan Akcay

Extended Magnetohydrodynamic Simulations of the Helicity Injected Torus (HIT-SI) Spheromak Experiment with the NIMROD Code

Cihan Akcay

A dissertation submitted in partial fulfillment
of the requirements for the degree of

Doctor of Philosophy

University of Washington

2013

Program Authorized to Offer Degree: Department of Physics

University of Washington

Abstract

Extended Magnetohydrodynamic Simulations of the Helicity Injected Torus (HIT-SI) Spheromak Experiment with the NIMROD Code

Cihan Akcay

Chair of the Supervisory Committee:

A comparative study of 3-D pressureless resistive (single-fluid) magnetohydrodynamic (rMHD) and 3-D pressureless two-fluid magnetohydrodynamic (2fl-MHD) models of the Helicity Injected Torus experiment (HIT-SI) is presented. HIT-SI is a spheromak current-drive experiment that uses two geometrically asymmetric helicity injectors to generate and sustain toroidal plasmas. The goal of the experiment is to demonstrate that steady inductive helicity injection (SIHI) is a viable method for driving and sustaining a magnetized plasma for the eventual purpose of electricity production with magnetic fusion power. The experiment has achieved sustainment of nearly 100 kA of plasma current for $\sim$1 ms. Fusion power plants are expected to sustain a burning plasma for many minutes to hours with more than 10 MA of plasma current.

The purpose of project is to determine the validity of the single-fluid and two-fluid MHD models of HIT-SI. The comparable size of the collisionless ion skin depth to the diameter of the injectors and resistive skin depth predicates the importance of two-fluid effects. The simulations are run with NIMROD (non-ideal magnetohydrodynamics code with rotation-open discussion), an initial-value, 3-D extended MHD code. A constant and uniform plasma density and temperature are assumed. The helicity injectors are modeled as oscillating normal magnetic and parallel electric field boundary conditions. The simulations use parameters that closely match those of the experiment. The simulation output is compared to the formation time, plasma cur-

rent, and internal and surface magnetic fields. Results of the study indicate 2fl-MHD shows quantitative agreement with the experiment while rMHD only captures the qualitative features. The validity of each model is assessed based on how accurately it reproduces the global quantities as well as the temporal and spatial dependence of the measured magnetic fields. 2fl-MHD produces the current amplification I_{tor}/I_{inj} and formation time τ_f demonstrated by HIT-SI with similar internal magnetic fields. rMHD underestimates I_{tor}/I_{inj} and exhibits a much longer τ_f. Biorthogonal decomposition (BD), a powerful mathematical tool for reducing large data sets, is employed to quantify how well the simulations reproduce the measured surface magnetic fields without resorting to a probe-by-probe comparison. BD shows that 2fl-MHD captures the dominant surface magnetic structures and the temporal behavior of these features better than rMHD.

In addition to the comparisons with the experiment, a detailed investigation of the rMHD and 2fl-MHD models is undertaken. λ ($\mu_0 \mathbf{J} \cdot \mathbf{B}/B^2$) and current density $\mathbf{J}$ are used to track the prominent structures. Both λ and $\mathbf{J}$ show dynamic, periodic patterns with significant toroidal non-uniformities, consistent with the magnetic energy spectrum. A spheromak-like object forms only in the toroidally-averaged sense. This structure never fully detaches itself from the regions directly-driven by injectors. Parameter scans are carried out to chart the dependence of I_{tor}/I_{inj} to plasma resistivity, viscosity, injector oscillation frequency, and the ratio of injector current to injector flux. An energetics analysis based on the evolution of the MHD and Hall dynamos is presented for both models. Results of this analysis indicates a large surge of energy into the spheromak mean-field (the $n = 0$ component) by both dynamos, followed by a steady energy transfer to the $n = 0$ predominantly by the MHD dynamo.

TABLE OF CONTENTS

LIST OF FIGURES

LIST OF TABLES

GLOSSARY

MHD: magnetohydrodynamics.

rMHD: resistive MHD (single-fluid model).

2fl-MHD: two-fluid MHD.

CD: current drive.

I_{tor}: the toroidally-symmetric plasma current, usually plotted as a function of time.

I_{tor}/I_{inj}: current amplification, ratio of I_{tor} to the amplitude of the injected current I_{inj}.

axisymmetric: means toroidally-symmetric.

midplane: the up-down symmetry axis of the device, $z = 0$ m.

n: toroidal mode (wave) number.

$n = 0$: Toroidal mode number (wavenumber) for an axisymmetric component.

HIT-SI: helicity injected torus with steady inductive helicity injection.

SIHI: steady inductive helicity injection.

ME: magnetic energy (usually plotted per toroidal mode n).

KE: kinetic energy.

NIMROD: non-ideal magnetohydrodynamics with rotation-open discussion.

2MHD7.5: this label indicates a two-fluid MHD simulation with $T_e = 7.5$ eV, *mutadis mutandis* for an rMHD simulation.

B: magnitude of the magnetic field.

β: ratio of plasma pressure to magnetic pressure: $p/(B^2/2\mu_0)$.

λ: field-aligned, normalized current density: $\mu_0 \mathbf{J} \cdots \mathbf{B}/B^2$.

I_{inj}: injector current.

ψ_{INJ}: injector flux

λ_{inj}: the ratio of injector current to injector flux: $\mu_0 I_{inj}/\psi_{inj}$. This quantity is a measure of the curl in the injected magnetic field.

K: magnetic helicity.

$\dot{K}_{INJ}$: helicity injection rate.

B_Z: the axial magnetic field (along $hatz$).

B_ϕ: the toroidal magnetic field.

B_θ: the poloidal magnetic field, at the mid-plane $B_\theta = B_z$.

TAU_F: formation time; how long it takes for $I_{tor}/I_{inj} = 1$.

τ_A: global Alfvén transit time; time scale for MHD waves to toroidally cross the domain. MHD instabilities grow at Alfvénic rates as well.

$\tau_{L/R}$: global resistive diffusion time; decay rate of the global axisymmetric magnetic field.

S: $\tau_{L/R}/\tau_A$

IMP: 3-axis internal magnetic probe.

SP: 3-axis surface (magnetic) probe.

BD: biorthogonal decomposition.

O-point: A magnetic null region shaped like the letter 'O'.

ACKNOWLEDGMENTS

I thank my advisor Professor Thomas Jarboe for his support, patience, and many years of instruction, for giving me a lot of latitude in the way I carried out my research, and finally for taking all of us to the space needle for lunch. I thank Professor Brian Nelson for advice and technical support, and for always praising me highly. I especially thank Dr. Charlson Kim for teaching me the ways of NIMROD, for guiding me, for supervising my progress closely even after taking a new job in CA, for providing support when I needed it, and for relentlessly reviewing, revising, and correcting my poster presentations, slides for talks, and dozens of paper drafts. I thank the former and current members of the HIT team and the PSI center, especially Doctors Jonathan Wrobel, Brian Victor, Eric Meier, Wes Lowrie, and Will Hamp, and graduate students Chris Hansen, Aaron Hossack, Kyle Morgan, and Derek Sutherland for their support, assistance, and willingness to come to my rescue whenever I needed help. I also want to thank my fellow graduate students for helping me edit this document. They made invaluable writing suggestions that would have and certainly did elude me. I thank Professor Carl Sovinec and the rest of the NIMROD team for remote assistance and support. I thank the members of the HIT team and PSI Center for being decent folks. I also thank Jonathan Wrobel, Sarp Akcay, Chelsea Anderson, and especially Rachel Ersoff for their help in editing parts of this thesis and other documents out of which parts of this thesis grew. I thank Rachel Ersoff for the support and patience she has shown me during the last six months of my PhD and the care she provided when I was too pressed for time to even feed myself. Finally, I thank the NERSC facilities for the use of their super computers and technical support.

This research is supported by the U.S. Department of Energy.

DEDICATION

For my parents, sister and brother, who have been waiting patiently for my graduation for many years. I could not be who I am and get to where I am today without them. I owe my essence in body and spirit to them.

Chapter 1

INTRODUCTION

1.1 Motivation

Magnetic confinement is one of the foremost candidates for realizing controlled fusion. The tokamak[1] is the magnetic confinement concept that has come closest to achieving conditions for a self-sustained burning plasma (ignition). It is a toroidal confinement device that externally applies a large toroidal magnetic field for plasma stability. Because it is a closed-loop device, it cannot use standard electrodes to drive an electrical current to confine and sustain the plasma against dissipative losses due to the small, but finite plasma resistivity. Instead, it relies on traditional transformer drive, where a solenoid threading the center of the torus, inductively drives an electrical current in the plasma. While, transformers are very efficient for current drive (CD) and work on a simple principle, they can only provide a finite amount of time-varying flux and thus cannot indefinitely sustain a steady-state system. Furthermore, tokamaks cannot be Ohmically (Joule) heated to ignition. They require auxiliary heating methods such as neutral beams or microwave heating[2]. Other toroidal devices like the reversed field pinch (RFP)[3] and spherical tori are also constrained by the limitations of transformers. In addition, the requirement of a central hole for the transformer coils amplifies the fusion reactor's size and makes it prohibitively expensive. Other confinement concepts like spheromaks and field reversed configurations (FRC)[4] make appealing platforms for fusion power generation because of their compact design. The simply-connected geometries of these concepts avoid the use of a transformer. Therefore, spheromaks, FRC's and compact tori require an alternate method for CD.

Current drive in a magnetized plasma requires injection of magnetic helicity, which is the best conserved quantity in a magnetized plasma as first proposed by Woltjer[5] and Taylor[6, 7]. Traditional Ohmic drive used on tokamaks is one example of magnetic helicity injection. Other methods include electrostatic injection with a coaxial gun for spheromaks[8, 9, 10, 11] and spherical tori[12, 13, 14], and inductive methods such as the oscillating field current drive (OFCD) used on the ZT-40M[15] and Madison symmetric torus (MST[16]) RFP's and steady inductive helicity injection (SIHI) on the helicity injected torus (HIT-SI)[17]. A summary of various helicity-injection methods can be found in a review article by Jarboe[18].

Taylor-relaxation theory predicts the final (relaxed) state of an isolated or driven system. However, the complex processes that let the plasma evolve toward a relaxed state are often difficult to measure and quantify. It is in this area that validated models play a vital role by illuminating plasma dynamics that are difficult to measure. Simulations must be run and calibrated against experiments to validate existing models and increase their accuracy. Accurate models can then be used to further the understanding of non-Ohmic current drive methods.

There have been numerous single and two-fluid MHD simulations of relaxation current-drive experiments with varying degrees of effort toward validation. Simulation studies of OFCD[19], sustained spheromak physics experiment (SSPX)[20], rotating magnetic field current drive (RMF) on field-reverse configurations (FRC)[21] and very recently Pegasus spherical torus[22] focused on demonstration of the key characteristics of the experiments and qualitative agreement. The paper by Gray *et al.*[23] on the MHD simulations of 3-D magnetic reconnection and merging in the Swarthmore spheromak experiment (SSX) provides a side-by-side comparison of the measured and simulated magnetic fields at the magnetic probe locations, but only at a single instant during fast relaxation. The authors add that dissipative coefficients in the simulations are "justified only *a posteriori* by comparison of the simulation results against the measurements". Other computational studies of helicity injection

current drive include zero β resistive MHD simulations of an electrostatically-driven spheromak by Sovinec *et al.*[24] and zero β, constant-density MHD simulations by Garcia-Martinez *et al.*[25] that show spheromak formation and sustainment by tangential boundary flows. Missing in all of the work cited above is a systematic comparison of measurements of the global and local signals from the experiments to their synthetic counterparts from the simulations. This is where the present research makes a significant scientific contribution as explained below.

MHD simulations of HIT-SI were first undertaken by V. A. Izzo and T. R. Jarboe[26, 27] using the 3D extended MHD code, NIMROD (non-ideal magnetohydrodynamics with rotation-open discussion)[28, 29, 30]. A resistive MHD (rMHD) model with uniform density and zero temperature was employed. These authors report a favorable scaling of magnetic fluctuations with increasing Lundquist number S. However, they see no plasma current for S comparable to that of the experiment, contrary to what HIT-SI has demonstrated.

The objective of the present research project is the validation of the single-fluid resistive MHD and two-fluid Hall MHD models through comparisons with experimental data. The validated model(s) are in turn used to help understand the physics of SIHI CD in HIT-SI. HIT-SI is a CD experiment that uses two geometrically asymmetric, semi-toroidal helicity injectors to generate and sustain toroidal plasmas via steady inductive helicity injection (SIHI). Magnetic helicity measures the twist in a magnetic field and is the best conserved quantity in a magnetized plasma. Two-fluid effects are important in HIT-SI because the ion inertial length, $d_i = 8$ cm, is larger than or comparable to the length scales of interest, which vary anywhere from the width of the injectors (12 cm) down to the resistive skin depth ($\lesssim 1$ cm). A crucial aspect of the validation is the use of parameters, including transport coefficients that closely match those of the HIT-SI experiment. The only exception to this is the electron mass m_e,

which appears in generalized Ohm's law[†] and is artificially enhanced a hundredfold in the two-fluid simulations for numerical convenience. The assumption of uniform and constant temperature is justified by Langmuir probe measurements[‡]. While the measurements of the chord-averaged electron density n_e by the far-infrared interferometer (FIR) justify the assumption of spatially-uniform n_e, the same measurements also show large oscillations in n_e[31, 32]. Thus, the present validation study is limited in that it does not address the influence of density evolution on the simulation results. Results of the validation study indicate 2fl-MHD shows quantitative agreement with the experimental data while rMHD only captures the qualitative features of the experiment. A detailed examination of the validated model(s) is conducted to understand the mechanism responsible for the generation and sustainment of a significant toroidally-symmetric plasma current, I_{tor} in HIT-SI and whether the method can sustain sufficiently closed flux to provide the confinement necessary for controlled fusion. The results of the single-fluid simulations are also studied to provide a baseline for the simulation work presented here and for further verification of the results and trends with different physical and injector parameters.

1.2 Relevant Concepts

1.2.1 Fundamental definitions

Only the quantities relevant to the present research are defined here. These definitions can be found in any text book on fundamental plasma physics (see texts by Chen[33] and Bellan[34] for further details).

The poloidal magnetic field of a plasma configuration B_θ is the component that wraps around a torus in the shorter periodic direction (the red arrow in figure 1.1). The toroidal component B_ϕ wraps around the torus in the longer periodic direction

[†]This is really the electron equation of motion in the most general sense.

[‡]These measurements have not been published yet.

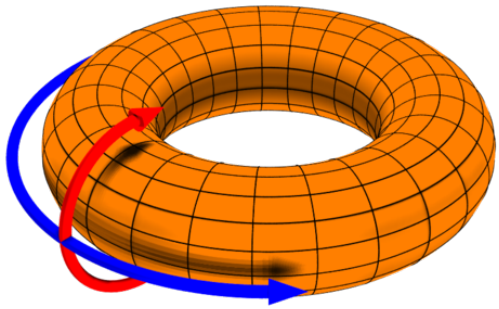

Figure 1.1: Toroidal and poloidal directions in a toroidal coordinate system. Red arrow indicates the poloidal direction and blue the toroidal direction. Image obtained from http://en.wikipedia.org.

(the blue arrow in figure 1.1). A straight cylinder assumption can be made for a large-aspect ratio torus where the toroidal circumference is much longer than the poloidal circumference, *i.e.*, the major radius greatly exceeds the minor radius. In that case, the magnetic field resembles the N-turn wire of a straight solenoid with the axial cylindrical direction ($\hat{z}$) corresponding to the toroidal direction.

A magnetic field with both toroidal and poloidal components is a current-carrying $\mathbf{B}$ and has certain amount of twist associated with it. The 'twistedness' can be measured with the safety factor, q, defined as

$$q = \frac{1}{2\pi} \int_0^{2\pi} \frac{rB_\phi}{RB_\theta} d\theta, \tag{1.1}$$

where r and R are minor and major radii, and θ represents the poloidal coordinate. Essentially, q measures how much current can flow along a magnetic field. An excessive amount of current along the field causes the field to become so twisted that it can no longer stabilize its own kinking perturbations, which eventually destroy the

magnetic configuration. This phenomenon, known as the kink mode, is a fundamental plasma instability. The maximum amount of current in a stable helical configuration is determined by the Kruskal[35]-Shafranov[36] limit.

An MHD plasma in equilibrium is subject to the basic force balance between the gradients of the magnetic stress and hydrodynamic stress, which includes the scalar plasma pressure p:

$$\nabla p = \mathbf{J} \times \mathbf{B} = -\frac{1}{\mu_0} \nabla \cdot \left[\frac{B^2}{2} \mathbf{I} - \mathbf{B}\mathbf{B} \right]. \tag{1.2}$$

A force-free equilibrium is one where $\mathbf{J} \times \mathbf{B} = 0$.

The ratio of the two pressures is measured by the dimensionless parameter β

$$\beta = \frac{p}{B^2/2\mu_0}. \tag{1.3}$$

Most magnetic confinement devices have $\beta \ll 1$.

Some additional terminology will be useful for the reader. Axisymmetric means toroidally-symmetric or a quantity that has $n = 0$ symmetry in the plasma physics parlance where n refers to the toroidal mode (wave) number. Non-symmetric or non-axisymmetric means all the other $n > 0$ modes, frequently referred to as the fluctuations.

1.2.2 Spheromaks

A spheromak, picture in figure 1.2 is a toroidal confinement configuration where no materials, such as the vacuum vessel or magnetic field coils, link the torus. The first wall of a spheromak is topologically equivalent to a sphere. The simply-connected geometry precludes the central hole required for transformer and toroidal field (TF) coils traditionally used in CD in tokamaks and other toroidal confinement devices. As a result, magnetic fields in a spheromak are generated almost entirely by internal currents. The spheromak toroidal and poloidal fields have comparable magnitudes, unlike a tokamak where the externally generated toroidal field is usually an order of magnitude greater than the poloidal field generated by the plasma current. The

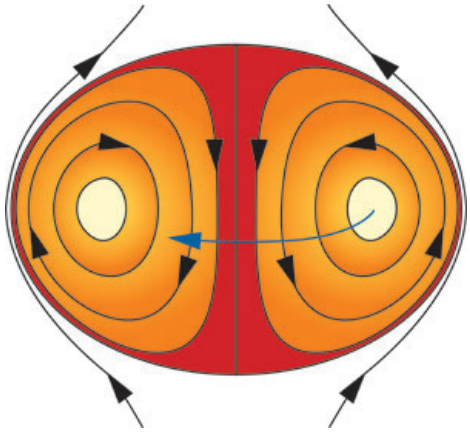

Figure 1.2: A spherical spheromak. The plasma is toroidal but the first wall surrounding the plasma is simply connected. It lacks the central hole that is normally used for TF and transformer coils on a tokamak. The black arrows represent the B_θ and the blue arrow the B_ϕ.

magnetic field is purely toroidal (B_ϕ) at the magnetic axis where the poloidal fields reverse to form an O-point. At the spheromak edge, the field is purely poloidal (B_θ). The O-point of B_ϕ is located near the geometric axis ($R = 0$). At other locations, the magnetic field is helical, having both poloidal and toroidal components. The resulting q decreases toward the edge and is less than one everywhere, opposite to that of a tokamak. Spheromaks have several advantages over tokamaks. The simply-connected vacuum vessel with no central hardware results in a cost-effective, compact device[18]. The equilibrium is not externally generated, which makes TF coils unnecessary. The neoclassical effects, which are a consequence of a large-aspect-ratio toroidal geometry[1] are not very significant in spheromaks. They can be Ohmically heated to ignition (burning plasma), which makes additional expensive auxiliary heating unnecessary. Spheromaks are also ideal MHD stable in the low β limit[37, 38]. There also now exists a theory that can potentially solve the CD problem, *i.e.*, whether nested closed flux surfaces can be stably driven and sustained with fluctuations imposed externally at the plasma edge[31].

Spheromaks also suffer from some drawbacks. They require close fitting walls for stability. The instability associated with the magnetic relaxation enhances transport, adversely affects confinement and should be avoided. Although most spheromaks are low β devices, it has been shown that $\beta \sim 0.2$, far greater than that of tokamaks, can be achieved by shortening the geometric axis[37, 39]. Additionally, spheromak experiments to date have only shown good confinement during decay[40], not sustainment.

1.3 Magnetic Helicity

Magnetic helicity is a measure of the topological properties of a magnetic configuration and is the best constant of motion in a magnetized plasma having low magnetic dissipation (resistivity). Magnetic helicity results from a flow of electrical currents parallel to a pre-existing (vacuum) magnetic field. The field induced by these currents adds a transverse component to the pre-existing field causing it to twist and assume a helical shape, hence the term helicity. It is defined as

$$K = \int_V \mathbf{A} \cdot \mathbf{B} \; d^3r, \tag{1.4}$$

where V is the volume of the domain of interest, $\mathbf{A}$ is the vector potential, and $\mathbf{B}$ is the magnetic field.

The topological aspect of eqn. (1.4) emerges upon carrying out the integral. For two fully linked flux tubes ϕ_1 and ϕ_2, eqn. (1.4), after some algebra[37], reduces to

$$K = 2\phi_1\phi_2, \tag{1.5}$$

where the factor of 2, which is the linkage number, appears because flux tube 1 fully links flux tube 2 and *vice versa*. For partially linked tubes, the linkage number is smaller than 2.

It can be shown with a variational approach, subject to the constraint of magnetic-helicity conservation that the minimum energy state for an isolated, low-β magnetic configuration is force-free ($\mathbf{J} \times \mathbf{B} = 0$) and thus obeys

$$\nabla \times \mathbf{B} = \lambda \mathbf{B} = \mu_0 \mathbf{J}, \tag{1.6}$$

where λ is a global constant and the low-frequency Ampère's law is used to re-express $\nabla \times \mathbf{B}$ as $\mu_0 \mathbf{J}$. Magnetic configurations satisfying eqn. (1.6) are known as Woltjer-Taylor states as this concept was first proposed by Woltjer, then Taylor to explain the reversal observed in an RFP[5, 6]. By taking the dot product of eqn. (1.6) with $\mathbf{B}$, it can be shown that the global constant λ is related to the current density along the magnetic field $j_\parallel$ by

$$\mu_0 \mathbf{J} \cdot \mathbf{B} = \frac{\lambda}{\mu_0} \mathbf{B}^2 \Rightarrow \lambda = \frac{\mu_0 j_\parallel}{B}. \tag{1.7}$$

As the configuration relaxes to the minimum energy state through turbulent activity, the non-uniform λ-profile evolves toward a globally uniform one while conserving the total helicity. This process, termed magnetic relaxation, continues until all of the plasma becomes stable. The final configuration is one where the current density is mostly field-aligned and is nearly force-free [†]. This provides a convenient way of sustaining the plasma (current): drive current high somewhere experimentally convenient in the volume, usually the plasma edge, and let magnetic relaxation drive current elsewhere inside the domain to make the overall λ-profile uniform. Once the instability due to relaxation activity ceases, *i.e.*, the λ-profile becomes mostly uniform, the imposed fluctuations can stably drive and amplify the newly-formed equilibrium to achieve sustained closed flux. This CD method termed the imposed dynamo current drive (IDCD) was recently discovered by Jarboe *et al.*[31]. Unlike the traditional relaxation CD methods, IDCD only relies on unstable relaxation activities for the formation of an initial equilibrium which is then sustained by the imposed fluctuations without further instability.

Eqn. (1.4) is only gauge invariant for an isolated volume, *i.e.*, $\mathbf{B} \cdot \mathbf{n}|_{\text{surface}}=0$ as in a perfectly conducting flux conserver. Eqn. (1.4) does not correctly account for the helicity of flux tubes linked outside. In that case, reference fields need to

[†]Confinement of a hot plasma requires a non-zero pressure gradient. Thus even in a stable, fully-relaxed spheromak $\mathbf{J} \times \mathbf{B}$ cannot exactly be zero.

be employed to construct a gauge-invariant helicity. The reference fields must have the same value of $\mathbf{B} \cdot n$ and $d(\mathbf{B} \cdot n)/dt$ on the surface. Vacuum magnetic fields are a convenient choice for these reference fields. Finn and Antonsen provide the most general gauge-invariant definition of helicity known as relative helicity [41]:

$$K_{rel} = \int (\mathbf{A} + \mathbf{A}_{vac}) \cdot (\mathbf{B} - \mathbf{B}_{vac}) dV. \tag{1.8}$$

Rewrite this as

$$K_{rel} = \int (\mathbf{A} \cdot \mathbf{B} - \mathbf{A}_{vac} \cdot \mathbf{B}_{vac}) dV - \int_S h \mathbf{B} \cdot \hat{n} dS. \tag{1.9}$$

Here the surface term explicitly treats the open flux through the boundary and h is a scalar function. For magnetic fields that have anti-symmetric spatial structure like odd-toroidal dependence, the surface integral has no net contribution to relative helicity.

Conservation of magnetic helicity implies that helicity can only be dissipated by collisional resistive processes[18]. For time scales that extend beyond the resistive diffusion time magnetic helicity must be injected into the volume of interest to achieve a steady state in helicity in order to sustain a magnetic configuration. The rate of change of relative helicity is obtained by taking the time derivative of eqn. (1.14) and substituting $\frac{\partial \mathbf{A}}{\partial t} = -\mathbf{E} - \nabla\phi$ and $\frac{\partial \mathbf{A}_{\rm vac}}{\partial t} = -\mathbf{E}_{\rm vac} - \nabla\phi_{\rm vac}$

$$\frac{dK_{rel}}{dt} = -2 \int_V d^3r (\mathbf{E} \cdot \mathbf{B} - \mathbf{E}_{vac} \cdot \mathbf{B}_{vac}). \tag{1.10}$$

The vacuum term can be rewritten as a surface integral by using $\mathbf{E}_{vac} = -\nabla\phi_{vac}$ and Gauss's theorem.

$$\begin{aligned} \frac{dK_{rel}}{dt} &= -2 \int_V d^3r \mathbf{E} \cdot \mathbf{B} - 2 \int_S d\mathbf{s} \cdot (\phi_{vac} \mathbf{B}_{vac},) \\ &= - \underbrace{2 \int_V d^3r \mathbf{E} \cdot \mathbf{B}}_{\text{Helicity dissipation}} + \underbrace{2\psi_{\rm vac}\phi_{\rm vac}.}_{\text{Helicity injection}} \end{aligned} \tag{1.11}$$

Hence, helicity can be injected into a system through the bounding surface by applying a voltage $\phi_{\rm vac}$ to a vacuum flux $\psi_{\rm vac}$ that intersects the electrodes as in the

case of electrostatic injection. Coaxial helicity injection (CHI)[9, 42] is a common method of electrostatic helicity injection where an axisymmetric vacuum magnetic field crosses and connects coaxial electrodes. The electric field in the electrode region causes the neutral gas to break down and generates a current across the electrodes. The current, in turn, gives rise to a toroidal magnetic field. When the (injector) current is sufficiently large, the Lorentz force due to the radial current and toroidal magnetic field accelerates the plasma downstream into the equilibrium region pulling the magnetic field along.

In electromagnetic (inductive) injection, the vacuum flux links the boundary of the device instead of intercepting the electrodes. Inductive helicity injection has the advantage of applying voltage to closed field lines without the need for electrodes. It reduces the amount of required power as it has no need for high density gas for plasma breakdown[18]. It also eliminates the transport of cold impurity ions from the electrodes to the equilibrium region. Transformer current drive on a tokamak is an example of inductive helicity injection. But, in a tokamak, the fields are mostly externally generated and controlled. The transformer only supplies a finite amount of flux swing, and hence, steady-state operation via the conventional transformer is not possible. Oscillating field current drive (OFCD)[16] and Steady Inductive Helicity Injection (SIHI)[8, 17, 43] are two examples of (electromagnetic) helicity injection.

1.4 Helicity Injected Torus Experiment with Steady Inductive Helicity Injection (HIT-SI)

HIT-SI is a current-drive (CD) experiment that investigates steady inductive helicity injection (SIHI) as a viable method for forming and sustaining toroidal plasmas (spheromaks)[8, 44, 43, 45]. In this respect, the experiment has shown tremendous success by producing and sustaining plasmas with currents as high as 90 kA. CD is accomplished by the injection of magnetic helicity into the spheromak region, completely electrode-free, by two semi-toroidal injectors that are denoted X and Y (figures

1.3(a) and 1.3(b)). All the plasma-facing surfaces are coated with an alumina (Al_2O_3) insulating layer to prevent electrical arcs to the copper walls of the flux conserver and guarantee inductive plasma discharges. The arc-free electrodeless operation makes HIT-SI an ideal platform for clean studies of helicity injection CD and current profile relaxation. The recently-discovered imposed dynamo current drive (IDCD) theory explains how HIT-SI plasmas can be sustained stably by the injector-imposed fluctuations with the possibility of current profile control[31].

HIT-SI flux conserver has three major components: the X and Y injectors whence the plasma is injected and the confinement vessel (volume) where the spheromak forms. The device is a little over 1 m in diameter. A cross section of the flux conserver with relevant dimensions is shown in figure 1.4(a).

Each injector is driven by two circuits: the flux and (loop) voltage circuit. The sets of windings generating the injector flux ψ_{inj} and injector voltage V_{inj} are shown in figure 1.5. The solenoidal flux coils, shown in figure 1.5(a), wind around the injector duct and produce flux inside that links the spheromak flux during operation. The voltage coils, shown in figure 1.5(b), form an air-core transformer with a series of windings which run along the injector and return along the surface of the confinement vessel. Driving current in these coils produces a time-varying magnetic flux through the air core, which induces a loop voltage inside the injector and results in a flow of current parallel to the injected magnetic flux. The overall injector magnetic field twists and as a result becomes helical in shape.

The surfaces of various colors in figure 1.3(b) indicate components of the copper flux conserver that are electrostatically insulated from one another. Insulating gaps (electrical breaks), shown as black dashed lines in figure 1.4(b) are needed on the injectors and confinement volume to allow the oscillating flux and voltage to enter the machine. There is an electrical break around the injector mouths, marked as "V_{inj} gaps" in figure 1.3(a), to prevent the copper from shorting out the injector loop voltage (it is the time derivative of the flux induced by this loop voltage that

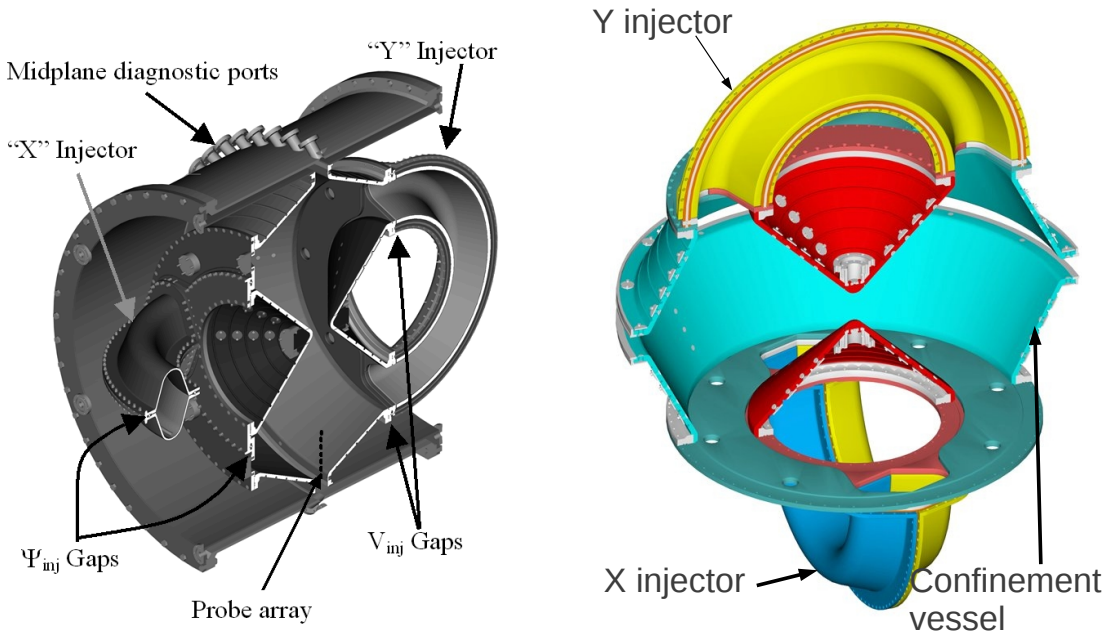

(a) HIT-SI with the vacuum vessel

(b) HIT-SI copper flux conserver

Figure 1.3: A cut-away view of the HIT-SI experiment (a) with and (b) without the stainless steel vacuum vessel. (b) shows the copper flux conserver, which serves as the first wall. The closed fitting walls of the confinement vessel stabilize the spheromak against a torque (tilt instability) caused by image currents that flow on the conducting walls. The shortened geometric axis, which results in the bow-tie poloidal cross section increases the operational β[39]. The X and Y injectors are the semi-toroidal ducts mounted on the top and bottom of the confinement vessel. Each color represents a modular component of the copper flux conserver that is electrostatically insulated from neighboring components to create insulating breaks. These breaks allow the time-varying magnetic flux to penetrate the injectors for SIHI.

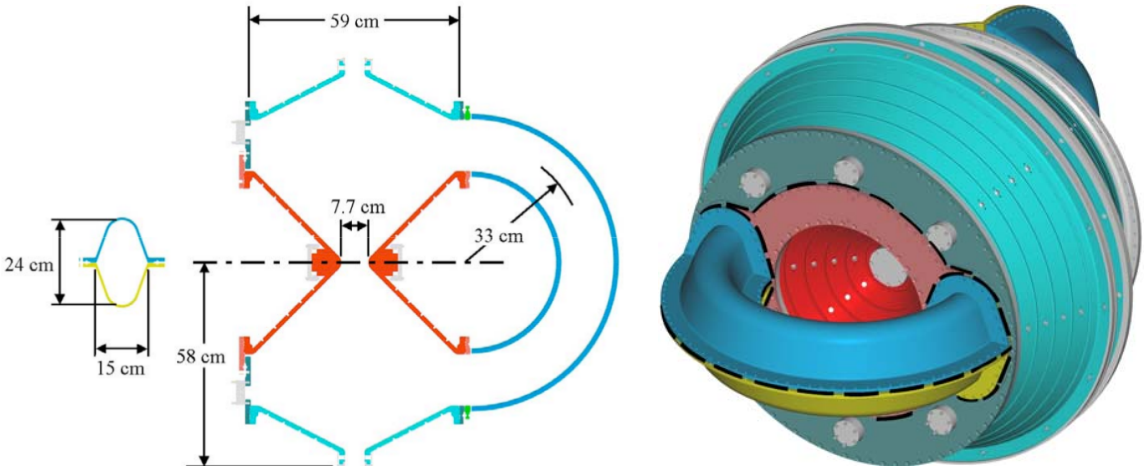

(a) Flux conserver cross section

(b) HIT-SI insulating gaps

Figure 1.4: (a) A cross section of the HIT-SI flux conserver and (b) the insulating gaps (dashed lines) on the flux conserver (drawings by P. Sieck[44] and J. Rogers). Insulating gaps are needed on the injectors and confinement volume to allow the oscillating flux and voltage to enter the machine.

slips through this break). A second electrical break, marked as "ψ_{inj} gaps" in figure 1.3(a), allows the flux into the confinement volume. This break connects the toroidal gaps on the inside of the injectors and those between the salmon-colored small plate and teal-colored large plate on the top and bottom of the confinement vessel (figure 1.4(b)) with the poloidal gaps around the injector mouths. A closed loop of magnetic flux can slip through these breaks in various ways.

The toroidal flux ψ_{inj} and loop voltage V_{inj} of each injector are sinusoidally oscillated in phase at any experimentally realizable frequency. A phase of 90 degrees between each oscillating injector ensures a constant helicity injection rate of $2\psi_{inj}V_{inj}$ (eqn. (1.11)) for symmetric helicity injection, that is, equal X- and Y-injector flux and voltage. This phase difference causes a toroidal rotation of the magnetic field. The standard operational procedure is to drive the X injector with cosine waveforms and the Y injector with sine waveforms. This results in a *modus operandi* where the

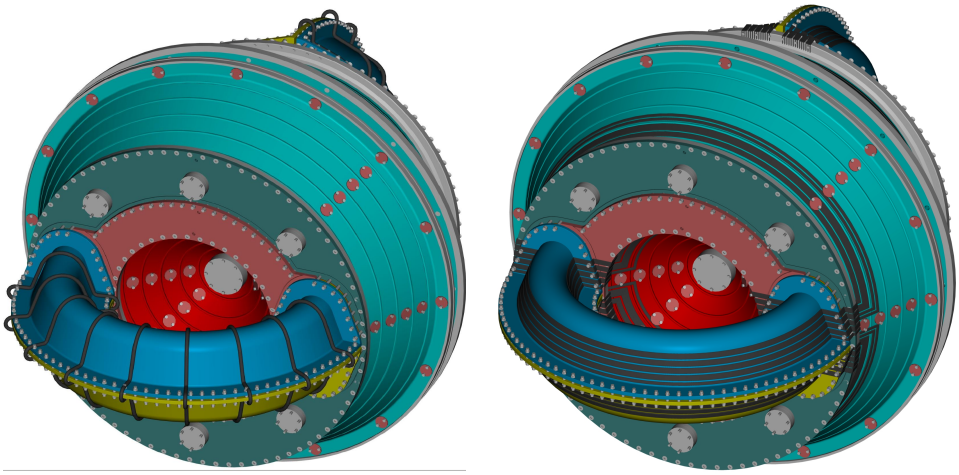

(a) Flux coils (b) Voltage coils

Figure 1.5: (a) The flux coils of SIHI wrap around the injector duct to create a magnetic field along the injector half-torus. The flux enters the injector/confinement region through the insulating gaps that split the injector and the annulus in half. (b) The voltage coils of SIHI are an air-core transformer. The coils go along the injector torus and close the current loop by wrapping half-way around the small (red) and large (teal) cones of the confinement vessel.

X injector leads the Y injector in the their respective injection cycles. The injectors are also spatially rotated 90 degrees with respect to each other to minimize a direct coupling between them. The fluctuations imposed by the non-symmetric injectors stably drive plasma (toroidal) current through dynamo action, eliminating relaxation and instability.

Two metrics of the experiment, relevant for simulations, are the current amplification I_{tor}/I_{inj} and formation time τ_f. I_{tor}/I_{inj} is the ratio of toroidally-symmetric plasma current I_{tor} to the amplitude of the injector current I_{inj}. τ_f measures how long it takes, from the plasma breakdown, to generate significant plasma current such that $I_{tor}/I_{inj} = 1$. Another important metric is the duration of the period with high I_{tor}/I_{inj} (the longer the better). However, this number is not relevant for the present numerical models, which do not include physical effects detrimental to I_{tor} sustainment such as radiation due to the introduction of impurity ions, plasma-wall interactions, density pile-up and neutral-particle dynamics.

The driving circuit for the voltage and flux coils can be modified to operate the machine at any frequency, which so far includes 5.8–68.5 kHz. Power is delivered to the circuits by charging the capacitors in the power supplies. The gas inventory in the machine affects the operation of the injector circuits. Hydrogen, deuterium, helium, and argon gases have been used as fuel although best results were obtained with deuterium. An $I_{tor}/I_{inj} \sim 3$ with $I_{tor} = 55$ kA was achieved during the $f_{inj} = 14.5$ kHz operations with deuterium[32]. An $I_{tor}/I_{inj} \sim 4$ with $I_{tor} = 90$ kA was most recently achieved during the $f_{inj} = 68.5$ kHz operations with deuterium (this work has not been published yet). The focus of the computational work presented in this thesis is the operations with $f_{inj} = 14.5$ kHz. References [17] and [43] are additional papers on the recent results from the HIT-SI experiment.

Comprehensive descriptions of the HIT-SI diagnostics can be found in Refs. [17, 44, 46] and Wrobel's[47] and Victor's[48] theses. A brief description of the diagnostic instruments relevant for the simulations is provided here. The internal magnetic

probe (IMP) is a three-stem array of 3-axis probes located at the toroidal angle $\phi = 225°$, spanning approximately 20 cm between the magnetic axis (plasma core) and the outboard side wall ($R \approx 53$ cm). Figure 1.3(a) shows the location of the IMP array as a black dashed line with the designation "Probe array". Surface magnetic probes (SP's) comprise four poloidal Ampèrian arrays each consisting of 16 3-axis probes located at four toroidal locations, $\phi = 0°$, 45°, 180°, and 225°, on the surface of the flux conserver. Figure 1.6 shows the poloidal and toroidal layout of the SP's, which are represented as green dots. The green L5 and L6 locations have no synthetic counterparts in the simulations because the mid-plane gap is excluded for numerical convenience (figure 2.1(a)). In addition to local measurements of $\mathbf{B}$, the Ampèrian arrays also provide toroidally-localized measurements of the toroidal current via Ampère's law. The I_{tor} from the experiment is computed by averaging over contributions from all four arrays. The ion Doppler spectrometer (IDS) has a 1-meter focal length and intensified CCD detector. Light collected from 20 chords is imaged onto a linear fiber array through a single wide-angle lens to measure ion velocities and temperature. The chords are located at mid-plane and view a region as wide as 35 cm near the geometric axis ($R = 0$).

1.5 The Helicity Balance Model for HIT-SI

The evolution of magnetic helicity for a driven system is governed by eqn. (1.11). By applying this equation to HIT-SI and assuming a steady state K_{rel}, $\frac{\partial K_{rel}}{\partial t} = 0$, an approximate scaling law can be obtained that shows how the spheromak current I_{tor} and current amplification I_{tor}/I_{inj} vary with key parameters like the plasma resistivity η and injector impedance Z_{inj}. This formalism is developed in the following paragraphs.

The helicity injection rate for each injector is $2V_{inj}\psi_{inj}$ and helicity dissipation rate is $K_{rel}/\tau_{L/R}$. $\tau_{L/R}$ is the resistive diffusion time defined as $\mu_0/(\eta\lambda_{sph}^2)$ where η is the plasma resistivity and $\lambda_{sph} = 10.3$ m^{-1} is the lowest eigenvalue of $\nabla \times \mathbf{B} = \lambda_{sph}\mathbf{B}$,

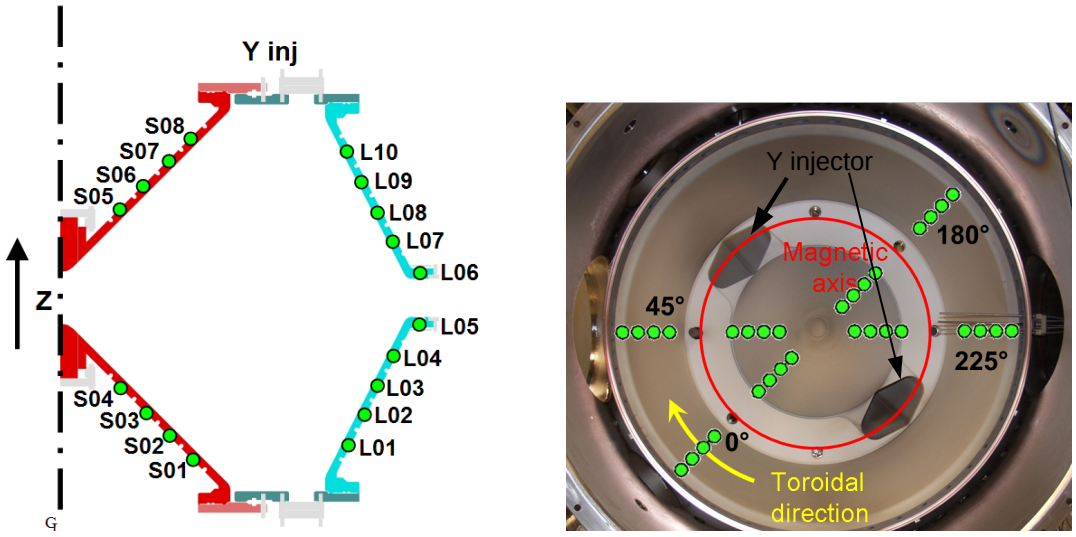

(a) (b)

Figure 1.6: (a) Poloidal layout of one of the four Ampérian surface probe (SP) arrays. SP's are shown as green dots. There are no synthetic probes in the NIMROD calculations that correspond to probes L5 and L6 as the diagnostic gap is excluded from the computational domain. (b) End-on view of the HIT-SI flux conserver showing the toroidal layout of the four Ampèrian SP arrays. Probes at $\phi = 0$ and 180° bisect the X-injector mouths. The $\phi = 45$ and 225° locations are half way between the X- and Y-injector mouths.

i.e., the Taylor state for HIT-SI. Combining the source and sink terms leads to the following equation for the evolution of magnetic helicity

$$\frac{\partial K_{rel}}{\partial t} = 2\left[V_{Xinj}\psi_{Xinj} + V_{Yinj}\psi_{Yinj}\right] - \frac{K_{rel}}{\tau_{L/R}} = 0. \tag{1.12}$$

According to HIT-SI equilibrium calculations by G. Marklin and C. Hansen presented in Ref. [46], the relative helicity in the confinement volume can be expressed in term of the I_{tor} and X- and Y-injector currents, I_{Xinj} and I_{Yinj}, respectively,

$$K_{rel} = C_1 I_{tor}^2 + C_2 I_{Xinj}^2 + C_3 I_{Yinj}^2 + C_6(I_{Xinj} I_{Yinj}). \tag{1.13}$$

Here $C_1 = 3.517 \times 10^{-14}$ represents the spheromak component's contribution to K_{rel}, and the other coefficients are the contributions from the injectors. $C_2 = C_3 = 4.981 \times 10^{-14}$, $C_6 = 3.954 \times 10^{-14}$. The current measurements are all in Ampères. C_6 is the strength of the coupling between the injectors. For symmetric helicity injection, the amplitudes of the X- and Y-injector currents are the same: $|I_{Xinj}| = |I_{Yinj}| \equiv I_{inj}$. Hence, these currents can be added in quadrature. K_{rel} then reduces to

$$K_{rel} = C_1 I_{tor}^2 + C_2 I_{inj}^2 + C_6 I_{inj}^2 sin(2\omega_{inj}t)/2 = C_1 I_{tor}^2 + \underbrace{(C_2 + C_6 f(t))}_{C_{inj}(t)} I_{inj}^2, \tag{1.14}$$

where the explicit time dependence is absorbed into C_{inj} and then neglected for the rest of the derivation. The injector voltage is $V_{inj} = Z_{inj} I_{inj}$ where Z_{inj} is the injector impedance. Combining this with eqns. (1.12) and (1.14) yields

$$2\mu_0 \frac{Z_{inj}}{\lambda_{inj}} I_{inj}^2 = \frac{10^{-14}}{\tau_{L/R}}(3.5 I_{tor}^2 + C_{inj} I_{inj}^2), \tag{1.15}$$

where $\mu_0 I_{inj}/\lambda_{inj}$ is substituted in for ψ_{inj}. Rearranging this equation produces

$$I_{tor}/I_{inj} = \left(\frac{\tau_{L/R}^{1/2}}{\sqrt{3.5}}\right)\left(8\pi \times 10^7 \frac{Z_{inj}}{\lambda_{inj}} - \frac{C_{inj}}{\tau_{L/R}}\right)^{1/2}. \tag{1.16}$$

Eqn. (1.16) indicates that I_{tor}/I_{inj} approximately goes as $\tau_{L/R}^{1/2} \sim \eta^{-1/2}$ for $Z_{inj} >> C_{inj}\lambda_{inj}/(8\pi\tau_{L/R}) \times 10^{-7}$. Helicity balance, as expressed in eqn. (1.16), holds true

regardless of the physical model. The model-dependent dynamic effects are accounted for by the injector impedance Z_{inj} which is where the single and two-fluid scaling differ as will be shown in §3.2 (figure 3.4).

1.6 Overview of this Research Project

A major achievement of this thesis is the validation of the single and two-fluid MHD models and the formulation and application of an efficient technique to determine quantitatively how closely the models capture the physics of HIT-SI. Validation as it is presented here entails comparisons of simulation results to both the global and local quantities to assess quantitatively how well each fluid model reproduces the experiment. The global quantities are the two metrics τ_f and I_{tor}. The local measurements comprise data from the internal and surface magnetic fields

Both the single-fluid and two-fluid models capture the qualitative aspects of HIT-SI: an initial period dominated by the $n = 1$ symmetric injector fields followed by a relaxation event culminating in the amplification of the axisymmetric mode ($n = 0$) and generation of significant I_{tor}. 2fl-MHD yields a τ_f and I_{tor}/I_{inj} that quantitatively agree with the those of HIT-SI, and an internal magnetic structure that resembles that of the experiment. The single-fluid (rMHD) model yields a much longer τ_f than the experiment and yields a lower I_{tor}/I_{inj}, therefore fails in quantitatively capturing the physics of HIT-SI. Further quantification of the simulations with respect to the experiment is achieved by biorthogonal decomposition (BD) of the simulated and measured surface magnetic fields. The emerging spatial and temporal eigenvectors are compared and correlated with experimental data, providing a metric for agreement and a prescription for validation. BD is the most conclusive analysis tool for showing the necessity of two-fluid effects for describing HIT-SI. To the best of the author's knowledge, the BD technique has never been employed as a validation tool, nor has any plasma model of a current drive experiment been validated to the extent presented in this work.

Since plasma temperature T_e (electron plasma temperature strictly speaking) and density n_e are not dynamically evolved, they enter the system of equations as free parameters. To determine the sensitivity of I_{tor}/I_{inj} to T_e and n_e, several values of n_e and T_e, within the experimentally measured uncertainties, are simulated for each model. Scans from the simulations indicate $I_{tor}/I_{inj} \propto T_e^{0.9} n_e^{-0.3}$ for 2fl-MHD and $I_{tor}/I_{inj} \propto T_e^{0.6} n_e^{-1/2}$ for rMHD. In the absence of density evolution, the density scan provides a measure for quantifying the effects of a lower or higher plasma density on the simulation results. The work summarized thus far is the topic of Chapter 3 and was accepted for publication in the September issue of Physics of Plasmas[49].

A detailed examination of the validated two-fluid calculations is provided in Chapter 4. Simulations with resistivities spanning a range from $\eta/\mu_0 = 25$ to 8.8 m^2/s, corresponding to $T_e = 6 - 12$ eV, show very similar spectral signatures (magnetic energy per toroidal mode). Partial parameter scans with respect to viscosity ν and λ_{inj} ($\mu_0 I_{inj}/\psi_{inj}$), the ratio of injector current I_{inj} to flux ψ_{inj}, are presented. The global characteristics are insensitive to a wide range of ν, however exhibit a strong variation with respect to λ_{inj}. Closed flux surfaces occupying a small volume appear intermittently for $T_e \geq 10$ eV. This is a transient effect that lasts a fraction of an injector cycle. However, the duration of the closed flux and the volume of the closed flux region both increase with plasma conductivity (temperature), hinting at the possibility of closed flux sustainment at a high enough T_e. The λ-profile becomes more uniform and less hollow as the simulations progress and an axisymmetric field is amplified. The magnetic field structure resembles that of a spheromak at certain times during an injector period; at other times, however, the injector fields dominate and fill up more of the volume. An energetics analysis based on the evolution of the MHD and Hall dynamos is also presented.

An analysis of a sample rMHD calculation is provided in Chapter 5 as a baseline for all simulations and to touch base with calculations by Izzo and Jarboe [27]. An additional parameter scan in η is run to verify the scaling obtained in

the validation simulations. The baseline rMHD scaling indicates I_{tor}/I_{inj} increases as $I_{tor}/I_{inj} \propto \eta^{-0.65} \propto T_e$. The $\eta^{-0.65}$ scaling differs from the scaling extracted from rMHD validation study ($I_{tor}/I_{inj} \propto \eta^{-0.4}$). The two series of calculations use a different λ_{inj}, which affects the dynamic injector impedance and therefore, is responsible for the difference. Additional parameter scans in λ_{inj} and injector oscillation frequency f_{inj} are carried out to establish trends and obtain scaling laws where appropriate. Scans of f_{inj} and λ_{inj} indicate relaxation activity leading to current amplification ($I_{tor}/I_{inj} \geq 1$) ceases for $\tau_A f_{inj} > 1$ and $\lambda_{inj} \lesssim 20$. The cutoff in λ_{inj}, denoted λ_c, is due to the helicity dissipation overcoming the helicity injection in accordance with the helicity balance model, eqn. (1.16). If $\lambda_{inj} < \lambda_c$ no steady state $n = 0$ with a large I_{tor} forms. λ_c varies with η because the helicity dissipation rate depends on η. Scans also indicate λ_c shows a weak sensitivity to toroidal resolution. The characteristics are robust to permutations of operational parameters like the injector phasing and handidness of the injected helicity. Energetics analysis tracking the flow of dynamo-mediated power and energy indicate electron-fluid dynamo (MHD+Hall dynamos for 2fl-MHD) channels considerably more energy into $n = 0$ than ion-fluid (MHD) dynamo.

Another highlight of the present undertaking is the use of three-dimensional visualization software VisIt[50], which has been essential in complementing the present analyses by identifying prominent structures that would have been difficult to capture with 1-D and 2-D diagnostics. It has been most illuminating to look at the current density $\mathbf{J}$ and λ because the absence of closed flux surfaces and plasma pressure makes the visualization challenging. VisIt analysis shows a high λ region corresponding to the injector current channels and a lower λ region associated with the $n = 0$. The injector current channels, observed in rMHD and 2fl-MHD, have a centerline (mirror) symmetry while the $n = 1$ mode dominates the magnetic spectrum. The mirror-symmetry of the current columns breaks when the $n = 0$ grows to global levels and the injector fields rearrange themselves to become aligned with the spheromak

poloidal and toroidal fields. The low-λ region, associated with the $n = 0$ mode, becomes more uniform, spreading out as I_{tor} increases and has the appearance of a thin and severely tilted spheromak. Regions of very low or negative λ representing image currents associated with injection of current into a conducting medium (plasma) appear throughout the simulations. No closed-flux surfaces are seen during sustainment in rMHD. 2fl-MHD shows a small volume of closed flux near the magnetic axis ($R = 0.325$ m) for $T_e \geq 10$ eV, that continually shifts around as the injectors oscillate.

Another major component of the present work is a basic reactor-scaling study termed 'big HIT', which could be a major milestone for the SIHI program and magnetically confined fusion as a whole. This is a two-fluid calculation with the HIT-SI geometry scaled up by a factor of 2.5 and with an η equivalent to $T_e = 110$ eV, estimated to yield $I_{tor}/I_{inj} = 10$. It has been run for over 30 ms and is by far the longest HIT-SI simulation to date in terms of simulated and computation time. It has achieved $I_{tor}/I_{inj} = 10$ and shows transient closed flux surfaces for $I_{tor}/I_{inj} > 6$. Periods of closed flux last as long as 20 injector cycles (longer than 1 ms) with the closed-flux region occupying nearly a quarter of the total volume. Up to 30% of the total field lines in the volume reach lengths over 2.5 km[†] equivalent to more than 500 toroidal transits during periods of extended closed flux. This is a crucial finding, as parallel (field-aligned) transport is the main cause of particle loss and good confinement in a spheromak requires many hundreds to thousands of toroidal transits for the hot ions.

This remainder of this document is organized as follows. Chapter 2 presents the numerical model including a short introduction to the NIMROD code and zero-β, constant-density extended MHD model and a description of the computational implementation required to model SIHI (§2.3). The validation of the single and two-fluid models via comparisons between the simulation and experimental data is

[†]2.5 km in this case is the cutoff for the line integration.

presented in Chapter 3, followed by a further investigation of 2fl-MHD results in Chapter 4. Chapter 5 contains the results of rMHD simulations starting with the baseline (§5.1) followed by spatial convergence tests, single injector simulations (§5.2), and parameter scans (§5.3). Finally, a summary of the research undertaken and discussion of future improvements are presented in Chapter 6, which also includes the 'big HIT' reactor-scaling study (§6.3).

Chapter 2

THE NUMERICAL MODEL

2.1 The NIMROD Extended Magnetohydrodynamic Model

The present model assumes a fully-ionized (deuterium) plasma of constant uniform density and temperature. Radiative effects and neutral physics are neglected and transport effects only enter through the plasma resistivity and the fluid stress. Under these assumptions, two-fluid MHD reduces to a system with only the pressureless momentum equation and generalized Ohm's law:

$$\frac{\partial \mathbf{v}}{\partial t} + \mathbf{v}\cdot\nabla\mathbf{v} = \frac{\mathbf{J}\times\mathbf{B}}{\rho} - \nabla\cdot\mathbf{\Pi}, \tag{2.1}$$

$$\mathbf{E} = -\mathbf{v}\times\mathbf{B} + \eta\mathbf{J} + \underbrace{\frac{1}{ne}\mathbf{J}\times\mathbf{B}}_{\text{Hall term}} + \underbrace{\frac{m_e}{ne^2}\frac{\partial \mathbf{J}}{\partial t}}_{\text{inertia}}, \tag{2.2}$$

$$\mathbf{J} = \frac{1}{\mu_0}\nabla\times\mathbf{B}, \tag{2.3}$$

where $\mathbf{v}$ is the center-of-mass velocity and ρ the mass density of a plasma with magnetic field $\mathbf{B}$, current density $\mathbf{J}$, and electrical resistivity η. m_e is the electron mass and $\mathbf{\Pi}$ is the hydrodynamic stress tensor representing the viscous effects. Eqn. (2.3) is the low-frequency limit of Ampère's law.

Eqns. (2.1) and (2.2) are solved with the Non-Ideal Magnetohydrodynamics code with Rotation-Open Discussion (NIMROD)[28, 29, 51], a 3-D extended MHD code for studying magnetic confinement configurations. Since NIMROD advances $\mathbf{B}$ and $\mathbf{v}$, $\mathbf{E}$ is eliminated in favor of $\mathbf{B}$ by taking the curl of eqn. (2.2). The resulting equation of motion for $\mathbf{B}$ (induction equation) is obtained by combining the generalized Ohm's

law with Faraday's law: $\partial\mathbf{B}/\partial t = -\nabla\times\mathbf{E} + \kappa_{\mathrm{divB}}\nabla\nabla\cdot\mathbf{B}$

$$\frac{\partial\mathbf{B}}{\partial t} = -\nabla\times\left(-\mathbf{v}\times\mathbf{B} + \eta\mathbf{J} + \frac{1}{ne}\mathbf{J}\times\mathbf{B} + \frac{m_e}{ne^2}\frac{\partial\mathbf{J}}{\partial t}\right) + \kappa_{\mathrm{divB}}\nabla\nabla\cdot\mathbf{B}, \tag{2.4}$$

where the last term is employed to diffuse $\nabla\cdot\mathbf{B}$ errors because the continuous finite element representation of vector components cannot impose a divergence constraint exactly. Here κ_{divB} adjusts the strength of the $\nabla\cdot\mathbf{B}$ diffusion operator.

The last two terms in eqn. (2.2), the Hall term and electron inertia, represent the two-fluid effects. The importance of the Hall term with respect to both $\eta\mathbf{J}$ and $\mathbf{v}\times\mathbf{B}$ must be assessed. The ratios of interest are the resistive Hall parameter $\frac{1}{ne}\mathbf{J}\times\mathbf{B}/\eta\mathbf{J}$, relevant for current drive and the MHD Hall parameter $\frac{1}{ne}\mathbf{J}\times\mathbf{B}/\mathbf{v}\times\mathbf{B}$, relevant for the dynamics. Upon substituting the Spitzer resistivity for η, as is done in Ref. [34], the resistive Hall parameter reduces to $\Omega_{ce}\tau_{ei}$ where Ω_{ce} is the electron cyclotron frequency and τ_{ei} is electron-ion (in this case, electron-deuterium) collision time. For HIT-SI, $\Omega_{ce}\tau_{ei} = 50$, thus the Hall term has a significant impact on current drive. The significance of the MHD Hall parameter is gauged by carrying out a dimensional analysis of the ratio $\frac{1}{ne}\mathbf{J}\times\mathbf{B}/\mathbf{v}\times\mathbf{B}$, which yields d_i/L (see eqn. 2.7)). A similar dimensional analysis is presented in chapter 3 of Ref. [52] and the references therein. The ion inertial length d_i is the length scale over which ions decouple from the magnetic field due to their inertia. L is the characteristic length such as $\frac{B}{\nabla\mathbf{B}}(\sim 5-10$ cm) or the width of a current layer ($\sim$ a few cm). $d_i = 8$ cm for HIT-SI, which yields $d_i/L \sim \mathcal{O}(1)$, which signifies the importance of the Hall term for the dynamics. Thus, one ends up with the following ordering of terms in the generalized Ohm's law: $\mathbf{v}\times\mathbf{B} \sim \frac{1}{ne}\mathbf{J}\times\mathbf{B} >> \eta\mathbf{J}$. A typical two-fluid calculation features flows of several tens of km/s and $\mathbf{J}$ of several$\times 10^5$ A.m^{-2}, yielding $\frac{\mathbf{v}\times\mathbf{B}}{\mathbf{J}\times\mathbf{B}/ne} \sim \mathcal{O}(1)$, consistent with the dimensional analysis.

An interpretation of the Hall term can be obtained by an inspection of the cross-field electric field $\mathbf{E}_\perp$, *i.e.*, the perpendicular component of the generalized Ohm's

law, eqn. (2.2)

$$\frac{\mathbf{E}\times\mathbf{B}}{B} \equiv \mathbf{E}_\perp = -\mathbf{v}_\perp B + \eta_\perp \mathbf{J}_\perp + \frac{1}{ne}\underbrace{(J_\parallel \mathbf{B} - \mathbf{J}B^2)}_{\mathbf{J}_\wedge B}, \tag{2.5}$$

where the inertia term is neglected and the perpendicular component of η[‡] is used. The blue term denotes the Hall term. In rMHD where $d_i << L$, when an external $\mathbf{E}$ is applied, $\eta\mathbf{J}_\perp$ responds first since the blue term is absent. The current penetrates a distance much greater than an ion skin depth (d_i) and the ions respond to the applied $\mathbf{E}$ as quickly as the electrons by being accelerated via the perpendicular component of the momentum equation, eqn. (2.1): $\rho\mathbf{v}_\perp \approx \Delta t \mathbf{J}_\perp B$. The effect of the Hall term is to prevent $\mathbf{J}_\perp$ with a back emf provided by the $\mathbf{J}_\wedge B$ term. Since $\mathbf{J}\times\mathbf{B}/\eta\mathbf{J} \gg 1$, $\mathbf{J}_\wedge B$ takes up most of the $\mathbf{E}_\perp$ and $\eta\mathbf{J}_\perp$ remains small. As a result, the plasma (ion) drift $\mathbf{v}_\perp$ is greatly reduced and only electrons get accelerated (remember $\mathbf{E} = -\mathbf{v}_e \times \mathbf{B}$ since the electron flow $\mathbf{v}_e = \mathbf{v} - \mathbf{J}\times\mathbf{B}/ne$) so long as $d_i \gtrsim L$.

The electron inertia, the last term of eqn. (2.2), breaks the frozen-in flux condition[53]. It scales as $(d_e/L)^2$ according to the dimensional analysis presented on the following page (eqn. (2.7)). d_e is the electron inertial length, which sets the grid size Δx for the two-fluid calculations. Keeping m_e in the calculation retains the natural cutoff at $\omega = \Omega_{ce}$ in the whistler-wave dispersion relation, limiting the high-frequency behavior. Although these time scales are not resolved in NIMROD, m_e is necessary for limiting the condition number of the matrix for the $\mathbf{B}$ advance[51], essential for keeping the iteration count reasonable for each time step. An enhanced electron mass ($m_i/m_e = 36$) is used not only to improve the preconditioning but also to make the induction equation more diagonally dominant for faster matrix inversion during each time step. A mass ratio of $m_i/m_e = 36$ yields $d_e = 1.3$ cm. Going to more realistic mass ratios requires more spatial resolution because d_e scales as $(m_i/m_e)^{-1/2}$. The convergence in m_e has been checked up to $m_i/m_e = 100$ for which $d_e = 0.8$ cm. With-

[‡]For this analysis it makes no difference which η is used as there is only a factor of 2 difference between $\eta_\perp$ and $\eta_\parallel$ and the Hall tern is 50 times bigger than $\eta\mathbf{J}$.

out the Hall and electron inertia terms, eqns. (2.1) and (2.2) reduce to the single-fluid description of a dissipative magnetized plasma, *i.e.*, resistive MHD (rMHD).

The last term in eqn. (2.1) represents the viscous effects due to the hydrodynamic stress. An isotropic stress with the zero-field expression is employed: $\mathbf{\Pi} = -\eta_0 \left(\nabla\mathbf{v} + (\nabla\mathbf{v})^T - \frac{2}{3}\mathbf{I}\nabla\cdot\mathbf{v}\right)$ where $\eta_0 = 0.96nkT_i\tau_i$ according to Braginskii[54], assuming an equal ion and electron temperature: $T_i = T_e$. In NIMROD this is achieved by `nu='iso_visc'` where the viscous dissipation ν in units of m^2/s is set to η_0. The assumption of an isotropic hydrodynamic stress is not a good one because HIT-SI has strongly magnetized ions, *i.e.*, the ion cyclotron frequency is faster than the ion-electron Coulomb collision frequency, resulting in an anisotropic stress dominated by the parallel component. To quantify the influence of the anisotropy on the general characteristics, a 2fl-MHD case with a parallel (along $\mathbf{B}$) viscosity ten times the perpendicular viscosity was simulated. This calculation produced very similar results, not shown here, to those of the 2fl-MHD calculation run with an isotropic stress. It was therefore inferred that the choice of hydrodynamic stress does not strongly influence the results presented in this work.

Two-fluid simulations are computationally intensive and require days of computation on hundreds to thousands of computer cores. A two-fluid calculation with modest parameters, 2×10^5 spatial degrees of freedom, and $m_i/m_e = 36$, takes approximately 40 hours on 700 National Energy Research Scientific Computing (NERSC) computer cores to simulate 1 ms. Calculations with a greater mass ratio or lower resistivity take longer to finish as they require more stringent numerical parameters. rMHD simulations require approximately a quarter of the time it takes 2fl-MHD simulations to complete.

Eqns. (2.1) and (2.4) can be cast into a dimensionless form in terms of an arbitrary magnetic field B_0, density ρ_0, and length L by making the following substitutions: $t \to t/t_A$, $\nabla \to L\nabla$, $\mathbf{B} \to \mathbf{B}/B_0$, $\mathbf{J} \to \mu_0\mathbf{J}L/B_0$ with Alfvén speed $v_A \equiv B_0/\sqrt{\rho_0\mu_0}$

and local Alfvén time $t_A \equiv L/v_A$.

$$\frac{\partial \mathbf{v}}{\partial t} + S\mathbf{v}\cdot\nabla\mathbf{v} = S\mathbf{J}\times\mathbf{B} - Pm\nabla\cdot\mathbf{\Pi}, \tag{2.6}$$

$$\frac{\partial \mathbf{B}}{\partial t} = -\nabla\times\left[-\mathbf{v}\times\mathbf{B} + \frac{\mathbf{J}}{S} + \frac{d_i}{L}\mathbf{J}\times\mathbf{B} + \left(\frac{d_e}{L}\right)^2\frac{\partial \mathbf{J}}{\partial t}\right], \tag{2.7}$$

where the $\nabla\cdot\mathbf{B}$ cleaning term has been omitted for clarity. Four dimensionless parameters emerge: the Lundquist number S, the magnetic Prandtl number Pm, the Hall parameter d_i/L, and electron inertia term d_e^2/L^2 where d_i and d_e are related via $d_e = d_i\sqrt{m_e/m_i}$. Note the emergence of intrinsic length scales d_i and d_e from eqn. (2.7) means 2fl-MHD has dispersive waves, one of which is the whistler wave. There are no intrinsic length scales in the single-fluid model, which only has non-dispersive waves.

$S \equiv \frac{\tau_{L/R}}{\tau_A}$, is the ratio of the resistive diffusion time ($\tau_{L/R}$) to the (global) Alfvén time (τ_A). $\tau_{L/R} \equiv \frac{\mu_0}{\eta\lambda_{sph}^2}$ where $\lambda_{sph} = 10.3$ m^{-1} is the lowest eigenvalue of $\nabla\times\mathbf{B} = \lambda_{sph}\mathbf{B}$, *i.e.*, the Taylor state[6, 37] for HIT-SI. $\tau_A = \frac{2\pi R_0}{v_A}$ corresponds to the toroidal Alfvén transit time, *i.e.*, how long it takes a magnetic disturbance to complete a full toroidal revolution around the confinement volume. v_A is the toroidal Alfvén speed and $R_0 = 0.33$ m is the radial location of the magnetic axis for HIT-SI. τ_A for each simulation is calculated *a posteriori* by using a root-mean-square (RMS), volume-averaged v_A extracted from the total magnetic energy U as follows

$$v_A^2 = \frac{B^2}{\mu_0\rho} \rightarrow \frac{2}{\int\rho dV}\frac{\int B^2 dV}{2\mu_0} = \frac{2U}{M_{\mathrm{tot}}}, \tag{2.8}$$

where M_{tot} is the total mass of the plasma. By substituting these definitions in $\frac{\tau_{L/R}}{\tau_A}$, S is re-expressed as

$$S = \frac{\mu_0}{\eta\lambda_{sph}^2}\frac{1}{2\pi R}\sqrt{\frac{2U}{M_{\mathrm{tot}}}}. \tag{2.9}$$

This is one hundredth the conventional tokamak Lundquist number S^* that uses the major radius to define both $\tau_{L/R}$ and τ_A. S can be scaled by varying either η or v_A. v_A can be adjusted with either the magnetic field ($v_A \propto B$) or plasma density

($v_A \propto \rho^{-1/2}$). The magnetic Prandtl number is the ratio of viscous dissipation to resistive dissipation, $Pm = \nu/(\eta/\mu_0)$. $Pm >> 1$ for HIT-SI plasmas.

There are three time scales of interest in the problem. From fastest to slowest, these are the (toroidal) Alfvén transit time τ_A, injector period τ_{inj}, and resistive diffusion time $\tau_{L/R}$. The separation of these three time scales, $\tau_A < \tau_{inj} \leq \tau_A$ is crucial for relaxation to take place and remains mostly invariant for the series of simulations presented in this work. The only exception to this is the injector frequency scan where f_{inj} is raised until $\tau_{inj} \lesssim \tau_A$. The Sweet-Parker (S&P)[55, 56] reconnection time, $\tau_{SP} = \sqrt{\tau_A \tau_{L/R}} \sim \eta^{-1/2}$, could also be significant as magnetic topology-changing phenomena (magnetic reconnection) occur on S&P rates in rMHD.

The equations are solved in a toroidal geometry defined by (R, Z, ϕ). The periodic coordinate ϕ in NIMROD corresponds to the azimuthal coordinate going in the clockwise direction $(-\theta)$ in a cylindrical coordinate system. To avoid further confusion, all the algebraic manipulations are performed in a cylindrical coordinate system where ϕ denotes the azimuthal coordinate. NIMROD uses high-order finite element (FE) representation to discretize the poloidal plane and Fourier decomposition in the periodic direction. A semi-implicit (SI)[57, 58] time-stepping scheme is used to advance the MHD equations. The SI operator admits considerably larger time steps Δt than otherwise allowed by the fast compressional and shear Alfvén waves in an explicit time-stepping algorithm. NIMROD employs an additional diffusion operator $\kappa_{\text{divB}} \nabla \nabla \cdot \mathbf{B}$ shown in eqn. (2.4) to minimize $\nabla \cdot \mathbf{B}$ errors. κ_{divB} adjusts the strength of the diffusion. It must be approximately equal to $\Delta x^2/\Delta t$ where Δx is the size of a FE cell. $\kappa_{\text{divB}} = 10^4$ m^2/s for the simulations presented in this work. Convergence of the results with respect to κ_{divB} was checked by performing two additional baseline rMHD simulations with $\kappa_{\text{divB}} = 10^3$ and 2×10^5 m^2/s. The following boundary conditions are applied everywhere on the boundary except where helicity is injected: $\mathbf{E} \times \hat{n} = \delta \mathbf{B} \cdot \hat{n} = 0$ and $\mathbf{v} = 0$ on all surfaces where $\delta \mathbf{B}$ represents the change in $\mathbf{B}$ over one time step. SIHI requires additional boundary conditions, described below in

section 2.3.

2.2 The NIMROD Simulation Domain and the 2-D mesh

The simulation domain is shown in fig. 2.1(a). Compare this with figure 1.3(b) to see the differences between the real and simulated geometries. The helicity injectors are excluded from the calculation because NIMROD requires toroidal-uniformity for the simulated geometry. Instead, boundary conditions (BC) mimicking SIHI are applied at the green annular surfaces shown in the figure. The diagnostic gap located at the mid-plane on the outboard side is also removed for numerical convenience. This eliminates the inside corners that cause numerical noise and increase the error in $\nabla \cdot \mathbf{B}$. These are issues Izzo and Jarboe had to contend with in their work[27] as the diagnostic gap was included in their simulation geometry. Figure 2.1(b) is an illustration of the poloidal plane with a typical poloidal mesh used in the simulations. The poloidal mesh includes a 1-mm wide resistive layer that simulates the effect of the insulating coating on the plasma-facing walls of HIT-SI.

An entirely new meshing algorithm was developed for shaped 2-D geometries in NIMROD. The motivation for this was to have an improved mesh for the HIT-SI geometry as well as a general mesh generator in NIMROD that could be applicable to a variety of non-trivial geometries with curvature. The mesh is created by splitting the poloidal domain into smaller 'sectors' that yield the most uniform shapes for FE's, mapping each sector to a logical square, 'blending' the four sides of each logical square via a technique known as the Boolean sum interpolation[59] to obtain logical coordinates for the square, remapping the logical coordinates back to real space, and finally joining the sectors together to form the global poloidal mesh. This technique is a major improvement over the original mesh used in Ref. [27] because it yields uniformly-shaped FE's with computationally-sound (non-negative) Jacobians. It also uses the same physical-to-logical space mapping to lay out the interior nodes of each

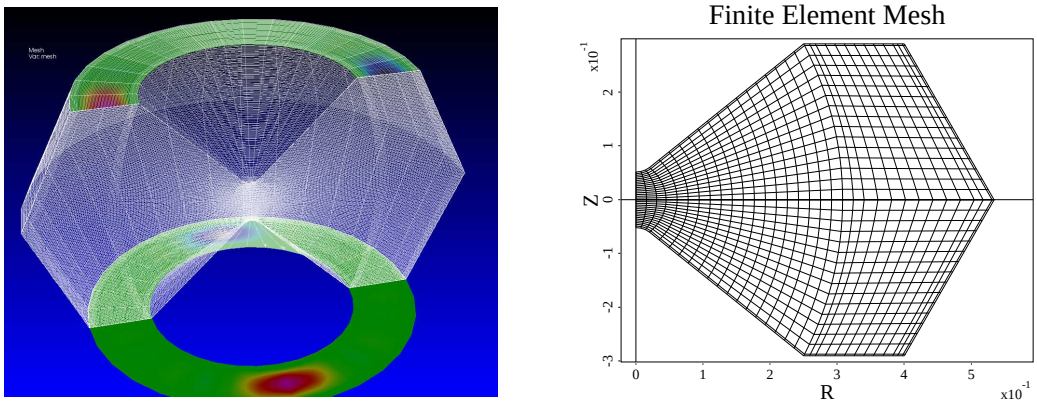

(a) Simulation domain

(b) Poloidal plane

Figure 2.1: (a) The simulation geometry of HIT-SI in NIMROD. The injectors are removed from the domain. SIHI is implemented by applying normal magnetic field (B_n), shown in pseudocolor and tangential electric (E_t) field boundary conditions (BC) applied at the upper and lower annular surfaces (in green) of the flux conserver. The mid-plane diagnostic gap on the outboard side is also removed for computational convenience. Note the bowtie shape. (b) The simulated poloidal plane. The resistive layer is a 1 mm wide thin strip that goes all the way along the boundary. Its thickness is enhanced to 3 mm for the illustration.

FE, thereby preserving the accuracy of the spatial representation[‡]. The new meshing method has made it possible to run large complex 3-D HIT-SI simulations on reliable meshes with clean numeric properties. The algorithm is described in detail with numerous illustrations in Appendix B

2.3 Boundary Conditions for the Numerical Implementation of SIHI

NIMROD implementation of SIHI requires the application of an oscillating normal magnetic field B_n and tangential electric field E_t at the upper and lower annular boundaries shown in green in figure 2.1(a). These overwrite the otherwise conducting BC imposed everywhere. The applied fields must reflect the $n = 1$ toroidal symmetry (odd-symmetry) of the injector fields. This implementation was originally developed by Izzo and Jarboe[26, 27]. Significant algorithmic improvements have been made to the computational mesh, FORTRAN 90 implementation of SIHI in NIMROD, including the elimination of the additional axisymmetric ($n = 0$) E_t, which was previously employed as the seed necessary for the growth of the $n = 0$ mode. The aim of this section is to reintroduce the numerical modeling of SIHI, complement the description by Ref. [27] with additional details and illustrations where necessary, and highlight the differences between the present BC implementation and that of Ref. [27].

2.3.1 Formulation of the tangential electric field E_t

To simulate the injected flux, a surface B_n is applied on the boundary (annular surfaces) as a function of (R, ϕ) and time t. The normal direction is $\hat{z}$, hence $B_n = B_z$. An E_t consistent with B_z is specified according to Faraday's law for $\hat{z}$,

$$\frac{1}{R}\frac{\partial(RE_\phi)}{\partial R} - \frac{1}{R}\frac{\partial E_R}{\partial \phi} = -\frac{\partial B_z}{\partial t}, \tag{2.10}$$

[‡]Other native meshing techniques in NIMROD use a linear mapping to lay out the internal nodes.

where R is the radial and ϕ is the azimuthal coordinate for a cylindrical coordinate system. $B_z(\mathbf{r},t) = B_z(\mathbf{r})e^{i\omega_{inj}t}$ where ω_{inj} is the injector oscillation frequency. Eqn. (2.10) is an underdetermined equation with two unknowns E_ϕ and E_R. The choice of a particular solution determines how electric fields inducing the injector field B_z enter the simulation domain. Choosing $E_\phi = 0$ allows the electric fields to be distributed on the annulus in a manner consistent with the location of the insulating gaps that let the vacuum (injector) flux through the flux conserver of the experiment (see figure 1.4(b)). With this choice, eqn. (2.10) becomes

$$-\frac{1}{R}\frac{\partial E_R}{\partial \phi} = -\frac{in}{R}E_R = -i\omega_{inj}B_z, \tag{2.11}$$

where the Fourier expansion was substituted to carry out the toroidal derivative. Eqn. (2.11) can be rearranged to solve for E_R for $n \neq 0$,

$$E_R = \frac{\omega_{inj}R}{n}B_z(\mathbf{r})e^{i\omega_{inj}t} + \text{c.c.}, \tag{2.12}$$

where c.c. indicates complex conjugation. Both E_R and B_z have odd toroidal symmetry to capture the $n = 1$ symmetry of the injected fields. No additional E_R is introduced for the special case when $n = 0$. The functional form of E_R depends on B_z, which is externally calculated using MATLAB[60]. Figure 2.2(a) represents the output from a flux-injection-only simulation that shows the applied B_z in pseudocolor and total vacuum magnetic field as arrows. B_z clearly has an $n = 1$ structure. Figure 2.2(b) shows the applied surface electric field E_R in black arrows consistent with the B_z on the annulus as required by Faraday's law (2.11). B_z and E_R as a function of ϕ are shown in upper left and lower right panels of figure 2.3. Note that the inclusion of the $n = 0$ bias, as was done in Ref. [27], results in a complete cancellation of E_R on one half of the annulus and a doubling of it on the opposite half. This is indicated by the purple trace in the lower right panel of figure 2.3.

An additional surface term E_t $(= -\nabla_t V)$ is applied on the annulus to simulate a net voltage drop between the two injector openings to drive current along the injector

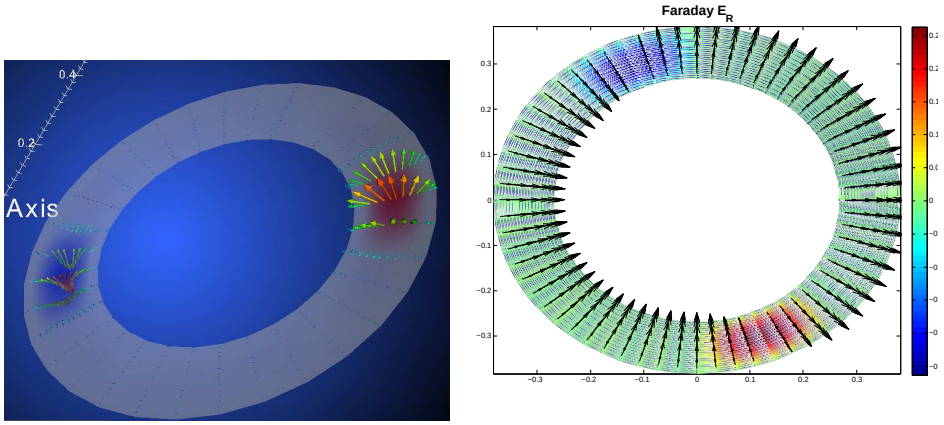

(a) Applied surface B_z

(b) Applied E_t (arrows) consistent with B_z (pseudo-color)

Figure 2.2: The applied normal magnetic and tangential electric field for the flux injection. (a) The pseudo-color plot represents the applied B_z and the arrows indicate the total resulting magnetic field on the annular surface for a flux-injection-only simulation. The colors red and blue represent equal and opposite magnitudes. In this case, B_z is scaled to yield a total magnetic flux of 0.47 mWb. (b) is an end-on view of the domain that shows the surface electric field, E_R consistent with the applied B_z according to Faraday's law (eqn. (2.11)).

magnetic field. Since the tangential gradient ∇_t is two-dimensional, it suffices to specify a surface scalar potential $V = V(R, \phi)$. V is assigned the same spatial profile and temporal dependence as $B_z(\mathbf{r}, t)$ to ensure a flat lambda profile ($\lambda_{inj} \equiv \frac{\mu_0 J_z}{B_z}$) across the injector openings (see Appendix A.1). E_t induces a tangential magnetic field B_t via $\int d\mathbf{S} \times E_t$. This term appears in NIMROD's time-advance for $\mathbf{B}$ as the surface contribution to the integral form of Faraday's law. B_t acts as the injector poloidal field. It induces a normal current J_z required to drive the injector current I_{inj}. The resulting total injected field is helical as indicated in figure 2.4(a), which is an end-on view that shows the vectors of the total applied $\mathbf{B}$ on the annular surfaces to simulate SIHI. Figure 2.4(b) shows the tangential and normal electric fields, E_t and E_z (black arrows), B_t (green arrows), and J_z (pseudocolor) associated with current

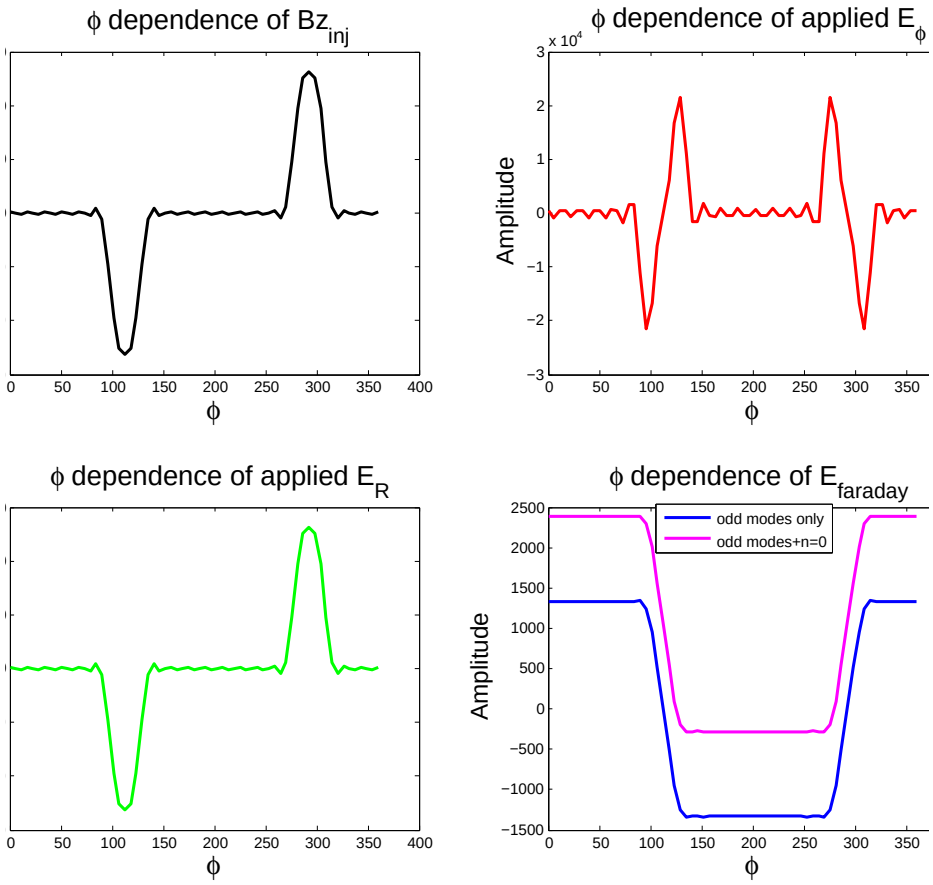

Figure 2.3: Top row: the B_z (left) and E_ϕ for the J_z (right) as a function of ϕ. Bottom row: the E_R for the J_z (left) and E_R for the B_z (right) as a function of ϕ. These are outputs from MATLAB for a 22-mode case. Observe that the inclusion of an (positive) axisymmetric bias E_t shifts the E_R up (blue to purple trace) and shorts it on one half of the annulus.

injection at one injector mouth. The J_z generates an E_z via the resistive Ohm's law, $\mathbf{E} = \eta\mathbf{J}$

By combining the E_t required for current injection with the E_R required for flux injection, a final expression for the total $\mathbf{E}_t$ applied at the annular surfaces is obtained

$$\mathbf{E}_t(\mathbf{r},t) = \left(\frac{R}{in}\frac{\partial B_z}{\partial t} - \frac{\partial V}{\partial R}\right)\hat{R} - \frac{inV}{R}\hat{\phi}. \tag{2.13}$$

Substituting for $V(= aB_z(\mathbf{r},t))$ and the time dependence of $B_z(\mathbf{r},t)$, the total tangential electric field required for SIHI can be expressed as a function $B_z(\mathbf{r})$,

$$\mathbf{E}_t(\mathbf{r},t) = \left[\left(\frac{R\omega_{inj}}{n} - a\frac{\partial}{\partial r}\right)\hat{r} - \frac{ina}{R}\hat{\phi}\right] B_z(\mathbf{r})e^{i\omega_{inj}t}, \tag{2.14}$$

where the numeric constant a with dimensions of m^2/s is used for normalizing V to yield the correct I_{inj}. Eqn. (2.14) indicates that the total applied surface electric field only depends on $B_z(\mathbf{r})$. The next section describes how B_z is calculated.

2.3.2 Normal magnetic field B_z

The functional form of the surface normal field $B_z(\mathbf{r})$ appearing in eqn. (2.14) is obtained by assuming it to be the toroidal field of a force-free ($\mathbf{J}\times\mathbf{B} = 0$), large-aspect ratio (full) torus representing the helicity injectors. This ideal torus is not part of the NIMROD simulation domain. It is used solely as a tool for determining B_z and has the same major radius as the actual injectors and similar cross sectional area (figure 2.5). The fields of the torus are assumed to be axisymmetric. A MATLAB[60] Grad-Shafranov (GS) solver is used to solve the force-free equilibrium

$$\Delta^*\psi + I\frac{dI}{d\psi} = 0, \tag{2.15}$$

where Δ^* is a second-order differential operator, $\psi = \psi(r,z)$ is the poloidal flux function, and I is the poloidal current due to the injector toroidal field. For a force-free configuration with a uniform λ, where $\lambda = \lambda_{inj}$, the following simplifications occur: $\frac{dI}{d\psi} = \lambda_{inj}$ and $I\frac{dI}{d\psi} = \lambda_{inj}^2\psi$. Eqn. (2.15) then reduces to

$$\Delta^*\psi + \lambda_{inj}^2\psi = 0 \text{ with } \psi(\text{wall}) = 0. \tag{2.16}$$

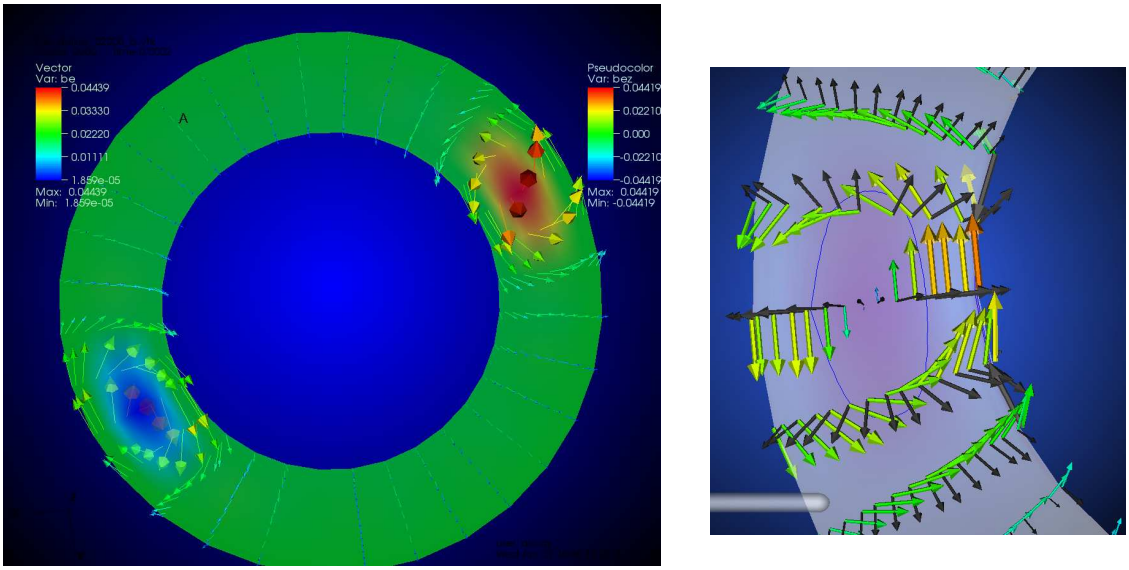

(a) Total surface **B**

(b) Fields associated with current injection

Figure 2.4: (a) Total magnetic field on the annulus as a result of the boundary conditions. Total surface magnetic field on the annulus is helical as a result of the applied B_n and E_t. The blue and red colors span a range of $-0.044 - 0.044$ T. (b) A close-up of an injector mouth showing the surface and normal electric fields, E_t and E_z ((black vectors) associated with the current injection. The E_t induces a surface magnetic field B_t (green, yellow, orange arrows) that acts as the injector poloidal field on the annulus and in turn induces a normal current density J_z (pseudo color) required to drive I_{inj}. The J_z generates to an E_z via the resistive Ohm's law, $\mathbf{E} = \eta\mathbf{J}$.

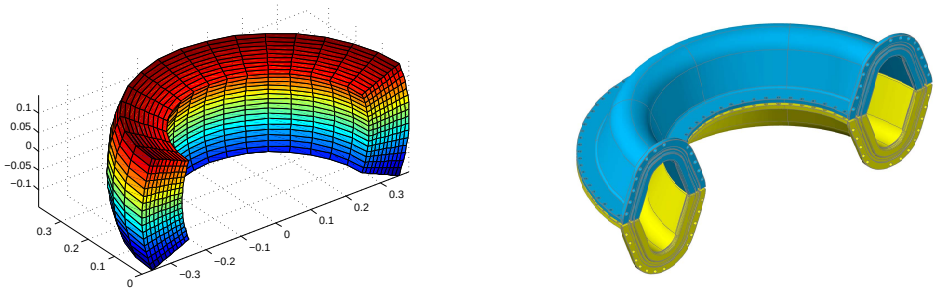

(a) The injector geometry used in the Grad-Shafranov solver

(b) An actual HIT-SI magnetic helicity injector

Figure 2.5: (a) The modeled injector geometry used for the MATLAB equilibrium calculations to solve for B_z. A force-free equilibrium, *i.e.*, $\mathbf{J} \times \mathbf{B} = 0$ is assumed. The actual geometry in MATLAB is a full torus. (b) An actual HIT-SI injector.

The toroidal field of this system $\mu_0 I(\psi)/R$ corresponds the B_z required to simulate SIHI.

Eqn. (2.16) is an eigensystem with a doubly-degenerate eigenfunction ψ with eigenvalues $\pm\lambda_{inj}$. The solution space is a discrete spectrum of λ_{inj} determined by the cross sectional area of the injector opening. The sign of the eigenvalue corresponds to the handedness of the helicity for the solution: + for right-handed and - for left-handed helicity. The former is a configuration where field and current are aligned and the latter a configuration where they are anti-aligned. A further simplification is made by choosing the injector opening to be a 45°-segment of the annulus, a convenient choice that allows separable solutions of radial and azimuthal functions for the injector fields. Figures 2.5(a) and 2.5(b) show a side-by-side comparison of a modeled (half torus) and actual injector from the experiment.

The dimensions of the injector opening are tailored so that the simulated λ_{inj} matches that of the experiment for a solution with no toroidal field at the walls, known as the "spheromak mode" solution with $\lambda_{inj} = 30.0$ m^{-1}. HIT-SI injectors

usually operate at lower λ_{inj} ($15 - 25$ m^{-1}). The geometry allows solutions to eqn. (2.16) for $\lambda_{inj} \geq 24$ m^{-1} for which the injector mouth spans the entire radial extent of the annulus (15 cm). For $\lambda_{inj} < 24$ m^{-1}, a deviation from the spheromak mode is required due to geometrical constraints. This is accomplished by scaling up the injector flux ψ_{inj} while keeping the injector current I_{inj} the same. This method results in an injector state that no longer corresponds to a true injector eigenstate and thus is alluded to as the improper-λ_{inj} solution henceforth. Section 5.3.2 contains a quantitative comparison between an rMHD simulation that uses the proper injector solution with $\lambda_{inj} = 24$ m^{-1} and one with an improper solution with the same λ_{inj}. The differences between the two approaches are minor. Therefore the choice of $\lambda_{inj} = 20$ m^{-1} for the validation simulations presented in Chapters 3 and 4 is justified.

The injector torus pictured in figure 2.5(a) is not part of the NIMROD simulation domain. In order to apply the injector toroidal field as the $B_z(\mathbf{r})$ required for SIHI (eqn. (2.14)), the injector solution is projected onto the two halves of the annulus with opposite signs to impose the $n = 1$ toroidal symmetry. The resulting B_z on the full annulus is expressed as a product radial and toroidal functions. The radial part is fit to a quartic polynomial. The toroidally-varying part of the solution is Fourier decomposed in MATLAB to obtain the coefficients necessary for the toroidal representation of B_z in NIMROD. Only odd modes contribute to the Fourier sum. The mode decomposition is carried out to the highest toroidal mode number allowed in the NIMROD simulation. The finite Fourier representation introduces a truncation error in the toroidal representation. The truncation error is 6% for 11 modes (5 odd modes) and less than 1% for 22 toroidal modes (11 odd modes). The coefficients for the radial fit and Fourier decomposition are then hard-coded into NIMROD. The procedure outlined here has to be repeated each time the total number of toroidal modes in NIMROD is changed.

2.3.3 The Resistive Edge Layer

The insulating layer of the experiment is modeled as a highly resistive edge layer with a resistivity of $9.36\times10^5\mu_0 = 1.176\ \Omega m$ and a thickness of 1 mm, approximately the skin depth of copper at 5 kHz of injector frequency. This edge resistivity is identical to the one used in Ref. [27] and is large enough, approximately 10^5 times the plasma resistivity, to simulate the effects of an insulator. A step function is used for the resistivity profile although other profiles can be specified as well. The orders of magnitude of change in the resistivity over a distance of 1 mm can cause an overshoot in the resistivity profile and lead to noise. The overshoot is eliminated by directly laying the resistivity profile on the FE quadrature points where FE integrations are carried out instead of placing them at the FE nodes.

Another source of concern was a possible lack of resolution in the plasma/edge-interface region where there is a jump in the FE size. A grid packing feature was incorporated into the construction of the poloidal mesh. This additional capability smoothes the transition in FE size between the plasma and edge region and allows more spatial resolution near the injector mouths as indicated by figure 2.6, which shows the upper half of the poloidal mesh for cases with and without grid packing. The poloidal convergence studies (§5.1.5) show the results to be insensitive to grid packing, suggesting that the large resistivity smoothes out the dynamics inside the edge layer and no additional resolution is needed to resolve the regions immediately outside the edge layer.

NIMROD requires a toroidally-uniform resistivity profile. Therefore, there is no break in the insulating layer where the injector openings are located. The large resistivity (impedance) in series with the high voltage sources turns the simulated injectors into a current source and requires the simulated voltage to be many times greater than that of the experiment. As a result, the magnitude of E_t driving the normal current is matched to the injector current (10–20 kA) rather than the injector voltage (250–400

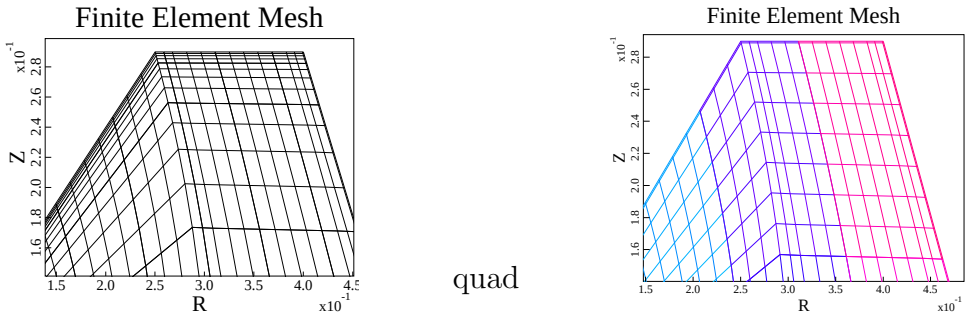

quad

(a) Mesh packed denser toward the injector mouths

(b) Unpacked mesh

Figure 2.6: The upper half of the poloidal mesh (aspect ratio is turned off) with and without mesh packing. (a) A 40×40 mesh with grid packing; the cells monotonically decrease in size to ease the transition in cell size between the plasma/edge region. The cell distribution is based on a hyperbolic tangent function. (b) 40×40 mesh with no grid packing. The cells are nearly the same size all the way up to the resistive edge.

V) of the experiment. Modeling the injectors as high-impedance current sources also prevents the line-tying of magnetic field lines. Without the resistive layer covering the injector mouths, the voltages between individual field lines would be prescribed at the boundary, *i.e.*, field lines would be frozen into the injector mouths from which they originate. In the presence of the resistive layer, the surface can admit parallel electric fields, allowing the potential between field lines to vary, effectively insulating field lines from each other. In this manner, field lines are allowed to move freely and are no longer frozen into the surfaces that they strike. This is a more accurate representation of the experiment where the field lines of the injectors are closed and not tied to a common electrode.

2.3.4 Injector Operation

For each injector, the B_z that generates the injector flux (ψ_{inj}) and E_t that drives the injector current (I_{inj}) are oscillated in phase as sinusoidal functions. The amplitudes of the B_z and E_t are normalized to produce the correct amount of ψ_{inj} and I_{inj}.

The two injectors are driven out of phase by a phase difference that enters as another input parameter, Φ_{inj}. SIHI is achieved when $\Phi_{inj} = |\pi/2|$. For all simulations except those in Chapter 5, $\Phi_{inj} = \pi/2$, *i.e.*, the X waveform leads that of the Y injector's based on the definitions of positive injector flux for each injector[47][†]. Phases other than $\pm\pi/2$ introduce a non-steady component to the helicity injection resulting in less than the maximum allowed helicity injection rate $2\psi_{inj}V_{inj}$. The injectors are linearly ramped up over 0.05–0.1 ms, then operated at constant amplitude (flat-top) for 0.6–1.5 ms, equivalent to one-to-two resistive diffusion times. The ramp-up time is significantly shorter than the relaxation time. In some cases, a linear ramp-down stage of 0.1 ms followed by a decay period of 0.3–0.4 ms is also programmed into the standard injector operational cycle to measure the global $\tau_{L/R}$ for $n = 0$.

2.3.5 Initial Conditions

Because single-fluid MHD dynamo can only amplify an existing seed field, an $n = 0$ perturbation has to be introduced into the simulations to break the strictly odd toroidal symmetry of the injector fields. Formation of an axisymmetric $\mathbf{B}$ requires odd–odd mode coupling of $\mathbf{v}$ and $\mathbf{B}$ via $\nabla \times (\mathbf{v} \times \mathbf{B})$. A toroidally-odd $\mathbf{v}$ in turn, requires a toroidally-even $\mathbf{B}$ via the Lorentz force $\mathbf{J} \times \mathbf{B}$. This is a circular problem and unless the odd symmetry of the $\mathbf{B}$ is broken, the constant-density single-fluid model will never produce an axisymmetric $\mathbf{B}$. Izzo and Jarboe[27] achieve the symmetry-breaking by adding an $n = 0$ bias term to the surface E_R inducing the B_z. This is a special case of eqn. (2.12). It provides a preferred direction for the injector flux to enter the simulation domain because the resistive layer is not a perfect insulator. The continuous injection of the additional $n = 0$ bias is misleading because it gradually builds an axisymmetric field, obscuring an MHD-type activity that would otherwise

[†]In the HIT-SI coordinate system, a positive X flux corresponds to the flux that is aligned with $\hat{x}$ direction of the geometry as the vacuum flux passes between the nose cones ($R = 0, Z = 0$). Similarly, positive Y flux is when Y-injector flux in the confinement volume is aligned with $\hat{y}$ direction as it is passing through the nose cones.

amplify it. Furthermore, in the experiment the injector flux redistributes itself indiscriminately and instantaneously through the perfectly insulating walls. Hence, for the present simulations, an initial perturbation in the form of a low-amplitude Taylor state ($\sim 10^{-6}$ T) is the only place where an $n = 0$ component is introduced. A smaller-amplitude initial condition results in a longer linear rise time until I_{tor} generation, resulting in an even greater disparity between rMHD and the experiment in terms of τ_f. This is a shortcoming of the single-fluid model. 2fl-MHD is insensitive to the initial perturbation because the Hall term readily breaks the odd toroidal symmetry of the magnetic fields and can amplify the $n = 0$ component with $n = 1$ sources. Thus, it is the superior model in this respect. Nevertheless, for consistency the two-fluid simulations are also initialized with the same low-amplitude Taylor state.

Chapter 3

VALIDATION OF SINGLE- AND TWO-FLUID MODEL OF HIT-SI

A paper that presents results and analysis of this chapter has been accepted for publication and is to appear in the September issue of Physics of Plasmas[49]

This chapter is dedicated to validating the single- and two-fluid models of the HIT-SI experiment. Validation through a rigorous comparison to experimental data is the ultimate test of a numerical model's applicability. The key computational and experimental parameters are listed in table 3.1. The models use parameters that closely match experimental ones from an ensemble of the best 14.5 kHz deuterium shots that yielded $I_{tor}/I_{inj} \geq 2.5$: 122354, 122359, 122380, 122385, and 122510. The only exception to this is the electron mass m_e, which is artificially enhanced to $m_i/36$ in the two-fluid simulations for numerical convenience. A constant and uniform plasma temperature T_e and density n_e are assumed. While the assumptions of uniform density and uniform and constant temperature are justified by chord-averaged FIR and Langmuir probe measurements, n_e exhibits large oscillations and therefore, is not constant. Thus, the present validation study is limited in the sense that it does not address the influence of density evolution on the simulation results. This is further discussed in Chapter 6.

Langmuir probe measurements indicate an electron temperature of $T_e = 6 \pm 3$ eV. To determine the sensitivity of I_{tor}/I_{inj} to T_e, which is a free parameter, several values of T_e are simulated for each model to obtain a scaling law for I_{tor}/I_{inj} as was done in §5.3.1. For this purpose, the magnetic dissipation is set to $\eta/\mu_0 = 25$, 17.8, 12.5, and 8.8 m^2/s corresponding to electron temperatures of $T_e = 6$, 7.5, 10, and 12 eV,

Table 3.1: Key computational and experimental parameters for high-performance HIT-SI shots. The first four parameters represent operational parameters related to SIHI. The plasma resistivity η and viscosity ν are expressed as dissipative parameters and calculated using the Spitzer and Bragiinski formulations, respectively. $\sim$ indicates an approximate figure for a given physical quantity and $\eta_{\|}$ means Spitzer resistivity[54]. n_e stands for average electron density. We adhere to Izzo's definitions[27] for τ_A and $\tau_{L/R}$, which are calculated *a posteriori* after the completion of a simulation based. Quadrature λ_{inj} $\left(= \mu_0(\sqrt{I_{injX}^2 + I_{injY}^2}/\sqrt{\psi_{injX}^2 + \psi_{injY}^2}\right)$ is used for the experimental λ_{inj}.

	Simulation	**Experiment**
Injector flux (mWb)	1.2	1.1-1.4
Injector current (kA)	20	19-20
λ_{inj} (m^{-1})	20	15-25
f_{inj} (kHz)	14.5	14.5
n_e (m^{-3})	1.5×10^{19}	$1\text{-}4\times10^{19}$
T_e (eV)	6–12	6 ± 3
Resistivity ($\eta_{\|}$) (m^2/s)	25–8.8	25–9
Viscosity ($\nu_{\|}$) (m^2/s)	260	$\sim$250-1000
$\tau_{L/R}$ (ms)	0.4-2.4	0.4 ($\eta_{\|}$)
τ_A (μs)	8-20	12-30

respectively for a deuterium plasma ($Z = 1$) based on Spitzer resistivity ($\eta \propto T_e^{-3/2}$). The cases with $T_e = 10$ and 12 eV were run to address the possibility of a higher T_e and as additional data points for quantifying the dependence of I_{tor}/I_{inj} on T_e (η). The simulations are labeled rMHD6, rMHD7.5, and rMHD12 for resistive MHD, and 2MHD6, 2MHD7.5, 2MHD10, and 2MHD12 for two-fluid MHD.

The FIR measured density n_e has large oscillations at the injector frequency. For shot 122385, the chord-averaged density n_e gradually rises from $1.7 \pm 1 \times 10^{19}$ to $2.5 \pm 1 \times 10^{19}$ m^{-3} during $t = 0.5 - 1.0$ ms (time as shown in figure 3.6). A time-smoothed trace of n_e from shot 122385 is included in figure 2 of Ref. [31]. $n_e = 1.5 \times 10^{19}$ was chosen for the simulations. Measurements along two separate chords as well as those by the Langmuir probe indicate a spatially-uniform density. To quantify the dependence of I_{tor}/I_{inj} on n_e, additional 2MHD6 simulations with $n_e = 0.7 \times 10^{19}$ and 2.5×10^{19} m^{-3} were run. These values approximately correspond to the range swept by density fluctuations. For rMHD only one additional 2MHD7.4 simulation with a lower density, $n_e = 0.7 \times 10^{19}$ was run, as partial scans indicate $I_{tor}/I_{inj} \propto n_e^{-1/2}$. Neither scan uses parameters that vary from the averages by more than a factor of 2 because staying within the vicinity of experimentally realizable n_e and T_e is key for the present validation work.

First, convergence of the results with respect to poloidal and toroidal resolutions are discussed. This is followed by a presentation of the characteristic results from both models. Both models capture the qualitative aspects of HIT-SI: an initial period dominated by injector fields ($n = 1$) followed by a relaxation event culminating in the amplification of $n = 0$ mode and generation of significant I_{tor} such that $I_{tor}/I_{inj} > 1$ with the exception of rMHD6. 2fl-MHD yields a much larger I_{tor} than rMHD, matching I_{tor}/I_{inj} of HIT-SI and exhibits a τ_f in agreement with that of HIT-SI. rMHD greatly underestimates I_{tor}/I_{inj} and displays a much longer τ_f than observed in the experiment. Parameter scans indicate $I_{tor}/I_{inj} \propto T_e^{0.9} n_e^{-0.3}$ for 2fl-MHD and $I_{tor}/I_{inj} \propto T_e^{0.6} n_e^{-1/2}$ for rMHD. Comparisons between the experiment and

simulations are provided in §3.3 and 3.4. Computational data are not only compared to the global quantities such τ_f and I_{tor}, but also to measurements of the internal and surface magnetic fields to assess quantitatively how well each fluid model reproduces the experiment. Comparisons to IDS-measured ion flows are included as well. Further comparison of the simulations to experiment is achieved by biorthogonal decomposition (BD) of the calculated and measured surface magnetic fields, which is the topic of §3.4. The emerging spatial and temporal eigenvectors are compared and correlated with the data, providing a metric for agreement. BD is the most efficient and conclusive analysis tool for showing the necessity of two-fluid effects for describing HIT-SI. To the best of the author's knowledge, this is the first use of BD as a validation tool.

3.1 Results of the Spatial Convergence Studies for the Validation Simulations

The temporal trace of I_{tor} is chosen to reflect the spatial convergence behavior as the amplitude and rise time of I_{tor} are good indicators of sensitivity to resolution. The temporal trace of I_{tor} from a series of 2MHD6 simulations with various poloidal resolutions, 12×12 biquartic to 48×48 bicubic FE's, is shown in figure 3.1(a). There is very little variation in I_{tor} as a function of increasing poloidal resolution. The robust poloidal convergence behavior of rMHD is documented in §5.1.5.

For both models a poloidal mesh comprising 24×24 biquartic FE's is employed to study toroidal convergence. Toroidal convergence of 2MHD6 has been checked up to a resolution of 86 Fourier modes, corresponding to 256 cells in the toroidal direction with $\Delta x_\phi = 0.8$ cm at the magnetic axis. 2MHD6 exhibits excellent convergence of results with respect to toroidal resolution as evidenced by temporal traces of I_{tor} from four simulations with different toroidal resolutions, plotted in figure 3.2(b). There is little variation in the rise time and final amplitude of I_{tor} with increasing toroidal resolution. Cases with 11, 22, 43, and 86 modes are represented by solid black, red, blue, and green lines, respectively. For 2MHD6 a standard deviation (SD) of 13% is

obtained with respect to 2fl-MHD simulations with higher resolution, better temporal accuracy, and a greater mass ratio ($m_i/m_e = 100$). This number represents a first attempt at estimating the error in the simulations due to discretization errors (DE) and is shown in figure 3.1(b). The blue band represents the standard deviation in I_{tor}. The quoted number is not exact since an exact number requires simulating cases with numerically-inconvenient parameters such as the true mass ratio and smaller time steps. There is no reason to suspect a different convergence behavior for the higher-T_e simulations as 2MHD6 shows consistent behavior with finer toroidal resolutions and $\lambda_{inj} > \lambda_c$ for all 2fl-MHD simulations. However, the SD due to DE may vary for a different T_e.

Toroidal convergence of rMHD6 and rMHD12 has been checked up to a resolution of 43 Fourier modes, corresponding to 128 cells in the toroidal direction with $\Delta x_\phi =$ 1.6 cm at the magnetic axis. rMHD6 displays a complex behavior as indicated by I_{tor} traces displayed in figure 3.2(a). As the mode number is doubled from 11 (solid black) to 22 (dashed red), rMHD6 develops an oscillatory solution instead of one with a large steady-state $n = 0$ component and I_{tor}, observed with 11 toroidal modes. The oscillatory behavior is confirmed by two additional rMHD6 simulations, one with 43 modes (dotted blue) and another with 22 modes and a finer poloidal mesh (36×36 biquartic FE's) shown as the dashed-dotted green trace in figure 3.2(a). The drastic change in relaxation behavior from 11 to 22 modes implies that a minimum of 22 Fourier modes is required to accurately capture the critical λ, which is actually in the vicinity of $\lambda_{inj} = 20$ m^{-1} instead of $\lambda_{inj} = 18$ m^{-1} as was established in §5.3.2. Because of rMHD's heightened sensitivity to toroidal resolution at $\lambda_{inj} = 20$ m^{-1}, only results from rMHD simulations with 43 toroidal modes are included for the validation. The toroidal convergence behavior of the 12-eV calculation is not shown but is consistent with increasing toroidal resolution. Convergence beyond 43 modes is not checked as there is no reason to suspect either rMHD calculation to yield qualitatively different behavior with 86 modes.

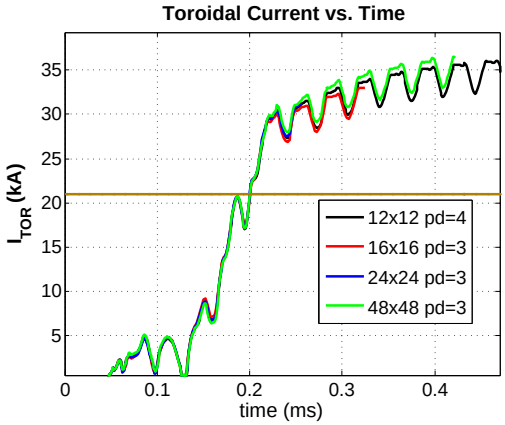

(a) 2MHD6 poloidal resolution

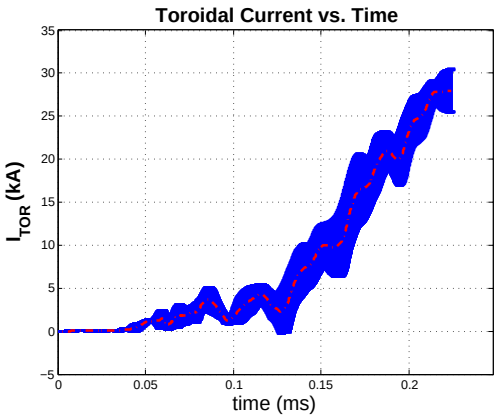

(b) Standard deviation

Figure 3.1: (a) I_{tor} as a function of time (ms) as calculated from a series of 2MHD6 calculations with different poloidal resolutions. The results have converged with a mesh comprising 12×12 biquartic FE's. (b) Standard deviation in I_{tor} as a function of time (ms) as calculated from all 2MHD6 simulations with different spatial and temporal resolutions as well as from a case with $m_i/m_e = 100$. This is a first estimate to quantify the discretization error in 2MHD6 calculations

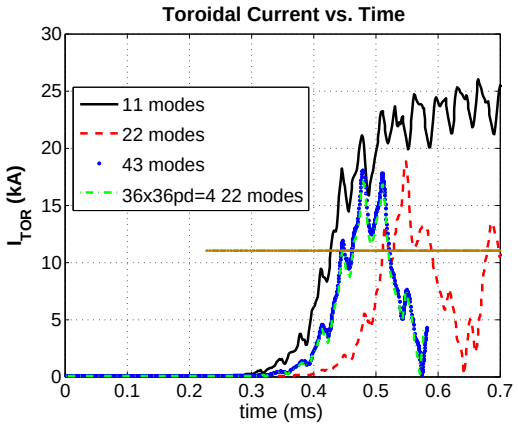

(a) I_{tor} vs. time for rMHD

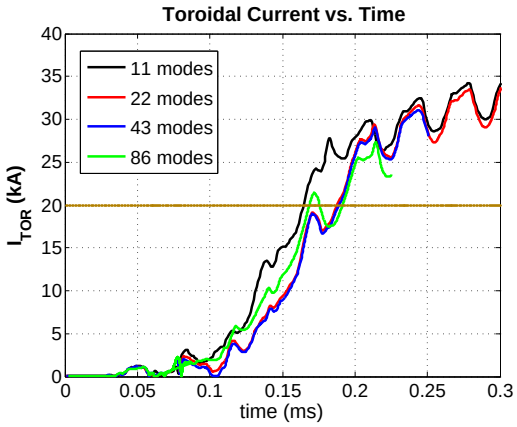

(b) I_{tor} vs. time for 2fl-MHD

Figure 3.2: I_{tor} as a function time (ms) from a series of (a) rMHD and (b) 2fl-MHD simulations with 11, 22, 43, and 86 toroidal Fourier modes respectively. rMHD has only been simulated up to 43 modes. 2fl-MHD shows convergence with 11 modes. rMHD shows consistent behavior going from 22 to 43 modes. Note that the time basis for 2fl-MHD is different from that of rMHD. An additional rMHD simulation with 36×36 biquartic FE's and 22 Fourier modes also shows similar and consistent behavior with the case with 43 modes and 24×24 biquartic FE's.

3.2 Characteristics Results of the single and two-fluid Validation Simulations

Simulations presented in this section use 24×24 biquartic ($pd = 4$) FE's to discretize the poloidal plane and 43 and 11 Fourier modes to discretize the toroidal direction for rMHD and 2fl-MHD, respectively.

The ME spectra from both models feature a period where the injectors couple to the $n = 1$ eigenmode and amplify it, resulting in a magnetic spectrum initially dominated by the $n = 1$ and a large energy difference between odd and even-symmetry modes. The $n = 1$-dominated period is followed by a relaxation event featuring the linear growth and nonlinear saturation of the even-symmetry modes culminating in an axisymmetric ($n = 0$) minimum energy state containing the magnetic helicity.

The formation of a large steady-state $n = 0$ component with significant I_{tor} ($I_{tor}/I_{inj} > 1$) is determined by whether helicity injection can overcome helicity dissipation in accordance with the helicity balance model[45]. Since the injector current amplitude is fixed, the amount of injected helicity depends on the injector impedance Z_{inj} which in turn depends on λ_{inj} and Ohm's law. The model dependence of Z_{inj} is discussed in the last paragraph of this section and illustrated in figure 3.4. It is crucial for all validation calculations to satisfy the impedance criterion to achieve current amplification, the most vital feature of HIT-SI. This holds true for all simulations except rMHD6, which is an example of a case with insufficient Z_{inj}. In this case, $\lambda_{inj} = 20$ m^{-1} cannot provide enough impedance for the I_{tor} generation. An oscillating configuration without a steady-state $n = 0$ or I_{tor} is produced where the helicity is passed back and forth between the $n = 0$ and $n = 1$. The other rMHD simulations with $T_e > 6$ eV have a lower magnetic dissipation, and therefore, $\lambda_{inj} = 20$ m^{-1} is high enough to satisfy the impedance criterion for $n = 0$ amplification. **In short, the single-fluid description fails in demonstrating the most prominent feature of the experiment for $T_e = 6$ eV.** This is the second shortcoming of rMHD; re-

call the first is the dependence of rMHD on the amplitude of the initial perturbation discussed in §2.3.5. Therefore, the comparisons between the models and experiment will be focused on the 7.5 eV calculations along with some results from the 12 eV simulations as an example of higher current amplification.

The evolution of the magnetic energy spectrum is inspected first. Figures 3.3(a) and 3.3(b) show the natural logarithm of magnetic energy (ME) per toroidal mode as a function of time in ms for a 43-mode rMHD and an 11-mode 2fl-MHD calculation with $T_e = 7.5$ eV. Only the first 11 toroidal Fourier modes are plotted. $\tau_A = 14$ μs for rMHD and 11 μs for 2fl-MHD. To facilitate the analysis, the mode evolution from rMHD7.5 is divided into three distinct stages each separated by a dashed vertical line shown in figure 3.3. Since these stages are clearly distinguishable from one another in rMHD, the characterizations are based on rMHD, and compared and contrasted with 2fl-MHD.

Stage I

Stage I corresponds to the pre-relaxation phase. It features a rapid linear growth across the entire toroidal spectrum during the first 0.05 ms ($4\tau_A$) while the injectors ramp up. The magnetic energy is entirely in the odd-symmetry modes at this time due to the odd-symmetry of the injector fields. As a result, all of the injected helicity builds the $n = 1$ at first, the lowest odd-symmetry state, which dominates the magnetic spectrum during stage I. The $n = 1$ ME reaches steady-state in approximately 0.5 ms (twice the energy e-folding time), when the helicity injection and dissipation rates match. As the $n = 0$ seeds all the even-symmetry modes due to the coupling of $\mathbf{v}$ and $\mathbf{B}$ in rMHD, $n \geq 2$ even-numbered modes only get as large as the initial $n = 0$, which shows very little activity during the first half of stage I. The resulting ME and KE spectra display a large energy difference between odd and even-symmetry modes. The even-symmetry modes begin to grow at the MHD growth rates ($\gamma\tau_A \simeq 1$ with $\gamma =$ 60 kHz) at $t = 0.18$ ms ($14\tau_A$). Some of the peculiar features such as the interruption

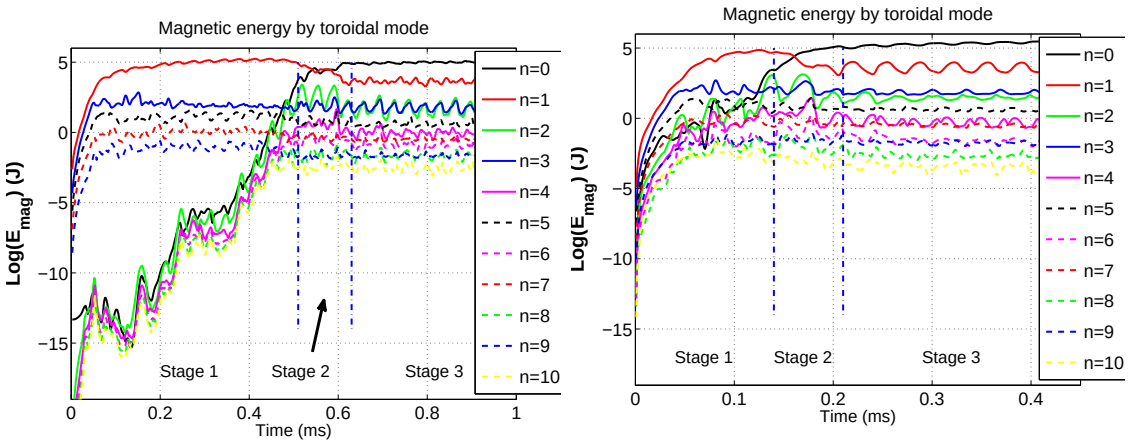

(a) ME spectrum for rMHD7.5

(b) ME spectrum for 2MHD7.5

Figure 3.3: Natural logarithm of magnetic energy per toroidal mode as a function of time (ms) from (a) rMHD7.5 and (b) 2MHD7.5. The spectrum is initially dominated by $n = 1$ mode, which is directly driven by the injectors. 2MHD7.5 achieves $n = 0$ amplification and I_{tor} generation much earlier in time than rMHD7.5. The traces for 2MHD7.5 are shown over a shorter time period to magnify stages I and II.

of the linear growth at $t = 0.27$ ms and the ensuing stagnant period exhibited by the even-symmetry modes before 0.4 ms are not well understood. However, they have no effect on the general trends described here as they occur in modes (wavelengths) with negligible energy. Stage I ends at $t = 0.51$ ms ($36\tau_A$) as the $n = 0$ starts taking energy from the $n = 1$.

2MHD7.5 ME spectrum displays similar features to rMHD7.5, although this is not immediately obvious from figure 3.3(b). It exhibits a similar but shorter stage I with comparable linear growth rates for the even-symmetry modes. All of the magnetic helicity and most of the ME initially accumulate in the $n = 1$, which dominates the ME spectrum in stage I. Numerous small-scale current filaments associated with the reversals of the injector flux appear periodically during this stage, in synchrony with

the injector oscillations[†]. The flux comes from the resistive walls and advances toward the core of the plasma.

Stage II

In stage II the $n = 0$ ME has grown large enough that the injectors can no longer supply the MHD growth power necessary to sustain it and its growth slows to a Sweet-Parker-like rate as it takes ME from the $n = 1$ through reconnection. This is a global reconnection event that causes the configuration to relax to a spheromak-like state as a result of the nonlinear $n = 1$ interactions similar to that seen in CHI discharges[61, 62]. In the meantime, the growth of $n \geq 2$ even-symmetry modes saturates. As the magnetic helicity flows from the $n = 1$ to $n = 0$ the excess energy is dissipated via a normal cascade, successively exciting $n \geq 2$ modes and leaving the $n = 0$ with all of the magnetic helicity and minimum energy. The energy cascade is signaled by bumps appearing in the $n = 2$ ME (green) trace at the beginning of stage II and later in the $n = 3$ and $n = 4$ (blue and purple) ME traces near the end of stage II shown in figure 3.3(a). Significant toroidally-averaged plasma current I_{tor} ($I_{tor}/I_{inj} > 1$) is generated as a consequence of the $n = 0$ amplification. Recall the time it takes to achieve $I_{tor}/I_{inj} > 1$ is defined as the formation time τ_f, which is nearly coincident with the end of stage II. For rMHD7.5 $\tau_f \approx 0.60$ ms ($43\tau_A$). Stage II ends at $t = 0.63$ ms ($45\tau_A$).

The duration of stage II is $7\tau_A$ for 2MHD7.5, nearly the same as in rMHD7.5 ($8\tau_A$). It features a similar energy transfer from the $n = 1$ to $n = 0$ which generates significant I_{tor}. Similar bumps in $n \geq 2$ modes representative of the energy cascade to shorter wavelengths appear.

[†]These current filaments are expected to appear in rMHD as well since the injectors are modeled identically for both models.

Stage III

Stage III corresponds to the post-relaxation phase featuring the steady-state sustainment of the $n = 0$ and I_{tor} against resistive decay by SIHI fluctuations. Figure 3.4 shows the temporal traces of I_{tor} from rMHD7.5, 2MHD7.5, rMHD12, and 2MHD12. The $n = 0$ ME no longer grows in stage III for rMHD7.5 because the total magnetic helicity and energy have attained steady-state in stage I. The remaining ME in the $n = 1$ corresponds to the energy of the pure injector state, which is proportional to $I_{inj}\psi_{inj}$ and therefore, the same for all validation calculations. Local reconnection events that align the injector currents with the I_{tor} periodically occur during this stage. Note that the $n = 1$ ME trace exhibits a frequency-doubling once the $n = 0$ is amplified. It is unclear what causes this effect.

In 2MHD7.5 stage III begins much earlier than rMHD7.5 at $t = 0.21$ ms ($19\tau_A$). It exhibits an ME spectrum that closely resembles that of rMHD7.5 with a dominant $n = 0$ and a large stable I_{tor}, sustained by injector fluctuations without further instability. Similar local reconnection events take place here as well. The frequency-doubling is not encountered in 2MHD7.5. The dispersive waves arising from the two-fluid effects such as the whistler wave could responsible for the absence of frequency-doubling.

The multi-stage relaxation event described above for either fluid model is common to all single- and two-fluid simulations that show an amplification of the $n = 0$. Some features of interest may very with simulation parameters, such as the early stages of the linear growth phase, and the start times and duration of the characteristic stages. However, the general characteristics remain the same. In summary, for $T_e \geq 7.5$ eV both models successfully capture the single most important property of the experiment: *amplification of an axisymmetric magnetic component and sustainment of toroidally-symmetric plasma current with steady inductive helicity injection.* For $T_e = 6$ eV, only 2fl-MHD shows full relaxation.

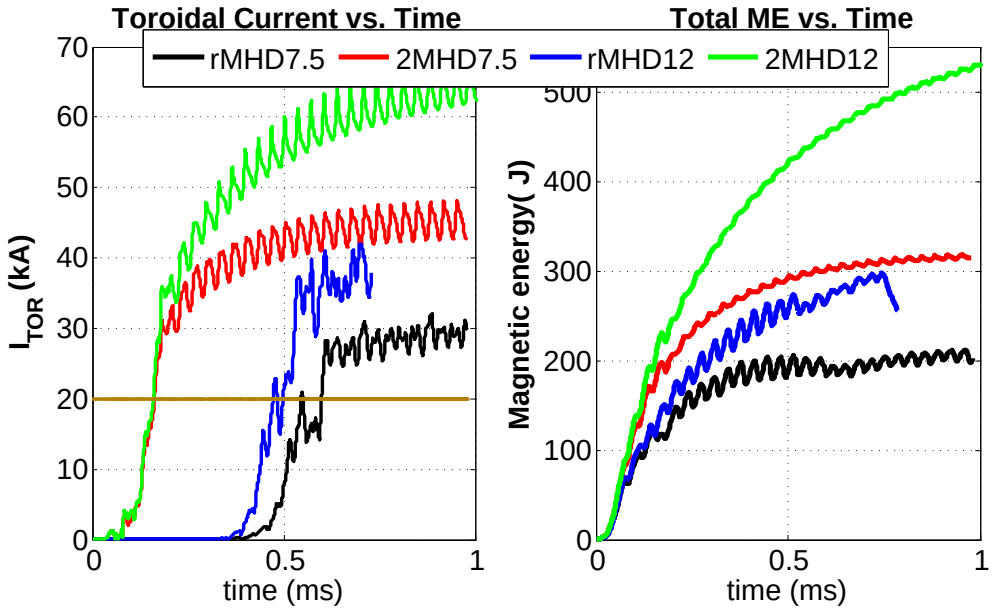

Figure 3.4: (a) I_{tor} and (b) total ME as a function of time (ms) from all four validation simulations. The black, red, blue, and green lines correspond to rMHD7.5, 2MHD7.5, rMHD12, and 2MHD12, respectively. 2fl-MHD yields more I_{tor} and total ME than rMHD because of greater injector impedance. The horizontal brown line in (a) corresponds to the amplitude of I_{inj} (20 kA).

Once it grows, I_{tor} maintains its direction. Injector oscillations appear as small amplitude fluctuations ($< 10\%$) on top of the DC component. This result is in stark contrast to rMHD calculations of OFCD that show substantial oscillations of the plasma current ($\sim 50 - 100\%$) for comparable or larger S[19]†. Directly driving the $n = 1$ mode on edge instead of the equilibrium gives SIHI an advantage over OFCD. The imposed SIHI fluctuations can sustain a stable equilibrium.

The local plasma current I_p from both models exhibits strong toroidal non-uniformities, indicated by plots of I_p vs toroidal coordinate ϕ, shown in figure 3.5. Traces of I_p from five different times during the tenth injector cycle from both rMHD7.5 (figure

†The S scans from the simulations indicate an inverse scaling of oscillations with S for SIHI.

3.5(a)) and 2MHD7.5 (3.5(b)) are plotted. Each trace is separated exactly by one quarter injector period ($\tau_{inj}/4 = 17$ μs) and shows a toroidal displacement of the prominent structure by 90°, as indicated by the black arrow. This implies a clockwise toroidal rotation of the prominent structure, caused by the out-of-phase operation of the injectors ($\Phi_{inj} = 90°$). This rotation, confirmed by the dual- and single-injector rMHD simulations of Chapter 5, is one of the key dynamics of the simulations and consistent with the experimental design of the injectors. The rotational period is τ_{inj} as evidenced by the two overlaying traces (solid black line and purple trace with crosses) separated in time exactly by τ_{inj}. The regions of maximum I_p is where both injectors' currents contribute to the I_{tor} (recall injector currents are aligned with the I_{tor} in stage III). The regions of minimum I_p correspond to the current that is generated as an outcome of $n = 0$ amplification. Similar non-uniformities in the plasma current are also observed in the experiment.

3.2.1 Discussion of the Effect of the Hall Term

The additional Hall term in the generalized Ohm's law (eqn. (2.2)) is responsible for the differences in the two models, as indicated by figures 3.3 and 3.4. This can be seen by inspecting the linear and nonlinear coupling of the major toroidal modes ($n \leq 1$) in eqns. (2.1)–(2.2) during stage I and first half of stage II, while the $n = 1$ mode still dominates the magnetic spectrum. The induction equation, curl of eqn. (2.2) and the momentum equation, eqn. (2.1), are integrated in time via a finite-difference method to obtain approximate expressions for the $n = 0$ magnetic field (B_0) and $n = 0, 1$ velocity (v_0 and v_1). Contributions from $n \geq 2$ are neglected. The letter n is dropped from the subscripts denoting the Fourier coefficients for brevity as well as the cross product signs and vector symbols. The governing equations of the system reduce to

$$B_0 \approx \Delta t \nabla \times \left[-v_0 B_0 - (v_1 B_{-1} + \text{ c.c.}) + \frac{1}{ne}\{J_0 B_0 + (J_1 B_{-1} + \text{ c.c.})\} \right] \qquad (3.1)$$

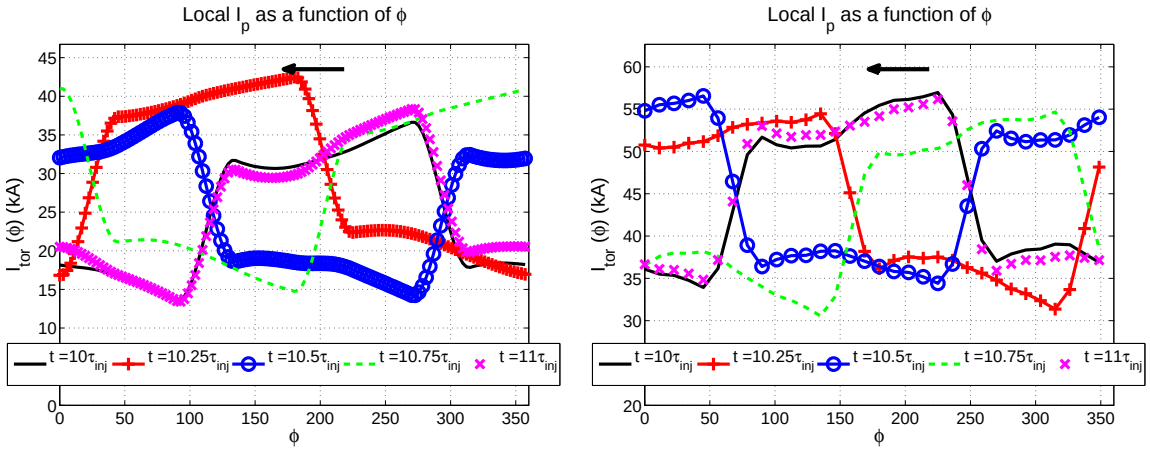

(a) I_{tor} vs. ϕ for rMHD13

(b) I_{tor} vs. ϕ for 2MHD13

Figure 3.5: Toroidal plasma current as a function of the toroidal coordinate ϕ from five different times during the tenth full X-injector cycle from (a) rMHD7.5 and (b) 2MHD7.5. The plasma current exhibits substantial non-uniformities with respect to ϕ. The black arrow indicates the direction of toroidal rotation. There are more data points in (a) than (b) because rMHD7.5 uses 43 toroidal Fourier modes, four times the toroidal resolution used in 2MHD7.5.

$$v_0 \approx \frac{\Delta t}{\rho}[J_0 B_0 + (J_1 B_{-1} + \text{ c.c.})] \tag{3.2}$$

$$v_1 \approx \frac{\Delta t}{\rho}[J_1 B_0 + J_0 B_1] \tag{3.3}$$

where the blue terms represent a direct or indirect consequence of the Hall term. B_1 and J_1 are directly driven by the injectors; B_0 and J_0 have to grow out of ideal or non-ideal MHD effects.

An inspection of eqns. (3.1)–(3.3) reveals two major effects of the Hall term. 1) In the Ohm's law, eqn. (3.1) there is an immediate generation of the B_0 (and other even-symmetry magnetic modes) by the Hall term which nonlinearly couples the $n = 1$ (and the other odd-symmetry) source terms together. This gives rise to a much larger initial B_0 and a much smaller energy difference, spanning only 6 orders of e-folding instead of 20, between odd- and even-symmetry toroidal modes.

2) In the momentum equation the B_0 generated by the Hall term gives rise to an $n = 1$-symmetric Lorentz force that builds up v_1 (eqn. (3.3)). The augmented v_1, in turn, enhances the MHD dynamo, $v_1 B_{-1} + v_{-1} B_1$, which plays as essential a role in the $n = 0$ amplification as the Hall dynamo. The v_1 is initially absent in rMHD due to the lack of a sufficiently large $n = 0$ component because of the strict odd toroidal symmetry of the injector drive. In fact, the evolution of the kinetic modes in rMHD mirror those of the magnetic modes with the roles of even- and odd-numbered modes switched. The v_0 term, eqn. (3.2), is only included for completeness and does not play a key role in the evolution of B_0. Note introducing an externally-driven axisymmetric term such as the $n = 0$ surface electric field used in Ref. [27] achieves similar effects to the Hall term. It increases the v_1 flows and provides a large B_0 initially, hence, enhances both the symmetric and nonlinear MHD dynamo terms appearing in eqn. (3.1).

In summary, the Hall term influences both the Ohm's law and the momentum equation. The combined effect of these two factors is a higher injector impedance that causes a 60–80% increase in the I_{tor} and total ME and a notably quicker growth of the $n = 0$ ($t < 0.15$ ms) with a much shorter formation time than rMHD, $\tau_f = 0.16$ ms ($15\tau_A$). Figures 3.4(a) and 3.4(b) show the temporal traces of the I_{tor} and total ME from the 7.5 and 12 eV validation simulations.

3.3 Comparisons to the Experiment

Data from the synthetic simulation diagnostics matching the diagnostics of the experiment allow a comparison of the partial physics of each model to the full physics of the experiment. The validation cases are the 7.5 eV calculations as 12 eV is outside measured temperature of HIT-SI. However, data from 12-eV calculations are also included as a demonstration of higher current amplification. The experimental data include measurements of the mid-plane internal magnetic field by the internal magnetic probe (IMP) and measurements of the surface magnetic field by surface probes (SP's) from

shot 122385, and measurements of impurity ion velocities by the ion Doppler spectrometer (IDS) from shot 126814. A brief description of these diagnostics is provided in §1.4.

3.3.1 Comparisons of Global Metrics: I_{tor}/I_{inj}, I_{tor}, and τ_f

As it was noted in the previous section, the two-fluid model generates more I_{tor} than the single-fluid model for the same parameters. rMHD7.5 and rMHD12 produce a steady-state I_{tor} of approximately 28 and 40 kA, equivalent to $I_{tor}/I_{inj} = 1.4$ and 2.0, respectively. 2MHD6, 2MHD7.5, 2MHD10 and 2MHD12 produce 36, 46, 58, and 68 kA of I_{tor} yielding $I_{tor}/I_{inj} = 1.8$, 2.3, 2.9, and 3.4, respectively. I_{tor} scales more favorably with T_e in 2fl-MHD than in rMHD: $I_{tor} \propto \eta^{-0.6} = T_e^{0.9}$ for 2fl-MHD, while $I_{tor} \propto \eta^{-0.4} = T_e^{0.6}$ for rMHD. The experiment has demonstrated I_{tor}/I_{inj} of $2.5 - 3$ with $I_{tor} \leq 58$ kA for $f_{inj} = 14.5$ kHz. Figure 3.6 shows the temporal traces of I_{tor} from four validation simulations: rMHD7.5, rMHD12, 2MHD7.5, and 2MHD12. I_{tor} from each simulation is plotted against the I_{tor} from an ensemble of five similar 14.5-kHz shots with $I_{tor}/I_{inj} \geq 2.5$ including shot 122385. The experimental traces are clipped to only include the interval between $t = 0.74 - 1.8$ ms, which excludes the pre-breakdown and decay periods. For HIT-SI it is estimated that $\tau_f \approx 0.1 - 0.2$ ms based on figure 3.6.

The two-fluid model matches the formation time ($\tau_f = 0.16$ ms) of the experiment and yields I_{tor}/I_{inj} similar to the levels demonstrated by HIT-SI at a comparable T_e. The 7.5 eV case underestimates the I_{tor}/I_{inj} by 20% while the 12 eV case overestimates it by as much. According to the scaling law, $I_{tor}/I_{inj} = 2.5 - 2.8$ requires $T_e = 8.5 - 10$ eV for 2fl-MHD. This range overlaps the measured T_e from HIT-SI: 6 ± 3 eV. Thus, the current amplification produced by 2fl-MHD quantitatively agrees with that of the experiment.

rMHD exhibits a much longer formation time ($\tau_f = 0.5$ ms) and grossly underestimates the current amplification. Significantly higher temperatures, $T_e = 17 - 21$ eV,

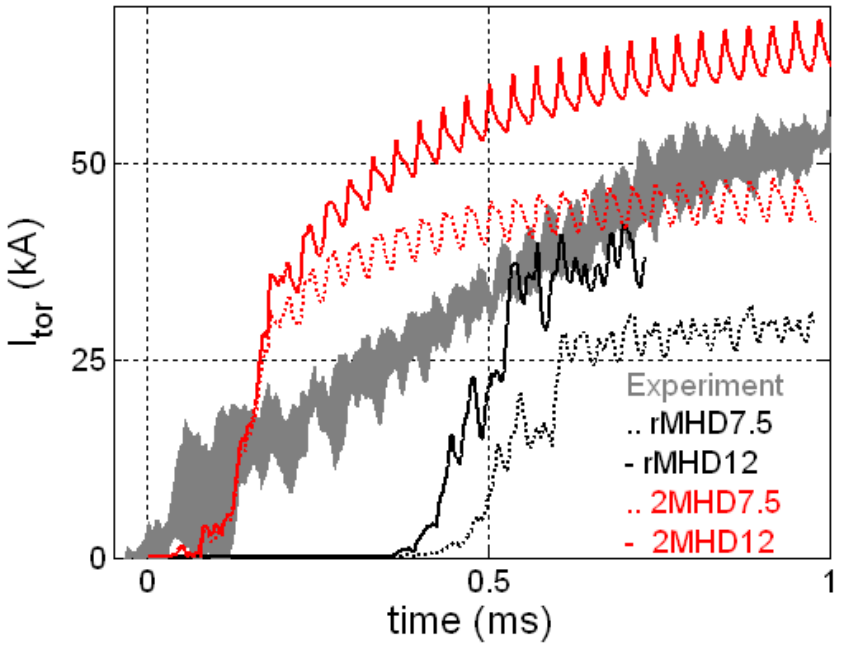

Figure 3.6: I_{tor} as a function of time in ms from the 2MHD12 (solid red), 2MHD7.5 (dotted red), rMHD12 (solid black), and rMHD7.5 (dotted black) validation calculations compared with I_{tor} traces of five similar shots from the experiment (gray patch). The experimental traces are clipped to only include the interval between $t = 0.74 - 1.8$ ms, which excludes the pre-breakdown and decay periods.

well outside the uncertainty in T_e as well as a significantly lower n_e below the measured density fluctuations are needed to achieve I_{tor}/I_{inj} demonstrated by HIT-SI. Recall in rMHD, saturation and therefore, formation times depend on the amplitude of the initial perturbation. Lowering the initial amplitude by several orders of magnitude to start from a more vacuum-like initial condition can easily yield formation times comparable to the duration of a plasma pulse (2 ms).

Neither model captures the linear rise in the I_{tor} during the interval $t \approx 0.2-0.7$ ms from the experiment. This effect, which is not modeled, is due to a feedback effect from the plasma, which causes a gradual increase in the I_{inj} from 16 to 20 kA over the course of the shot. The linear ramp in I_{tor} was reproduced by an additional simulation

(not shown here) that used a sloping injector waveform similar to that of shot 122385, instead of a constant-amplitude waveform.

3.3.2 Comparison of Internal Magnetic Fields

A synthetic **B** diagnostic corresponding to the physical locations of the 3-axis probes along the IMP stems is constructed for the purpose of comparing the calculated and measured internal magnetic fields and the resulting profiles.

Figures 3.7 and 3.8 illustrate a mid-plane measurement of the poloidal field B_z[‡] by the IMP array overlaid with synthetic probe output from 2MHD7.5, rMHD7.5, 2MHD12, and rMHD12 simulations. The experimental traces are shown in black and those from the simulations in red. Great care was taken to correctly match the relative phase between the modeled and actual X-injector flux waveforms to correctly align the phases of the real and synthetic signals. A vacuum shot was simulated and compared with a similar HIT-SI vacuum shot to verify the toroidal locations of all the synthetic probes, a crucial step for matching the phases correctly (see Appendix A.2). In addition to the relative phase, the experimental traces are also shifted backward in time by 10 or 11 injector cycles to line up the beginning of the simulation with the breakdown time. For clarity, only traces from five different radial locations are included although a total of 17 locations are available from the experiment. For each additional radial location the y-axis is offset by 0.05 and 0.08 T for B_z and B_ϕ from 2fl-MHD, respectively, (figures 3.7(a), 3.7(c), 3.8(a), and 3.8(c)); and by 0.06 and 0.08 T for B_z and B_ϕ from rMHD, respectively (figures 3.7(b), 3.7(d), 3.8(b), and 3.8(d)).

2MHD7.5 shows remarkable agreement with the experiment. It matches the magnitude (DC level) of both B_z and B_ϕ, plotted in figures 3.7(a) and 3.7(c), as well as the amplitude of the oscillations during the flat-top period of I_{tor} (the interval

[‡]At the mid-plane, the poloidal and axial directions become aligned. Thus $B_\theta = B_z$.

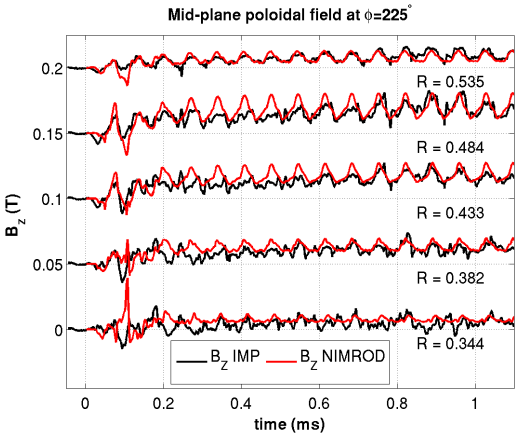

(a) B_z vs. time(ms) for 7.5 eV 2fl-MHD

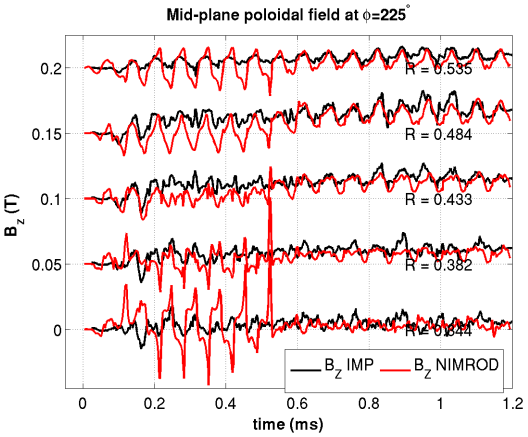

(b) B_z vs. time(ms) for 7.5 eV rMHD

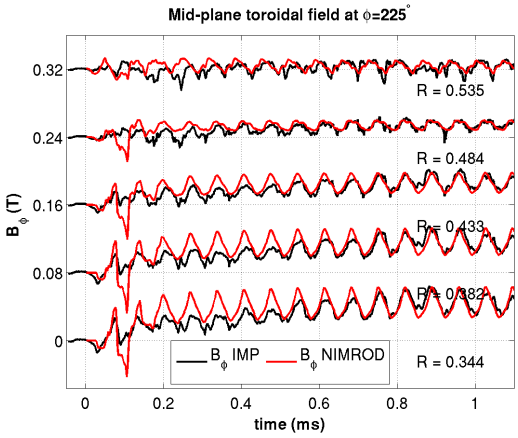

(c) B_ϕ vs. time(ms) for 7.5 eV 2fl-MHD

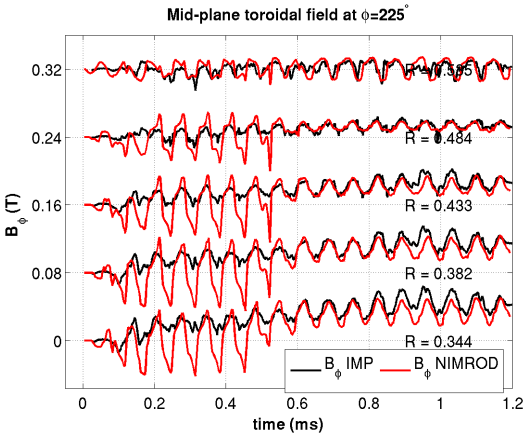

(d) B_ϕ vs. time(ms) for 7.5 eV rMHD

Figure 3.7: Time traces of the mid-plane poloidal magnetic field B_z at five different radial locations from shot 122385 as measured by IMP (black) and extracted from a 7.5-eV (a) 2fl-MHD and (b) rMHD simulation (red). (c) and (d) shows the same traces for B_ϕ. Measurements from only five locations are plotted although a total of 17 locations are available from the experiment. The y-axis is offset by 0.05 T in (a), 0.06 T in (b), 0.08 T in (c), and 0.08 T in (d) for each additional radial location. 2MHD7.5 produces internal magnetic fields that match the magnitude of the measured internal fields as well the amplitude of their oscillations.

$t = 0.7 - 1.0$ ms in figure 3.6). 2MHD12 slightly overestimates B_ϕ near the axis ($R = 0.344$ m) and B_z everywhere except near the wall ($R = 0.535$ cm), consistent with the greater I_{tor} that it yields as a consequence of a higher T_e. Prior to the flat-top period, 2MHD7.5 overestimates the internal profiles, consistent with a faster I_{tor} rise time. It also overestimates B_z nearest to the magnetic axis. A larger simulated B_z near the axis implies a farther shift of the magnetic axis toward the inboard side in the calculations (also see B_z vs. R plots in figure 3.9). What is referred to as the magnetic axis here is not the O-point of the poloidal field as there are no closed flux surfaces, but merely where B_z changes polarity. The two-fluid simulations yield larger internal fields than those of shot 122385 during the first half of the simulations because I_{tor} from the simulations grows more rapidly than the measured I_{tor} once the initial formation stage is complete. As for rMHD, the delayed onset of relaxation characteristic of rMHD is clearly visible in both cases illustrated by figures 3.7(b), 3.7(d), 3.8(b), and 3.8(d). The pre-relaxation period of rMHD exhibits large oscillations with an amplitude that greatly exceeds that of the experimental traces. Just as in the two-fluid case, a DC component of similar amplitude with comparable oscillations forms upon nonlinear saturation. The fact that rMHD generates a larger internal magnetic field in proportion to its I_{tor} suggests a greater plasma inductance in rMHD than in 2fl-MHD.

Cycle-averaging the measured and simulated internal magnetic profiles provides a clear measure of how well each model predicts the magnitude of the internal fields. First, a time interval from the period of near-peak steady-state I_{tor} (stage III) from the simulations and shot 122385 is chosen. Second, a running time-average of the magnetic fields is performed over one injector period within this interval. And lastly, a single point in time is selected from the chosen interval for the plots. This time is approximately 0.75 ms for rMHD7.5 and 2MHD7.5, $t \approx 0.6$ ms for rMHD12 and 2MHD12, and $t \approx 0.8$ ms for shot 122385 (time as shown in figure 3.6). Note that choosing a period of peak I_{tor} for the time-averaging disregards the delayed formation

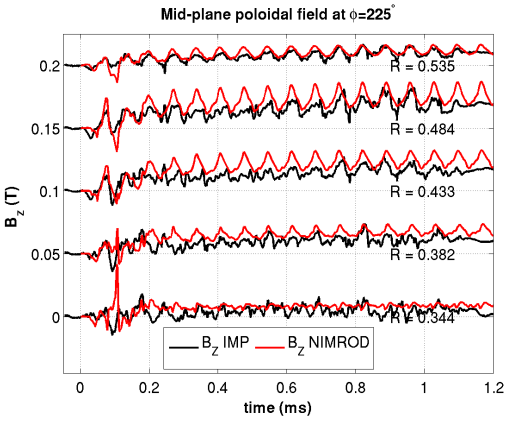

(a) B_z vs. time(ms) for 12 eV 2fl-MHD

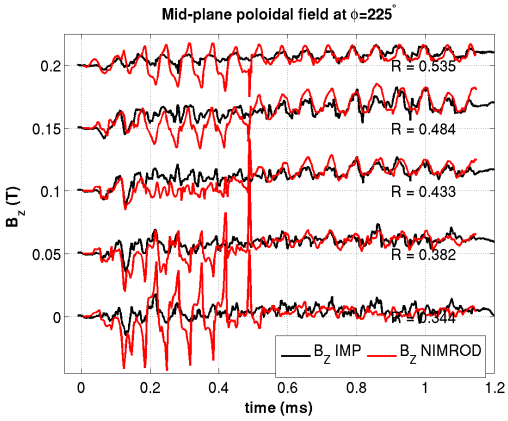

(b) B_z vs. time(ms) for 12 eV rMHD

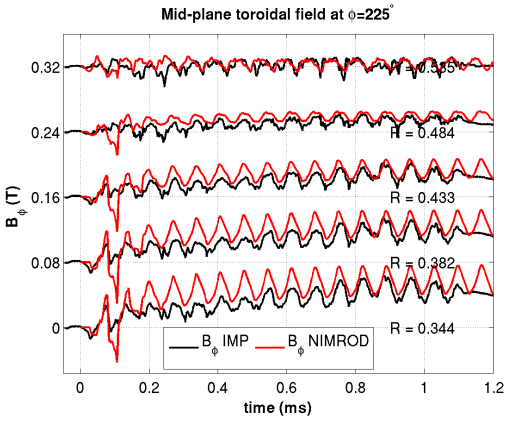

(c) B_ϕ vs. time(ms) for 12 eV 2fl-MHD

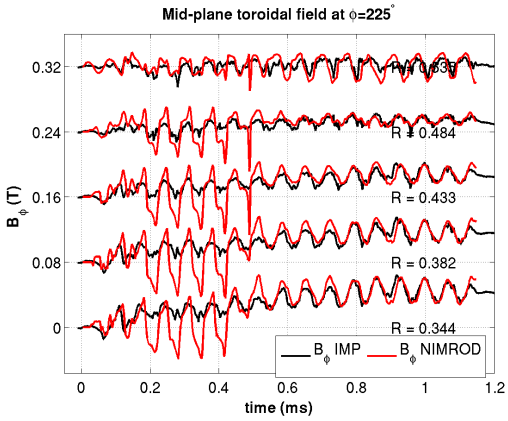

(d) B_ϕ vs. time(ms) for 12 eV rMHD

Figure 3.8: Time traces of the mid-plane poloidal magnetic field B_z at five different radial locations from shot 122385 as measured by IMP (black) and extracted from a 12-eV (a) 2fl-MHD and (b) rMHD simulation (red). (c) and (d) shows the same traces for B_ϕ. Measurements from only five locations are plotted although a total of 17 locations are available from the experiment. The y-axis is offset by 0.05 T in (a), 0.06 T in (b), 0.08 T in (c), and 0.08 T in (d) for each additional radial location. Similarly, 2MHD12 produces internal magnetic fields that match the magnitude of the measured internal fields as well the amplitude of their oscillations albeit the DC level is slightly higher in this case than it is in 2MHD7.5. rMHD12 also shows good agreement with the experiment once the $n = 1$ prevalence ceases.

time characteristic of the rMHD calculations. Figure 3.9 shows the cycle-averaged mid-plane B_z and B_ϕ profiles as a function of the major radius R from 2MHD7.5, rMHD7.5, 2MHD12, and rMHD12 against shot 122385 (red circles). rMHD profiles are shown on the right and 2fl-MHD profiles on the left. 7.5-eV profiles are plotted on the top half and 12-eV profiles on the bottom half. The subcaption for each figure indicates the I_{tor}/I_{inj} achieved by a particular simulation.

The shape of the profiles from 2MHD7.5 closely match those of shot 122385. rMHD7.5 and rMHD12 show some deviations from the measured profiles. rMHD12 exhibits strong deviations from the measured profiles, partly because the interval used in cycle-averaging is immediately after the $n = 1 - n = 0$ transition, which exacerbates the profile distortions. Both rMHD7.5 and 2MHD7.5 underestimate the internal profiles, consistent with the temporal traces of B_z and B_ϕ. All simulations[‡] show an inward shifting of the magnetic axis, evidenced by the gentler slope of the B_z. Finite plasma pressure is believed to be responsible for the outward shift of the magnetic axis in the experiment. There are deviations from the measured profiles on the outboard side, $R \geq 0.5$ m, caused by the exclusion of the diagnostic gap from the simulation geometry. Both fluid models outperform a prediction based on Taylor relaxation theory (green traces), which accounts for none of the relaxation dynamics. A comparison of the time-dependent IMP traces from HIT-SI against those predicted by the Taylor model is presented in Ref. [48].

The calculations give rise to a greater internal field than the experiment relative to the I_{tor}/I_{inj} they yield. This effect is more severe in rMHD, as rMHD12 generates greater internal fields than shot 122385 with only $I_{tor}/I_{inj} = 2$. This is indicative of a greater plasma inductance in rMHD than 2fl-MHD and also of a greater plasma inductance in both models than the experiment. It also points to a diamagnetic effect suppressing the measured internal fields, possibly a pressure gradient that is

[‡]rMHD12 could be an exception to this observation as indicated by figures 3.8(b) and 3.9(d)

not captured by the models. The existence of this pressure gradient is consistent with outward shift of the magnetic axis in the experiment as mentioned above.

In addition to comparisons of the magnetic field, plasma flow from an additional two-fluid simulation with $T_e = 6$ eV is compared to ion flows measured by IDS. This simulation employs a higher injector frequency, $f_{inj} = 36.8$ kHz due to the lack of available IDS data at $f_{inj} = 14.5$ kHz at the time this comparison was made. The results of this comparison are preliminary and included only as a preview of the future validation efforts with a fuller suite of diagnostic measurements from HIT-SI. Section 5.3.3 covers the effects of increasing f_{inj} on the global characteristics of rMHD. Similar effects are seen in the two-fluid model, which are briefly discussed here. For higher f_{inj}, the dormant period prior to linear growth lasts longer, delaying the onset of the relaxation event in the calculation. The I_{tor} and thereby, I_{tor}/I_{inj} are reduced with increasing f_{inj}. These trends are consistent with the expectation that the results should exhibit a dependence on f_{inj} as the injector period becomes comparable to τ_A. I_{tor} trace from shot 126814 is shown in the rightmost panel of figure 3.10. It does not exhibit a linear ramp, instead it asymptotes to a value similar to what is seen in 2fl-MHD. Proper feedback control on the higher f_{inj} HIT-SI shots is responsible for eliminating the linear ramp in I_{tor}.

The flow from the simulation is output along 32 synthetic chords that spatially match the locations of the instrument chords. The ion velocities are calculated with respect to a location in the simulation geometry that matches the location of the collecting lens, at $z = 0$ m and $\phi = 71°$. Blue shift corresponds to ion motion toward and red shift to ion motion away from the collecting lens. Chord-averaged flows are also calculated. The simulation output is compared to a shot 126814 with similar I_{tor} (~ 30 kA). For consistent comparison, the simulated plasma flow along each chord is time-averaged over 20 μs, which is the maximum temporal resolution of IDS. Note that the simulation duration is shorter than the 2-ms shot length. Figure 3.10 (courtesy of A. Hossack) shows the calculated (left panel) and measured (center panel) flow

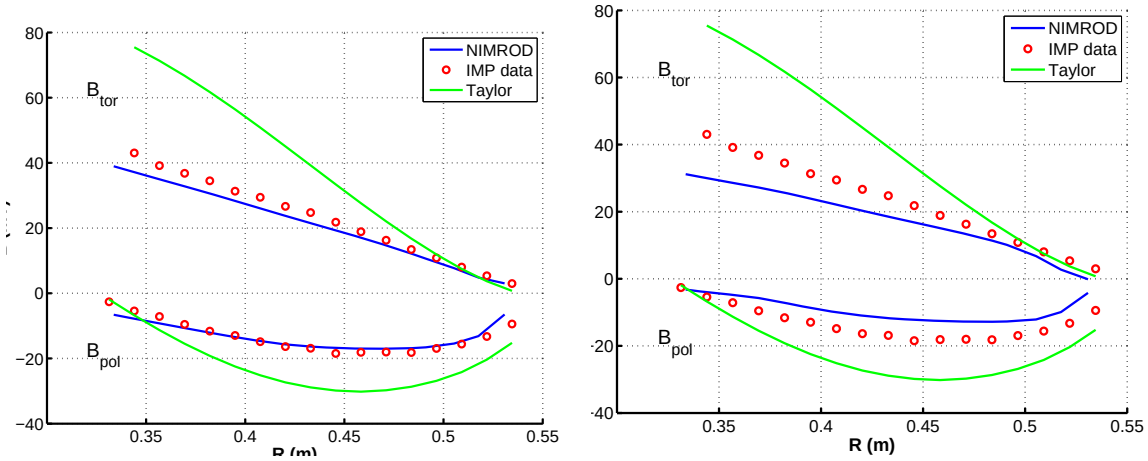

(a) 2MHD7.5 with $I_{tor}/I_{inj} = 2.3$

(b) rMHD7.5 with $I_{tor}/I_{inj} = 1.4$

(c) 2MHD12 with $I_{tor}/I_{inj} = 3.4$

(d) rMHD12 with $I_{tor}/I_{inj} = 2$

Figure 3.9: Cycle-averaged mid-plane magnetic field profiles from (a) 2MHD7.5, (b) rMHD7.5, (c) 2MHD12, and (d) rMHD12 (all solid blue lines) simulations overlaid with measured profiles from shot 122385 (red dots) and those calculated from Taylor relaxation theory (green). All the calculations overestimate the magnitude of the internal fields relative to I_{tor}/I_{inj} they yield, implying a more inductive plasma in the simulations than in the experiment or a diamagnetic effect in the experiment.

profiles. The horizontal axis represents the impact parameter, defined as distance to the right or left of the geometric axis as viewed from the collection lens at $z = 0$ and $\phi = 71°$. The vertical axis is time in ms. Both the simulation and shot 126814 display a reversal of the initial flow profile once the configuration relaxes and significant I_{tor} is generated. This does not necessarily imply that the NIMROD 2fl-MHD calculation is predictive of the observed flow structure. The results presented here are preliminary and require further work as does the IDS itself. The IDS measurements can usually exhibit significant shot-to-shot variation. Furthermore, the model does not evolve density or account for neutral particle dynamics, which might strongly alter the flow profile.

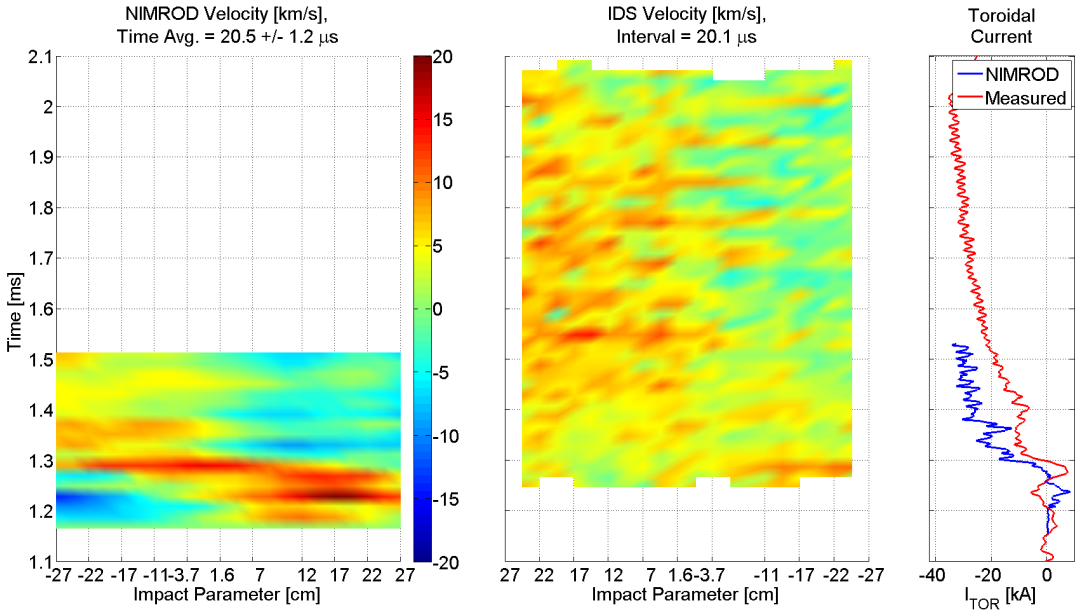

Figure 3.10: A comparison of the calculated and measured ion velocity profiles. The measured velocity profiles shown are for C II doublet at 514.4 nm. for shot 126814. NIMROD output is from the 6-eV 2fl-MHD simulation with $f_{inj} = 36.8$ kHz. The horizontal axis represents the impact parameter, defined as distance to the right or left of the geometric axis as viewed from the collection lens at $z = 0$ and $\phi = 71°$. The vertical axis is time in ms. The rightmost panel shows the I_{tor} traces for both the 2MHD6 (blue) and shot 126814 (red). The figure is courtesy of Prof. Aaron Hossack.

3.4 Comparison of Surface Magnetic Fields Using Biorthogonal Decomposition (BD)

The previous section covered comparisons of simulation output to the internal magnetic fields from shot 122385. This section focuses on comparing the simulation results to measurements of the surface magnetic field from shot 122385 to complement the analysis of the previous section. There are a total of 64 local measurements by the 3-axis surface probes (SP's) for the toroidal and poloidal components of the surface magnetic field amounting to 128 signals (radial measurements are not digitized). The standard approach for treating such a large data set is to Fourier decompose all the signals and compare the resulting mode structure to that from the NIMROD simulations. However, the sparseness of the SP arrays in the toroidal direction allows Fourier decomposition only up to the $n = 1$ mode for the experiment. In addition, the bow-tie-shaped poloidal cross section and lack of toroidal symmetry make the interpretation of Fourier analysis challenging in both poloidal and toroidal domains. Biorthogonal decomposition (BD) offers an alternative to Fourier decomposition for reducing the large SP data to an eigensystem of manageable size. By concentrating the available data into a few dominant spatial and temporal structures, one can efficiently gauge how accurately the calculations capture the overall surface magnetic structure without resorting to a probe-by-probe comparison. This is an unbiased and effective way to show the validity of the present models. BD differs from Fourier in that as a multivariate analysis tool it simultaneously investigates both the spatial and temporal characteristics of a data set.

BD is performed on all four validation simulations analyzed in the previous section: rMHD7.5, 2MHD7.5, rMHD12, and 2MHD12. First, the formalism of BD is introduced followed by a presentation of the BD eigenvalue spectrum and interpretation of the dominant modes that come out of BD. A correlation analysis is carried out to quantify how well each simulation reproduces the dominant features of the surface

magnetic fields from the experiment. The correlation analysis is the best quantitative evidence available for demonstrating the necessity of two-fluid effects for SIHI. Lastly, the spatial structure of the first few dominant modes from the experiment are compared to those from the simulations.

3.4.1 Overview of BD

The first application of BD to a toroidal confinement experiment is presented in the paper by Dudok de Wit *et al.* [63], which includes a comprehensive description of the method. Ref. [64] contains a detailed analysis of BD and its mathematical properties. A brief overview is presented here to familiarize the reader with the general aspects of the method. The BD nomenclature used in Ref. [63] is adhered to here as it is the standard.

Consider a generic scalar signal $B(\mathbf{x}, t)$ measured at M spatial locations with N-many time samples. This could be local measurements of any physical quantity like temperature or a component of a vector field. The measurements are arranged into an $M \times N$ matrix where each row represents a spatial location and each column a discrete time point: $(B)_{mn} = B(x_m, t_n)$ with $m = 1, ..., M$ and $n = 1, ..., N$. BD uses standard singular value decomposition (SVD) to project the discrete signal $B(x_m, t_n)$ onto a basis orthonormal in time and space, decorrelating the temporal and spatial dependence of $B(x_m, t_n)$ as follows:

$$B(x_m, t_n) = \sum_{k=1}^{K} A_k \psi_k(x_m) \phi_k(t_n) \tag{3.4}$$

with the following orhonormality relations

$$\sum_{n=1}^{N} \psi_k(t_n) \psi_l(t_n) = \sum_{m=1}^{M} \phi_k(x_m) \phi_l(x_m) = \delta_{kl} \tag{3.5}$$

where A_k corresponds to the singular values called weights (eigenvalues), ϕ_k and ψ_k to the spatial and temporal eigenvectors called topos and chronos respectively, and k

to the component order (mode number), which indicates the rank of each eigenvector. The global dimension of the data set K is determined by the smaller dimension of $(B)_{mn}$, *i.e.*, $K = min(N, M)$. A_k's are either positive or zero. For the present analysis A_k's are normalized such that their sum equals 1. "The components that are associated with large weights represent highly correlated structures and reflect dominant features of the signal"[63]. In matrix form, BD is expressed as $B(x_m, t_n) = USV^T$ where S is an $M \times N$ diagonal rectangular matrix containing the weights A_k, U is an $M \times M$ unitary matrix containing the topos $\phi_k(x_m)$, and V is an $N \times N$ unitary matrix containing the chronos $\psi_k(t_n)$ of the system. The topos and the chronos are calculated directly from the data and are not predefined basis functions, which Fourier decomposition presupposes. This implies BD of different signals can highlight different characteristics. An example of this is shown in the next subsection. An examination of the weight distribution to identify the dominant components is key to the interpretation of the results of BD. Chronos of these dominant components can then be compared to temporal traces of the data to associate the BD spectrum with physically meaningful signals as will be shown below.

3.4.2 Weights, Chronos, and Correlations

BD is performed on the poloidal and toroidal components of measured and simulated surface magnetic fields both simultaneously and separately. Results from both decompositions are presented. The experimental data comprise measurements by all the working SP's from shot 122385 spanning an interval between $t = 0.74 - 1.8$ ms that excludes the pre-breakdown and decay periods. These data are arranged into a 123×1081 matrix. 123 corresponds to 61 poloidal and 62 toroidal signals[†], and 1081 is the number of discrete time points in the chosen interval. The simulation data comprise synthetic signals extracted from 2MHD7.5, rMHD7.5, 2MHD12, and rMHD12

[†]There are a total of five dead probes, which are also accounted for in the BD of simulation data.

at locations along the boundaries that best match the physical locations of the SP's. These are arranged into a data matrix of identical size. NIMROD usually produces non-uniformly spaced time steps, so obtaining an equal number of discrete time points requires interpolating the NIMROD time basis onto the experimental time basis. All the simulations were run for at least 1.1 ms to ensure that the temporal extent of the experimental and simulation BD's match. The simulation data are also shifted forward in time by 29 μs to correctly match the phase of the experimental and simulated chronos and approximately align the rise time of I_{tor} from the simulations and experiment. The separate decomposition of the poloidal and toroidal fields require the construction and decomposition of two separate data matrices: one, a 62×1081 matrix representing the poloidal field, another, a 61×1081 matrix representing the toroidal field.

Figure 3.11 shows plots of the normalized weight spectrum from rMHD7.5 and rMHD12 (dashed red), 2MHD7.5 and 2MHD12 (solid black with +'s) and from shot 122385 (dashed blue with crosses). The top row corresponds to 7.5-eV results and the bottom row to 12-eV results. Figures on the left are plotted on a linear scale to emphasize the level of agreement between simulations and the experiment in the first few components. The figures on the right are plotted on a semi-log scale over a greater range to illustrate the exponential flattening. Note that BD components are arranged monotonically in order of decreasing weight. The component number has no significance other than to indicate rank. The lowest numbers correspond to higher ranks and their relative weights give a quantitative measure of their dominance. Of interest are the first three components which together contain 98% of the signal energy, $\sum_{k=1}^{3} A_k^2 / \sum_{k=1}^{K} A_k^{2\dagger}$, in 2MHD7.5 and 88% of the signal energy in rMHD7.5. 12-eV simulations yield similar signal energies for the first three components. This means that most of the signal features are contained in the first three topo-chrono pairs for

---

†as defined by eqns. (9) and (10) in Ref. [63]

both rMHD and 2fl-MHD. Note the large gap between the first and second components. For $k \gtrsim 7$ the weight spectrum flattens, usually an indication of noise. Both 2MHD7.5 and 2MHD12 show remarkable agreement with the experiment in the first four weights. This, however, does not mean that the corresponding spatio-temporal structures represent the same physical features and therefore are in agreement. The chronos and topos associated with these weights must be compared to one another, which is the topic of the following paragraphs. The dominant weights from rMHD deviate significantly from those of the experiment.

Associations between the dominant BD components (1–3) and physically meaningful signals are made by plotting the first few chronos as a function of time. Figure 3.12 is a plot of the first three poloidal chronos from 2MHD7.5 (left) and rMHD7.5 (right). Each chrono is multiplied by the appropriate weight to correctly reflect its relative amplitude. The solid black, dashed red, and dotted blue traces represent 1^{st}, 2^{nd} and 3^{rd} chronos respectively. The resemblance of the first poloidal chrono from 2fl-MHD (figure 3.12(a)) and rMHD (figure 3.12(b))) to temporal traces of I_{tor} (figure 3.6) implies that the first poloidal chrono represents the zeroth order spheromak component, the structure responsible for generating the I_{tor}. Similarly, an inspection of the second and third poloidal chronos (figure 3.12) reveals that they are associated with the injector fluctuations. They oscillate with a fixed amplitude at the injector frequency and mimic the $n = 1$ ME trace. Both injector chronos are out of phase with respect to the oscillations of the X and Y injectors suggesting they represent a linear combination of the injectors. These associations are also true for the first three poloidal chronos from shot 122385.

The first and second toroidal chronos, not shown here, correspond to the injector fluctuations. There is no toroidal component associated with the spheromak (I_{tor}) because the spheromak toroidal field is zero at walls of the confinement vessel. Thus, the signals giving rise to the toroidal BD spectrum come predominantly from the injectors.

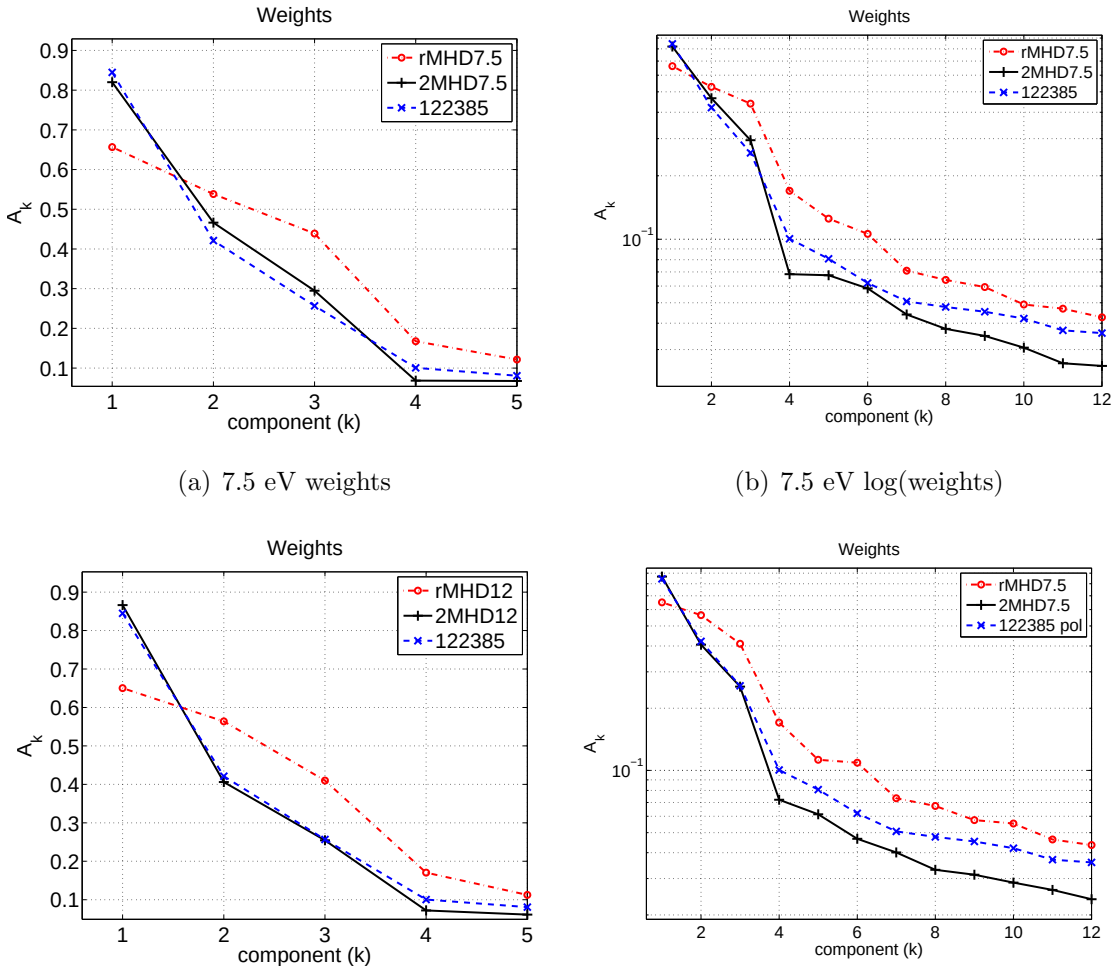

(a) 7.5 eV weights

(b) 7.5 eV log(weights)

(c) 12 eV weights

(d) 12 eV log(weights)

Figure 3.11: Linear plots of the first five weights from BD for (a) 7.5 eV and (c) 12 eV, and semilog plots of the first 12 weights for (b) 7.5 eV and (d) 12 eV simulations. Weights from rMHD is shown in red, 2MHD in black, and shot 122385 in blue. Both 2MHD7.5 and 2MHD12 show remarkable agreement with shot 122385 in the first four weights. The dominant weights from rMHD deviate significantly from those of the experiment. Note what is plotted in Ref. [63] is A_k^2, not A_k.

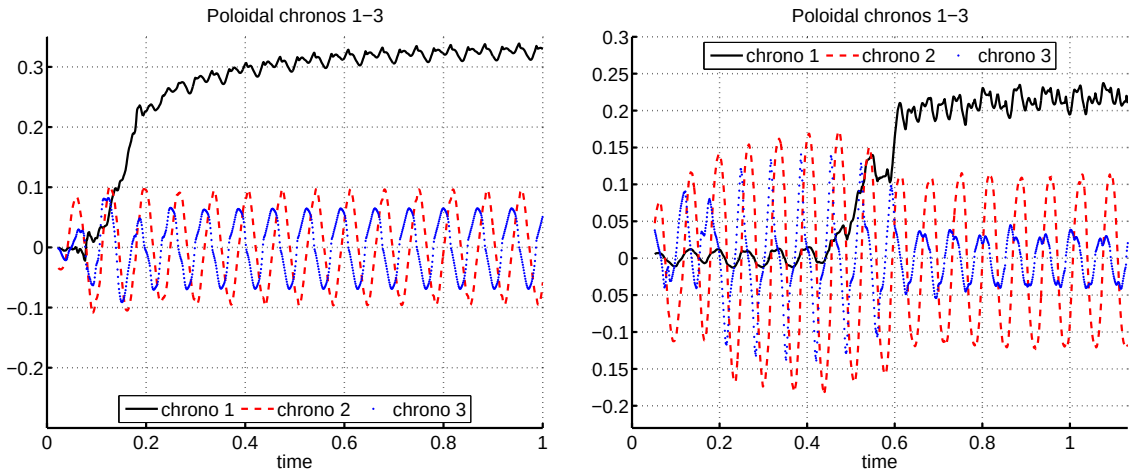

(a) Poloidal chronos from 2MHD7.5

(b) Poloidal chronos from rMHD7.5

Figure 3.12: The first three poloidal chronos as a function of time from the (a) 2MHD7.5 and (b) rMHD7.5 simulations. The first chrono (black) is assumed to represent the zeroth order spheromak component because of its resemblance to the temporal trace of I_{tor}. The second and third chronos correspond to the injector fluctuations.

The BD spectrum is strongly influenced by τ_f and the magnitude of I_{tor}. The more delayed the τ_f, the more the $n = 1$ field dominates the highest-ranked (first) component and can cause a shift in the BD spectrum. The correlation analysis presented below contains one such example from rMHD where the dominant component does not correspond to the one associated with I_{tor} due to a long τ_f and low I_{tor}/I_{inj}.

The uneven distribution of the SP arrays in the toroidal direction resolves the X side better than the Y side and tips the weight spectrum in favor of X. Furthermore, the narrow separation of the 2$^{\text{nd}}$ and 3$^{\text{rd}}$ poloidal weights and their association with the two injectors hint at a degeneracy. This is verified by creating 4 additional synthetic Ampèrian arrays and re-performing the BD for 2MHD12 with synthetic probe data from eight (toroidally) equally-spaced Ampèrian arrays that resolve both injectors equally. The result is plotted in figure 3.13. The case with the existing SP arrays

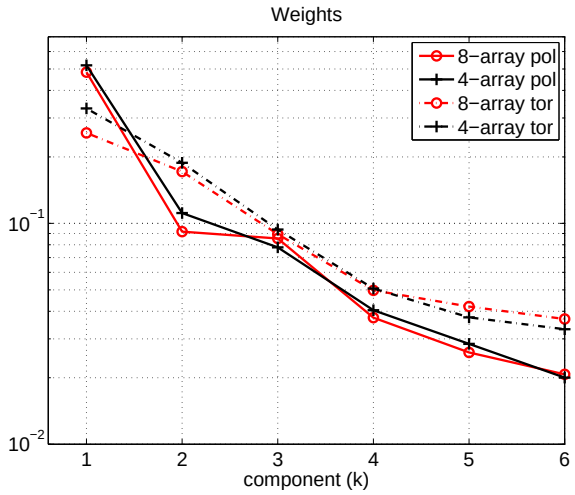

Figure 3.13: A semi-log plot of the weight spectrum based on the BD of the simulated surface **B** from the four existing Ampèrian arrays (black traces with +'s) and another from eight (toroidally) equally-spaced Ampèrian arrays (red traces with circles). The solid lines represent poloidal weights and the dashed lines toroidal weights. BD of 8 Ampèrian arrays reveals a degeneracy between the two injector components. Toroidal spectrum is not altered significantly.

is represented by the black lines and the case with 8-SP arrays by the red lines. Poloidal weights are shown as the solid lines and toroidal weights as the dashed lines. The figure shows that the 2^{nd} and 3^{rd} poloidal components are nearly degenerate, consistent with a symmetric helicity injection by the two injectors. The toroidal weight spectrum, shown as dashed lines, is not strongly altered by increasing spatial resolution.

An additional feature that comes out of BD is quantification of how closely the dominant features representative of the surface magnetic fields from the simulations match those from shot 122385. Correlations between the BD eigenvectors from simulations and the experiment can be used as a metric for quantifying how well the models reproduce the experimental data. A correlation $\mathcal{C}_i^{(k)}$ is defined as the overlap (inner product) between the k^{th} experimental and i^{th} simulation eigenvector:

$\mathcal{C}_i^{(k)} \equiv \left(\psi_k^{(e)}\right)^T \cdot \psi_i^{(s)}$, where ψ is a generic eigenvector of length $K(\equiv (min(M,N))$, superscripts e and s denote experiment and simulation, respectively, and T stands for the transpose. For example, the correlation between the 1^{st} experimental and 5^{th} simulation eigenvectors is $\mathcal{C}_5^{(1)} = \left(\psi_1^{(e)}\right)^T \cdot \psi_5^{(s)}$. Correlations can be positive or negative, unlike a probability, which is $\left(\mathcal{C}_i^{(k)}\right)^2 \geq 0$. An exact match means a perfect correlation for $i = k$, mathematically equivalent to $\mathcal{C}_i^{(k)} = \delta_{ik}$, *i.e.*, a $K \times K$ identity matrix. Values close to one indicate a strong correlation and therefore close agreement. Values significantly smaller than one indicate a weak correlation, and therefore poor agreement between the experiment and calculation. In that case, a particular data eigenvector emerges as a linear combination of multiple simulation eigenvectors. For graphical convenience, the absolute value of $\mathcal{C}_i^{(k)}$ is plotted in figures 3.14 and 3.15.

Correlations for both the spatial (topo) and temporal (chrono) eigenvectors are computed. Figure 3.14 shows how well the first five topos from shot 122385 correlate with the topos from 2MHD7.5 (top left), rMHD7.5 (top right), 2MHD12 (bottom left), and rMHD12 (bottom right). The integers along the abscissa represent the component number from a simulation. Each integer contains five bars of assorted colors that indicate how well the first five eigenvectors from the experiment, *i.e.*, shot 122385, correlate with a particular eigenvector from each simulation. Both two-fluid calculations display strong correlations ($\geq 50\%$) in the first three topos as indicated by figures 3.14(a) and 3.14(c). The agreement between the experiment and two-fluid is over 95% ($\mathcal{C}_1^{(1)} > 0.95$) for the first topo (dark blue bar), 90% ($\mathcal{C}_2^{(2)} = 0.9$) for the second topo (cyan bar) and over 80% in the third topo (green bar). Topos for higher components ($k \geq 3$) show weak correlations ($\mathcal{C}_k < 0.5$) with the experimental topos. The correlations worsen for the higher components because they contain subtle dynamics obscured by noise. Hence, getting good agreement in higher components is more significant for a quantitative match but also more suspicious. For rMHD, the

correlations between the simulations and experiment show drastic differences. The two most dominant components from shot 122385 are no longer strongly correlated with the two most dominant components from rMHD. Figure 3.14(b) indicates that the strongest topo correlations are actually the off-diagonal elements, e.g. $\mathcal{C}_3^{(1)}, \mathcal{C}_1^{(2)}$, and $\mathcal{C}_2^{(3)}$ for rMHD7.5. The weight spectrum shifts in such a way that the component associated with I_{tor} (the zeroth order spheromak component) no longer has the highest rank. This is an artifact of both the long formation times and lower current amplification typical of the rMHD simulations, and is an excellent indicator of disagreement between rMHD and the experiment.

Correlations between the chronos of the simulation and those of the experiment are shown in figure 3.15. The plots are arranged in the same order as in figure 3.14. The data from the simulations are shifted forward in time by 29 μs prior to BD to correctly match the phase between the experimental and simulated chronos. Both 2MHD7.5 and 2MHD12 display excellent agreement with the experiment in the first three chronos (figures 3.15(a) and 3.15(c)), each yielding a correlation greater than 90%. Similar to the topo correlations, rMHD7.5 shows strong chrono correlations (> 0.8) with shot 122385 in the off diagonal components due to long τ_f and lower I_{tor}/I_{inj} characteristic of the single-fluid model. Figure 3.15(a) indicates that the dominant component from rMHD7.5 is the one associated with the injectors rather than I_{tor}. Chrono correlations for rMHD12 indicate a BD spectrum more aligned with that of shot 122385 than rMHD7.5 because of a higher I_{tor}.

The final component of the BD analysis is side-by-side comparisons of the first three topos from shot 122385 against those from 2MHD7.5 and rMHD7.5 For this part, the poloidal and toroidal components of the synthetic and real surface $\mathbf{B}$ are decomposed separately. The topos describe the spatial structure of the measured and simulated surface magnetic fields. Figures 3.16 and 3.17 show pseudocolor contours of 1$^{\text{st}}$ and 2$^{\text{nd}}$ toroidal and poloidal topos from shot 122385 (left) and 2MHD7.5, (center) and rMHD7.5 (right). The rectangular plane displayed in the figures is an unwrapped

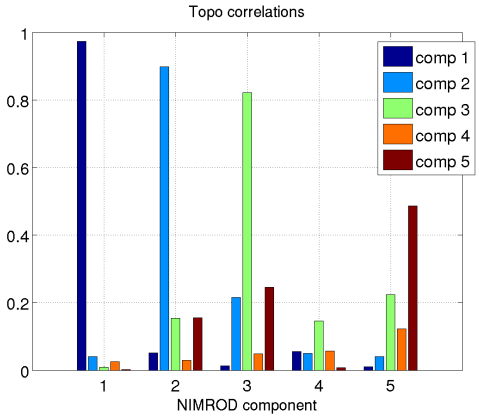

(a) Topo correlations for 2MHD7.5

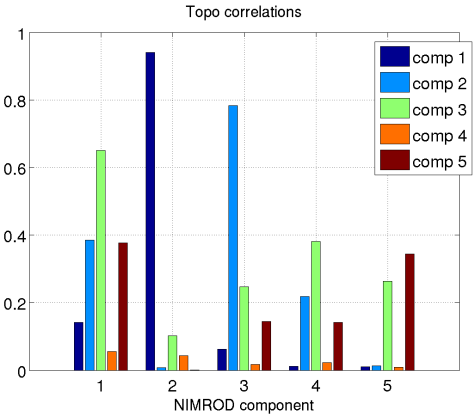

(b) Topo correlations for rMHD7.5

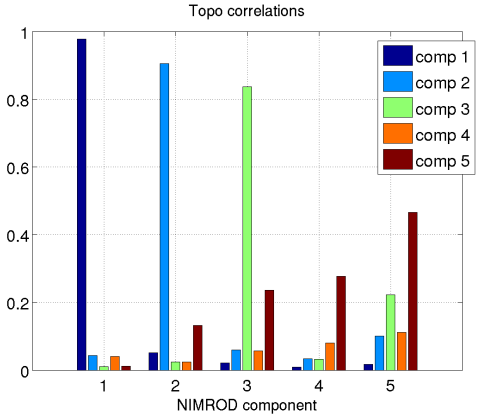

(c) Topo correlations for 2MHD12

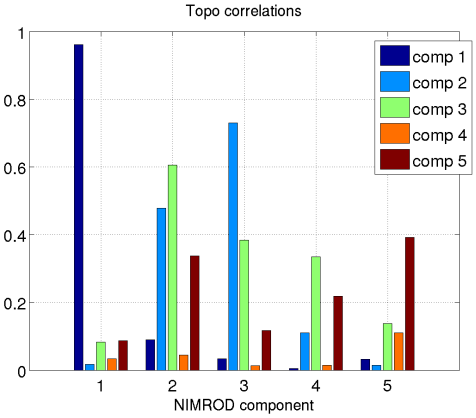

(d) Topo correlations for rMHD12

Figure 3.14: Correlations of the first five topos from shot 122385 with those of (a) 2MHD7.5, (b) rMHD7.5, (c) 2MHD12, and (d) rMHD12. The integers along the horizontal axis represent the first five components from each simulation. Each integer contains five bars of assorted colors that indicate how well the first five topos from shot 122385 correlate with a particular topo from a simulation. The legend represents the first five components from shot 122385.

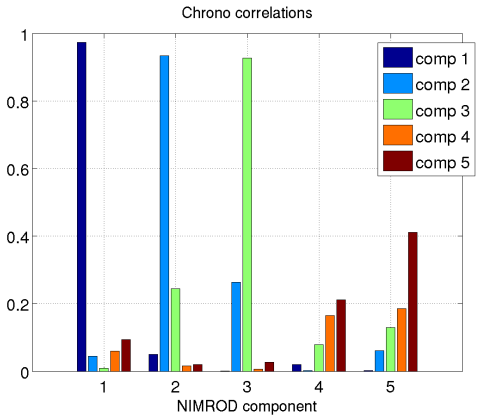

(a) Chrono correlations for 2MHD7.5

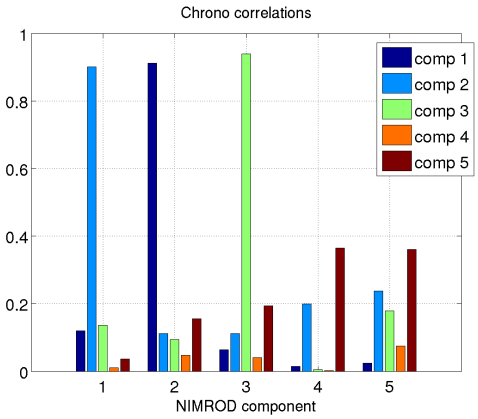

(b) Chrono correlations for rMHD7.5

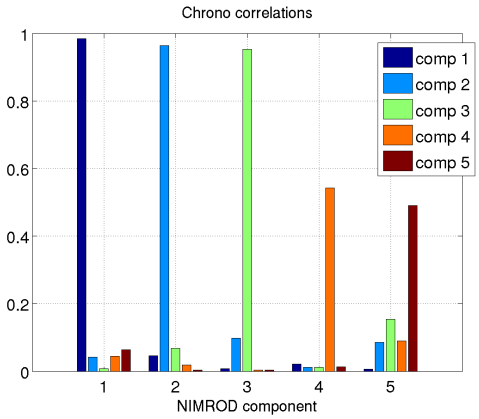

(c) Chrono correlations for 2MHD12

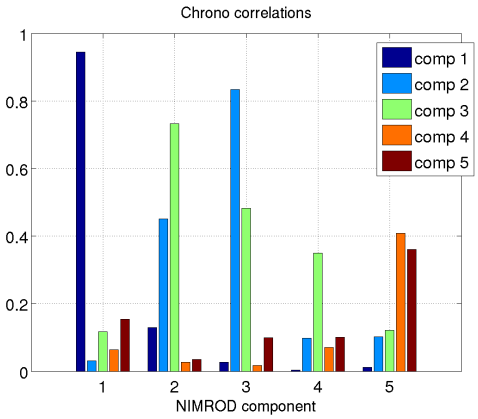

(d) Chrono correlations for rMHD12

Figure 3.15: Correlations of the first five chronos from shot 122385 with those of (a) 2MHD7.5, (b) rMHD7.5, (c) 2MHD12, and (d) rMHD12. The integers along the horizontal axis represent the first five components from each simulation. Each integer contains five bars of assorted colors that indicate how well the first five chronos from shot 122385 correlate with a particular chrono from a simulation. The legend represents the first five components from shot 122385.

representation of the surface of HIT-SI. The vertical axis corresponds to the poloidal direction (θ) and horizontal axis to the toroidal direction (ϕ). The SP arrays appear as four separate lines comprising 16 black dots spanning the poloidal direction. Fewer than 16 dots means a dead probe in a given Ampèrian array. The dead probes are also excluded from the BD of the simulated surface fields. The gray diamond shapes mark the locations of the injector mouths at $\theta = 270°$, $\phi = 0°$ and $180°$ for the X side, and $\theta = 90°$, $\phi = 90°$ and $270°$ for the Y side. Each topo is normalized to 1. The topo figures from the experiment as well as all the MATLAB codes required for BD are courtesy of Brian Victor.

An inspection of figures 3.16(a)-3.16(b) reveals that both fluid models accurately reproduce the 1st poloidal topo associated with the spheromak component. This is expected since topos by construction do not convey any time-dependent information and thus, have no memory of the formation time of I_{tor} in either model. Due to the bow tie shape, the poloidal field pushes up against the inboard-side probes ($\theta \leq 90°$ and $\theta \geq 270°$) more than the outboard-side probes producing a larger surface structure along the inboard side. Neither model exactly reproduces the 2nd poloidal topo from shot 122385. Nevertheless, 2MHD7.5 (figure 3.16(e)) outperforms rMHD7.5 (figure 3.16(f)). The fact that the 2nd topo from 2MHD7.5 is visibly different from the experimental topo while they are strongly correlated suggests that the correlations quantify agreement in an average sense and can smooth out the positive and negative differences so long as they are approximately equal and opposite, similar to time-averaging a sinusoidal function.

Figure 3.17 shows the first two toroidal topos from shot 122385 (left), 2MHD7.5 (center), and rMHD7.5 (right). The first two toroidal topos from 2MHD7.5 (figure 3.17(b)) closely resemble those from shot 122385 (figure 3.17(a)), soundly implying that 2MHD7.5 accurately captures the surface magnetic structure of the data from HIT-SI. This is not the case for rMHD7.5. The sustained $n = 1$ activity in rMHD amplifies the $n = 1$ to a much greater level than in shot 122385, leading to significant

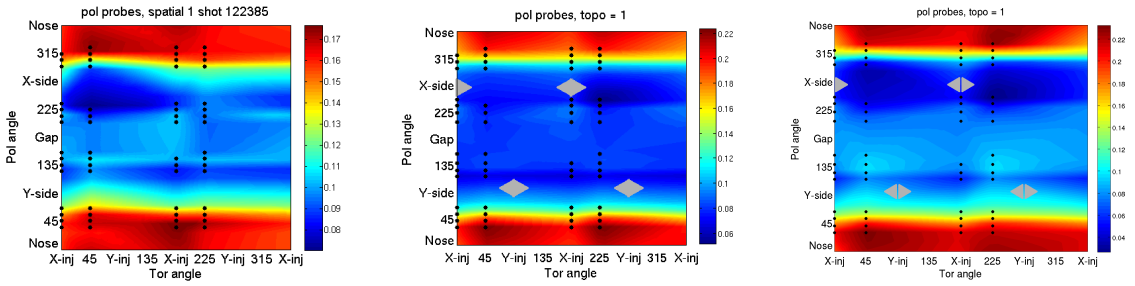

(a) 1st data topo (b) 1st 2MHD7.5 topo (c) 1st rMHD7.5 topo

(d) 2nd data topo (e) 2nd 2MHD7.5 topo (f) 2nd rMHD7.5 topo

Figure 3.16: Comparison of first (top row) and second (bottom row) poloidal topos from shot 122385 with those of 2MHD7.5 (center), and rMHD7.5 (right). The square domain represents the unwrapped HIT-SI walls. The vertical and horizontal axes correspond to the poloidal and toroidal coordinates θ and ϕ. The black dots mark the locations of the real and synthetic SP's. Dead probes are excluded. The gray diamonds mark the locations of the injector mouths. Both models reproduce the 1st poloidal topo.

differences in the toroidal BD topos and shifting orders of the components. Because of this, the topos from rMHD7.5 have been swapped so that 2nd topo appears in lieu of the 1st and *vice versa* in figures 3.17(f) and 3.17(c). The first rMHD7.5 toroidal topo displays both similarities with shot 122385 in the top half of figure 3.17(c) and differences from shot 122385 in the bottom half of the same figure. Figures 3.17(d)–3.17(f), showing the 2nd toroidal topos, further illustrate the superiority of 2fl-MHD over rMHD in capturing the structure of the surface magnetic fields and the usefulness of BD as a validation tool.

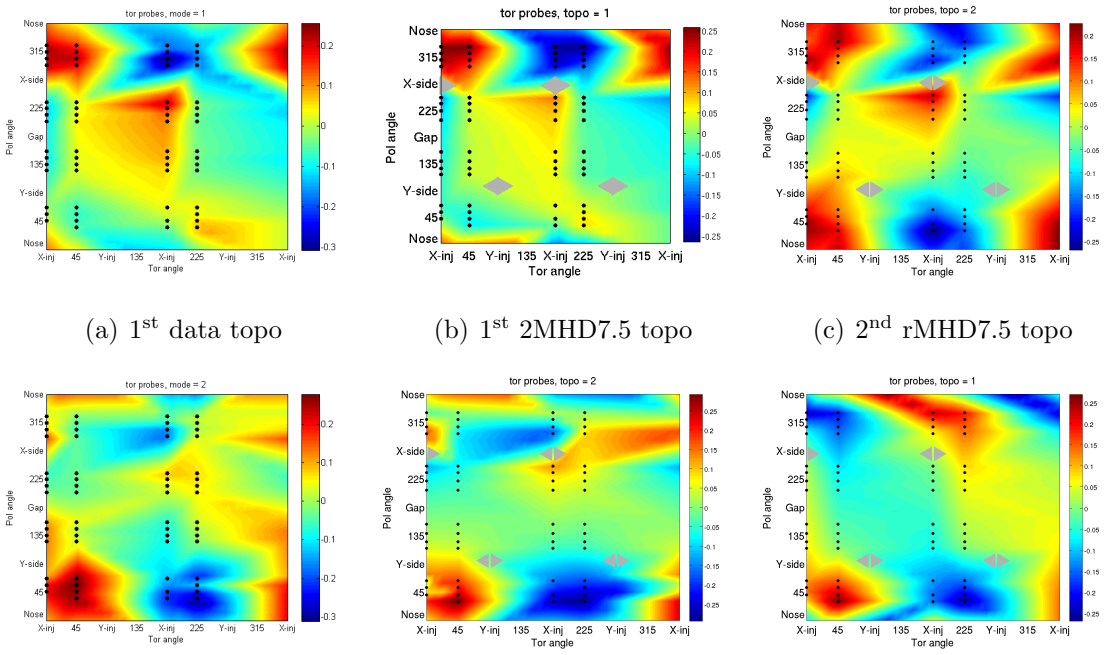

(a) 1st data topo (b) 1st 2MHD7.5 topo (c) 2nd rMHD7.5 topo

(d) 2nd data topo (e) 2nd 2MHD7.5 topo (f) 1st rMHD7.5 topo

Figure 3.17: Comparison of first and second (left) toroidal topos from shot 122385 with those of 2fl-MHD (center), and rMHD (right). The square domain represents the HIT-SI walls unwrapped. The vertical axis corresponds to the poloidal angle and horizontal to the toroidal direction. The black dots correspond to the locations of the real and synthetic SP's. Fewer than 16 dots indicates dead probes in a particular Ampèrian array. Topos 1 and 2 have been swapped for rMHD7.5 based on the results of the correlations. 2fl-MHD reproduces the prominent structures more accurately than rMHD.

Chapter 4

RESULTS OF THE TWO-FLUID MHD SIMULATIONS

This chapter investigates the two-fluid model of HIT-SI. Results from all four two-fluid validation simulations, 2MHD6, 2MHD7.5, 2MHD10, and 2MHD12, are included and discussed as needed to better illustrate the emerging trends. Recall these four simulations use the following values of magnetic dissipation: $\eta/\mu_0 = 25$, 17.8, 12.5, and 8.8 m^2/s, corresponding to $T_e = 6$, 7.5, 10, and 12 eV, and Lundquist number, $S =$ 29, 32, 58, and 62, respectively. 2MHD6 is used for the spectral analysis. Prominent structures from 2MHD10 and 2MHD12 are presented for the 3-D visualization. Partial scans of the parameters η, ν, and λ_{inj} are included as well.

The chapter on validation, Chapter 3, contains a detailed analysis of the evolution of the magnetic mode structure for 2MHD7.5. The ME spectrum for the 6-eV simulation, 2MHD6, as well that for the other 2fl-MHD simulations, 2MHD10 and 2MHD12, are nearly identical to that of the 7.5 eV simulation. Therefore, the analysis of §3.2 holds for all two-fluid simulations, and will not be repeated. Hence, only a few additional spectral features, mostly regarding the kinetic energy evolution, are covered in this section.

The evolution of (linear) magnetic and kinetic energy per mode n is shown in figures 4.1(a) and 4.1(b). The logarithmic plots of ME and KE per mode are shown in figures 4.1(c) and 4.1(d). The spectral evolution is once again split into three stages to facilitate the analysis. Only the first 6 modes ($n \leq 5$) are included in the energy traces with the exception of figure 4.1(c). The initial behavior of the even-numbered modes, occurring between the injector ramp-up and the beginning of the linear growth at $t \approx 0.1$ ms, varies with the injector phase Φ_{inj} (lead-lag). For example, the sharp

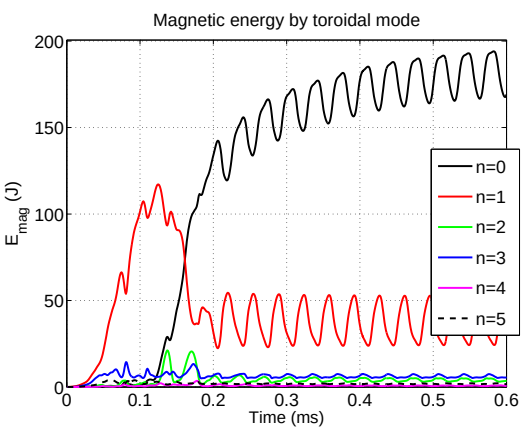

(a) ME per mode for $n = 0 - 5$ vs. time (ms)

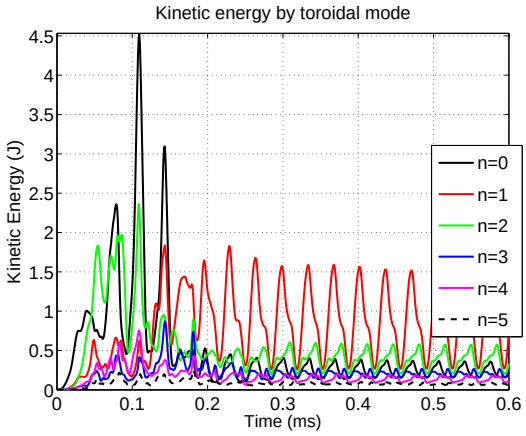

(b) KE per mode for $n = 0 - 5$ vs. time(ms)

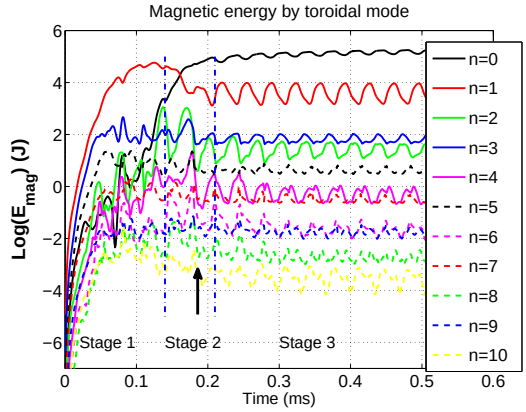

(c) Log magnetic energy per mode for all n

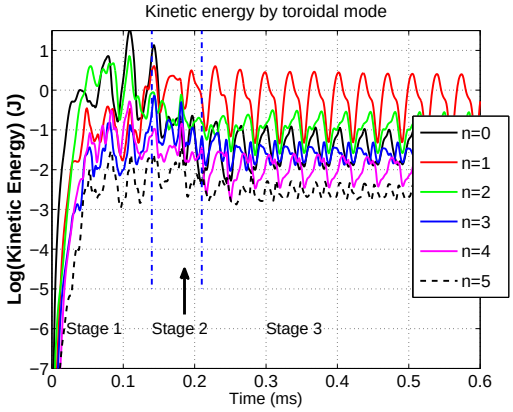

(d) Log kinetic energy per mode for all n

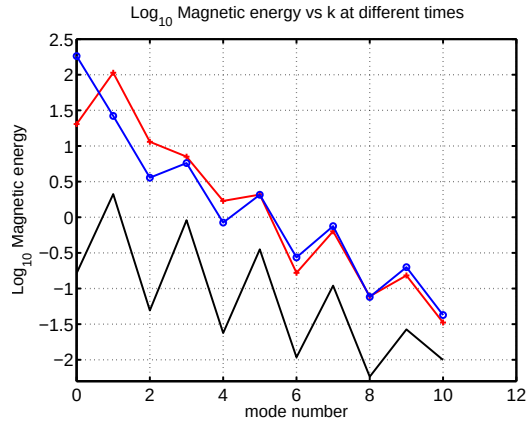

(e) Log ME vs. n from three separate times

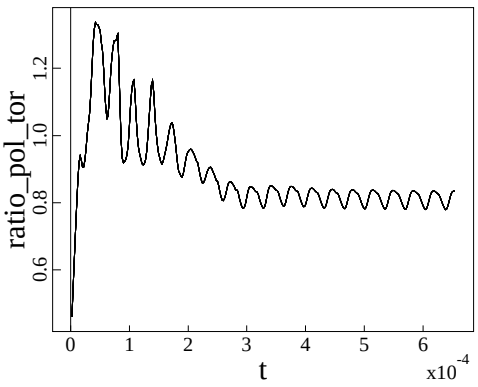

(f) Ratio of toroidal to poloidal ME

Figure 4.1: Spectral characteristics of the 6eV 2fl-MHD simulation. (a) and (b) are plots of ME and KE per toroidal mode as a function of time (ms). (c) and (d) the natural logarithm of (a) and (b). The blue dashed lines separate the three characteristic stages of mode evolution described in §3.2. (e) is a plot of log ME as a function of n at the three instants from the three distinct stages, marked by the blue dashed lines. Finally, (f) is the ratio of the total poloidal to toroidal ME as a function of time.

and rise drop in the $n = 0$ log(ME) at $t \approx 0.075$ ms is absent for $\Phi_{inj} = -\pi/2$, when the Y injector leads X. As mentioned in the previous chapter, the energy cascade into shorter wavelengths (higher n), associated with magnetic relaxation, manifests itself as excitations (bumps) of the $n = 2 - 4$ (and higher) modes during stage II.

Figure 4.1(e) shows ME as a function of n from three instants representative of the three distinct stages from 2MHD6. The blue trace corresponds to ME spectrum from stage III, the period of steady-state current sustainment. It shows that the final ME spectrum for $n > 3$ is not fully monotonic; instead exhibits a sawtooth-like pattern. For example, the $n = 5$ ME is greater than the $n = 4$ ME. This is a result of the continuing coupling of the injector drive to the odd-numbered modes.

The ratio of the poloidal ($U_\theta = \int dV \frac{B_\theta^2}{2\mu_0}$) to toroidal ($U_\phi = \int dV \frac{B_\phi^2}{2\mu_0}$) magnetic energy increases initially, favoring the poloidal component. However, relaxation activity converts B_θ to B_ϕ, resulting in a gradually declining $\frac{U_\theta}{U_\phi}$, which asymptotes to a value less than unity in stage III (figure 4.1(f)). This conversion of B_θ into B_ϕ is encountered in rMHD as well (figure 5.1(f)).

The kinetic energy (KE) spectrum is initially dominated by the $n = 0$ and $n = 2$ modes, which exhibit periodic spikes, associated with bursts of plasma caused by the injector oscillations. There is also significant $n = 1$ activity, which is a consequence of the Hall effect as explained in §3.2. Once a large $n = 0$ forms and significant I_{tor} is generated, the $n = 1$ becomes the dominant kinetic mode. Figure 4.2 shows the plasma flow out of the X-injector mouths. The image corresponds to a time in the simulation (2MHD10) when the $n = 1$ is prevalent, and the X injector is near its peak output. The plasma flow is zero right at the boundary due to the zero-flow BC, but there is significant acceleration of the plasma outside the resistive layer all the way to the mid-plane region ($z = 0$). The flow is always directed toward the magnetic axis, *i.e.*, into the region of lower magnetic pressure and away from the injector mouths, the region of high pressure, regardless of the direction of injector flux and current. The $n = 1$ flow generated by the Hall term makes the overall flow asymmetric with

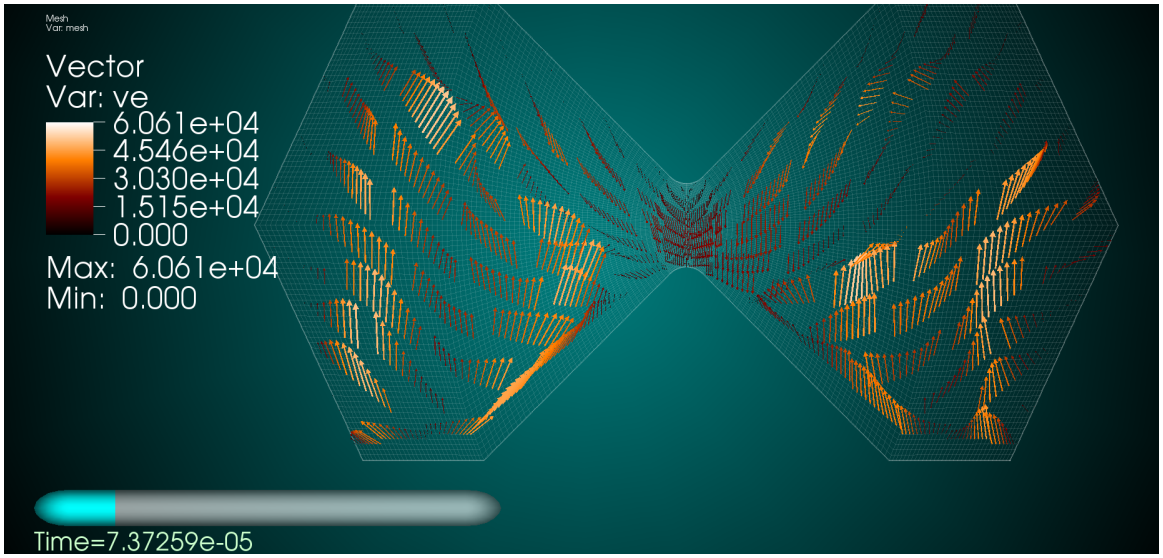

Figure 4.2: Plasma flow out of the X injector at $t = 0.0737$ ms ($1.07\tau_{inj}$), as the X-injector flux and current are decreasing. The flow pattern is asymmetric with respect to the centerline ($R = 0$) because of significant $n = 1$ flow in the domain.

respect to the centerline during the stage I. This is not the case for rMHD, which shows centerline-symmetric plasma flows during the $n = 1$-dominated stage as indicated by figure 5.2. Plasma flows with odd-toroidal symmetry are initially absent in rMHD.

4.1 Partial Parameter Scans

4.1.1 η (T_e or S) scan

The Lundquist number S depends on η, which in turn depends on T_e via the Spitzer resistivity. Therefore, a scan in η is equivalent to a scan in T_e or S and all these quantities will be used interchangeably here. The steady-state I_{tor} reaches 36, 46, 58, and 68 kA equivalent to $I_{tor}/I_{inj} = 1.8, 2.3, 2.9$, and 3.4, respectively for the four 2fl-MHD simulations with the various values of T_e, shown in figure 4.3. It was established in Chapter 3 that $I_{tor} \propto T_e^{0.9} \propto \eta^{-0.6}$. Reducing η to raise T_e (and S) builds up more total magnetic energy and speeds up τ_A, resulting in a greater $n = 0$

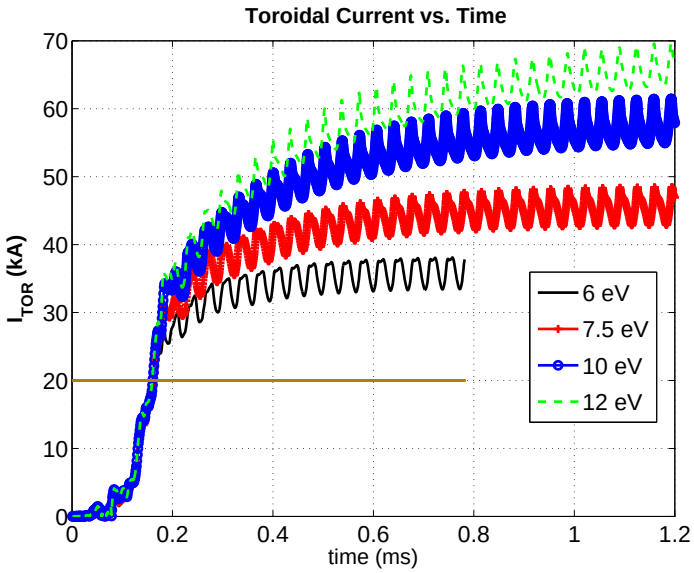

Figure 4.3: I_{tor} as a function of time (ms) from all four two-fluid validation calculations, 2MHD6 (black), 2MHD7.5 (red), 2MHD10 (blue), and 2MHD12 (green). I_{tor} increases as η is lowered to raise T_e.

and I_{tor}. Figure 4.3 shows temporal traces of I_{tor} from all four 2MHD simulations with a different η. Note the identical I_{tor} rise times for all four cases, which implies the same formation time τ_f for all four simulations. This means the dimensionless formation time τ_f/τ_A, normalized by τ_A, gets longer as $T_e(S)$ increases, contrary to the trend observed in rMHD scans that indicate a shortening of τ_f with increasing S (figure 5.28(a)) and an approximate invariance of time scales and growth rates with respect to τ_A. This suggests the growth of the $n = 0$ and other unstable modes is governed by a non-ideal MHD process for the two-fluid simulations; this is of course the Hall effect as discussed in the previous chapter. Similar to rMHD, it takes I_{tor} longer to reach a steady state as η is lowered, since I_{tor} and energy steady state occur on resistive time scales. The time that elapses between when $I_{tor}/I_{inj} = 1$ and when I_{tor} attains a stead state increase.

4.1.2 Viscosity (ν) Scan

A scan in viscous dissipation ν is conducted for the 6 eV two-fluid calculations to determine the sensitivity of the general trends on ν. For that purpose, two additional 2MHD6 simulations with twice ($\nu = 520$ m^2/s) and five times (1560 m^2/s) the viscous dissipation of the original 2MHD6 case were performed. A higher viscosity reduces turbulence and gives rise to more laminar flows. The temporal trace of I_{tor} from the three simulations with a different ν is shown in figure 4.4(a). ν = 260, 520, and 1560 m^2/s are shown as black, red, and blue traces, respectively. I_{tor} is slightly reduced as ν increases, and the local maxima corresponding to the peaks of both injector oscillations begin to be resolved due to reduced turbulence. The enhanced viscous dissipation damps the plasma flow, as evidenced by a clear reduction in the total kinetic energy (KE) shown in figure 4.4(b). The mode activity prior to and during the relaxation event leading to I_{tor} generation is different for $\nu = 1560$ m^2/s, as indicated by the temporal traces of ME per toroidal mode for $n = 0 - 5$ shown in figure 4.4(d). Compare this figure with figure 4.1(a). The figure indicates that it takes two relaxation events to fully convert the $n = 1$ to the $n = 0$ and reach a steady state. The bumps in $n = 2$ ME that appear at the times of large energy transfer from the $n = 1$ to the $n = 0$ ($t = 0.1$ and 0.2 ms) are the usual $n = 2$ excitations caused by the energy cascade associated with relaxation. Note that as the $n = 1$ ME goes through another growth spurt, the I_{tor} begins to drop and eventually crashes at $t \approx 0.175$ ms (figure 4.4(a)). The total ME is not strongly affected by ν; it decreases by 10% as ν is raised from 260 to 1560 m^2/s (figure 4.4(c)). The total ME decreases because there is a reduction of the MHD dynamo —essential in $n = 0$ amplification— due to the damping of flows at large ν. A lower viscosity ($\nu = 52$ m^2/s) has no effect on the amplitude of I_{tor}. In summary, the characteristics show a very weak dependence on the viscosity for a wide range of viscosities.

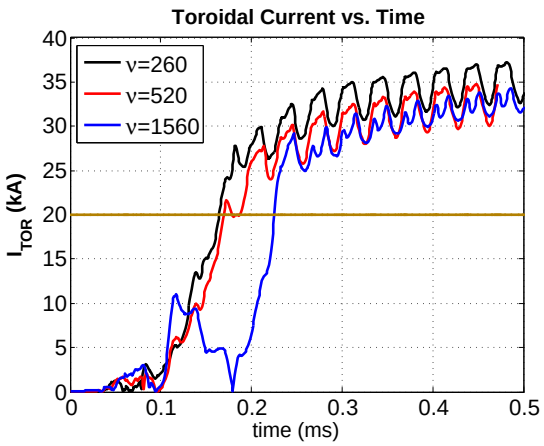

(a) I_{tor} vs. time(ms)

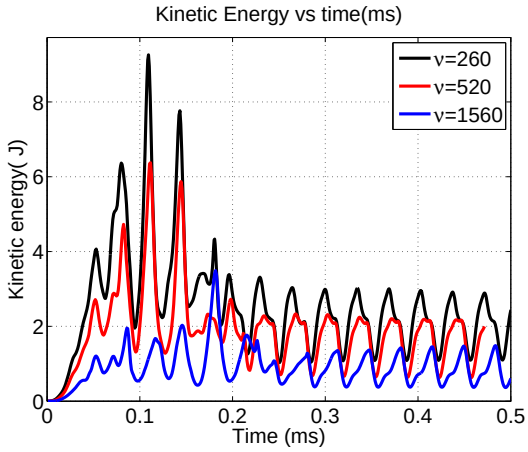

(b) Total KE vs. time (ms)

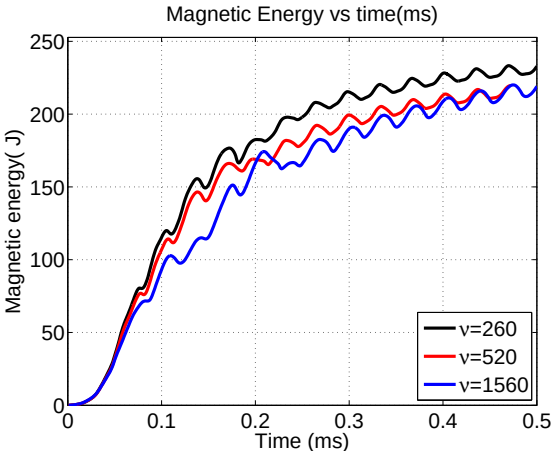

(c) Total ME vs. time(ms)

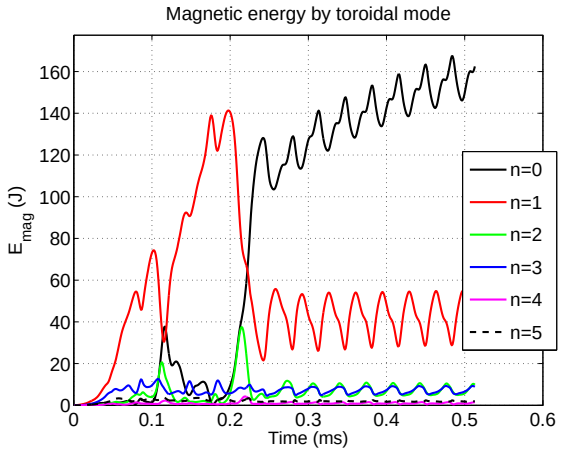

(d) ME per n for $n = 0 - 5$ vs. time(ms) for $\nu = 1560$ m$^2/s$

Figure 4.4: (a) I_{tor} as a function of time (ms), (b) total KE as a function of time (ms), and (c) total ME as a function of time (ms) for the three 2MHD6 simulations with a different viscous dissipation, ν = 260, 520, and 1560 m^2/s. (d) ME per mode as a function of time for $n = 0 - 5$ for the simulation with $\nu = 1560$ m$^2/s$. Cases with $\nu \leq 520$ behave similarly. The mode activity prior to steady-state I_{tor} sustainment is significantly altered for $\nu = 1560$ m^2/s. The total KE is reduced notably as a result of enhanced viscous damping. The total ME only decreases by 10%.

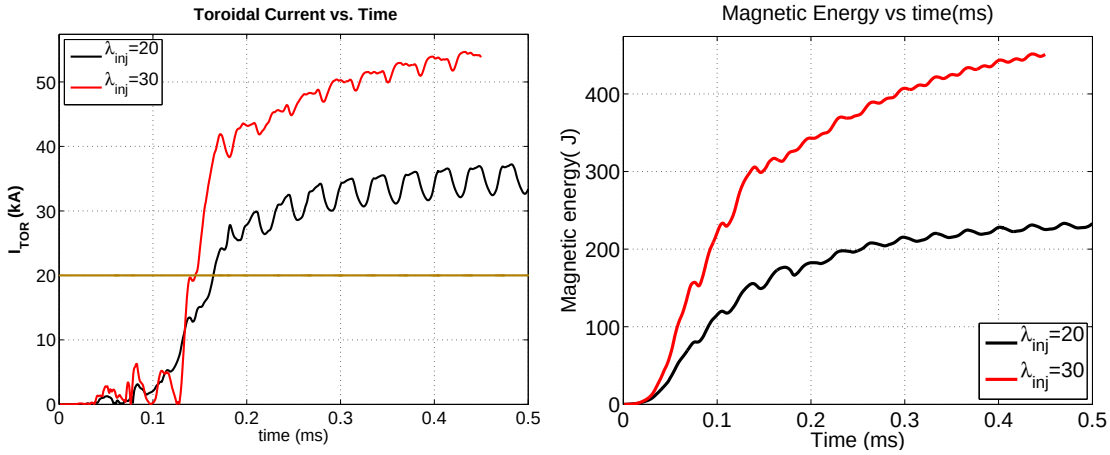

(a) I_{tor} vs. time(ms)

(b) $n = 0$ ME vs. time (ms)

Figure 4.5: (a) I_{tor} as a function of time (ms) and (b) total ME as a function of time (ms) for two 2MHD6 simulations with $\lambda_{inj} = 20$ m^{-1} (black) and 30 m^{-1} (red). The case with $\lambda_{inj} = 30$ m^{-1} yields significantly more total ME and I_{tor} than the case with $\lambda_{inj} = 20$ m^{-1}, suggesting the helicity injection rate increases as λ_{inj} is raised, in this case, almost linearly with λ_{inj}. This indicates $Z_{inj} \propto \lambda_{inj}^3$.

4.1.3 λ_{inj} scan

λ_{inj} is the ratio of injector current I_{inj} to injector flux ψ_{inj}: $\lambda_{inj} = \mu_0 I_{inj}/\psi_{inj}$. To conduct a partial scan of λ_{inj}, an additional 2MHD6 case with $\lambda_{inj} = 30$ m^{-1} is simulated. This calculation uses a ψ_{inj} that is greater by a factor of $\sqrt{3/2}$ and an I_{inj} smaller by the same amount to keep the injected power and helicity the same as the $\lambda_{inj} = 20$ m^{-1} case, while increasing λ_{inj} by a factor of 3/2 to 30 m^{-1}. The traces of the total ME and I_{tor} as a function of time indicate that the case with $\lambda_{inj} = 30$ m^{-1} (red traces) generates more I_{tor} and ME (figures 4.5(a) and 4.5(b)) than the case with $\lambda_{inj} = 20$ m^{-1} (black traces). There is an increase of 50% in I_{tor}, suggesting a linear scaling of I_{tor}/I_{inj} with respect to λ_{inj}. Recall current amplification is governed by helicity balance (eqn. (1.16)). That I_{tor}/I_{inj} increases linearly with λ_{inj} implies that the injector impedance $Z_{inj} \propto \lambda_{inj}^3$ since $I_{tor}/I_{inj} \sim \sqrt{Z_{inj}/\lambda_{inj}}$. For rMHD, λ_{inj} scans presented in §5.3.2 indicate $I_{tor}/I_{inj} \approx \lambda_{inj}^{1/2}$ or possibly a weaker power of

λ_{inj}. This result is consistent with the earlier conclusion that the Hall term leads to a greater Z_{inj} than rMHD (§3.2).

4.2 Visualization

The visualization analysis features the magnitude of current density J and $\lambda = \mu_0 j_\parallel / B$ from 2MHD10 because these quantities convey the greatest amount of information about the prominent structures in the absence of plasma pressure and closed flux. Field line traces from 2MHD10 and 2MHD12 are included as well to provide a picture of the magnetic structure through different phases of an injector cycle after $n = 0$ amplification.

Figures 4.6(a) and 4.6(b) show a planar view of λ in the poloidal planes bisecting the Y injector mouths from two instants in time: $t = 0.125$ and 0.305 ms, *i.e.*, pre- and post-relaxation stages. Only $\lambda = -10 - 24$ m^{-1} values are plotted. The orange color corresponds to $\lambda = 20$ m$^{-1} = \lambda_{inj}$. The bluish colors correspond to regions of very low or negative λ's. Figure 4.6(a) indicates a mirror (centerline)-symmetric λ-profile (with respect to the geometric axis) during stage I when the $n = 1$ is dominant and the $n = 0$ component is absent. Figure 4.6(b) shows the planar λ-profile after the $n = 0$ amplification. The Y injector current channel, containing the fields and current of the Y-injector, adjusts its path to realign itself with the fields of the spheromak-like object. When the Y-injector current and field reverse, the direction in which the Y-injector channel leans switches to realign the injector field with the spheromak fields once again. This 'windshield wiper'-like motion, oscillating exactly at f_{inj}, is illustrated in figures 4.7(a) and 4.7(c) that are be separated by approximately $\tau_{inj}/2$ in time. The wide regions of high λ near the inner cone above $z = 0$ in figure 4.6(a) correspond to where the X-injector fields puncture the Y-injector plane. Note during the $n = 1$ dominance, the X-injector strike points on the Y-injector plane are mirror-symmetric as well. The X-injector fields strike the inner cone head-on and get split into two major streams that circumnavigate the cone.

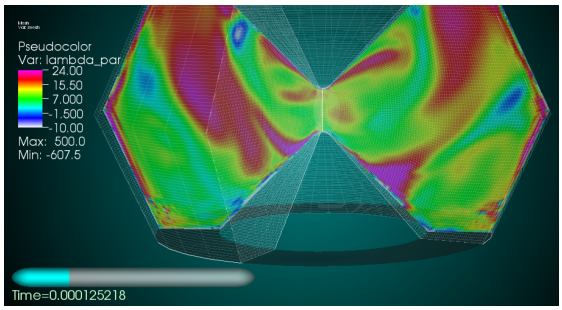

(a) λ at $t = 0.125$ ms

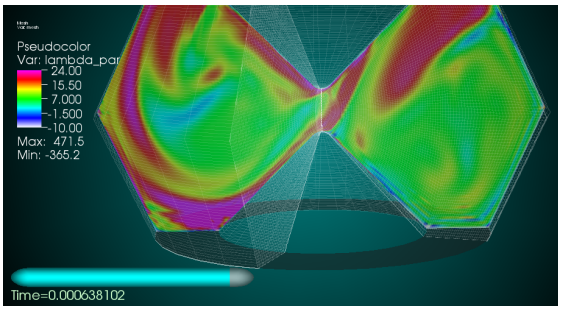

(b) λ at $t = 0.305$ ms

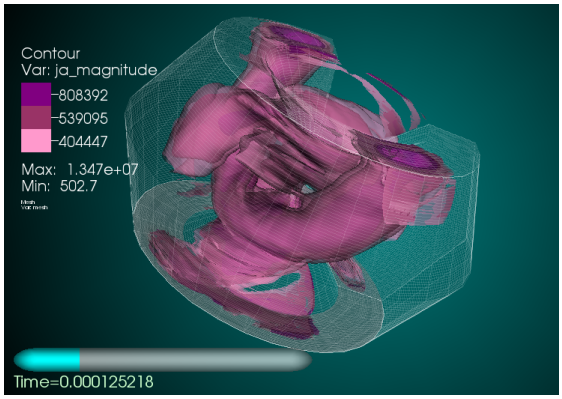

(c) J at $t = 0.125$ ms

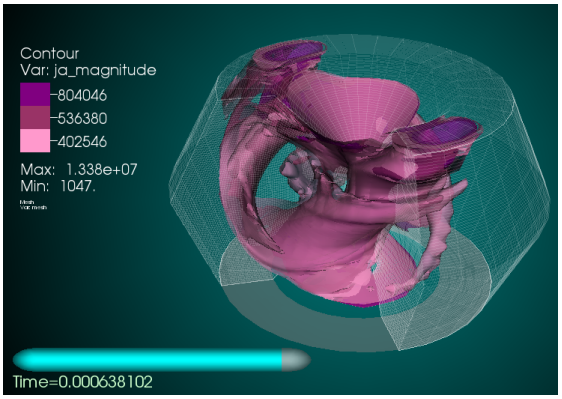

(d) J at $t = 0.305$ ms

Figure 4.6: (a) and (b) Pseudo-color plots of λ in the poloidal plane bisecting the Y- injector (upper injector) mouths before and after $n = 0$ amplification. λ profile is mirror-symmetric while the $n = 1$ dominates the magnetic spectrum. The $\lambda \simeq 20$ m^{-1} region is represented by the orange color. (c) and (d) show magnitude of current density J. The prominent J structures in this case represent the injector current channels. These channels lean further from the cones and follow a more circular around them as the $n = 0$ grows.

The bluish colors in the planar λ figures correspond to the image currents that are generated in the plasma due to the current injection. Since the plasma is a conducting medium, the back EMF caused by the injected current creates an opposing current in the plasma. The black circles shown in figures 4.7(a) and 4.7(c) enclose the locations where the X-injector current channel (red) and its image current (blue) puncture the Y-injector plane. The image currents do not have an equal and opposite λ_{inj} (-20 m^{-1}), because local currents within the spheromak region add to the image currents, raising their λ. Note that the X-injector structure has also lost its mirror symmetry at this time and punctures the Y-injector plane either to the left or right of the inner cones, depending on its oscillation cycle, consistent with the $n = 0$ dominance. The λ-profile from rMHD presented in §5.1.2 bears a close resemblance to the λ-profiles shown here. The injector current paths of 2fl-MHD and rMHD during stage III are as described in the papers by Victor *et al.* [32] and Jarboe *et al.* [31].

A sketch of the expected trajectory of the injector field lines (red lines) when a spheromak-like object is present is provided in figures 4.7(b) and 4.7(d) (figure 15 of Ref. [65]) to aid the visualization. These figures are in the same plane —bisecting the Y-injector mouths— as the planar λ-profiles of figures 4.6(a) and 4.9(b). They show the Y-injector fields (red lines) at a time of maximum (absolute value) Y-injector flux and zero X-injector flux. The Y-injector path in the sketches is consistent with the regions of high λ the simulations. The blue lines represent the spheromak poloidal field enclosing an I_{tor} that points out of the page in the right half of the figure and into the page in the left half of the figure, 180 degrees around the torus. Note that the Y-injector fields in the sketches also undergo the same windshield-wiper motion encountered in the simulations. Figures 4.7(b) and 4.7(d) show a minimal disruptive effect of the injectors on the spheromak as they represent the ideal and aimed behavior of the experiment. The simulations show that the injectors have a disruptive effect on the spheromak region ($\lambda \sim 10$ m^{-1}) for low-to-intermediate current amplification ($I_{tor}/I_{inj} \leq 6$). They distort and tilt the spheromak much more notably than depicted

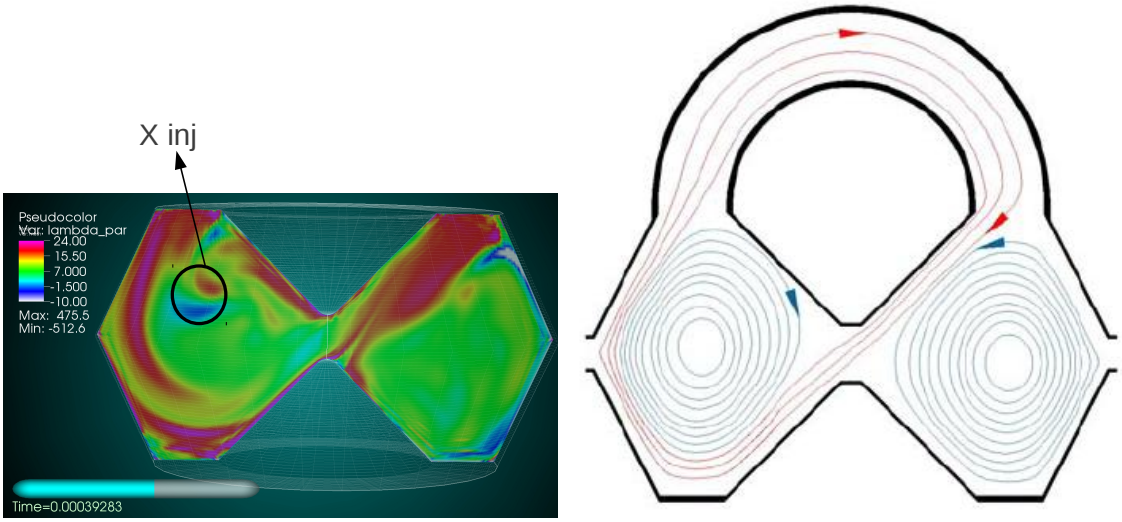

(a) λ at $t = 0.393$ ms

(b) Field line sketch

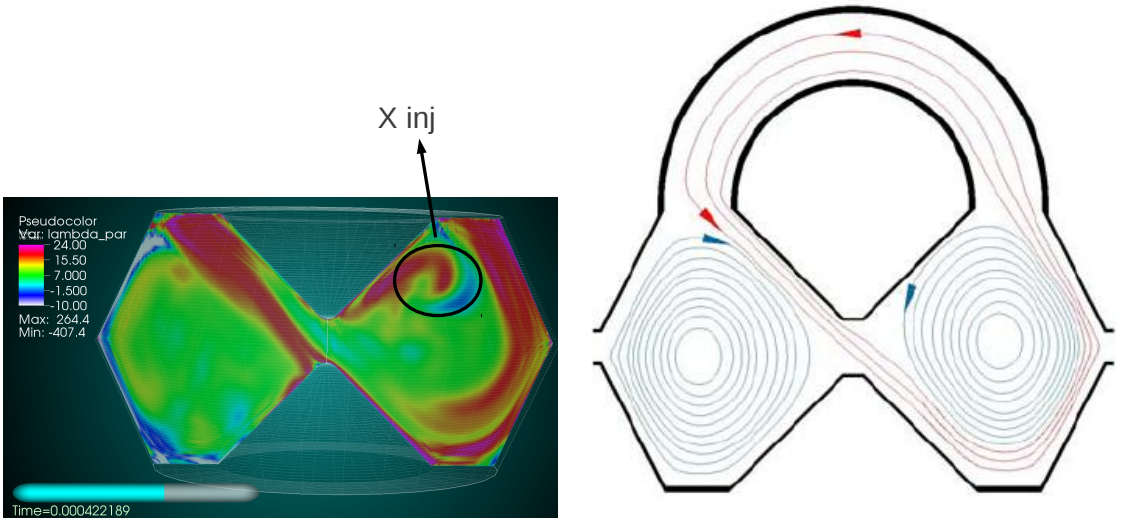

(c) λ at $t = 0.422$ ms

(d) Field line sketch

Figure 4.7: (a) and (c), the λ-profile when the Y injector is near its maximum compared with (b) and (d), sketches of the trajectory of the Y-injector field lines when a spheromak-like object is present. The concentrated λ region representing the injector column from the simulation is very similar to the expected trajectory of the injector fields. The circled red and blue patches correspond to where the X injector current channel and its image current puncture the Y-injector plane. (b) is shown in Refs. [65] and [66] and similar figures were included in [67].

in the idealization of SIHI because they occupy a much larger region than the injector region shown in the sketches.

Figure 4.6(c) shows a Y-injector J structure from the $n = 1$-prevalent stage (stage I) that is consistent with the centerline-symmetric λ-profile pictured in figure 4.9(a). To clarify the picture, J in regions where $B < 0.04$ T is excluded to remove the boundary layers where current piles up, reaching 10^7 A/m^2. Only three J isosurfaces with 3, 4 and 6% of the maximum J ($J_{max} = 1.347 \times 10^7$ A/m^2) are plotted. An additional configuration encountered here (and in rMHD, figure 5.8) during stage I features the two-oppositely directed axial ($\hat{z}$) current channels that connect the X and Y sides together as illustrated by figure 4.8. Figure 4.6(d) shows J at the exact same time as figure 4.6(b) when $I_{tor}/I_{inj} \approx 2$. The current channel follows an increasingly more circular (toroidal) path around the central cones, leaning farther away from the centerline as the $n = 0$ grows. It crosses either in front or behind the central cones depending on where it is in its respective injection cycle to align itself with the direction of I_{tor}. The similarity between the J and λ evinces that the configuration is always almost force-free ($\mathbf{J} \times \mathbf{B} = 0$).

Figure 4.9 shows four snapshots of the isosurfaces of $\lambda = 9, 10$ and 11 m^{-1}. These values were chosen because of their closeness to the spheromak λ, $\lambda_{sph} = 10.3$ m^{-1} and because the low λ regions exclude the injector channels. Each snapshot corresponds to a time that is a quarter period into an X-injector cycle when both X and Y injectors output the same amount of power. The chosen times are 1.25, 2.25, 4.25, and $9.25\tau_{inj}$ in terms of τ_{inj}. Regions of low field ($B < 0.035$ T) are once again excluded from the picture. At earlier times, $\lambda = 9-11$ m^{-1} surfaces are nearly absent. The low-λ-profile relaxes and redistributes itself as the simulation progresses with $\lambda \approx \lambda_{sph}$ isosurfaces increasingly occupying a greater fraction of the volume, as shown by figures 4.9(c) and 4.9(d). The emerging structure resembles a strongly tilted, thin spheromak that is likely responsible for generating the component of I_{tor} that does not come directly from the injectors. The current contained in this structure should be approximately

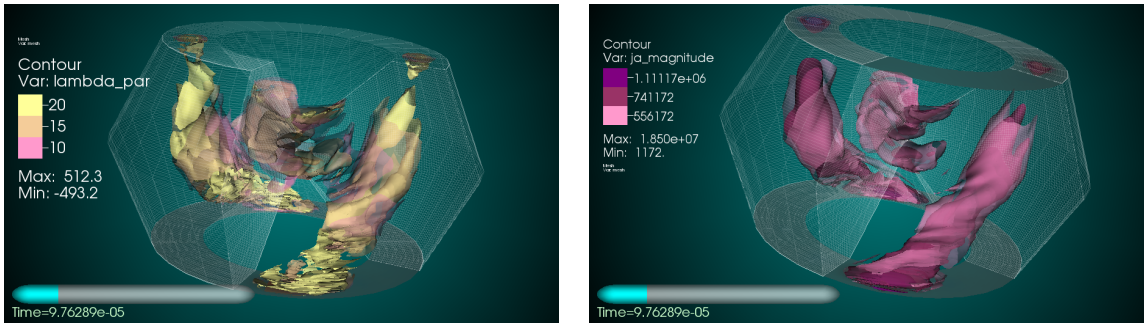

(a) λ at $t = 0.125$ ms (b) J at $t = 0.125$ ms

Figure 4.8: 3-D plots of (a) λ and (b) J at a time ($t = 0.0976$ ms) from stage I that features two oppositely-directed axial current channels that connect the X and Y sides together, very similar to the structure observed in the baseline rMHD calculation shown in figure 5.8. The structure of J closely resembles that of λ.

$I_{tor} - mI_{inj}$, where m is an integer that tracks the number of times I_{inj} wraps toroidally around the domain.

4.3 Magnetic Topology: Flux Surfaces and Magnetic Field Lines

The magnetic field structure is traced with a series Poincaré puncture plots that are computed every 100 time steps during the last $0.2 - 0.3$ ms of both simulations, when I_{tor}/I_{inj} is nearly maximized. Field lines are launched from a grid of 96 evenly-spaced points that spans a region bounded by $0.275 \leq R \leq 0.375$ and $|z| \leq 0.05$ cm at $\phi = 0°$. Puncture plots indicate that both 2MHD10 and 2MHD12 feature small regions of transient closed flux surfaces that last a fraction of an injector period. Figure 4.10(a) shows one of the brief occurrences of closed flux from 2MHD10. 2MHD12 displays more frequent occurrences of closed flux than 2MHD10, suggesting that the frequency and volume of closed flux increase as η is lowered to increase I_{tor}/I_{inj}. The closed flux structures migrate in the poloidal plane following a trajectory that approximately orbits the magnetic axis, however, they vanish after completing only a fraction of their orbit. The absence of closed flux in 2MHD6 and 2MHD7.5 suggests a threshold

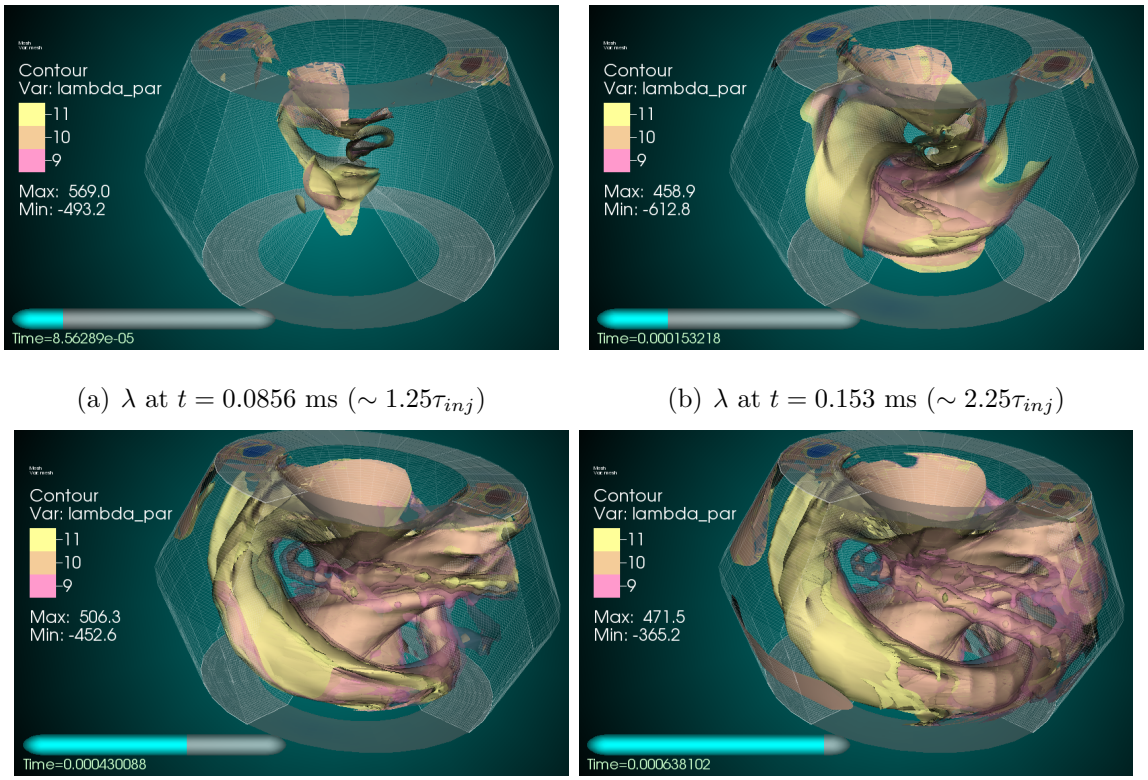

(a) λ at $t = 0.0856$ ms ($\sim 1.25\tau_{inj}$)

(b) λ at $t = 0.153$ ms ($\sim 2.25\tau_{inj}$)

(c) λ at $t = 0.430$ ms ($\sim 6.25\tau_{inj}$)

(d) λ at $t = 0.638$ ms ($\sim 9.25\tau_{inj}$)

Figure 4.9: Isosurfaces of $\lambda = 9$, 10 and 11 m^{-1}. Each snapshot corresponds to a time that is a quarter period into an X-injector cycle. The λ-profile becomes more uniform as the simulation progresses. The emerging structure has the appearance of an extremely tilted and thin spheromak.

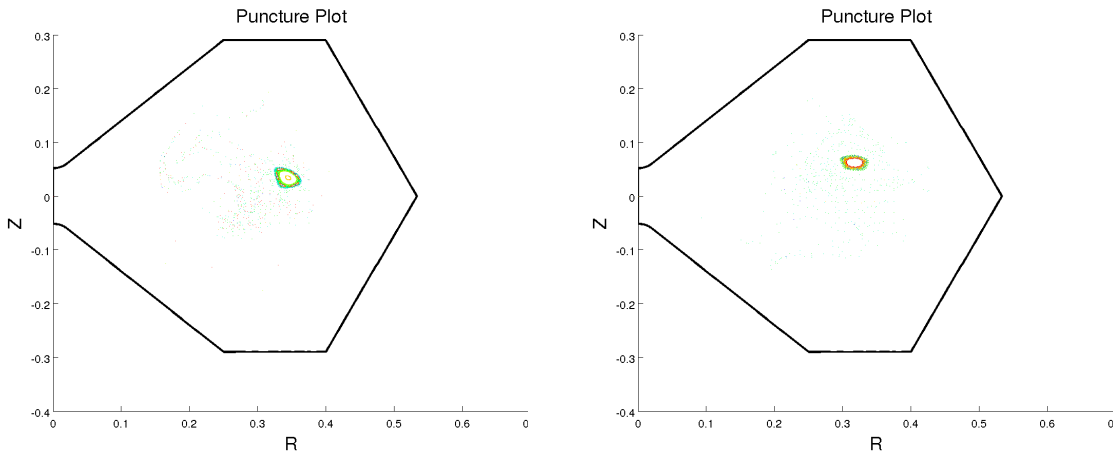

(a) (b) I_{tor} vs time (ms)

Figure 4.10: Poincaré puncture plots through the poloidal plane at $\phi = 0°$ toroidal slice from (a) 2MHD10 at $t = 0.867$ ms (dump.30300) with $I_{tor} = 54$ kA and (b) 2MHD10 with $\nu = 52$ m^2/s at $t = 0.7257$ ms (dump.56700) with $I_{tor} = 54$ kA, showing a small region of closed flux near the outboard side at the mid-plane.

in I_{tor}/I_{inj} for forming closed flux. This threshold is estimated as $I_{tor}/I_{inj} = 2.3 - 2.9$ based on present results. For 2MHD10, the times of closed flux coincide with the local minima in I_{tor}. This is approximately true for 2MHD12 as well.

In the absence of plasma pressure, viscosity can lead to anomalous closed flux surfaces with peculiar shapes such as the one displayed in figure 5.27. To confirm the authenticity of the closed flux, an additional 2MHD10 simulation with one fifth the viscous dissipation ($\nu = 52$ m^2/s) of the original 2MHD10 simulation was run. This calculation shows structures similar to those seen in 2MHD10 with $\nu = 260$ m^2/s, as shown in figure 4.10(b). For both cases, the first appearance of closed flux occurs approximately when $I_{tor} = 54 - 55$ kA, equivalent to $I_{tor}/I_{inj} \geq 2.7$.

3-D field line tracing is a useful tool for visualizing the magnetic topology of the configuration. The emphasis here is on the 2MHD12 simulation as this is the case with the greatest I_{tor}/I_{inj} and thereby, the most frequent occurrences of closed flux.

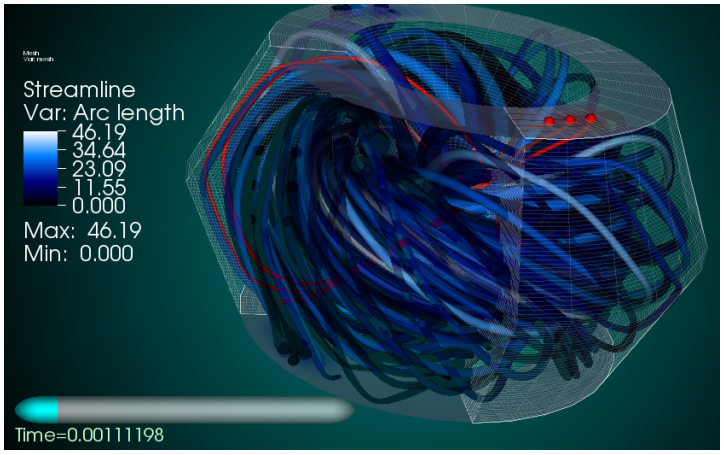

(a) Field lines at $t = 1.112$ ms ($16.1\tau_{inj}$)

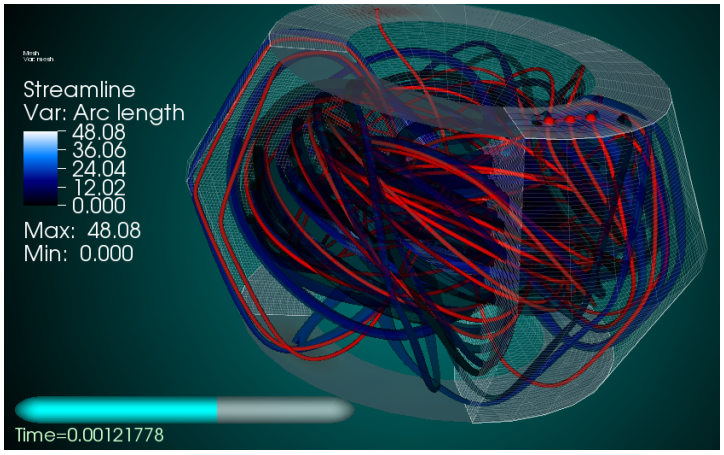

(b) λ at $t = 1.218$ ms ($17.7\tau_{inj}$)

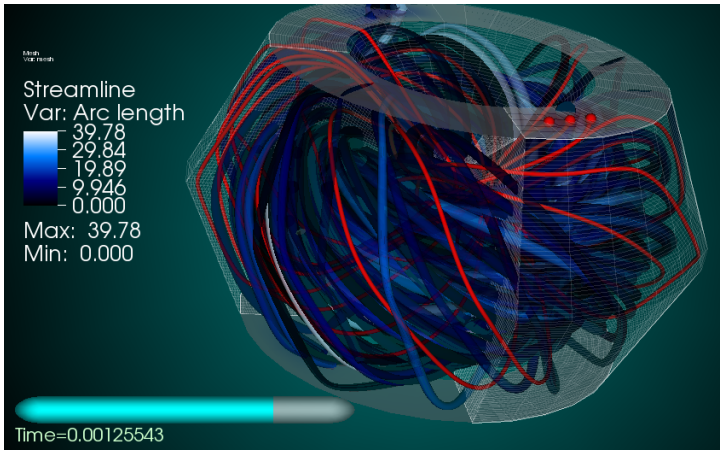

(c) λ at $t = 1.255$ ms ($18.2\tau_{inj}$)

Figure 4.11: Field-line traces launched from one of the Y-injector mouths (red lines) and from a 3×3 array of points centered at the magnetic axis (dark lines) from a time near the end of 2MHD12 simulation when $I_{tor}/I_{inj} \approx 3.4$. Cases representing (a) minimal injector wrap up and a spheromak-like structure, (b) significant injector wrap up, and (c) moderate injector wrap up with a approximate spheromak-like structure are shown.

Figure 4.11 shows three snapshots of field line traces near the end of the simulation when $I_{tor}/I_{inj} \approx 3.4$. The red field lines are the Y injector field lines, launched from three points along a line centered at one of the Y-injector mouths. The darker field lines are the confinement volume field lines, launched from a 3×3 array of 9 points centered at the magnetic axis, $(x, y, z) = (0.325, 0, 0)$ m. To showcase an advanced feature of VisIt, the radius of the confinement volume field lines are allowed to vary with respect to B (any scalar quantity can be chosen for this option). In the absence of closed flux, all of the field lines are open and the confinement volume field lines should eventually connect to the one of the four injector mouths. Figure 4.11(a) at $t = 16.1\tau_{inj}$, a time when Y injector is near its minimum, shows minimal wrap-up of the injector field lines and a magnetic structure resembling that of a spheromak with the outer fields being predominantly poloidal and inner fields toroidal. Figure 4.11(b) at $t = 17.7\tau_{inj}$, a time when Y injector is near its maximum shows increased injector wrap-up and a lot of overlap between the injector and confinement volume field lines, suggesting most of the darker field lines are tied to the Y injector. Figure 4.11(c) shows a moderate amount of injector wrap up with once again a structure more reminiscent of a spheromak with some poloidal field the near the walls of the confinement volume. Lastly, figure 4.12 is included as an illustration of field line structure in the presence of closed flux. The figure shows the field lines and Poincaré puncture plot through the $\phi = 0^\circ$ plane, figures 4.12(a) and 4.12(b), at $t = 1.190$ ms ($17.25\tau_{inj}$). The field line tracing finds a small volume of closed flux field lines that cross the $\phi = 0^\circ$ plane (the clipped surface whose normal lies in the plane of the page) exactly where the Poincaré puncture plot registers a closure. There are clearly strong non-uniformities in this structure as it exhibits a tilting and a shifting motion (modes with an $n = 1$ toroidal symmetry).

Figures 4.11(a)-4.12(a) indicate a confinement volume filled with field lines of similar length (up to 47 m). In VisIt, the length of each individual field line is constrained by the total number of steps that the field line integrator is set to take,

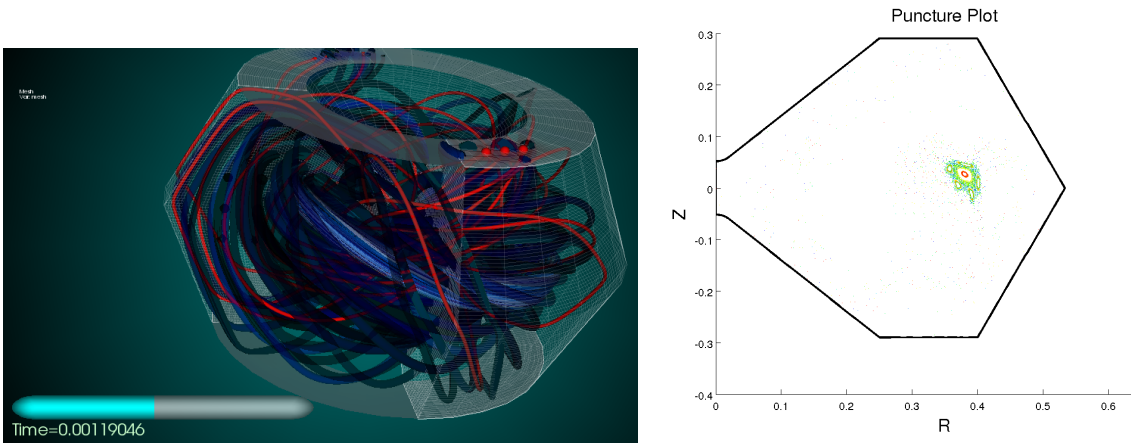

(a) Field lines at $t = 1.190$ ms ($17.25\tau_{inj}$)

(b) Poincaré puncture plot at $t = 1.190$ ms

Figure 4.12: (a) Magnetic field line traces and (b) a Poincaré puncture plot through the $\phi = 0°$ plane at $t = 1.190$ ms ($17.25\tau_{inj}$) showing a small volume of closed flux. Observe the light region of field lines in (a).

which is 10000 in this case. Thus, lengths are not accurately reflected for field lines that require more than 10000 steps to integrate along. Poincaré puncture plots[†] are ideal for determining the length of the field lines inside the confinement volume because of their greater computational accuracy and as they can integrate tens of field lines up to tens of kilometers in length in a reasonable amount of time. Thus, they are superior to 3-D streamlines of VisIt in this respect. Puncture plots indicate field lines as long as 3 km in the closed flux region. In this case, the lengths are constrained by the number of punctures through the $\phi = 0°$ plane, which was set to 1500. 1500 toroidal transits near the magnetic axis amounts to a length of 3 km as the toroidal circumference is 2 m at the magnetic axis. Figure 4.13(a) and 4.13(b) show a history

[†]Puncture plots are computed with a NIMROD post-processor nimfl, which resides in the directory `nimfl` and is a fully parallelized field line integrator that uses the native FE data structure of NIMROD to integrate along magnetic field lines, using an ODE solver. It is a highly accurate and very useful tool.

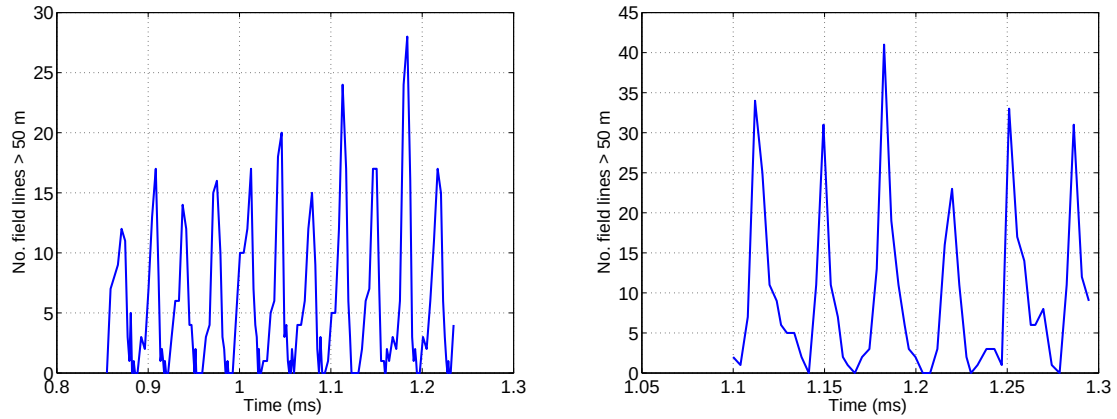

(a) Field lines > 50 m from 2MHD10

(b) Field lines > 50 m from 2MHD12

Figure 4.13: A history of the number of field lines exceeding 50 m from the sustainment phase of 2MHD10 and 2MHD12.

of the number of field lines longer than 50 m for 2MHD10 and 2MHD12, respectively. The peaks, *i.e.*, when long field lines are most numerous, correspond to times when neither injector outputs peak current.

4.4 Dynamo Analysis

The fluctuation dynamo analysis, introduced in §5.1.3, is crucial for uncovering the role of each mode in the $n = 0$ amplification and I_{tor} generation. This numerical tool measures the amount of power transferred to the $n = 0$ (mean-field) by the dynamo action of each toroidally non-symmetric ($n > 0$) mode (fluctuations). In the parlance of dynamo theory, $n > 0$ are called fluctuations and the $n = 0$ component is termed the mean-field (MF). The time integral of the fluctuation dynamo terms reveals how much energy is transferred to the MF. By summing over the contribution from all fluctuations, one can look at the bulk energy transfer into the MF. To gain a good understanding of the key physical quantities that arise and their interpretation, the reader is strongly recommended to peruse §5.1.3, which uses the baseline rMHD

calculation to illustrate the full features of the dynamo analysis tool. Here, the analysis is performed on all four 2fl-MHD simulations: 2MHD6, 2MHD7, 2MHD10, and 2MHD12, for which the Lundquist number is $S = 29, 34, 56$, and 62 and $\eta/\mu_0 = 25, 17.8, 12.5$, and 8.8 m^2/s, respectively.

Figure 4.14 shows that the overall energy transfer to the MF by both the MHD and Hall dynamos, denoted E_D, changes only slightly as η is lowered (S and T_e are raised). This term measures the action of the electron fluid fluctuations on the MF as $-\mathbf{v}\times\mathbf{B} + \frac{1}{ne}\mathbf{J}\times\mathbf{B} = -\mathbf{v_e}\times\mathbf{B}$. The rate of increase of E_D is the same for all four cases, indicating the same amount of power is delivered for each case. The only difference is in the initial jump in E_D occurring at $t = 0.2$ ms. As S is raised (η is lowered), a greater amount of power is delivered to the $n = 0$ initially. This activity is associated with the large surge of power from the $n = 1$ that occurs during stage II. Next two figures, figures 4.15(a) and 4.15(b) show the bulk energy transfer to the MF separately by the MHD (E_D^{MHD}) and Hall (E_D^{Hall}) dynamos (defined in §5.1.3). E_D^{MHD} shows very little sensitivity to S (T_e). E_D^{Hall}, on the other hand, exhibits quite a variation as S is raised. The Hall dynamo has a significant impact on the MF initially during stage II and transfers nearly as much bulk energy into the MF as the MHD dynamo. However, the rate of change E_D^{Hall}, *i.e.*, the Hall dynamo power into the MF, is only positive for $S = 29$. Going from $S = 29$ to 32, the Hall dynamo stops contributing to the MF and eventually causes a power leakage out of the MF, acting like an anti-dynamo. It is as though the Hall dynamo term acts as a regulator that ensures the total power transfer to the MF happens at

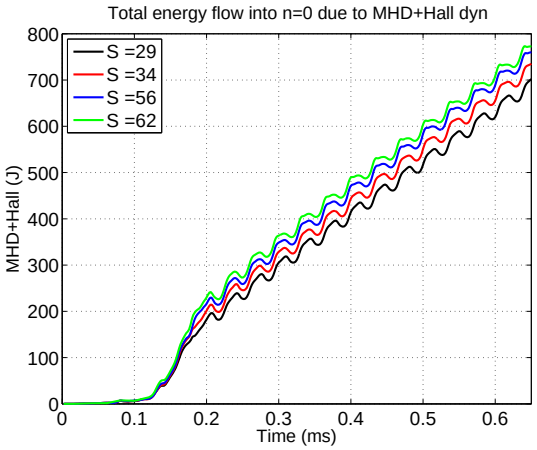

Figure 4.14: Total bulk energy transfer to the MF ($n = 0$) due both MHD and Hall dynamos as a function of time (ms). The contribution from each term is added together.

a constant rate for all cases with a different S.

The overall effect of the dynamo terms can be gauged by comparing the bulk energy transferred to the MF in 2MHD7.5 and 2MHD12 with that of rMHD calculations with the same $\eta(T_e)$: rMHD7.5 and rMHD12. The Hall term enhances the MHD dynamo term by generating perpendicular currents that can strongly influence the (center-of-mass) fluid motion. This is illustrated in figure 4.16(a), which shows that the $E_D^{\rm MHD}$ from 2MHD7.5 (black) and 2MHD12 (red) is $10-15\%$ greater than that from rMHD7.5 (dashed black) and rMHD12 (dashed red). The Hall term also enhances the total energy transfer to the MF, indicated by a $25-30\%$ increase in E_D in 2MHD7.5 (black) and 2MHD12 (red) than in their resistive counterparts (dashed black and red lines), as shown in figure 4.16(b). The difference in E_D is more pronounced for lower T_e (S) because the Hall dynamo impedes $n=0$ amplification at higher T_e. Note for both figures the traces from the rMHD simulations are shifted forward in time to align the start time of the energy transfer to the MF for all four cases.

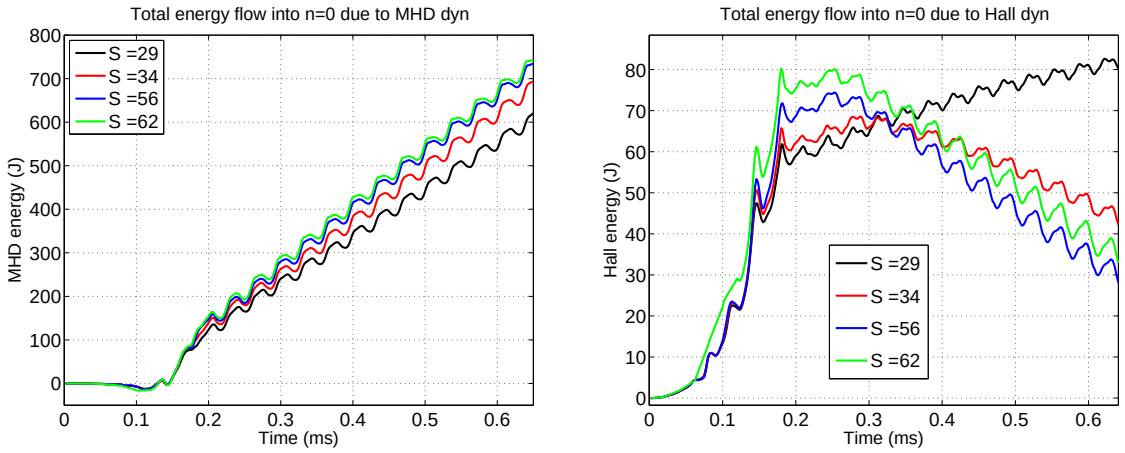

(a) MHD dynamo bulk energy transfer vs. time (ms)

(b) Hall dynamo bulk energy transfer vs. time (ms)

Figure 4.15: Bulk energy transfer due to (a) MHD (E_D^{MHD}) and (b) Hall (E_D^{Hall}) dynamos as a function of time (ms). E_D^{MHD} increases as S is raised while E_D^{Hall} shows increasingly more leakage of power out of the MF for higher S. After the initial surge of power into the MF during stage II, the Hall dynamo acts like anti-dynamo and works against $n = 0$ amplification except for $S = 29$.

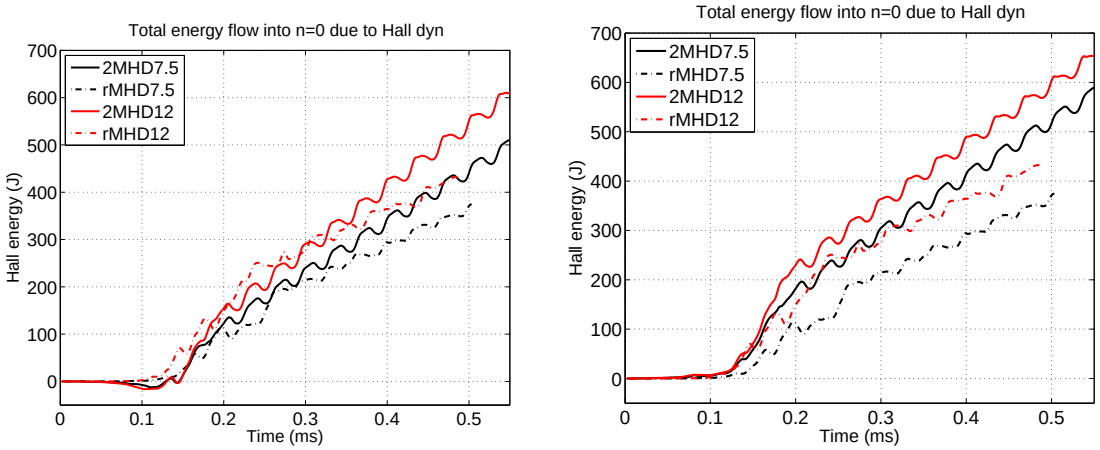

(a) MHD dynamo bulk energy transfer vs. time (ms)

(b) Total dynamo bulk energy transfer vs. time (ms)

Figure 4.16: Comparison of (a) E_D^{MHD} and (b) $E_D = E_D^{\mathrm{MHD}} + E_D^{\mathrm{Hall}}$ from two-fluid MHD with those of resistive MHD. The Hall term enhances the MHD dynamo-mediated energy transfer into the MF.

Chapter 5

VERIFICATION: LOW S RESISTIVE MHD (RMHD) SIMULATIONS

This chapter is dedicated to the verification of resistive MHD (rMHD) model of the HIT-SI experiment. Since rMHD does not quantitatively validate, the results do not describe HIT-SI. This chapter is included for comparison to other rMHD simulations. The first section is a presentation of results and analysis from a baseline simulation that serves as an overview because it exhibits features common to all the rMHD simulations that show current amplification. This is followed by a discussion on the convergence of the results with respect to toroidal and poloidal resolution. Single-injector simulations are included to complement analyses of the baseline results and provide cleaner illustrations of the relaxation dynamics. The robustness of the results against operational permutations are covered in this chapter as well, in §5.1. The experiment has a large parameter space and high number of operational permutations because of two independently oscillating injectors with two separate circuits (flux and voltage), the relative phases between each injector, and also the phase difference between the oscillating flux and voltage of each injector. Only a small subset of these permutations is presented as additional verifications of the baseline calculation. These simulations include a case with left-handed-helicity-injection and another case where the leading and lagging injectors are swapped, and finally a scan of the relative phase between the two injectors, Φ_{inj}. The general characteristics show little sensitivity to the handedness of helicity and lead-lag of the injectors. However, the oscillations in the plasma current and in other axisymmetric quantities increase as $|\Phi_{inj}|$ deviates from $\pi/2$ where Poynting flux and rate of helicity injected into the plasma are maximized.

Following the section on baseline results and convergence are parameter scan studies that investigate how current amplification I_{tor}/I_{inj} scales with η (S), λ_{inj}, and the injector oscillation frequency f_{inj} (§5.3). The findings indicate that I_{tor}/I_{inj} scales as $\eta^{-0.65}$ and S has to be significantly greater than that of the experiment—the background conductivity has to be much higher, *i.e.*, much hotter simulated plasmas—to yield high current amplification ($I_{tor}/I_{inj} \simeq 3$) measured in the experiment. Recall the validation rMHD simulations ran with $\lambda_{inj} = 20$ m^{-1} yield $I_{tor}/I_{inj} \propto \eta^{-0.4}$. The difference in the two rMHD current amplification scaling laws is attributed to λ_{inj} and corroborates the earlier claims that the injector impedance term Z_{inj} appearing in eqn. (1.16), representative of the dynamics, has an implicit dependence on λ_{inj} and possibly η. The λ_{inj}-scan uses an improper scaling of the injector flux and current, previously discussed in §2.3.2. It shows a cutoff in λ_{inj}, λ_c, below which no amplification of the $n = 0$ mode takes place. The frequency scan too exhibits a cutoff beyond which no relaxation, that is, $n = 0$ amplification takes place. This happens when $\omega_{inj}\tau_A \gtrsim 1$, *i.e.*, when injector period is shorter than the global Alfvén time.

5.1 Baseline Simulation

The baseline simulation uses 40×40 bicubic ($pd = 3$) FE's to discretize the poloidal plane and 11 Fourier modes for the toroidal direction, corresponding to 32 toroidal slices. Scans indicate the results of the baseline calculation to be sufficiently converged at a poloidal resolution as coarse as a mesh comprising 12×12 bicubic FE's. Toroidal convergence has been checked up to a resolution of 43 Fourier modes corresponding to a toroidal cell size $\Delta x_\phi = 1.6$ cm. The results exhibit more sensitivity to toroidal resolution in the form of an increasingly delayed current amplification time (or formation time) as the mode number increases. However, the characteristic features such as the magnitude of the $n = 0$ component and amplitude of I_{tor} remain mostly unaltered. Details on the convergence of results with respect to spatial resolution are provided in §5.1.5.

Table 5.1 is a summary of the salient parameters for both the simulation and the experiment. For the baseline case $S = 20$, low enough that the computation is inexpensive but high enough for current amplification ($I_{tor}/I_{inj} > 1$) and $n = 0$ growth. The injector flux ψ_{inj}=0.47 mWb, the injector current I_{inj}=11 kA, and $\lambda_{inj} = 30$ m^{-1}. The magnetic and viscous diffusivities are $\frac{\eta}{\mu_0} = 11.7$ m^2/s, equivalent to $T_e = 10$ eV, and ν=100 m^2/s. The chosen values of η and ν correspond to a resistivity of 1.5×10^{-5} Ωm and viscosity of 10^{-5} kg/m/s, respectively, which together yield a magnetic Prandtl number, $Pm = \frac{\nu}{\eta} = 9$. $f_{inj} = 5$ kHz equivalent to an injector period $\tau_{inj} = 0.2$ ms. After an initial ramp-up of 0.1 ms, the injectors are run at constant amplitude (flat-top) for a minimum of 6 cycles (1.2 ms).

Table 5.1: Key parameters of the baseline rMHD simulation and their comparison with experimental parameters. A broader range of HIT-SI parameters are presented in this table.

	Simulation	**Experiment**
Injector flux (mWb)	0.47	0.6–1.4
Injector current (kA)	11	10–20
λ_{inj} (m^{-1})	30	15–25
$\langle n_e \rangle$ (m^{-3})	$3{\times}10^{19}$	$1{-}4{\times}10^{19}$
f_{inj} (kHz)	5	5.8–70
$\tau_{L/R}$ (ms)	.81	0.40 ($\eta_\parallel$)
τ_A (μs)	40	12–30
S	20	$\sim 10 - 100$

5.1.1 Characteristics

The evolution of the magnetic energy (ME) spectrum is inspected first. The energy traces displayed in figure 5.1 indicate that most of the energy is stored in the magnetic

field and the kinetic energy only makes up a few percent of the total energy. Time traces of the linear and logarithmic ME per toroidal mode (n) shown in figures 5.1(a) and 5.1(c) indicate that the spectrum is initially dominated by n = odd modes due to the direct coupling of the dynamics to the source terms (through the boundary), which have n = odd toroidal symmetry. The $n = 1$ mode contains the bulk of the ME during this period. Consequently, the kinetic energy is mostly in the even modes initially, especially in $n = 0$, and 2 modes due to the self-coupling of the injected fields via the Lorentz force, $\mathbf{J} \times \mathbf{B}$. An outcome of this self-coupling is the cyclic spikes exhibited by $n = 0$ and $n = 2$ KE corresponding to periodic bursts in the plasma flow in synchrony with the extrema of the injector oscillations during the first half of the simulation (figure 5.1(b)). The plasma flow is zero right at the boundary due to zero-flow BC, but there is significant acceleration of the plasma outside the resistive layer all the way to the mid-plane region ($z = 0$). The flow is always directed toward the magnetic axis, *i.e.*, into the region of lower magnetic pressure and away from the injector mouths, the region of high pressure, regardless of the direction of injector flux and current. This is consistent with the measurements of ion flows by the IDS instrument from HIT-SI. Figure 5.2 shows vectors of plasma flow at the toroidal locations that bisect the X injector mouths during a maximum of the X-injector cycle. Note the flow pattern in the figure is symmetric with respect to the centerline ($R = 0$).

The trends of the verification rMHD simulations are mostly identical to those of the rMHD validation simulations presented in Chapter 3. Thus, most of the following discussion will be identical to that of §3.2. Relaxation event described previously occurs unimpeded in this case because $\lambda_{inj} = 30$ m^{-1}, well above the critical λ. Recall $\lambda_c \lesssim 20$ m^{-1} based on results of validation simulations and λ_{inj}-scan presented further below. The ME spectrum features a period early growth where the injectors couple to the $n = 1$ eigenmode and amplify it, resulting in a magnetic spectrum initially dominated by the $n = 1$ and a large energy difference between odd and even-symmetry

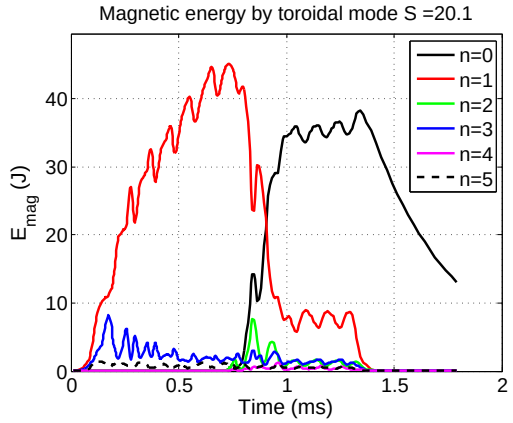

(a) Magnetic energy per mode for $n = 0 - 5$

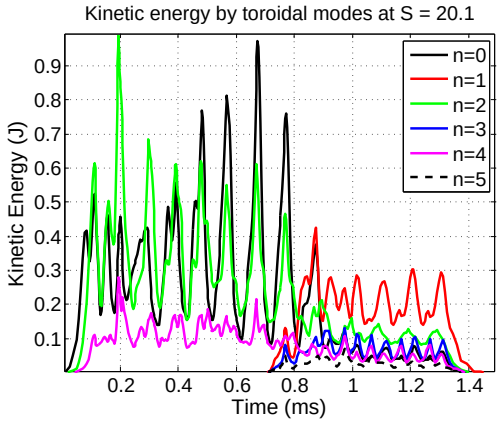

(b) Kinetic energy per mode for $n = 0 - 5$

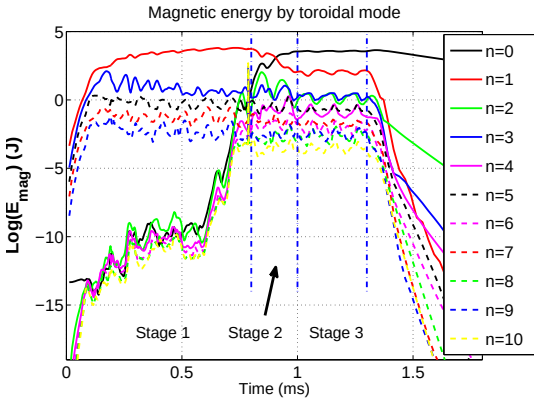

(c) Log magnetic energy per mode for all n

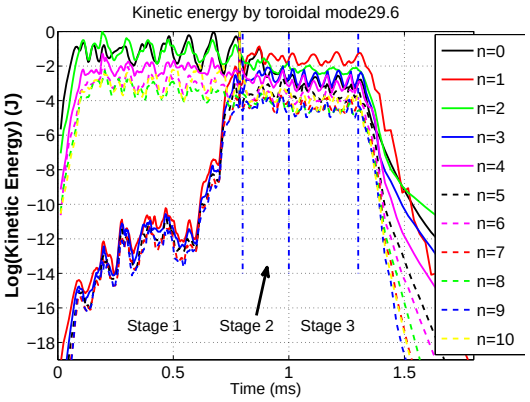

(d) Log kinetic energy per mode for all n

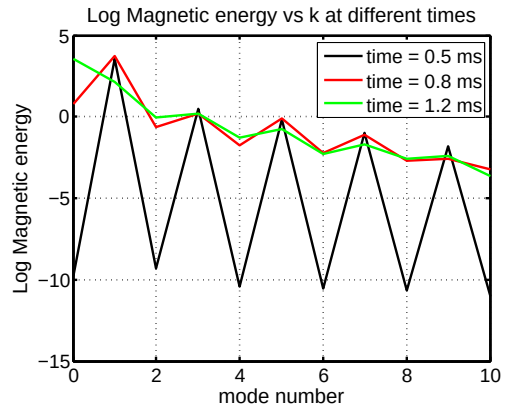

(e) Log ME vs. n from three separate times

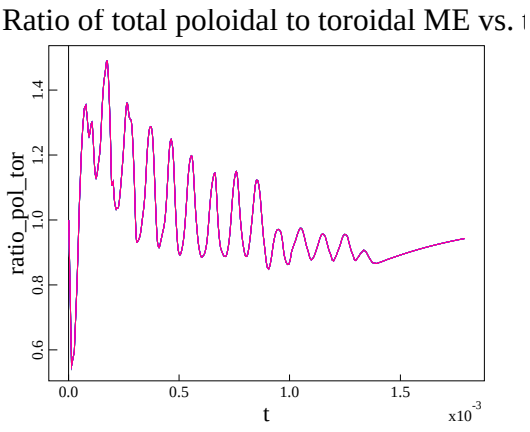

(f) Ratio of toroidal to poloidal ME vs. time(ms)

Figure 5.1: (a) and (b) are plots of magnetic and kinetic energy per n vs. time(ms). (c) and (d) the natural logarithm of ME and KE per n vs. time. The blue dashed lines correspond to three instants in time representative of the three characteristic stages of mode evolution described above. Linear growth of the unstable modes onsets around $t = 0.6$ ms. (e) is a plot of log ME vs. mode number n at the three separate times marked by the blue dashed lines. Finally, (f) is the ratio of the total poloidal to toroidal ME vs. time indicating $n = 0$ amplification converts B_θ to B_ϕ.

modes. The $n = 1$-dominated period is followed by a relaxation event featuring the linear growth and nonlinear saturation of the even-symmetry modes culminating in an axisymmetric ($n = 0$) minimum energy state containing the magnetic helicity. To facilitate the analysis the mode evolution is divided up into three distinct stages, each separated by a dashed vertical line, as was done in Chapter 3 (figure 5.1(c)).

Stage I corresponds to the pre-relaxation phase. It features a rapid linear growth across the entire toroidal spectrum during the first 0.1 ms ($2.5\tau_A$) while the injectors ramp up. The magnetic energy is entirely in the odd-symmetry modes at this time due to the odd-symmetry of the injector fields. As a result, all of the injected helicity builds the $n = 1$ first, which dominates the magnetic spectrum during stage I. The $n = 1$ ME reaches steady-state in approximately 1.0 ms (twice the energy e-folding time), when the helicity injection and dissipation rates match. As the $n = 0$ seeds all the even-symmetry modes due to the coupling of $\mathbf{v}$ and $\mathbf{B}$ in rMHD, $n \geq 2$ even-numbered modes only get as large as the initial $n = 0$, which shows very little activity during the first half of stage I. The resulting ME and KE spectra display a large energy difference between odd and even-symmetry modes. The even-symmetry modes begin to grow at the MHD growth rates ($\gamma\tau_A \simeq 2$ with $\gamma = 50$ kHz) at $t = 0.6$ ms ($15\tau_A$). The duration of this dormant period is nearly the same as in the rMHD validation simulations in terms of normalized time (t/τ_A). It is not clear why the non-driven modes do not grow right away and instead, remain idle for nearly an energy e-folding time. This behavior suggests that the MHD growth requires a certain threshold in ME (equivalently in S), which increases as the ME and helicity build up. The growth of the even-numbered modes is triggered when $S \gtrsim 7$, based on the results of the validation and verification simulations. As the total ME builds up, energy begins to gradually transfer from the poloidal B_θ to the toroidal field B_ϕ, as indicated by a gradual decline in the ratio of poloidal to toroidal ME, $\frac{U_\theta}{U_\phi}$ vs. time shown in figure 5.1(f). Here $U_\theta = \int dV \frac{B_\theta^2}{2\mu_0}$ and $U_\phi = \int dV \frac{B_\phi^2}{2\mu_0}$. Stage I ends at $t = 0.8$ ms ($20\tau_A$) as the $n = 0$ starts taking energy from the $n = 1$.

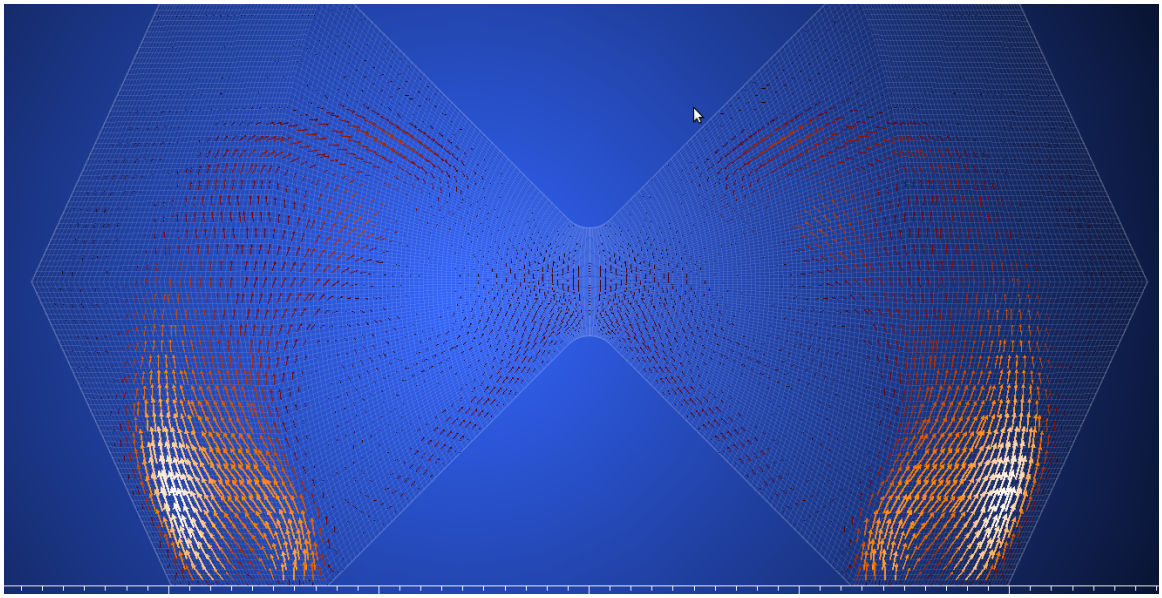

Figure 5.2: Arrows of plasma flow out of the injectors during an injector maximum. The plot is in the $R-Z$ plane that bisects the X (lower) injector mouths. The flow pattern is symmetric and always points inward whether flux enters or exits the domain. The flow attains speeds as large as 25 km/s. Compare this with figure 4.2 of Chapter 3.

In stage II the $n = 0$ ME has grown large enough that the injectors can no longer supply the MHD growth power necessary to sustain it and its growth slows to a Sweet-Parker-like rate (0.19 ms) as it takes ME from the $n = 1$ through magnetic reconnection. In the meantime, the growth of $n \geq 2$ even-symmetry modes saturates. As the magnetic helicity flows from the $n = 1$ to $n = 0$ the excess energy is dissipated via a normal cascade, successively exciting $n \geq 2$ modes and leaving the $n = 0$ with all of the magnetic helicity and minimum energy. The energy cascade is signaled by bumps appearing in the $n = 2$ ME (green) trace at the beginning of stage II and later in the $n = 3$ and $n = 4$ (blue and purple) ME traces near the end of stage II shown in figure 5.1(c). During this time ME surges from the poloidal field B_θ into the toroidal field B_ϕ as evidenced by an abrupt drop in $\frac{U_\theta}{U_\phi}$ taking place at $t \approx 0.9$ ms ($22.5\tau_A$). Significant toroidally-averaged plasma current I_{tor} ($I_{tor}/I_{inj} > 1$) is generated as a

consequence of the $n = 0$ amplification. The formation time $\tau_f = 0.9$ ms ($22.5\tau_A$), as indicated by where the red horizontal line representing the amplitude of I_{inj} intersects the I_{tor} (black) trace in figure 5.4(a). Stage II ends at $t = 1.0$ ms ($25\tau_A$).

Stage III corresponds to the post-relaxation phase featuring steady-state sustainment of the $n = 0$ and I_{tor} against resistive decay by SIHI fluctuations. The $n = 0$ ME no longer grows in stage III because the total magnetic helicity and energy have already attained steady-state in stage I. The remaining ME in the $n = 1$ corresponds to the energy of the pure injector state, which is proportional to $I_{inj}\psi_{inj}$. The injector fluctuations are too high at these low I_{tor}/I_{inj} for there to be any closed flux in the confinement volume. The mid-plane ($z = 0$) magnetic field profiles plotted at four different toroidal locations (figure 5.3(a)) during stage III show a clear toroidal non-uniformity and a significant deviation from Taylor-state profiles (solid lines) consistent with the non-axisymmetric mode activity associated with the injector fluctuations. The energy spectra monotonically decrease with toroidal wavelength as illustrated by figure 5.1(e), which shows ME as a function of toroidal mode number n from three different instants in the simulation corresponding to the three separate stages (log KE vs. n is omitted). During this stage, $\frac{U_\theta}{U_\phi}$ remains constant, slightly below 1.

Once the injectors are shut off at $t = 1.4$ ms, the non-axisymmetric mode activity quickly ceases, as the remaining structure resistively decays with a dissipation time of $\tau_{L/R} = 0.8$ ms. The measured $\tau_{L/R}$ is in excellent agreement with the theoretical resistive diffusion time for a fully relaxed spheromak (Taylor state) in the modeled geometry: $\tau_{L/R}^{(th)} = 0.81$ ms. An additional bump occurs in I_{tor} at $t = 1.4$ ms associated with the reconnection of the previously-open injector currents with the I_{tor}. The internal magnetic structure becomes Taylor-like as indicated by the midplane magnetic profiles shown in figure 5.3(b). $\frac{U_\theta}{U_\phi}$ approaches unity during the decay phase. This is the expected energy equipartition for an isolated spheromak in a Taylor state[37].

I_{tor} grows proportionally to $n = 0$ and reaches a steady-state value of 13 kA yielding $I_{tor}/I_{inj} = 1.2$ (figure 5.4(a)). As previously explained in §3.2, the amplitude

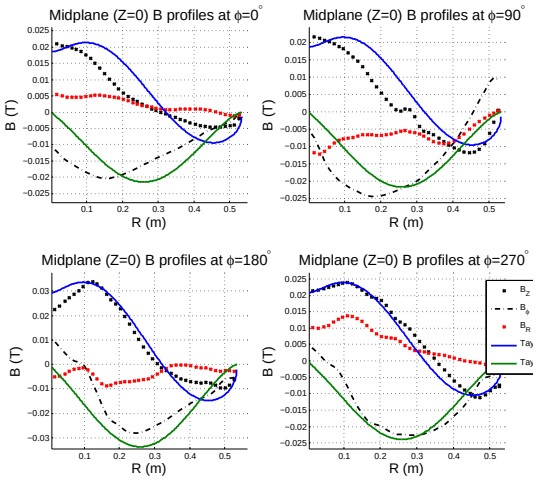

(a) Mid-plane **B** profiles during stage III

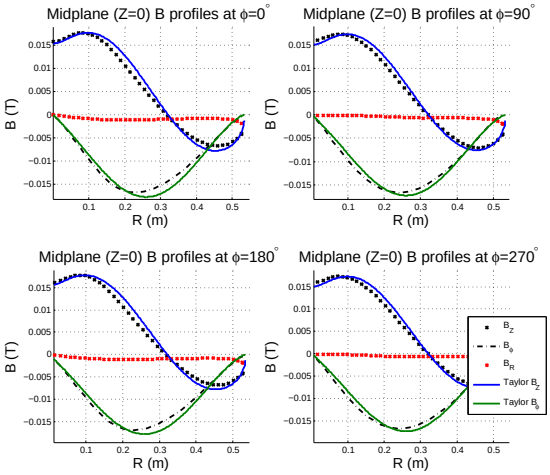

(b) Mid-plane **B** profiles during decay

Figure 5.3: Midplane magnetic field profiles at four different toroidal locations, $\phi = 0$, 90, 180 and 270 degrees. (a) shows a comparison of the profiles from the simulation with the Taylor profiles (solid blue and green curves) during sustainment when I_{tor} is at its maximum. (b) is comparison of the profiles from the decay phase of the simulation, which is in much closer agreement with Taylor profiles.

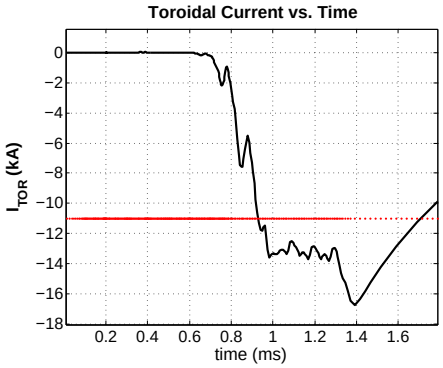

(a) I_{tor} vs. time(ms)

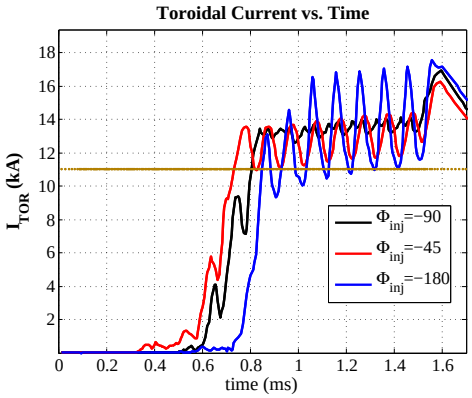

(b) I_{tor} vs. time(ms) for different Φ_{inj}

Figure 5.4: (a) I_{tor} as a function of time (ms). After the saturation I_{tor} steadies out at an average of 13 kA, which yields $I_{tor}/I_{inj} = 1.2$. Once the injectors are turned off, the current previously connected to the injector openings detaches and connects with the $n = 0$ plasma current. This causes a further increase in I_{tor}, as evidenced by the jump in the I_{tor} trace occurring at 1.4 ms. (b) I_{tor} as a function of time (ms) for various relative injector phases, Φ_{inj}. The oscillations grow larger as Φ_{inj} is walked further from $\pm\pi/2$.

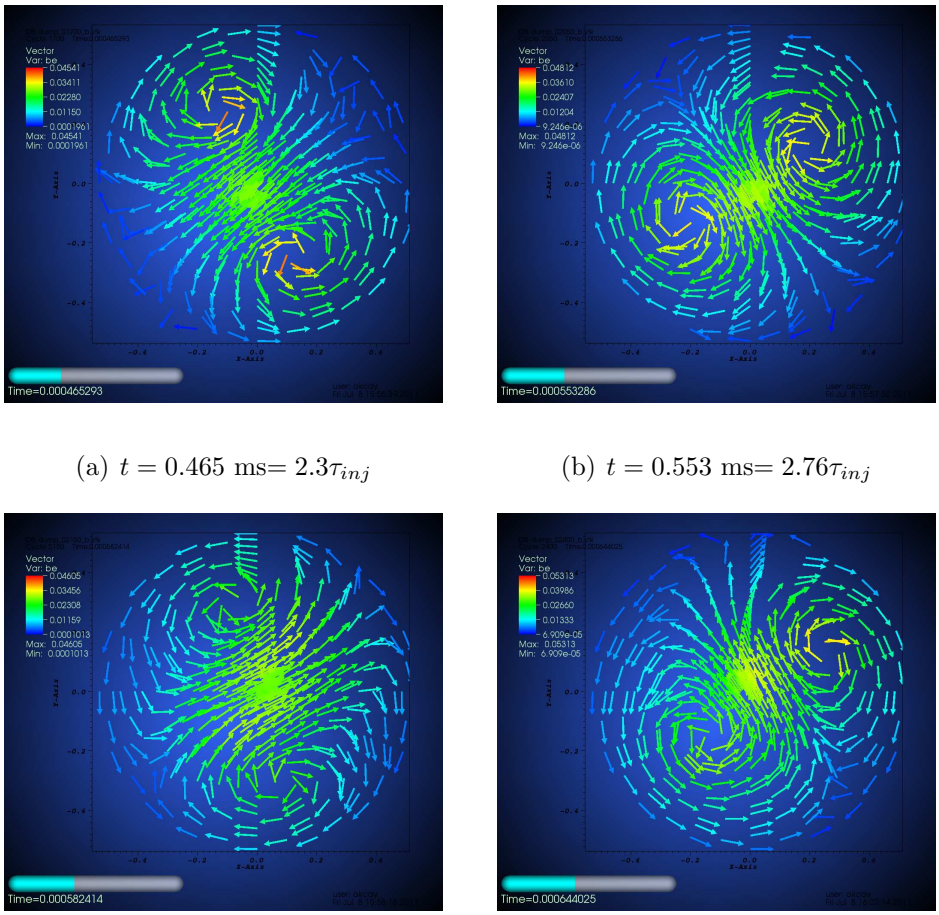

(a) $t = 0.465$ ms$= 2.3\tau_{inj}$

(b) $t = 0.553$ ms$= 2.76\tau_{inj}$

(c) $t = 0.582$ ms$= 2.91\tau_{inj}$

(d) $t = 0.644$ ms$= 3.2\tau_{inj}$

Figure 5.5: Arrow plots of $\mathbf{B}$ projected onto the mid-plane ($z = 0$) showing a counter-clockwise rotation of $\mathbf{B}$. This is an end-on view of the geometry. The times correspond nearly to the extrema of the Y injector and zero crossing of the X injector oscillations which occur at t$= 0.1m + 0.05$ ms where m is an integer. The curling of the magnetic field is where the injector channel punctures the mid-plane, twice, to close the current path from one mouth to the other. Red vectors correspond to approximately 50 mT and blue vectors to 1 mT.

of the oscillations in I_{tor} depends on the phase difference (Φ_{inj}) between the helicity injectors and grows as Φ_{inj} is walked further from $\pm\pi/2$ as shown by figure 5.4(b). A phase difference of $\pm\pi/2$ between the injectors causes the global magnetic field to rotate at the injector frequency consistent with the design of the experiment. Figure 5.5 shows snapshots of the mid-plane magnetic field, projected onto 2-D as the simulation progresses from $t = 0.47$ to 0.64 ms. The magnitude of the field spans approximately a range from 1 mT (blue vectors) to 50 mT (red arrows) for each snapshot, The field is strongly $n = 1$ during this interval, consistent with the ME spectrum, and rotates with an angular frequency $\omega_{inj} \equiv 2\pi f_{inj}$ in the counter-clockwise direction. As previously discussed, the direction of rotation is determined by which injector leads and which one lags, in other words the sign of Φ_{inj}. Reversing the sign of Φ_{inj} amounts to swapping the leading and lagging injectors resulting in a reversal of I_{tor} and toroidal rotation of magnetic field. For the simulations presented in this section $\Phi_{inj} = -\pi/2$, equivalent to the upper injector (Y) leading the lower injector (X).

The local plasma current I_p exhibits toroidal non-uniformities similar to the ones shown in figure 3.5. This is shown in figure 5.6, which plots traces of $I_p(\phi)$ from five different times separated exactly by $\tau_{inj}/4(= 50\ \mu\text{s})$. There is a clear migratory pattern in the counter-clockwise toroidal direction indicated by the black arrow, consistent with the direction of rotation indicated by the snapshots of $\mathbf{B}$ from figure 5.5. The rotational period is τ_{inj}, as evidenced by the two (nearly) overlaying traces (solid black line and purple crosses) separated in time exactly by τ_{inj}. The background current (~ 9 kA) is the current that is generated as a result of $n = 0$ amplification, and can be regarded as the 'separatrix' current if a separatrix were actually present.

Further verification cases include quantifying the dependence on:

- the injector power P_{inj}: the $n = 0$ amplification takes place regardless of the level of the injector power P_{inj} so long as λ_{inj} is above the critical λ and there is

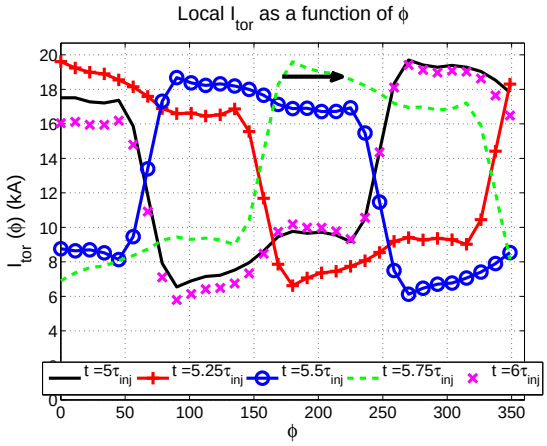

Figure 5.6: I_{tor} as a function of the toroidal angle ϕ at five different times during stage III. $I_{tor}(\phi)$ resembles a step function in ϕ. The region of concentrated toroidal current ($\sim$20 kA) corresponds to the where the injector currents and I_{tor} add up.

enough P_{inj} to exceed the threshold in S to trigger linear growth. A lower P_{inj} results in slower (absolute) growth rates and a delayed onset of the instability (even-numbered mode growth) as measured in absolute time (in ms). This result is consistent with the slowing down of τ_A with lower P_{inj} in accordance with eqn. (2.8), which states $v_A \propto \sqrt{U/\rho}$. Since the total ME (denoted U in eqn. (2.8)) is linearly proportional to P_{inj}, the above relation can be recast in terms of ρ and P_{inj}

$$\tau_A \sim \sqrt{\rho/P_{inj}}. \tag{5.1}$$

Since growth rates are Alfvénic, this equation states that linear growth rates slow down as P_{inj} is lowered consistent with simulation results.

- ρ/P_{inj}: lowering the plasma mass density ρ linearly with P_{inj} results in little to no change in the times of occurrence of significant phases and linear growth rates in terms of absolute time because τ_A remains unchanged, as can be seen from eqn.(5.1).

- the amplitude of the initial perturbation: as mentioned in §2.3.5 a lower-amplitude initial perturbation delays the time at which the $n = 0$ becomes global and results in a longer τ_f, *i.e.*, when $I_{tor}/I_{inj} > 1$. This is because there is a larger energy difference that the $n = 0$ mode has to cover to become global. The growth rates are unaffected since they depend on $U(P_{inj})$ and ρ via τ_A.

5.1.2 VisIt Visualization Analysis

The 3-D visualization analysis features the magnitude of current density J and $\lambda \equiv \frac{\mu_0 j_\parallel}{B}$ because they yield the most informative three-dimensional pictures in the absence of closed flux surfaces and plasma pressure. The midplane **B** vector plots of figure 5.5 show a clear curling of the magnetic field caused by the injector current column crossing the midplane. The two oppositely directed curls correspond to the current entering and exiting the mid-plane. Figure 5.7(a) is a planar view of λ in the poloidal planes bisecting the lower injector mouths at $t = 0.6$ ms. $|\lambda| > 40$ m^{-1} are excluded from the figure. The orange color correspond to $\lambda = 30$ m$^{-1} = \lambda_{inj}$ and bluish colors represent low or negative λ's, corresponding to image currents of the injectors similar to the ones observed in 2fl-MHD (see §4.2). The mid-plane view of figure 5.5 corresponds to a straight line splitting the domain symmetrically at the midplane in figure 5.7(a). During stage I when the $n = 1$ is dominant, the λ profile is mirror-symmetric with respect to the geometric axis as shown in figure 5.7(a). The three-dimensional rendering of J in figure 5.7(b) shows the injector current channels (columns) emanating from the X injector openings connecting across the cones in a manner consistent with the mirror-symmetry of λ shown in the planar view. To clarify the picture, J in regions where $B < 0.015$ T is excluded to remove the boundary layers where the current piles up and only two J isosurfaces with 4 and 6% of the maximum J ($J_{max} = 6.136 \times 10^6$ A/m^2) are plotted. The figure shows the columns lie mostly in the poloidal plane with a negligible toroidal component. They undergo a repeating cycle of formation and dissolution in synchrony with the injector oscilla-

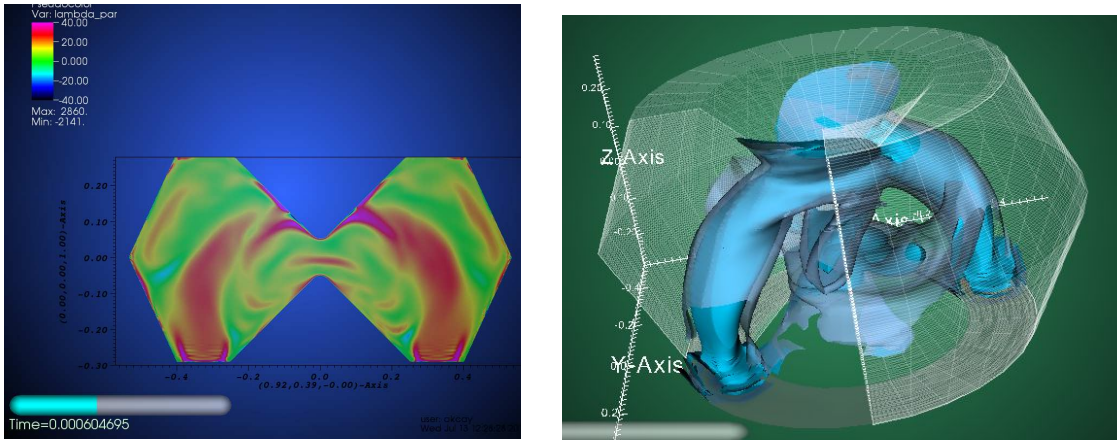

(a) λ at $t = 0.6$ ms

(b) J at $t = 0.6$ ms

Figure 5.7: (a) Pseudo-color plot of λ in the poloidal plane bisecting the lower injector mouths prior to mode saturation. The λ-profile is mirror-symmetric while the $n = 1$ dominates the magnetic spectrum. The $\lambda \simeq 30$ m^{-1} region is represented by the orange color. (b) Magnitude of current density (J) shows the injector current column in the simulation volume. The exact time of the chosen frame is $t = 0.6015$ ms, nearly coincident with a maximum of the X injector and the zero crossing of the Y injector.

tions. Both figures 5.7(a) and 5.7(b) look very similar to their two-fluid counterparts shown in figures 4.6(a) and 4.6(c).

Another $n = 1$-symmetric magnetic configuration encountered in stage I occurs when the injectors output nearly the same amount of current and flux. This happens four times during each injector cycle, an eighth of a period (0.025 ms) before or after every half period (0.1 ms), *e.g.*, at $t = 0.625, 0.675, 0.725, \cdots$ ms. Figure 5.8 illustrates 3-D J for one such case, at $t = 0.625$ ms. Again only two J isosurfaces, one at 4 and the other 6% of the $J_{max} = 10^7$ A.m^{-2}, are plotted. In this example, the X injector is ramping down from its maximum at t =0.6 ms while the Y injector is ramping up to its maximum at $t = 0.65$ ms. As X ramps down, X injector column connects across the domain to Y injector footprints, joining the X and Y sides together. This union results in two separate axially-directed ($\hat{z}$) opposite current channels. Note the same

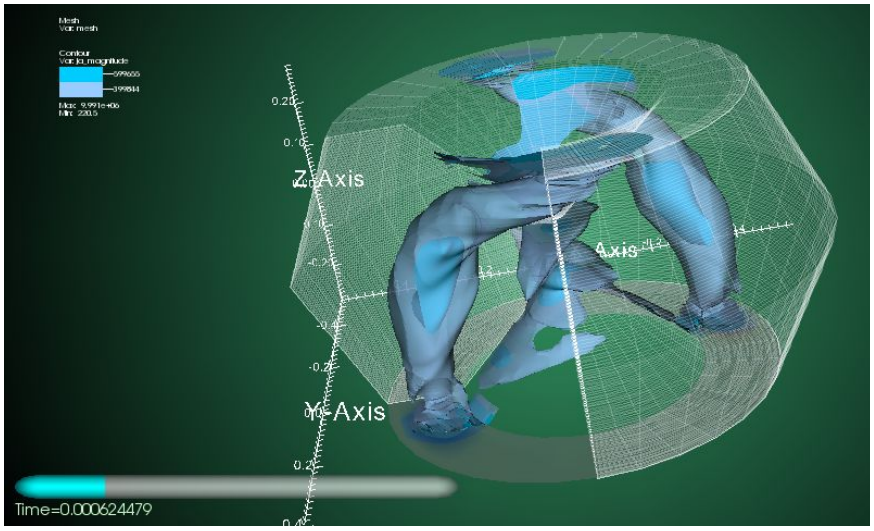

Figure 5.8: J at $t \approx 0.625$ ms when both injectors have nearly the same current and flux. The X-injector column breaks up and joins with the columns of the opposing (Y) injector across the domain creating two oppositely-directed axial current channels. As the X injector nears its zero crossing, the two current columns connected across the volume detach from the X-injector mouths and once again rejoin across the cones similar to what is seen in figure 5.7(b).

axial injector current channels appear in 2fl-MHD as well when the $n = 1$ is prevalent (see figure 4.8(b)). The configuration breaks up as the X injector approaches its zero crossing and the Y injector its extremum. The injector columns detach from the X side and the configuration reassumes the shape displayed in figure 5.7(a), except it is now inverted and 90° rotated. This cycle repeats itself during stage I with the configuration going back-and-forth between the half-hoop of current emanating from either side (X or Y) and two separate current channels electrically connecting the two sides. The $n = 0$ is still too small to have a noticeable effect at this time.

Once the $n = 0$ grows to global levels, the injector channels lose their mirror symmetry, bend into the toroidal direction, toroidally encircling the inner cones to align themselves with the spheromak fields that generate the I_{tor}. The resulting configuration, shown in figures 5.9(a) and 5.9(b) is once again very similar to that

encountered in the two-fluid simulations, shown in figures 4.6(b) and 4.6(d). The regions of high local plasma current I_p (see figure 5.6) correspond to regions where the injector current adds to I_{tor}. Depending on which way I_{inj} is coming out of the injector mouths, one extremity of the injector column will lean into the inner cone and the other away from it to properly align the injector fields with spheromak poloidal field as indicated by figure 5.9(a), which closely resembles figure 4.6(b). The injector current paths appearing during stage III are as described in the papers by Victor *et al.*[32] and Jarboe *et al.*[31]. §5.2 on single injector simulations contains a detailed visual account of the dynamics during the steady-state period (stage III) for a Y-injector-only simulation. The absence of Φ_{inj}-induced rotation and of the cross-coupling between the two injectors greatly clears the physical picture and helps single out the injector dynamics. Figures 5.7(b), 5.8 and 5.9(b) along with numerous figures included in §5.2 illustrate how crucial three-dimensional visualization has been in capturing some of the prominent features in the present calculations.

5.1.3 Mean-field (MF) and Nonlinear Dynamos

The motion of a conducting fluid (plasma) through a magnetic field creates an electromotive force or a dynamo that can drive electrical currents. According to Cowling's dynamo theorem[68] an axisymmetric configuration can only be sustained by a dynamo driven by non-axisymmetric fluctuations. These are all the toroidal Fourier modes with $n > 0$. The dynamo action of the fluctuations builds and sustains the spheromak mean-field ($n = 0$) and current against resistive decay. It is expressed as a convolution of the Fourier coefficients of $\mathbf{v}$ and $\mathbf{B}$: $\mathbf{E}_f^{(n)} \equiv -\mathbf{v}^{(n)} \times \mathbf{B}^{(n)*} +$ c.c. where $\langle \ldots \rangle$ indicates a toroidal average and c.c. is for the complex conjugate. $\langle \mathbf{J} \rangle$ is the toroidally-symmetric current density and thus represents the mean-field (MF). The product of the complex-valued Fourier coefficients $\mathbf{v}^{(n)}$ and $\mathbf{B}^{(n)*}$ results in an axisymmetric $\mathbf{E}_f^{(n)}$. For the generalized Ohm's law $\mathbf{E}_f = -\mathbf{v}^{(n)} \times \mathbf{B}^{(n)*} + \mathbf{J}^{(n)} \times \mathbf{B}^{(n)*}/ne +$ c.c., assuming a toroidally symmetric plasma density, n. The total contribution from all

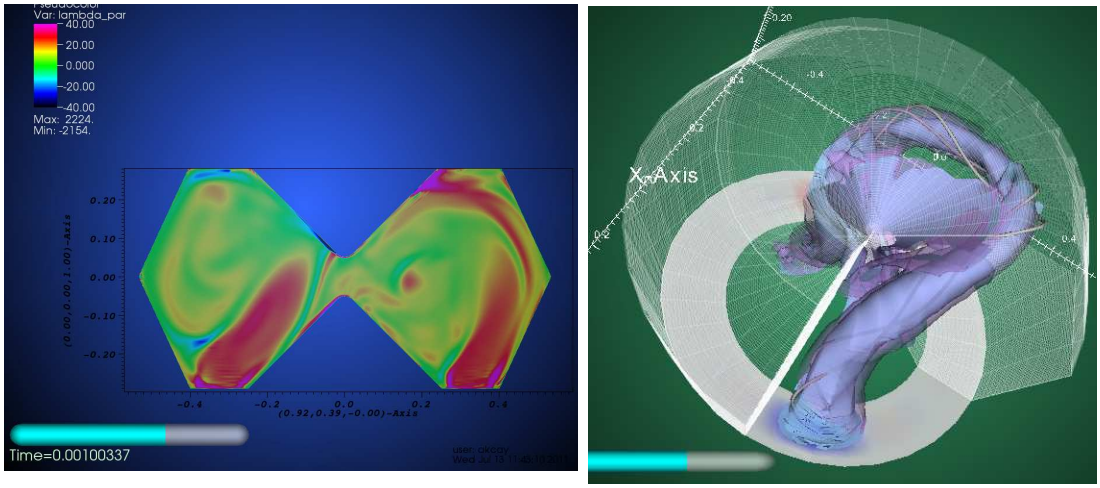

(a) λ at $t = 1.0$ ms (b) J after saturation $t = 1.07$ ms

Figure 5.9: (a) J at $t = 1.0$ ms showing the structure of the saturated state. The injector current column leans to one side, wrapping toroidally half-way around the volume. (b) shows the pseudo-color plot of λ in the poloidal plane bisecting the X-injector mouth around the same time ($t = 1.0$ ms). The broken symmetry of the λ distribution is consistent with the 3-D J plot. The chosen time corresponds to one of the extrema of the X injector and the zero crossing of the Y injector

fluctuations is $\mathbf{E}_f = \sum_{n>0} \mathbf{E}_f^{(n)}$. The relationship $-\mathbf{E}_f \cdot \langle \mathbf{J} \rangle$ provides spatial information about where SIHI power (density) is deposited for sustaining the MF. $-\mathbf{E}_f \cdot \langle \mathbf{J} \rangle > 0$ corresponds regions of current drive (sustainment) while $-\mathbf{E}_f \cdot \langle \mathbf{J} \rangle < 0$ to regions of anti-current drive. Because of injector oscillations the power density continually fluctuates throughout the volume. Averaging over two injector cycles shows where positive and a negative power (density) transfer from the fluctuations ($n > 0$) to MF ($n = 0$) occurs. Overall the greatest contributions come from the $n = 1$ and $n = 2$ modes. Figure 5.10 displays time-averaged (over two periods) contour plots and midplane radial profiles of $-\mathbf{E}_f^{(n=1,2)} \cdot \langle \mathbf{J} \rangle$ from stage III. The $n = 1$ contribution is strongly concentrated on the inboard side as indicated by positive $-\mathbf{E}_f^{(n=1)} \cdot \langle \mathbf{J} \rangle$ regions (red contours) in figure 5.10(a). These regions correspond exactly to the physical location of the injector channels. The $n = 2$ contribution has a peaked profile that is distributed into the interior regions, near the vicinity of the magnetic axis (figure 5.10(b)). There is still too much spatial variation in the dynamo-generated power density even after cycle-averaging to determine which fluctuation dynamo terms make a positive and which ones make a negative contribution to the $n = 0$ component.

The volume integral of $-\mathbf{E}_f \cdot \langle \mathbf{J} \rangle$ removes the spatio-temporal variations due to injector oscillations, enabling one to quantify the role of each mode in the dynamo process more lucidly in terms of a bulk power and energy transfer. A similar power transfer analysis was presented in papers by Ho and Craddock[69], and Sovinec *et al.*[70].

For static, uniform mass density, magnetic energy per toroidal mode evolves as

$$\frac{\partial}{\partial t} \int \frac{|B_n|^2}{2\mu_0} dV + \underbrace{\int \frac{1}{\mu_0} d\mathbf{S} \cdot \mathbf{E} \times \mathbf{B}}_{\text{source terms}} = \underbrace{- \int (\mathbf{J}_n^* \cdot \mathbf{E}_n) dV + \text{c.c.},}_{\text{power transfer}} \tag{5.2}$$

where the right-hand-side (rhs) term labeled power transfer contains the dynamo and dissipative terms. The surface integral is the inflow of electromagnetic (Poynting) power due to SIHI and is strictly a source term. It is not Fourier decomposed as

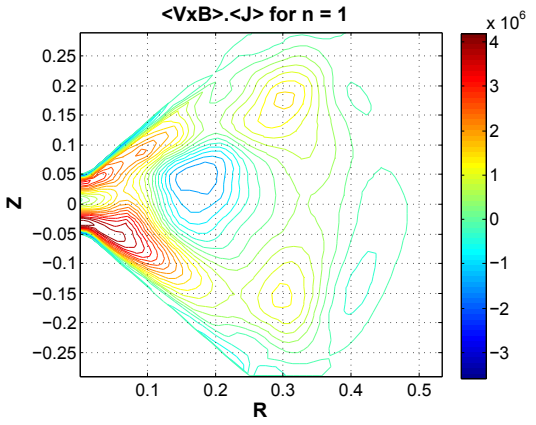

(a) $-\mathbf{E}_f^{(n=1)} \cdot \langle \mathbf{J} \rangle$ contours cycle-averaged over t=0.8–1.2 ms

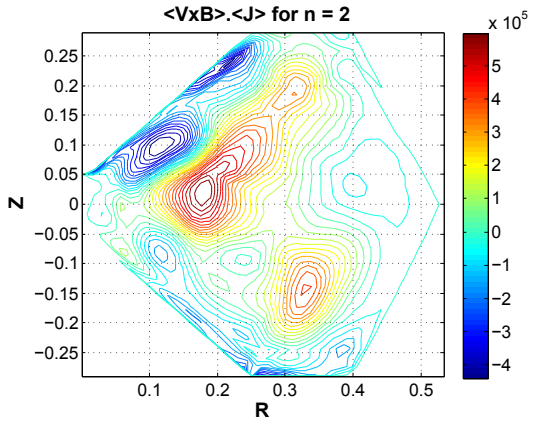

(b) $-\mathbf{E}_f^{(n=2)} \cdot \langle \mathbf{J} \rangle$ contours cycle-averaged over t=0.8–1.2 ms

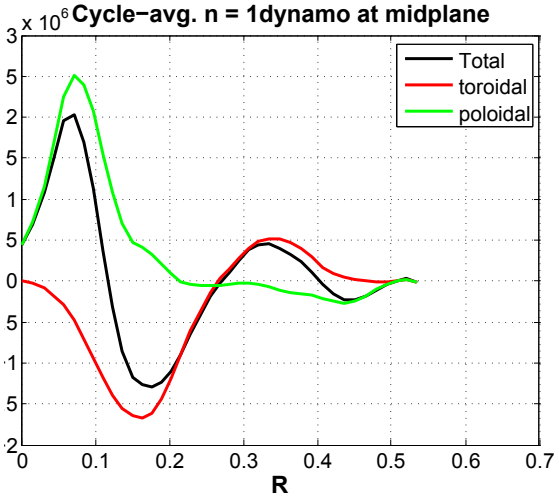

(c) $-\mathbf{E}_f^{(n=1)} \cdot \langle \mathbf{J} \rangle$ midplane profiles cycle-averaged over t=0.8–1.2 ms

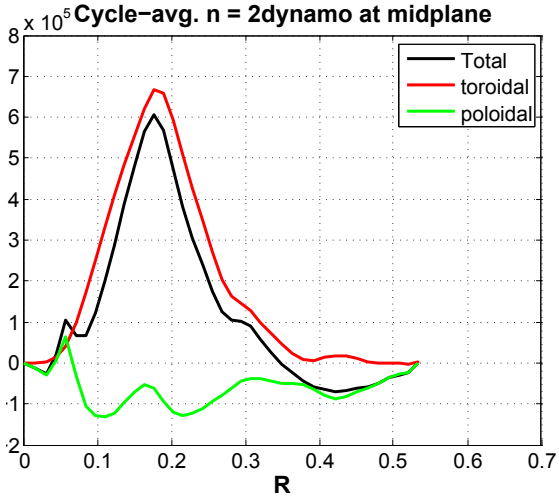

(d) $-\mathbf{E}_f^{(n=2)} \cdot \langle \mathbf{J} \rangle$ midplane profiles cycle-averaged over t=0.8–1.2 ms

Figure 5.10: Poloidal distribution of the cycle-averaged power transfer to the MF by (a) $n = 1$ and (b) $n = 2$ MHD fluctuation dynamos and their profiles at the mid-plane (c) and (d). The cycle-averaging is over two injector periods from $t = 0.8$ to 1.2 ms. Red contours represent regions of current drive and blue regions of anti-current drive.

it plays no role in the dynamo process under study here. The terms on the rhs are strictly dissipative but can have a net positive contribution to a particular component of the magnetic energy as will be shown below.

The power transfer term on the rhs of eqn. (5.2) is split into three parts:

$$\frac{\partial}{\partial t}\int |B_n|^2/\mu_0 dV + \int \frac{1}{\mu_0} d\mathbf{S}\cdot\mathbf{E}\times\mathbf{B} = \underbrace{\Omega_{MF}}_{n=0 \text{ only}} + \Omega_{nl}^{(n>0)} + \Omega_D^{(n)}, \tag{5.3}$$

where Ω_{MF} is the mean-field, Ω_{nl} nonlinear, and Ω_D Ohmic power terms. Of particular interest is the evolution of the $n = 0$ magnetic energy denoted $U^{(n=0)}$:

$$\frac{\partial}{\partial t}U^{(n=0)} = \text{source} + \Omega_{MF} + \Omega_D^{(n=0)}, \tag{5.4}$$

where $\Omega_{MF} = -\int dV \mathbf{E}_f \cdot \langle \mathbf{J} \rangle$ is the MHD dynamo due to all fluctuations including the MF ($n \geq 0$). The contribution from each mode can be expressed individually as $\Omega_{MF}^{(n)} = -\int dV \mathbf{E}_f^{(n)} \cdot \langle \mathbf{J} \rangle$. $\Omega_{MF}^{(n)}$ represents the rate at which energy is exchanged between the plasma and the axisymmetric magnetic field (mean-field) due to the mean (axisymmetric) MHD fluctuation dynamo $\mathbf{E}_f^{(n)}$ induced by each toroidal mode n as introduced above. When $\Omega_{MF}^{(n)} > 0$, the perpendicular plasma motion by the fluctuation n sustains the mean-field (MF) against dissipation by doing work on the MF at a positive rate and amplifying it. When $\Omega_{MF}^{(n)} < 0$, the MF magnetic energy is lost to the plasma motion and eventually to viscous and resistive dissipation. When the Hall term is included in the generalized Ohm's law, $\Omega_{MF}^{(n)}$ and the total MF power Ω_{MF} are further split into two parts: $\Omega_{MF}^{\text{MHD}} + \Omega_{MF}^{\text{Hall}}$ where

$$\Omega_{MF}^{\text{Hall}} = \sum_n \int dV \left\langle \frac{1}{ne}\mathbf{J}^{(n)} \times \mathbf{B}^{(n)*} \right\rangle \cdot \langle \mathbf{J} \rangle + \text{ c.c} \tag{5.5}$$

represents the total power transfer due to Hall term. This is the electromotive force generated by perpendicular currents arising from all of the fluctuations [§].

Fluctuation ($n > 0$) energy evolves as follows:

$$\frac{\partial}{\partial t}U^{(n>0)} = \text{source} + \Omega_{nl} + \Omega_D^{(n>0)}, \tag{5.6}$$

[§]Omit the final sum over all n to inspect the contribution from each fluctuation.

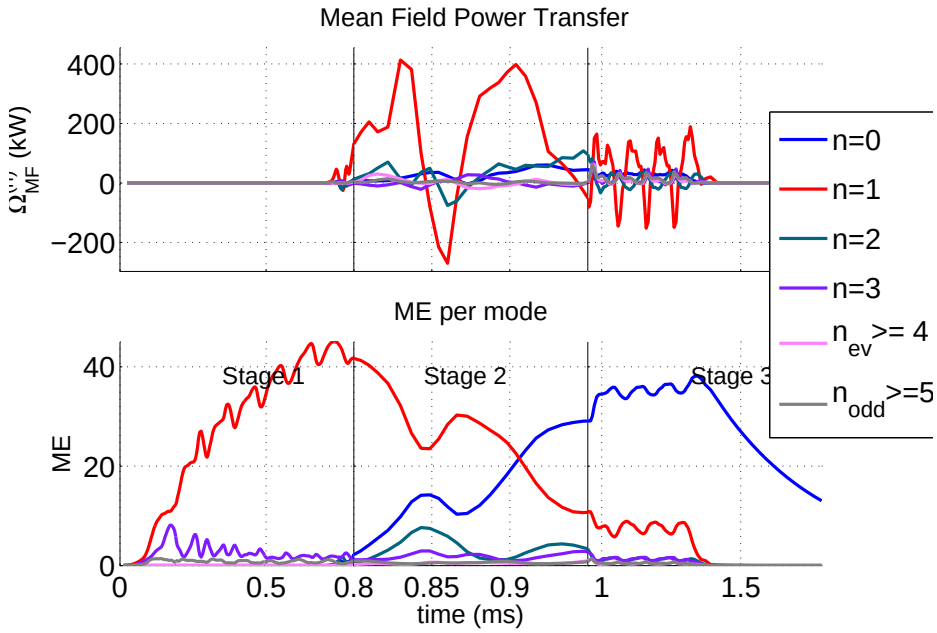

Figure 5.11: (a) Power transfer to the axisymmetric $\mathbf{B}$ (mean-field, MF) $\Omega^{(n)}_{MF}$ (upper plot), and ME per n (lower plot) as a function of time in ms. For clarity contributions from $n > 3$ are added together, separately for even and odd-numbered modes. Thus, the $n = 4$ represents the sum of all contributions from all even $n > 3$ modes and the $n = 5$ represents the total contribution from all odd $n > 3$ modes.

where $\Omega^{(n)}_{nl} \equiv -\int dV \langle \mathbf{E}^{(n)} \cdot \mathbf{J}^{(-n)} \rangle$ is the nonlinear dynamo term that measures the leakage of power into or out of a particular mode due to nonlinear interactions between the plasma and magnetic field. $\Omega^{(n)}_{nl}$ does not pinpoint the specific channel through which the energy is transferred. The Ohmic heating term, $\Omega^{(n)}_{D} \equiv -\eta |J_n|^2 < 0$ is always dissipative for all n, and therefore, is of no interest.

Initially, interactions are strictly nonlinear because the $n = 1$ is dominant and there is no MF. The mean-field fluctuation power term ($\Omega^{(n)}_{MF}$) registers strong activity near the end of stage I and in stage II when the $n = 0$ mode reaches a sufficient amplitude. The greatest contribution to the MF comes from the $n = 1$ fluctuation dynamo in the form of two large positive spikes occurring at $t = 0.8 - 1.0$ ms in $\Omega^{(n=1)}_{MF}$.

This is represented by the red trace in figure 5.11. Large spikes of dual-polarity in $\Omega_{MF}^{(n=1)}$ indicate SIHI fluctuations both add energy to and remove energy from the MF. But the area under the curve (energy) is overwhelmingly positive signaling that the injector-induced dynamo on average amplifies the MF during stages II and III. This is confirmed by an additional diagnostic that integrates the fluctuation dynamo power terms in time to track the bulk energy contribution to the MF (figure 5.13). After the nonlinear saturation, the MF becomes self-sustaining, as indicated by the strictly positive $\Omega_{MF}^{(n=0)}$ contribution.

Stage III exhibits a repeating pattern of reversals in fluctuation-power transfer to the MF. Figure 5.12 is an excellent illustration of the cyclic nature of the dynamo-mediated power transfer. It shows $\Omega_{MF}^{(n)}$ and $\Omega_{nl}^{(n)}$ vs. time from a calculation with a slightly higher S ($\eta/\mu_0 = 8.8$ m^2/s) programmed to run on flat-top mode for 10 cycles. Zero crossings of $\Omega_{MF}^{(n=1)}$ coincide with local extrema of the $n = 0$ and $n = 1$ ME. When $\Omega_{MF}^{(n=1)}$ crosses zero from the positive to negative side, *i.e.*, when the area under the curve, $\int \Omega_{MF}^{(n=1)} dt$, is a maximum, local maxima and minima are observed in $n = 0$ and $n = 1$ ME, respectively at $t = 1.35$, 1.45, and 1.55 ms, coincident with the extrema of the Y (upper) injector and zero-crossings of the X injector. Conversely, when $\Omega_{MF}^{(n=1)}$ crosses zero from the negative to positive side, that is, when $\int \Omega_{MF}^{(n=1)} dt$ is a minimum, local minima are observed in the $n = 0$ ME while the $n = 1$ ME displays local maxima at $t = 1.38$, 1.48, and 1.58 ms, nearly when both injectors are outputting the same amount of power. Power reversals in the $n = 1$ and higher fluctuation dynamo terms are also present in the single-injector calculations (see §5.2), implying that the leakage of power out of the MF is caused by injector oscillations rather than a competing effect between the two injectors. The timing of the peaks and dips in the fluctuation power per mode is determined by the phase difference between the two injectors. When lead-lag is swapped so that X leads Y, identical power transfer traces (not shown here), shifted forward in time by $\tau_{inj}/4$, are observed.

Integrating $\Omega_{MF}^{(n)}$ in time enables one to look at the energy transfer into the MF by

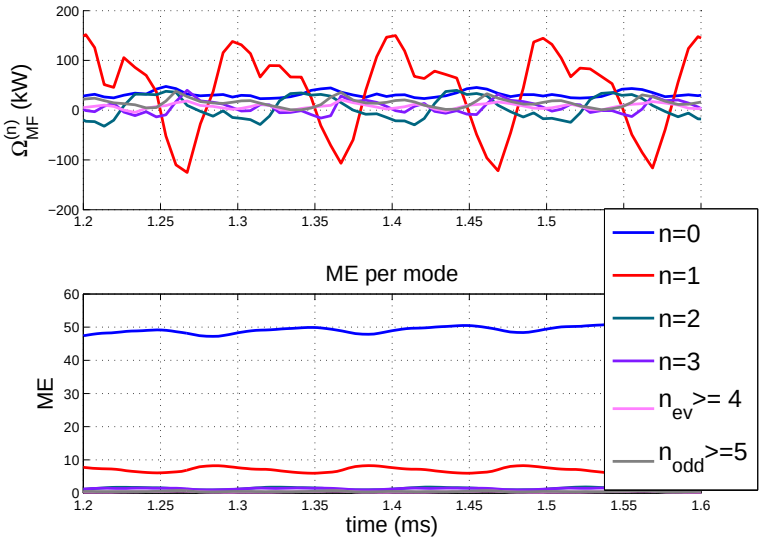

Figure 5.12: (a) Power transfer to the MF by the fluctuation dynamo terms, $\Omega_{MF}^{(n)}$ (upper plot) and ME per n (lower plot) as a function of time during stage III from a rMHD calculation with $\eta/\mu_0 = 8.8$ m^2/s. This calculation is run on flat-top mode for 10 injector cycles. Once again, for clarity contributions for $n > 3$ are added together, separately for even and odd-numbered modes. Thus, the $n = 4$ represents the sum of all contributions from even $n > 3$ and the $n = 5$ represents the total contribution from all odd $n > 3$. Zero-crossings of the $n = 1$ dynamo power temporally coincide with the local maxima of the $n = 0$ ME.

each fluctuation dynamo term and the total energy transfer from all dynamo terms as a function of time. $E_D^{(n)} = \int \Omega_{MF}^{(n)} dt$ shows a continual flow of energy into the MF in spite of reversals exhibited by $\Omega_{MF}^{(n)}$. This is illustrated in figure 5.13, which plots $E_D^{(n=1,2,3)}$ (for $n = 1 - 3$). The energetic contribution by each dynamo term is further split into the toroidal and poloidal components of the MF, represented by the red and blue traces, respectively. The energy transfer into the toroidal MF $\langle B_\phi \rangle$ is defined as $\int dt \int dV \left(-\mathbf{E}_f^{(n)} \cdot \langle \mathbf{J}_\theta \rangle \right)$ and that into the poloidal MF $\langle B_\theta \rangle$ as $\int dt \int dV \left(-\mathbf{E}_f^{(n)} \cdot \langle \mathbf{J}_\phi \rangle \right)$. The black traces represent the total energy transfered to the MF by each mode, *i.e.*, the sum of the toroidal and poloidal terms. Not surprisingly, the greatest energetic contribution (50 J) to the MF comes from the $n = 1$, which mostly builds up the toroidal MF while the $n = 2$ amplifies the poloidal MF. The contribution from the $n = 2$ is lower, roughly 10 J. Toroidal field amplification usually requires high edge current, consistent with a hollow $n = 1$ current profile. Poloidal field amplification requires current drive on the interior, which is consistent with a peaked $n = 2$ current profile. Figure 5.13 also suggests that the $n = 2$ acts as an intermediary for converting toroidal field to poloidal field. The bulk (total) energy contribution to the MF from all of the fluctuation-dynamo terms $E_D^{(n)}$, black trace in figure 5.14, is obtained by carrying out a sum over all the fluctuations: $E_D = \sum_{n \geq 0} E_D^{(n)}$. This is 90 J, approximately twice the final $n = 0$ ME ($\sim$ 40 J). The excess energy is balanced out by Ohmic dissipation, resulting in the steady-state configuration achieved approximately one $\tau_{L/R}$ time into the simulation. Figure 5.14 also includes the breakdown into the toroidal and poloidal components as is done above. More energy flows into $\langle B_\phi \rangle$ (red trace) than $\langle B_\theta \rangle$ (blue trace), consistent with the declining ratio of poloidal to toroidal ME (figure 5.1(f)). It will be shown in the η scan (§5.3.1) that raising S (lowering η) builds up the toroidal field more relative to the poloidal field, resulting in a decreasing ratio of poloidal to toroidal ME. For the generalized Ohm's law, $E_D^{(n)}$ and E_D are split into two parts to look at the energetic contribution from the MHD (E_D^{MHD}) and Hall (E_D^{Hall}) dynamos separately.

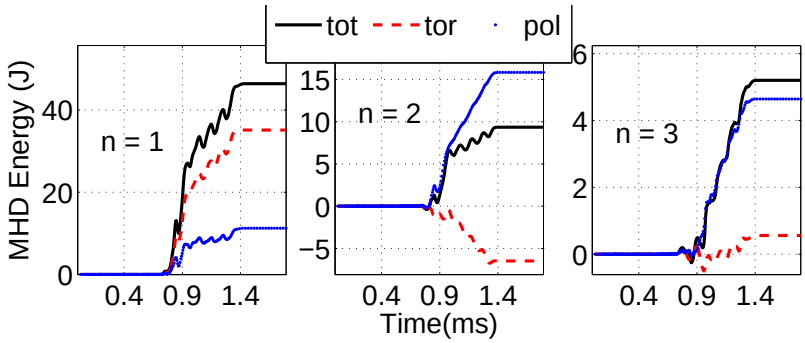

Figure 5.13: Energy transfer into the MF by the $n = 1-3$ fluctuation dynamos as a function of time in ms. These are running time integrals of $\Omega_{MF}^{(n)}$ for the $n = 1$ (left), $n = 2$ (center), and $n = 3$ (right). The dotted blue trace represents the contribution to the poloidal MF, the dashed red trace to the toroidal MF, and the solid black line to the total MF (sum of red and blue traces). The $n = 1$ mostly builds up the toroidal MF while $n = 2$ amplifies the poloidal MF.

$E_D^{\text{Hall}}) = \int dt \Omega_{MF}^{\text{Hall}}$ where $\Omega_{MF}^{\text{Hall}}$ is defined in eqn.(5.5).

The lower-dimensional diagnostics combined with 3-D visualization show a complex and dynamic system, featuring the collimated injector current channels. These structures evolve from a mirror-symmetric $n = 1$ state to a largely axisymmetric state when a significant I_{tor} is present. Energetics analysis helps elucidate how the axisymmetric (mean) field is formed and sustained with a continuing energy transfer due to the dynamo force, driven by the plasma motion and imposed injector fluctuations.

5.1.4 Effects of Handedness on the Characteristic Results

Handedness of the final helicity depends on the handedness of the injected helicity. Right-handed helicity injection ($\lambda_{inj} = 30$ m^{-1}) results in a final configuration with a right-handed helicity and likewise left-handed helicity injection ($\lambda_{inj} = -30$ m^{-1}) produces a helically left-handed final configuration. Left-handed helicity can be injected with a negative injector voltage or negative flux. The two methods are equivalent and produce identical results. The handedness of the initial equilibrium used as the $n = 0$

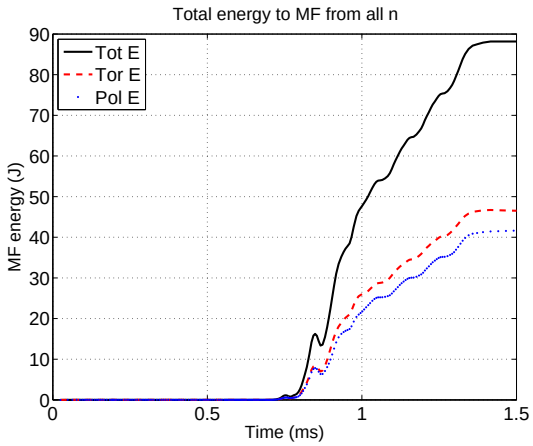

Figure 5.14: The bulk energy transfer to the MF (E_D) by all the fluctuation dynamo terms as a function of time (ms), including a breakdown into toroidal (dashed red trace) and poloidal (dotted blue trace) components. The solid black line shows the total energy transfer to the overall MF (sum of red and blue traces). In this case, there is slightly more energy going into the toroidal MF than the poloidal MF.

perturbation has no effect on the dynamics and the handedness of the final saturated state. Figure 5.15 indicates that the onset of mode growth is delayed by approximately a half period for the right-handed (RH) helicity injection. The rotating $n = 1$ field acquires an additional 180° phase when the handedness of the injected helicity is reversed. This phase difference corresponds to the observed lag time of $\tau_{inj}/2$ since the configuration rotates at $\omega_{inj}(= 2\pi\tau_{inj})$. It is not clear why mode activity for the LH helicity precedes that of RH helicity but the difference seems to suggest the existence of a 'sweet spot' in space as well as in time for the onset of mode growth. The direction of I_{tor} (figure 5.15(b)) is the same for both handedness of injected helicity.

5.1.5 Convergence

To check the spatial convergence of the calculations a series of simulations is performed starting with a coarse poloidal grid comprising 12×12 bicubic ($pd = 3$) elements and approximately doubling the resolution up to a fine mesh comprising 48×64 biquartic

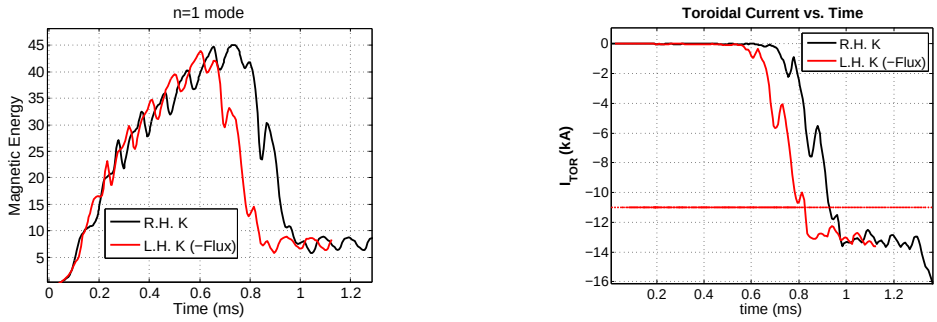

(a) $n = 1$ magnetic energy vs. time(ms)

(b) I_{tor} vs. time(ms)

Figure 5.15: A comparison of (a) $n = 1$ ME as a function of time and (b) I_{tor} as a function of time for right-handed (RH) and left-handed (LH) helicity injection. Mode growth onsets approximately one half injector period sooner for the left-handed helicity injection.

($pd = 4$) elements. This scan is conducted for two different plasma resistivities, $\frac{\eta}{\mu_0} =$ 11.7 and 8 m^2/s in anticipation of higher S calculations. In addition, to understand possible effects of grid packing, the cases with 48×48 and 48×64 FE's use a mesh that is densely packed toward the injector openings along $\hat{z}$ to provide a smooth transition in element size going from the plasma to the resistive edge region (see figure 2.6(a)). Grid-packing eliminates the noise in the plasma flow seen near the vicinity of the injector mouths. Plots of figure 5.16 indicate that for $\eta/\mu_0 = 11.7$ m^2/s, even the coarsest mesh comprising 12×12 FE's is able to adequately capture the main features of the calculations provided the polynomial representation is sufficiently high, *i.e.*, $pd \geq 3$. The two simulations with the coarsest meshes produce slightly more magnetic energy in the $n = 1$, then later in the $n = 0$ following the mode saturation, but the differences are within 10% as indicated by $n = 0$ and $n = 1$ ME vs time plots in figure 5.16. The final amplitude of I_{tor} shows an excellent agreement between the coarsest and finest-resolution cases as shown in figure 5.16(c). Contour plots (not shown here) of plasma flow, magnetic field and current density for each toroidal mode show nearly identical structures for all four resolutions. Grid-packing has a negligible

effect because the regions of tight-packing are also regions of low plasma flow due to the zero-flow boundary condition. The error in $\nabla \cdot \mathbf{B}$ reduces in a manner consistent with increasing grid resolution or polynomial representation as illustrated by the $\log_{10}$ plot of volume averaged $\nabla \cdot \mathbf{B}/B$ in figure 5.16(d). The higher S poloidal convergence scan yields results very similar to those of the lower-S convergence scan. The general characteristics remain mostly invariant down to a poloidal resolution of 12×12 bicubic elements (results are not shown here).

To understand the effect of increasing toroidal resolution, two additional simulations each with twice the toroidal resolution of the previous one, *i.e.*, with 22 and 43 Fourier modes were performed. 11, 22, and 43 modes correspond to 32, 64, and 128 toroidal cells with width $\Delta x_\phi = 6, 4$, 3.2, and 1.6 cm at the magnetic axis, respectively. The poloidal mesh for the 22-mode calculation consists of 40×40 bicubic FE's and that for the 43-mode calculation consists of 36×36 bicubic FE's. The total ME decreases by 10% as the toroidal resolution is doubled from 11 to 22 modes. At 22 modes and beyond the total ME no longer increases, as the increased toroidal resolution eliminates the additional source terms that would normally appear at locations other than the injector openings on the annular boundaries with 11 modes. The $n = 0$ and $n = 1$ ME from all three cases are shown in figures 5.17(a) and 5.17(b), respectively. The solid black line represents the 11-mode case, dashed red line the 22-mode case, and dotted blue line the 43-mode case. The final saturation amplitude of the $n = 0$ ME (and I_{tor}) shows good convergence with 22 Fourier modes, but nonlinear saturation occurs increasingly later in time as the toroidal resolution is increased as shown in figure 5.17. Growth rates of the unstable magnetic (and kinetic) modes slow down with increasing toroidal resolution. Furthermore, with 22 and more modes the linear growth phase in stage II shows intermittent interruptions, undergoing multiple cycles of linear growth, saturation separated by extended periods of stagnation before the $n = 0$ becomes global (not shown here). In conclusion, both the validation and verification rMHD simulations show an undesirable sensitivity to toroidal resolution

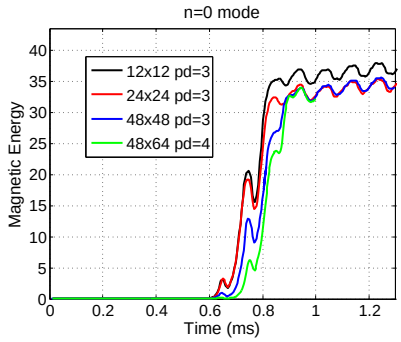

(a) $n = 0$ ME vs. time(ms)

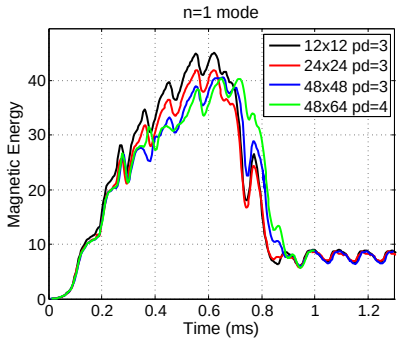

(b) $n = 1$ ME vs. time(ms)

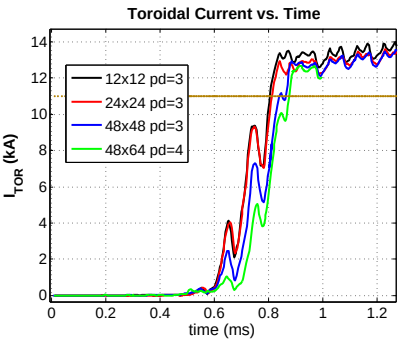

(c) I_{tor} vs. time(ms)

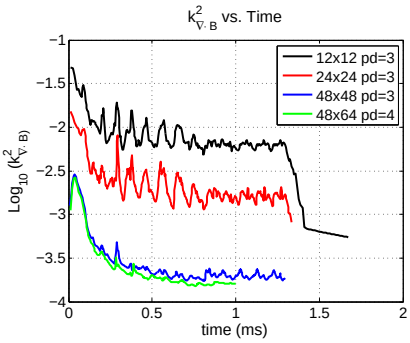

(d) Volume-averaged $\nabla \cdot \mathbf{B}$ error vs. time(ms)

Figure 5.16: Poloidal convergence study for the baseline rMHD calculation ($\eta/\mu_0 = 11.7$ m^2/s). (a) $n = 0$ ME , (b) $n = 1$ ME, (c) I_{tor}, and (d) volume-averaged $\nabla \cdot \mathbf{B}$ error as a function of time (ms) from four simulations with different poloidal resolutions. The dashed brown line in (c) represents the amplitude of the injector current. All the traces are nearly overlaid indicating poloidal convergence is achieved with the coarsest mesh comprising 12×12 bicubic FE's. Note that the error in $\nabla \cdot \mathbf{B}$ is reduced by increasing either the number of FE's or the polynomial representation.

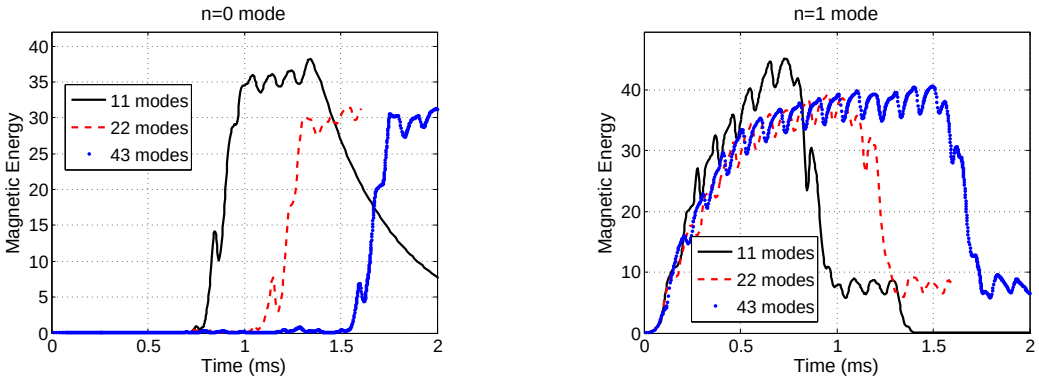

(a) I_{tor} vs. time (ms)

(b) $n = 1$ ME vs time (ms)

Figure 5.17: Toroidal convergence study for the baseline rMHD calculation. (a) $n = 0$ ME and (b) $m = 1$ ME as a function of time (ms) for simulations with 11, 22, and 43 Fourier modes. The saturation amplitude of the $n = 0$ ME (I_{tor}) converges with 22 modes, but saturation time is increasingly delayed as the toroidal resolution increases.

and therefore, require a high toroidal resolution.

Figure 5.18 shows logarithmic (base 10) plots of magnetic energy as a function of toroidal mode number n at two different instants from all three simulations with different toroidal resolution. The first chosen time corresponds to the latest time from stage I such that $I_{tor} < 1$ kA. The second chosen instant is the longer of the following two times: τ_f, *i.e.*, the time when $I_{tor}/I_{inj} = 1$ and the end of the sixth flat-top injector cycle. The black, red, and blue traces correspond to ME spectra with 11, 22, and 43 modes, respectively. The plots show that the energy contained in the highest modes is nearly three to four orders of magnitude lower than the energy contained in the lowest modes. The energy spectrum does not decrease monotonically in n during stage I because the injectors directly drive the odd-numbered toroidal modes (figure 5.18(a)). After the nonlinear saturation, the spectrum rearranges itself showing a monotonic decline in ME spectrum as indicated by figure 5.18(b). An upward tail appearing in both ME and KE spectra is the only deviation from this trend. The last few highest modes contain more energy than the few modes preceding them regardless

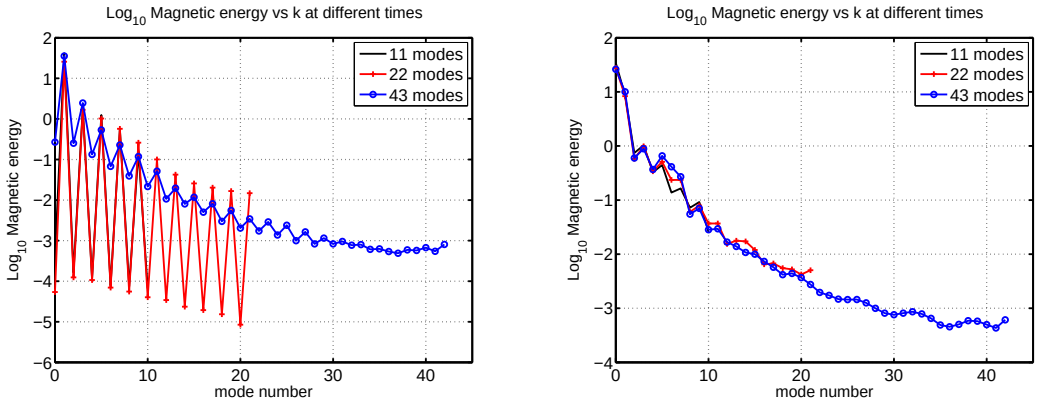

(a) Log_{10} ME vs n from stage I

(b) Log_{10} ME vs n from stage III

Figure 5.18: Plots of the logarithm (base 10) of ME as a function of toroidal mode number n for 11, 22, and 43-mode simulations from (a) a time in stage I and (b) a time in stage III when $I_{tor}/I_{inj} > 1$. The spectrum becomes monotonic during stage III. The upward tail in the energy spectrum is an artifact of the finite Fourier representation of the toroidal direction.

of the toroidal resolution. This upward tail in the energy spectrum is an artifact of the finite Fourier representation in the toroidal direction. With a truncated Fourier series, the energy that would normally go to all of the higher modes up to the continuum limit ($n \to \infty$), instead, accumulates in the last (highest) mode that is retained in the Fourier decomposition. The excess energy is distributed to the neighboring modes via the regular MHD coupling, creating an upward tail.

5.2 Single Injector Simulations

To get a clearer picture of plasma dynamics due to SIHI, a series of single-injector simulations have been run. These calculations are performed on a coarse, 12×12 mesh with $pd = 3$ and 11 Fourier modes. The remaining physical and numerical parameters are identical to those presented and described in the baseline section (§5.1). The X injector is driven with a cosine waveform for the X-only simulation and the Y injector with a sine waveform for the Y-only simulation unless otherwise specified. The energy

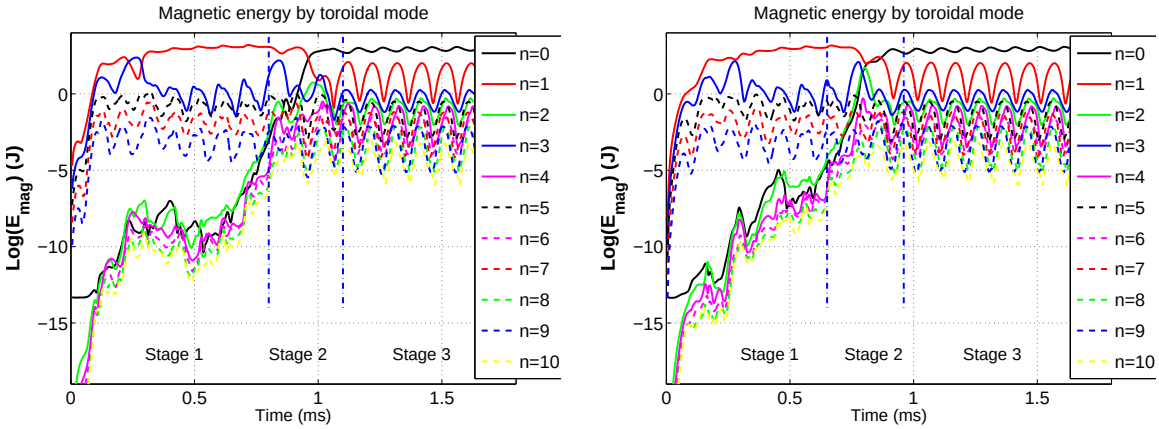

(a) Log ME per n vs. time for X-only

(b) Log ME per n vs. time for Y-only

Figure 5.19: Logarithm of the magnetic energy per toroidal mode as a function of time (ms) for an (a) X- and (b) Y-injector-only simulation. Note that the mode spectrum is very similar to the dual-injector spectrum displayed in figure 5.1(c)

spectra for single injector calculations, shown in figure 5.19, are very similar to those of the dual-injector calculations indicating that $n = 0$ amplification in rMHD does not require a steady rate of helicity injection. Mode evolution follows the same three-stage process described in §3.2 and 5.1. The onset of the linear growth stage, however, seems to depend on the injector waveform, as evidenced by the earlier onset of linear mode growth for the Y-only case than X-only case, as indicated by the plots of the logarithm of magnetic energy per toroidal mode in figures 5.19(a)(X) and 5.19(b)(Y). This finding suggests that fluctuations imposed by Y injector (sine wave) couple better to the initial state while the X injector fluctuations (cosine wave) are slightly misaligned with the initial state.

The single-injector calculations produce and sustain toroidal currents in the simulation domain with an opposing direction of toroidal current observed for each injector. The simulated X-injector case produces an I_{tor} in $+\hat{\phi}$ (counter clockwise) direction while Y-only simulation gives rise to a clockwise toroidal current. Temporal traces

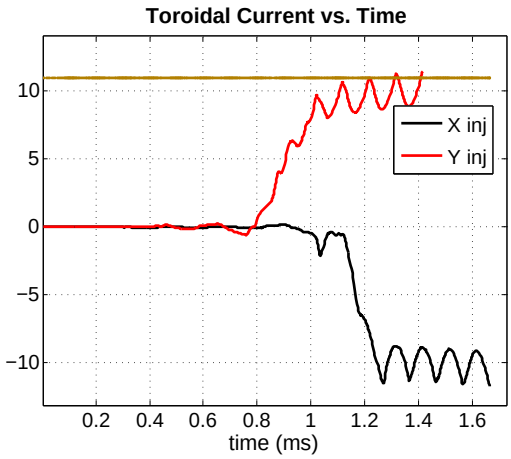

Figure 5.20: I_{tor} as a function of time (ms) for X- (black) and Y-injector-only (red) baseline resistive MHD simulations. The direction of toroidal current produced by the X-injector is opposite to that of the Y-injector. The brown line represents the amplitude of I_{inj}. There are two local maxima and minima in I_{tor} per period as observed in the single-injector shots from the experiment.

of I_{tor} are shown in figure 5.20. Here the black trace corresponds to X-only and the red trace to Y-only. Switching the handedness of the injected helicity for either single injector results in a reversal of the I_{tor} direction. These findings agree with the results of single injector operations of HIT-SI, reported by Ennis *et al.*[43]. An additional Y-only simulation is performed where the injector is driven with the cosine waveform of the X injector instead of the usual sine waveform. This simulation yields results identical to the X-only (not shown here). This further verifies that the results are robust to the operational permutations and do not discriminate between the injectors when the two are driven identically.

The power transfer to the mean field ($\Omega_{MF}^{(n)}$) mediated by the fluctuation dynamo $\mathbf{E}_f$ exhibits spikes similar to those seen in the dual-injector baseline simulation during stage II (figure 5.11). The power surge into MF does not proceed in an identical manner for X and Y-only simulations. The Y-only simulation shows significant power flow to the MF from the $n = 2$ and $n = 3$ modes prior to the surge from the $n = 1$

while higher mode ($n > 1$) dynamo activity is nearly non-existent in the X-only case during stage II. In both cases, stage III exhibits a cyclic pattern of oscillations in $\Omega_{MF}^{(n)}$ with a period of $\tau_{inj}/2 = 0.1$ ms, which is illustrated in figure 5.22 for both X and Y-only simulations. This is most obvious for $\Omega_{MF}^{(n=1)}$. As was previously established in §5.1.3, positive-to-negative zero-crossings of $\Omega_{MF}^{(n=1)}$ are nearly coincident with the $n = 0$ ME maxima and $n = 1$ ME minima, while negative-to-positive zero-crossings of $\Omega_{MF}^{(n=1)}$ nearly coincide with the $n = 0$ ME minima and $n = 1$ ME maxima. In either case, the $n = 0$ ME maxima lag the injector zero-crossings ($t = 1.25, 1.35, 1.45, \cdots$ ms for X and $t = 1.2, 1.3, 1.4, \cdots$ ms for Y) by 10–15 μs and the $n = 0$ ME minima ($n = 1$ ME maxima) lag the injector extrema ($t = 1.2, 1.3, 1.4, \cdots$ ms for X and $t = 1.25, 1.35, 1.45, \cdots$ ms for Y) by 10–15 μs.

The time integral of the total dynamo-mediated power, $E_D \equiv \int dt \sum_n \Omega_{MF}^{(n)}$ indicates an equal amount of bulk energy transferred to the MF ($n = 0$) for both single-injector simulations. Figures 5.23(a) and 5.23(b) show E_D vs time (black trace) as well as the breakdown of E_D into the toroidal (red trace) and poloidal (blue trace) MF, as defined in §5.1.3, for X- and Y-only simulations, respectively. The energy transfer to the MF begins a little sooner for the Y-only case, consistent with the time evolution of its toroidal spectrum. For either single-injector case, the dynamo energy is nearly equipartitioned into the poloidal and toroidal components of the MF with slightly more energy in the toroidal MF, as encountered in the dual-injector simulation (figure 5.14).

To better illustrate the dynamics of the injector channels, visualization output during the steady-state period (stage III) from a Y-injector-only simulation is presented. It is in this area that single injector SIHI simulations are most beneficial because they yield a much clearer picture of the injector channels in the absence of the toroidal rotation and cross coupling between the two injectors. Figure 5.24 is a series of snapshots showing the evolution of the injector current column (channel) during an interval from stage III, $t = 1.34 - 1.39$ ms. The injector current column

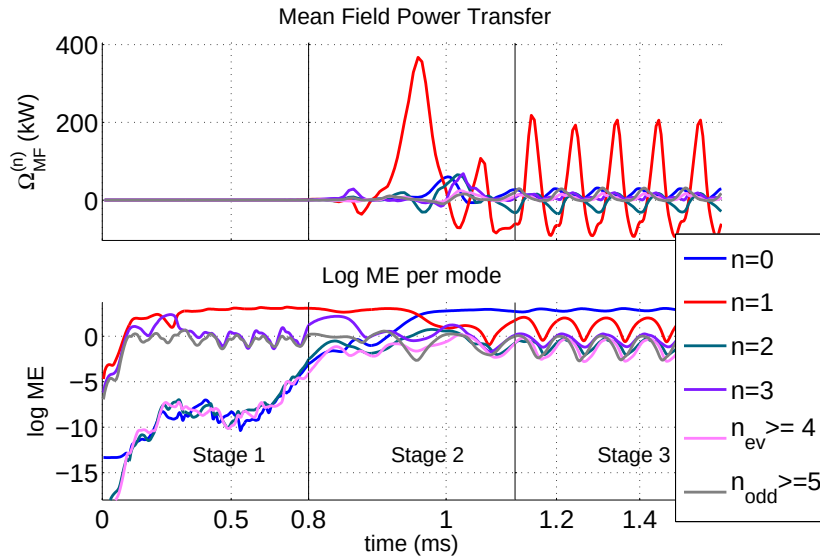

(a) $\Omega^{(n)}_{MF}$ per n vs. time(ms) for X-only simulation

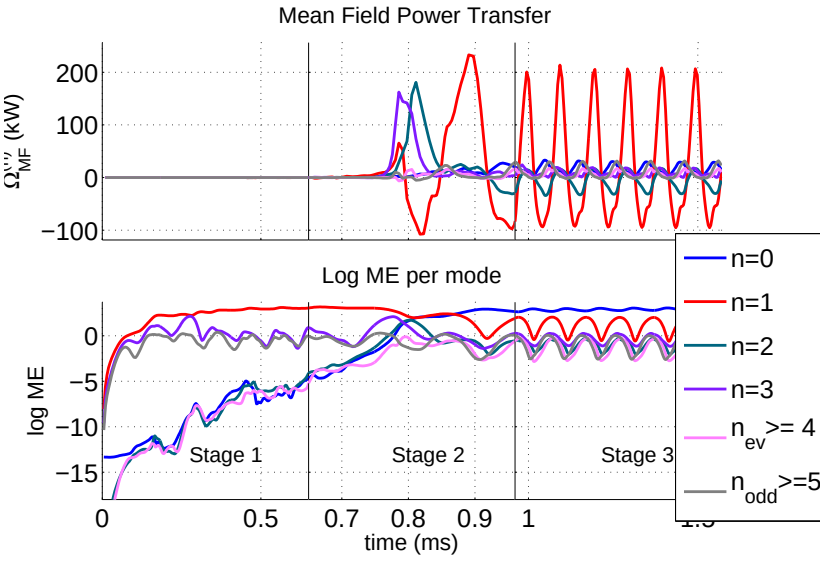

(b) $\Omega^{(n)}_{MF}$ per n vs. time(ms) for Y-only simulation

Figure 5.21: Power transfer to the mean field ($\Omega^{(n)}_{MF}$) by the fluctuation dynamo terms from (a) X-injector-only and (b) Y-injector-only baseline rMHD simulations. The horizontal axis (time in ms) during stage II is stretched to better illustrate the power transfer during stage II. Log(ME) as a function of time for each calculation is included in the lower halves of each figure. The power surge to the $n = 0$ during stage II does not happen identically for the X- and Y-only cases. The Y-only case shows significant contributions from the $n = 2$ and $n = 3$ while the $n = 1$ is the only major participant for the X-only case.

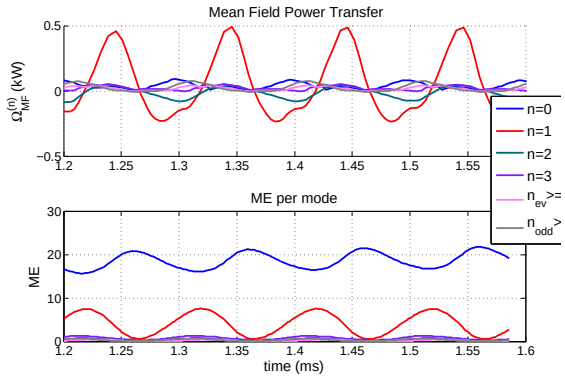

(a) $\Omega_{MF}^{(n)}$ per n during stage III for X-only simulation

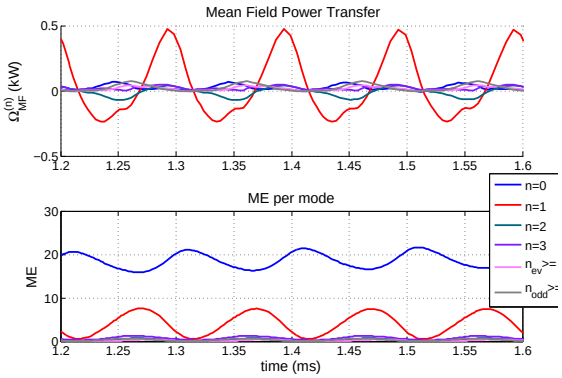

(b) $\Omega_{MF}^{(n)}$ per n during stage III for Y-only simulation

Figure 5.22: Power transfer to the MF by the fluctuation dynamo terms, $\Omega_{MF}^{(n)}$ (upper plot) and ME per n (lower plot) as a function of time during stage III for (a) X- and (b) Y-injector-only baseline rMHD simulations. A cyclic pattern of oscillations with a period of $\tau_{inj}/2 = 0.1$ ms appears in $\Omega_{MF}^{(n)}$ just as it was seen in the baseline simulation.

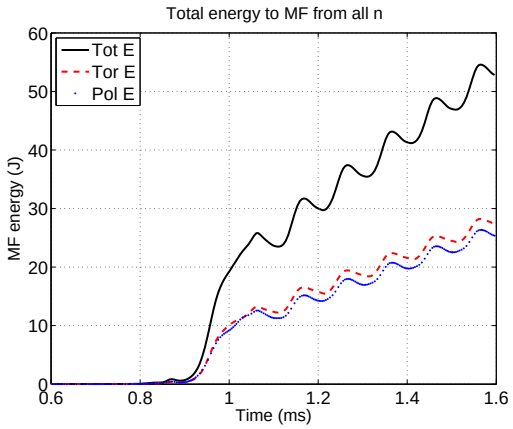

(a) Total bulk energy into MF for the X-only case

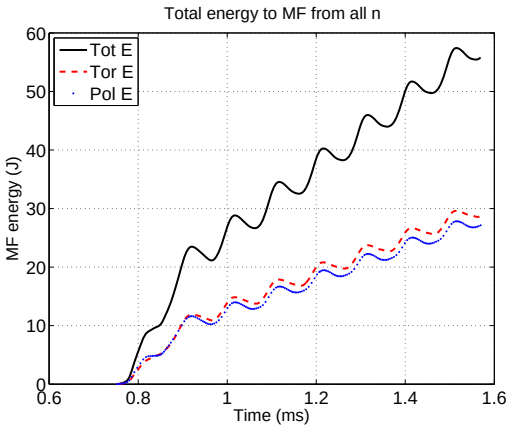

(b) Total bulk energy into MF for the Y-only case

Figure 5.23: The total (bulk) energy transfer into the MF by all the fluctuation dynamos terms, $E_D = \sum_n \int dt \Omega_{MF}^{(n)}$, as a function of time for (a) an X-injector-only and (b) a Y-injector-only baseline rMHD simulations. A breakdown into toroidal (red) and poloidal (blue) MF is included.

is represented by three isosurfaces of the magnitude of current density J, each corresponding to 2, 3, and 4% of the maximum $J(= 1.7 \times 10^7$ A/m$^2)$. Once again J in regions where $B < 0.015$ T is excluded to remove the boundary layers. The injector column bends to properly align itself with the I_{tor} as it forms. When I_{inj} crosses zero and reverses, the injector column reappears on the opposite side and leans in the opposite direction to realign itself with the I_{tor}. Since there is no toroidal rotation of the field, the structure formation alternates back and forth between the same two physical locations in the western and eastern hemispheres (figure 5.25). The full current column formation lags the Y-injector maxima. For the interval covered in figure 5.24, the full formation occurs at 1.37 ms, 0.02 ms after the injector maximum. The longevity of the column is approximately 70 μs, nearly twice τ_A and slightly shorter than the injector half period (100 μs).

Because the lifetime of the injector column is so close to $\tau_{inj}/2$, it is not clear whether a factor other than f_{inj} determines the longevity of these structures. For example, the injector channels can be kink-unstable if they carry too much current and can then break up over the course of a few τ_A as this type of instability occurs on Alfvénic time scales. To answer this question, an additional Y-only simulation with a tenth of the original frequency, *i.e.*, $f_{inj} = 0.5$ kHz, was run to separate out the two time scales. This calculation shows successive occurrences of the injector channels in the same location until I_{inj} reverses after a half injector period. The channels form, get distorted, and eventually break up only to repeat this life-cycle several times over during an injector half period. Therefore, it can be inferred that it is the kink instability that determines the longevity of the injector columns for $\tau_A f_{inj} \ll 1$. Stable injector operation requires faster f_{inj} so that instability does not have enough time to fully onset, but not so fast that the injector reversals overtake τ_A: $\tau_A f_{inj} > 1$. It is shown in §5.3.3 that too high a f_{inj} completely changes the characteristics observed thus far and results in no $n = 0$ amplification.

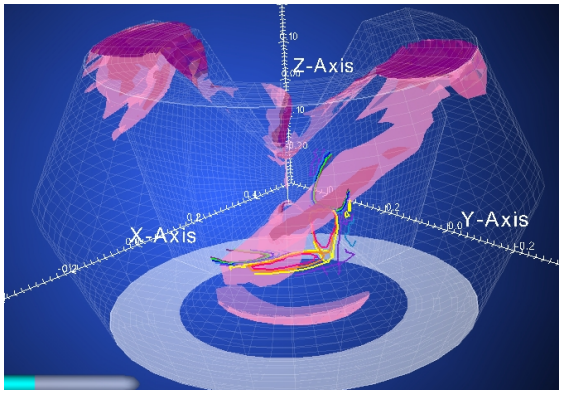

(a) J isosurfaces at $t = 1.342$ ms

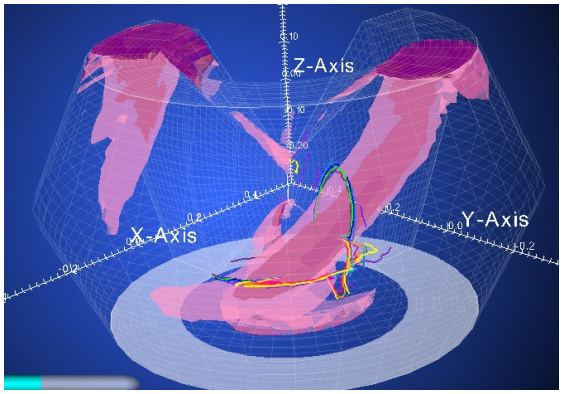

(b) J isosurfaces at $t = 1.355$ ms

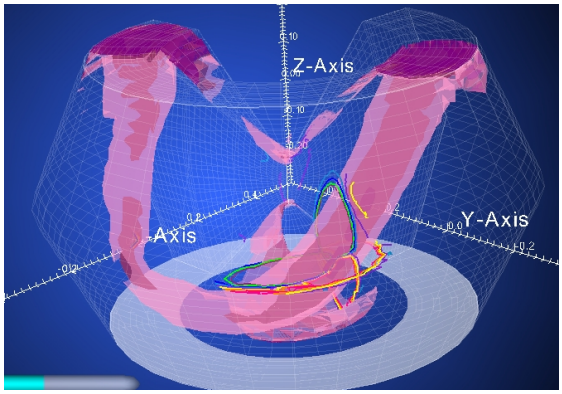

(c) J isosurfaces at $t = 1.362$ ms

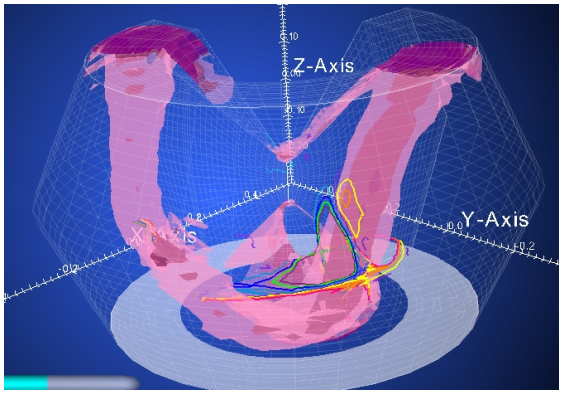

(d) J isosurfaces at $t = 1.370$ ms

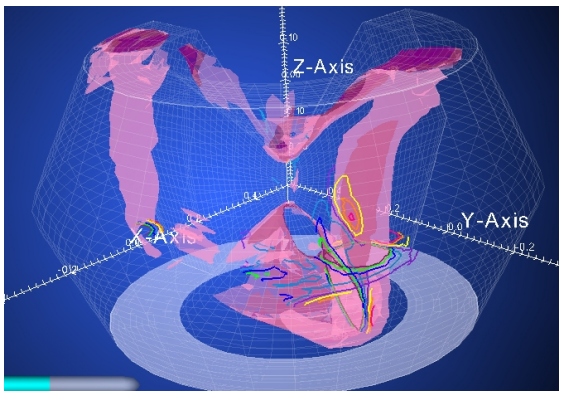

(e) J isosurfaces at $t = 1.380$ ms

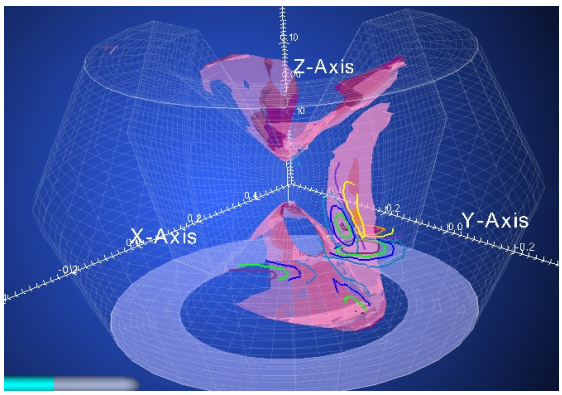

(f) J isosurfaces at $t = 1.393$ ms

Figure 5.24: Snapshots of J isosurfaces showing the formation, breakage and dissolution of a Y injector column during the post-saturation stage (stage III) for a Y-injector-only simulation. $I_{tor}/I_{inj} \approx 1$ for this case. The contours indicate $-\mathbf{E}_f \cdot < \mathbf{J} >$, *i.e.*, fluctuation dynamo power density. J is nearly 10^6 A/m^2 in the dark pink regions. The injector maximum current and flux occur exactly at 1.35 ms. The lifetime of the injector column is too close to $\tau_{inj}/2$ to reliably determine what factor rules the existence of the injector channels.

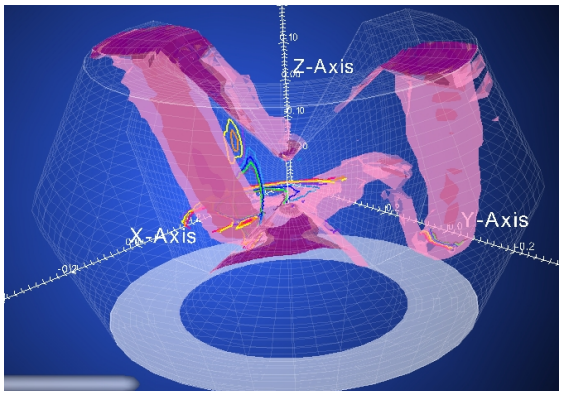

(a) Isosurfaces of J at t= 1.07 ms

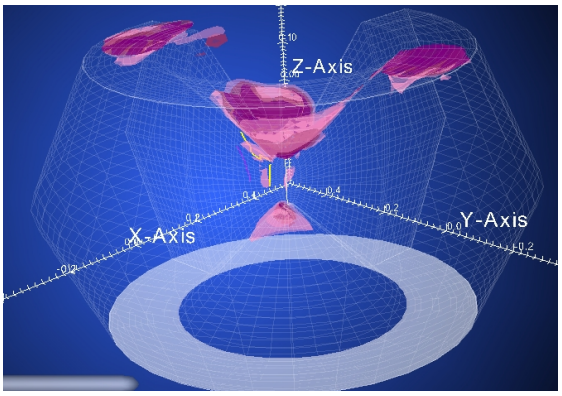

(b) Isosurfaces of J at t= 1.123 ms

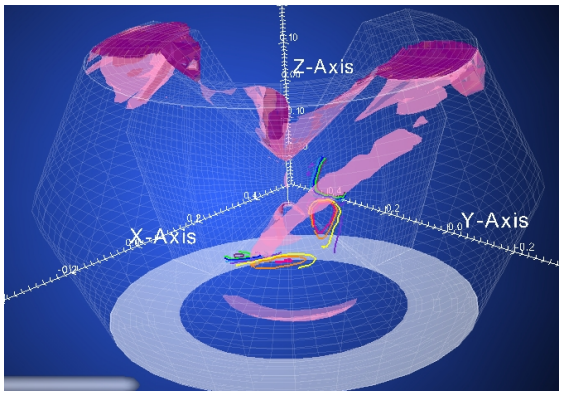

(c) Isosurfaces of J at t= 1.137 ms

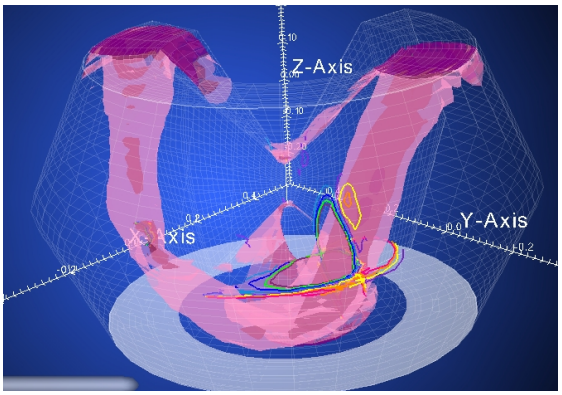

(d) Isosurfaces of J at t= 1.167 ms

Figure 5.25: Snapshots of J isosurfaces showing the evolution of the Y-injector current channel over a half injector period. The frames are from four different times in the simulation. The injector crosses zero at t= 1.10 ms. The current column switches hemispheres once the injector current reverses.

5.3 Parameter Scans

The aim of this section is to understand how current amplification demonstrated by the rMHD model of HIT-SI varies as a function of certain key physical parameters like the Lundquist number (S), λ_{inj}, and f_{inj}. S is controlled by adjusting the plasma resistivity η while keeping all the other parameters presented in Table 5.1 the same. Since $S \sim \eta^{-1}$, the present S scan is equivalent to a scan in η and therefore, is a further verification of the finding from the validation rMHD simulations that yielded $I_{tor}/I_{inj} \propto \eta^{-0.4}$. The reciprocal relation between S and η is not exact because S as it is defined by eqn. (2.9) has an additional implicit dependence on η via the total magnetic energy. Nevertheless, the two terms, S or η scan, will be used interchangeably in this section. Numerical scans indicate $I_{tor}/I_{inj} \sim S^{1/2}$. For the cases that demonstrate relaxation and current amplification, the characteristics weakly depend on λ_{inj} and f_{inj}. However, in both cases, there exist cut-offs below or above which no relaxation, and consequently no current amplification occurs.

5.3.1 Investigating the Scaling of Current Amplification with $S(\eta)$

S is increased by lowering the plasma resistivity η while keeping all the other parameters the same. The following values of resistive dissipation η/μ_0 are used: 25, 11.7, 8.8, and 5.0 m^2/s corresponding to $S = 7$, 20, 33, and 61 respectively. A narrow range is used to stay in the vicinity of experimentally realizable S. Note as η is lowered the magnetic Prandtl number ($Pm \equiv \nu/\eta$) increases because the viscous dissipation ν is held fixed at 100 m^2/s. Table 5.2 lists the values of τ_A and $\tau_{L/R}$ for each simulation with a different S. Injector period τ_{inj} is held constant at 0.2 ms for all five simulations.

Several trends emerge. Reducing η to raise S builds up more total magnetic energy and leads to faster Alfvén transit times, resulting in a greater $n = 0$ amplification and I_{tor}. Figure 5.28(a) shows I_{tor} as a function of time in ms from all four calculations

Table 5.2: The two prominent time scales, Alfvén time τ_A and resistive diffusion time $\tau_{L/R}$ for each S. The injector period τ_{inj} is kept at 0.2 ms for all five simulations.

S	**7**	**20**	**33**	**61**
η/μ_0 (m^2/s)	**25**	**11.7**	**8**	**5**
τ_A (ms)	0.053	0.042	0.036	0.031
$\tau_{L/R}$ (ms)	0.38	0.81	1.19	1.90

with different η. Since energy steady-state occurs on resistive time scales ($\sim \tau_{L/R}/2$), it takes longer for the total magnetic energy to reach a steady state as η is lowered. As a result, the disparity between the formation time when $I_{tor}/I_{inj} = 1$ and steady-state time when I_{tor} flattens increases.

Figure 5.26 shows the natural logarithm of ME for even modes $n = 0 - 6$ as a function of time for all the simulations with different η. Each panel represents a different mode. Growth rates γ_n for each mode is extracted from the slope of each ME trace. $\gamma_{n=0}$ = 22, 49, 120, and 97 kHz for S = 7, 20, 31, and 61, respectively. All things being equal with the exception of η, the absolute growth rates γ_n should speed up as η is lowered while the normalized growth rates $\gamma_n\tau_A$ should remain the same since relaxation activity occurs on Alfvénic time scales. There are deviations from this trend because as η is lowered to access higher S, the ratio S/Pm increases, enhancing viscous effects over the Lorentz force term in the dimensionless momentum equation (eqn. (2.6)). Enhanced viscous dissipation impedes the ion motion, which, in turn lessens the MHD dynamo, critical for the $n = 0$ amplification. As a result, linear growth rates speed up for intermediate S and slow down for higher S.

Another artifact of high viscosity ($Pm \gtrsim 100$) is the appearance of irregularly-shaped (triangular and pentagonal) closed magnetic structures during steady-state I_{tor} sustainment in stage III. These structures occupy a small fraction of the total

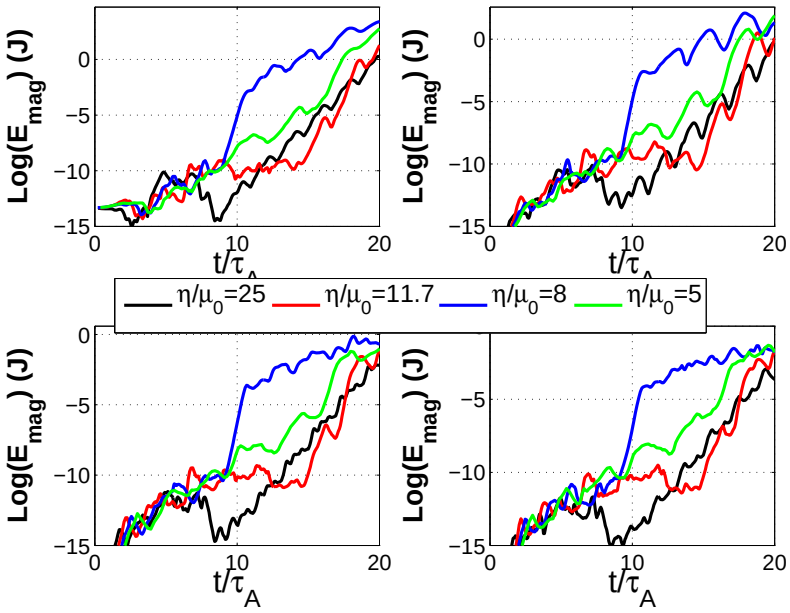

Figure 5.26: Logarithm of ME per even toroidal modes up to $n = 6$ as a function of normalized time, t/τ_A from four calculations with a different η/μ_0. Going counter clockwise from the top left panel, the illustrated modes are $n = 0$, 2, 4, and 6. The onset of the linear growth phase is nearly coincident in all simulations in terms of the normalized time.

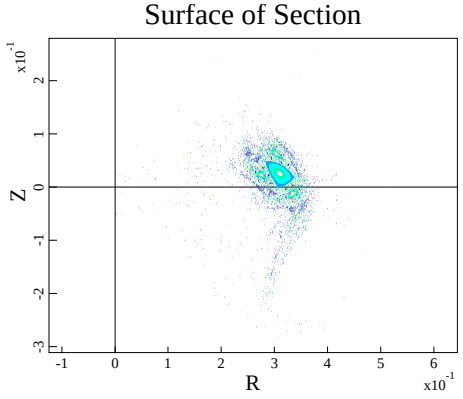

Figure 5.27: Poincaré puncture plots from an instant during sustainment from a simulation with $\eta/\mu_0 = 1.0$ m^2/s. The punctures are plotted through the poloidal plane at $\phi = 0°$ toroidal location. Triangular closed flux surfaces form as an artifact of the increased Pm (ratio of viscous to resistive diffusion).

volume and migrate in the poloidal plane in a random fashion. Figure 5.27 shows an example from a calculation with $\eta/\mu_0 = 1.0$ m^2/s. The closed surfaces are an outcome of high viscosity that balances out the Lorentz force, arising from small perpendicular currents when $\beta = 0$. The width of the structures is on the order of the viscous dissipation scale. The occurrence of similar viscosity-supported steady state surfaces is discussed in the paper by Sovinec *et al.*[24].

The steady-state plasma current I_{tor} reaches 8, 13, 17, and 21 kA, respectively for the various values of η/μ_0 shown in figure 5.28(a). A linear fit to the logarithm of I_{tor} vs. logarithm of η shown in figure 5.28(b), indicates that the steady-state plasma current I_{tor} and current amplification I_{tor}/I_{inj} scale as $\eta^{-0.65\pm0.05}$ and $S^{1/2\pm0.04}$. The difference between the present scaling and that extracted from the validation rMHD simulations, which yields $I_{tor}/I_{inj} \propto \eta^{-0.4}$, is attributed to the different λ_{inj} used in the two simulations, which impacts the injector impedance term Z_{inj} appearing in eqn. (1.16). All of the model-dependent dynamic effects are encompassed by Z_{inj}, which has an implicit dependence on λ_{inj} and possibly η.

Consistent with the growing amplitude of the I_{tor} and total magnetic energy stored in the $n = 0$, the bulk energy transfer into the $n = 0$ by the fluctuation dynamo terms increases as S is raised. This is shown in figure 5.29 where $E_D = \sum_{n\geq 0} \int dt \Omega_{MF}^{(n)}$ from all four simulations with different S values is plotted as a function of time in ms. The slope of E_D, *i.e.*, the power transfer to the $n = 0$, is the same for all four cases during stage III, however, the initial power surge, occurring at the end of stage I and during stage II, increases with S. Another emerging pattern is that the MHD dynamo channels more energy into the toroidal component of the MF as S increases. The ratio of the dynamo energy transferred into the toroidal MF to that transferred into the poloidal MF increases, yielding the following values: 1.0, 1.1, 1.2, and 1.3 for $S = 7$, 20, 31, and 61, respectively. The toroidal, poloidal, and total E_D from the $S = 7$ and 61 simulations are plotted as a function of time in figure 5.30. The role of the $n = 3$ mode also changes with increasing S. For low S, both the toroidal and

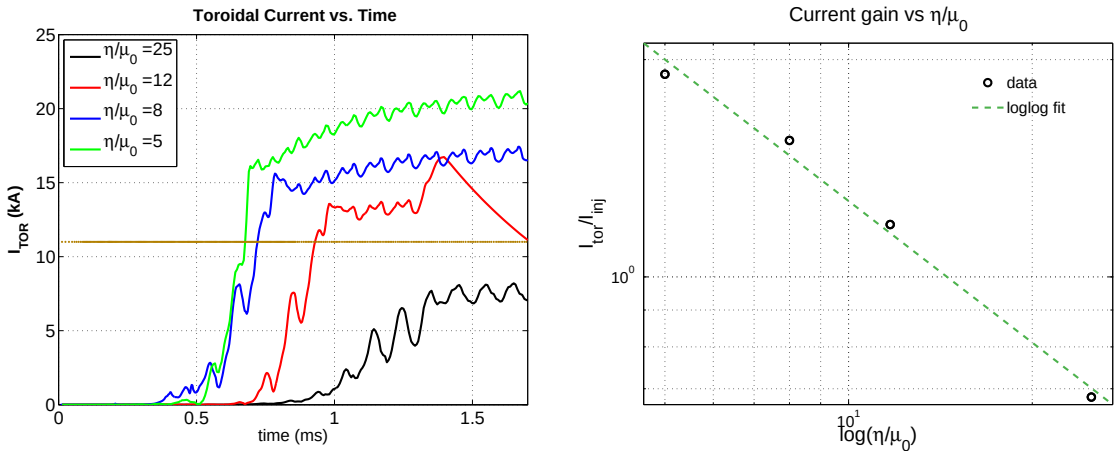

(a) Plasma current I_{tor} vs. time (ms) for various S

(b) $Log_{10}(I_{tor}/I_{inj})$ vs. $log_{10}(S)$

Figure 5.28: I_{tor} as a function of time and I_{tor}/I_{inj} as a function of η. (a) I_{tor} as a function of time from four simulations with different values of η/μ_0. The brown line again corresponds to the amplitude of I_{inj}. (b) A log-log plot of current amplification as a function of η indicates that the plasma current (and current amplification) scales approximately as $\eta^{-0.65}$ and $S^{1/2}$

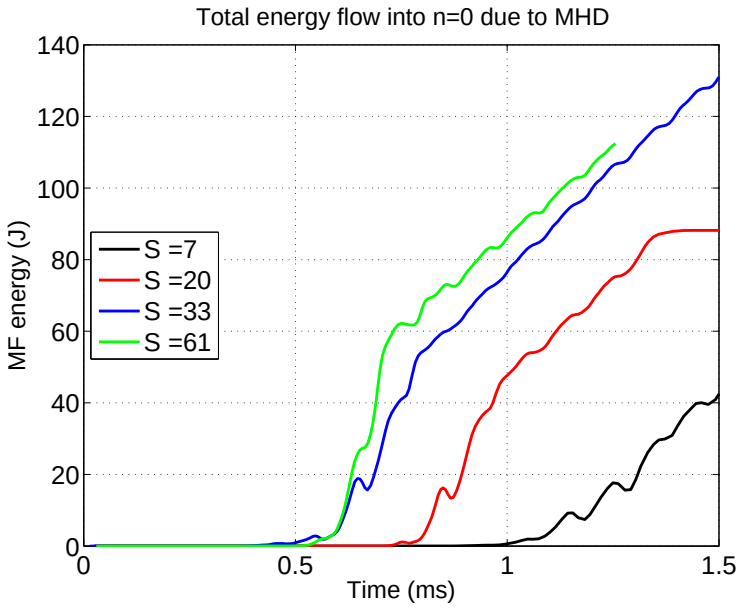

Figure 5.29: Total energy transfer into the $n = 0$ (E_D) from all the dynamo terms as a function of time(ms) from four simulations with different S. The MHD dynamo channels more energy into $n = 0$ as S is raised.

poloidal components of the $n = 3$ mode make positive contributions to the MF, as indicated by the running time integrals $\int \Omega^{(n)}_{MF} dt$ for $n = 1-3$ for the simulation with $S = 20$ plotted in figure 5.31(a). However, for higher S the $n = 3$ no longer helps sustain the toroidal MF but instead channels energy out of it. An example of this power reversal is shown for $S = 61$ in figure 5.31(b) where the energy transfer to the MF by the $n = 1 - 3$ fluctuation dynamo terms ($\int \Omega^{(n)}_{MF} dt$) are once again plotted. The role and necessity of the higher fluctuations ($n \geq 2$) in the dynamo process for amplifying and sustaining the MF is not well understood.

5.3.2 The λ_{inj} scan

λ_{inj} is defined as $\frac{I_{inj}}{\psi_{inj}}$ where μ_0 is absorbed into I_{inj} for brevity. The λ_{inj} scan uses the following values of λ_{inj}: 30, 24, 20, and 15 m^{-1}. Recall from section § 2.3 that

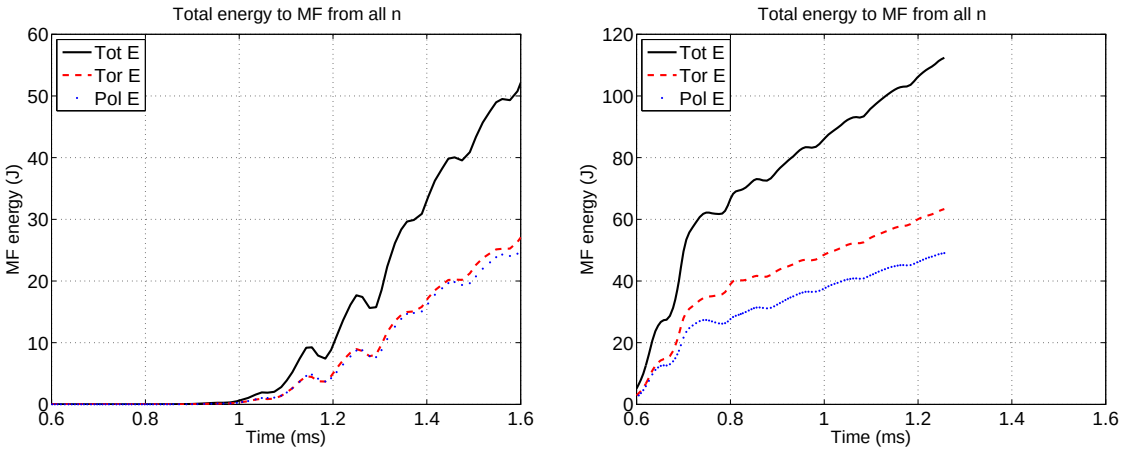

(a) E_D vs. time(ms) for $S = 7$

(b) E_D vs. time(ms) for $S = 61$

Figure 5.30: Breakdown of the dynamo-mediated energy transfer to the MF into toroidal (dashed red trace) and poloidal (dotted blue trace) components for (a) $S = 7$ and (b) 61. The solid black represents the sum of the two components, the total energy transfer to the MF by all dynamo terms. The dynamo energy is increasingly channeled into the toroidal MF as S increases.

the modeled injector geometry allows no solution with an eigenvalue $\lambda_{inj} < 24$ m^{-1}. This scan uses an improper scaling where the desired λ_{inj} is obtained by scaling the injector flux ψ_{inj} and current I_{inj} to satisfy $\frac{I_{inj}}{\psi_{inj}} = \lambda_{inj}$ while retaining the functional form corresponding to a solution of eqn. (2.16) with eigenvalue, $\lambda_{inj} = 30$ m^{-1}. This results in a (deliberate) mismatch between the eigenvalue λ_{inj} and its eigenvector as they appear in eqn. (2.15). For the remainder of this section, the proper unit of λ_{inj} is omitted.

It is important to understand how sensitive the calculations are to the improper scaling of λ_{inj}. A quantitative comparison between a simulation with a proper $\lambda_{inj} = 24$ and one with an improper $\lambda_{inj} = 24$ is presented below. The results show acceptable differences between the two cases and therefore, support the validity of the present λ_{inj}. The proper $\lambda_{inj} = 24$ solution requires a larger injector opening

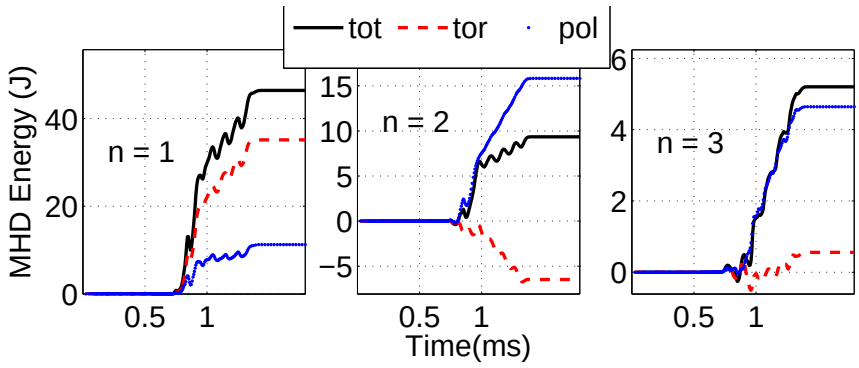

(a) $\int dt\Omega_{MF}^{(n=1-3)}$ vs. time(ms) for $S = 20$

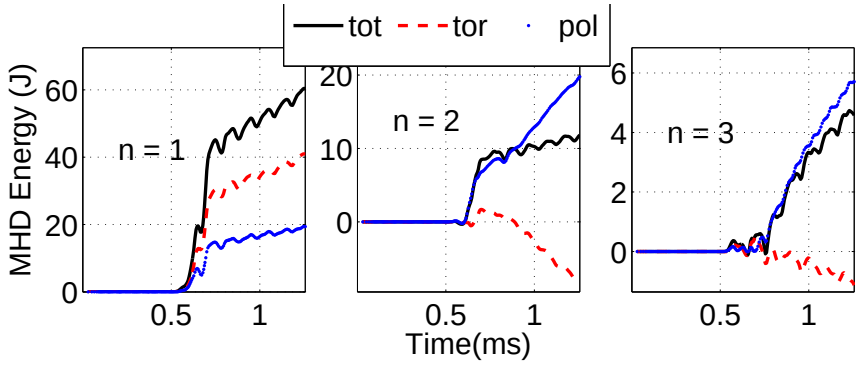

(b) $\int dt\Omega_{MF}^{(n=1-3)}$ vs. time(ms) for $S = 61$

Figure 5.31: Energy transfer into the MF by the $n = 1 - 3$ fluctuation dynamos ($\int dt\Omega_{MF}^{(n=1-3)}$) as a function of time in ms from (a) $S = 20$ and (b) $S = 61$, including a breakdown into the toroidal and poloidal components. The $n = 1$ is shwon on the left, the $n = 2$ in the center, and the $n = 3$ on the right. The dotted blue trace represents the contribution to the poloidal MF, the dashed red trace to the toroidal MF, and the solid black line to the total MF (sum of red and blue traces) from each n. The $n = 3$ dynamo transitions from sustaining the MF to opposing it as S is increased from 20 to 33.

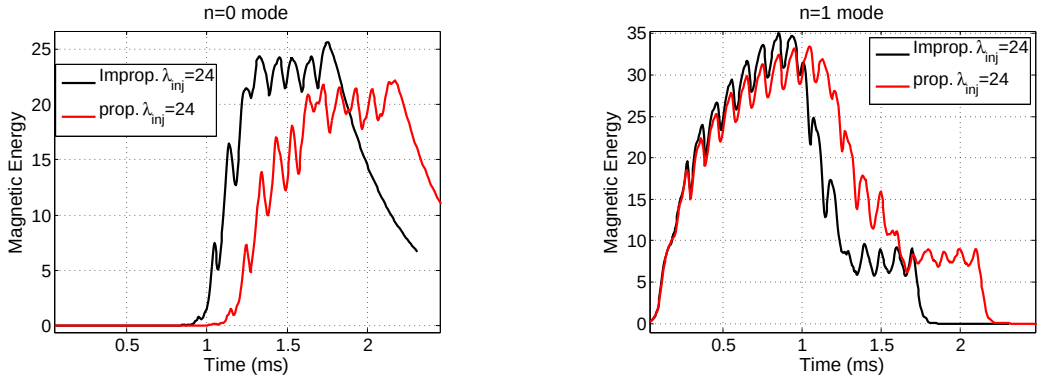

(a) $n = 0$ ME vs. time(ms)

(b) $n = 1$ ME vs. time(ms)

Figure 5.32: A comparison of the $n = 0$ (a) and $n = 1$ (b) magnetic energies between a simulation that uses a properly scaled λ_{inj} (red trace) and another that uses an improperly scaled λ_{inj} (black trace). $\lambda_{inj} = 24$ m^{-1} for both cases. The differences between the two approaches are small enough to justify conducting a λ_{inj} scan with an improperly scaled λ_{inj}.

than the one used for the improper $\lambda_{inj} = 24$ simulation. Both simulations employ the same injector flux and current to keep the rate of injected helicity the same, which is also equal to that used for $\lambda_{inj} = 30$ simulations. This requires the following injector settings: $\psi_{inj} = 0.52$ mWb and $I_{inj} = 9.9$ kA. Helicity injection rate, $\dot{K} = 2V_{inj}\psi_{inj} \propto 2I_{inj}\psi_{inj}$ since injector current and voltage are linearly proportional. The constraint of fixed $\dot{K}$ results in more injector flux and less current for $\lambda_{inj} = 24$ than for $\lambda_{inj} = 30$. The traces in figure 5.32 show the differences between proper and improper λ_{inj}. Mode saturation onsets one injector period sooner for the case with the improper $\lambda_{inj} = 24$ than proper λ_{inj}. The linear growth rates (not shown here) are approximately the same for both simulations ($\gamma\tau_A = 1.3$). The final amplitudes of the $n = 0$ ME and plasma current are within 10% each other. For both cases, $I_{tor}/I_{inj} \approx 1$ with $I_{tor} \simeq 10 - 10.5$ kA. The results are similar enough to justify carrying out the scan in λ_{inj} with an improperly scaled λ_{inj}.

The λ_{inj} scan is conducted in two ways: one where the injector current I_{inj} is

kept fixed and another where the injected helicity is kept fixed while λ_{inj} is lowered. The former approach leads to a greater $\dot{K}$ as ψ_{inj} needs to be raised to lower λ_{inj}, whereas the latter requires that I_{inj} and ψ_{inj} be adjusted simultaneously to keep $\dot{K}$ constant as is done above for the proper-improper λ_{inj} comparison. Results from the first approach are presented followed by brief comments on the outcome of the second approach.

The characteristics of the constant-I_{inj} λ_{inj} scan show a weak dependence on λ_{inj} for $\lambda_{inj} \geq 20$. The final amplitudes of $n = 0$ magnetic energy and I_{tor} do not deviate too far from the values observed for $\lambda_{inj} = 30$. However, as λ_{inj} is lowered from 30, the onset of mode growth is increasingly delayed belating the I_{tor} generation as indicated by the different rise times of I_{tor} in figure 5.33(a). Logarithm of the even magnetic modes in figure 5.33(b) show that the unstable modes go through a flat period for $\lambda_{inj} = 25$, while those of $\lambda_{inj} = 20$ undergo a brief decay prior to the linear growth phase. The 'severity' of the initial decay grows as λ_{inj} is decreased further until the $n = 0$ amplification completely shuts down at $\lambda_{inj} = 18$. For $\lambda_{inj} < 18$, no mode growth occurs as shown by the purely decaying traces of $\lambda_{inj} = 15$ (green) in figure 5.33(b) (The trace for $\lambda_{inj} = 18$ is not included in figure 5.33). Linear growth rates slow down as λ_{inj} decreases showing a monotonic decline: 45, 32, and 24 kHz for $\lambda_{inj} = 30$, 24, and 20, respectively (figure 5.33(b)). As a result, $n = 0$ amplification and I_{tor} generation take longer as λ_{inj} decreases.

This trend of delayed and gradually-lessening current amplification with decreasing λ_{inj} suggests that the helicity injection term of eqn. (1.16) varies with λ_{inj}. This term is proportional to Z_{inj}/λ_{inj} where Z_{inj} is the injector impedance. The fact that I_{tor}/I_{inj} decreases as λ_{inj} decreases implies that the injector impedance Z_{inj} has a stronger than linear dependence on λ_{inj}. For example, it was determined in §4.1.3 that $Z_{inj} \sim \lambda_{inj}^3$ for 2fl-MHD. When λ_{inj} is below the critical λ, denoted λ_c, the helicity dissipation overwhelms the helicity injection —eqn. (1.16) ends up with an imaginary square root— and no $n = 0$ amplification takes place. $\lambda_c = 18$ in this case.

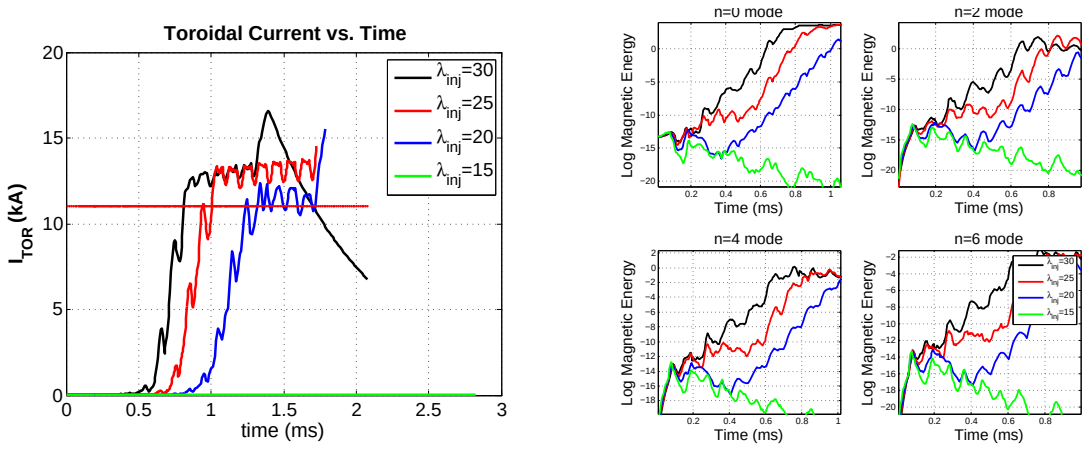

(a) $|I_{tor}|$ vs. time (ms)

(b) Logarithm of magnetic energy per even toroidal modes

Figure 5.33: (a) I_{tor} as a function of time for various λ_{inj}, (b) natural logarithm of magnetic energy per even-numbered toroidal modes for various λ_{inj}. The global quantities exhibit have a weak dependence on λ_{inj} for $\lambda_{inj} \geq 20$. However, for $\lambda_{inj} < 20$ no mode growth occurs.

λ_c also exhibits a weak dependence on η; partial scans indicate λ_c shifts to lower values as η decreases.

The constraint of fixed helicity injection rate ($\dot{K}_{inj}$) leads to less injected power than the fixed-I_{inj} constraint for the same λ_{inj}. This causes the fixed-$\dot{K}_{inj}$ λ_{inj} scan to underperform with respect to the fixed-I_{inj} λ_{inj} scan for the same values of λ_{inj}. Lower values of I_{tor}/I_{inj} are produced for matching values of λ_{inj}. Similar to the fixed-I_{inj} scan, linear growth rates slow down as λ_{inj} decreases. The absolute growth rates of the fixed-$\dot{K}_{inj}$ λ_{inj} scan are slower than those of the fixed-I_{inj} λ_{inj} scan. For $\lambda_{inj} = 24$ growth rates are approximately 24 kHz, 60% of those of the fixed-I_{inj} λ_{inj} scan while they drop to 12 kHz for $\lambda_{inj} = 20$, half of those of the fixed-I_{inj} λ_{inj} scan for the same λ_{inj}. $\lambda_c = 20$, slightly shifted upward in this case. At $\lambda_{inj} = 20$, I_{tor} generation is extremely delayed, occurring nearly at $t = 3$ ms, longer than average shot duration in HIT-SI.

5.3.3 Injector frequency (f_{inj}) scan

Results of the poloidal convergence studies in §5.1 indicate that meshes as coarse as 12×12 FE's with a high polynomial representation adequately capture the crucial features of the calculations like the growth rates, τ_f, the large energy exchange between the $n = 1$ and $n = 0$ modes, final saturation amplitudes, and I_{tor}. Therefore, the frequency scan is conducted with poloidal mesh comprising 12×12 biquartic ($pd = 4$) FE's. The chosen range in frequency extends from a frequency slower than the resistive diffusion time up to a frequency that exceeds the global Alfvén time: $f_{inj} = 0.5$, 2.5, 5, 15, and 30 kHz. The corresponding injector periods are 2, 0.4, 0.2, .067 and 0.033 ms. All other parameters for these simulations are identical. Recall from Table 5.2 that for $S = 20$, $\tau_{L/R} = 0.81$ ms and $\tau_A = 0.042$ ms for the baseline parameters. τ_A is a volume averaged-quantity that depends on the total magnetic energy, which exhibits a weak dependence on f_{inj}. In this case, τ_A speeds up by 5–10% with increasing f_{inj}.

Since the $n = 0$ amplification proceeds on Alfvénic time scales for rMHD, the characteristics are insensitive to f_{inj} for $\tau_A f_{inj} \ll 1$. In other words, so long as the injectors oscillate at a rate slow compared to τ_A, f_{inj} does not affect the saturated state. This is confirmed by the simulations with $f_{inj} = 0.5$, 2.5, and 5 kHz that exhibit similar linear growth rates and τ_f, yielding the same I_{tor} (black, red, and blue traces in figure 5.34(b)). For $\tau_A f_{inj} > 1$, no $n = 0$ amplification occurs because the injectors complete a cycle faster than the duration of reconnection between injector and spheromak fields. The calculation with $f_{inj} = 30$ kHz exemplifies such a case. Initially, it shows rapid mode growth that gets interrupted one injector cycle into the simulation. Beyond this point, all of the modes not directly driven by the injectors decay and I_{tor} never grows larger than a fraction of a kA. $f_{inj} = 15$ kHz represents the intermediate regime in f_{inj}, that is, $f_{inj}\tau_A \lesssim 1$ where some deviations from the low-f_{inj} behavior is observed. This calculation produces the same amount of I_{tor} as

the lower-f_{inj} simulations, but with a longer τ_f and slower growth rates (green traces in figure 5.34(b)). Cases with $f_{inj} = 15 - 30$ kHz deviate further from the low-f_{inj} trends with slower linear growth rates and increasingly longer τ_f. However, final I_{tor} remains unaffected since the helicity balance is independent of f_{inj}.

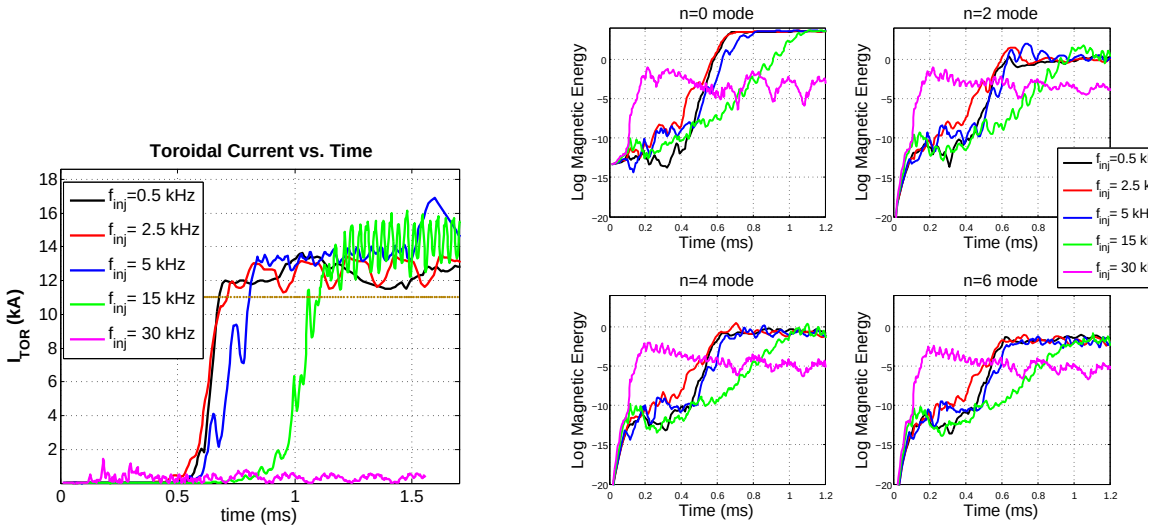

(a) I_{tor} vs. time (ms)

(b) Natural logarithm of the even magnetic energy modes vs. time

Figure 5.34: (a) I_{tor} as a function of time for different injector oscillations frequencies. No I_{tor} is generated for $f_{inj} = 30$ kHz ($\tau_A f_{inj} > 1$). (b) Log(ME) per even-numbered n as a function of time for the different f_{inj} cases shows an initial rapid mode growth for $f_{inj} = 30$ kHz that saturates before the $n = 0$ attains global scales. Lower frequencies all behave very similarly. Growth rates slow down for $f_{inj} > 5$ kHz as f_{inj} approaches 30 kHz.

Chapter 6

SUMMARY AND DISCUSSION

6.1 Summary of Present Research

The aim of this research project has been to validate 3-D extended MHD (xMHD) models and use them to study the relaxation dynamics of the HIT-SI spheromak. Both the single-fluid and two-fluid models have been applied. The models assume constant and uniform plasma density and temperature. The remaining equations describing the evolution of the plasma velocity and magnetic field are solved with NIMROD, an initial-value, 3-D extended MHD code. The helicity injectors of the experiment are modeled as non-axisymmetric oscillating flux and current boundary conditions on the toroidally-symmetric spheromak boundary that excludes the helicity injectors and diagnostic gap. The insulating wall of the experiment is approximated as a highly resistive thin edge layer. A very low-magnitude Taylor state is used as an initial condition for spheromak formation.

Both models capture the qualitative aspects of HIT-SI: an initial period dominated by injector fields ($n = 1$ toroidal symmetry) featuring linear growth of toroidally-even magnetic modes that is followed by a relaxation event, culminating in $n = 0$ amplification and generation of significant toroidally-symmetric plasma current I_{tor}. Both models show a robust convergence of results with respect to poloidal resolution. Two-fluid MHD (2fl-MHD) shows excellent convergence with respect to the toroidal resolution. Resistive MHD (rMHD) —the single-fluid model— is more sensitive to the toroidal resolution at the experimental parameters and requires a greater number of Fourier modes.

6.1.1 Summary of Validation Simulations

Results of rMHD and 2fl-MHD calculations have been compared to data from the HIT-SI experiment with the goal of validating each model. The validation simulations use physical parameters that match those of shot 122385 and four other similar shots with high current amplification ($I_{tor}/I_{inj} > 2.5$). The simulation results are compared mostly with the data from shot 122385. The following values of plasma resistivity η were used: $\eta/\mu_0 = 25$, 17.8, and 8.8 m^2/s corresponding to $T_e = 6$, 7.5, and 12 eV, respectively, for a deuterium plasma based on Spitzer resistivity. An additional two-fluid simulation with $T_e = 10$ eV was also run for 2fl-MHD. Results indicate that 2fl-MHD shows quantitative agreement with HIT-SI, confirming the original hypothesis that two-fluid effects are necessary for describing the HIT-SI experiment. 2fl-MHD yields the current amplification demonstrated by the experiment with similar formation times. Comparison of internal magnetic field measurements to simulations indicates 2fl-MHD reproduces an internal magnetic structure closely resembling that of HIT-SI. New validation metrics are used for assessing the agreement based on biorthogonal decomposition (BD) of the measured and simulated surface magnetic fields. In the absence of toroidal symmetry and a circular poloidal cross section, BD offers an effective alternative to Fourier decomposition for reducing large data sets to a few dominant spatio-temporal modes. BD shows, without a probe-by-probe comparison, that 2fl-MHD captures the dominant magnetic structures and the temporal behavior of these features better than rMHD. BD is the most efficient and conclusive analysis tool employed in this research for showing the necessity of two-fluid effects in describing HIT-SI and for validating models in general.

The rMHD model fails in demonstrating current amplification for $T_e = 6$ eV. For higher T_e, rMHD produces a final state that captures the qualitative features of HIT-SI, such as the amplification of the $n = 0$ and generation of significant I_{tor}. But, it underestimates the current amplification and yields much longer formation times.

6.1.2 Summary of Two-fluid MHD Simulations

Simulations with resistivities spanning a range from $\eta/\mu_0 = 25$ to 8.8 m^2/s, corresponding to $T_e = 6 - 12$ eV, show very similar spectral signatures (magnetic energy per toroidal mode). Scans indicate the following scaling for current amplification: $I_{tor}/I_{inj} \propto \eta^{-0.6}$. The general characteristics are robust to a wide range of viscosities. A partial λ_{inj}-scan indicates current amplification increases linearly with λ_{inj}, implying the injector impedance scales as λ_{inj}^2. Closed flux surfaces occupying a small volume appear intermittently for $T_e \geq 10$ eV. The duration and size of the closed flux region increases as η is lowered. This is a transient effect, as the lifetime of closed flux is very short compared to the resistive dissipation time of the plasma. The λ-profile becomes more uniform and less hollow as the simulations progress and the $n = 0$ component is magnified. Plots of λ and J indicate an alignment of the injector fields with the $n = 0$ fields upon the formation of the $n = 0$ component, consistent with the designed operation of the experiment. The magnetic field structure resembles that of a spheromak at certain times during an injector period; at other times, however, the injector fields dominate and fill up more of the volume. Fluctuation dynamo analysis indicates similar contributions to the $n = 0$ field from the MHD and Hall dynamos during stage II. During stage III, the $n = 0$ component is sustained mostly by the MHD dynamo as the Hall dynamo's contribution drops. The Hall dynamo eventually reverses and begins to take energy out of the $n = 0$ as η is raised.

6.1.3 Summary of Resistive MHD (rMHD) Simulations

Analysis of a baseline rMHD calculation representative of the characteristics of the single-fluid model shows an energy spectrum very similar to that observed in the validation rMHD simulations. Initially, there is large difference in energy between the $n = 0$ and $n = 1$ modes. Current amplification takes a long time ($1 \sim$ ms) because the $n = 0$ and other even-numbered are not directly coupled to the $n = 1$

source terms and only grow out of the MHD coupling between the $n = 0$ and $n = 1$ modes, whereas the Hall term in two-fluid MHD nonlinearly couples the $n = 1$ source terms. Plasma flow is mostly toroidally-symmetric during the $n = 1$ prevalence. The salient structures that appear here resemble those of the two-fluid model (J and λ). An alignment of the injector fields with the $n = 0$ fields upon the formation of the $n = 0$ component is observed. Single injector simulations are also performed to eliminate the injector cross-coupling. They show that the longevity of the injector channels (current-carrying injector fields) is determined by Aflvénic time scales and independent of f_{inj}. For a low f_{inj} such that $f_{inj}\tau_A \ll 1$ injector channels go kink-unstable and completely break apart.

Parameter scans of both operational and physical parameters have been carried out. The general characteristics are insensitive to operational variables like the injector phase, Φ_{inj} and the handedness of injected helicity. Handedness of injected helicity determines the handedness of the final configuration. A deviation from $|\Phi_{inj}| = 90°$ amplifies the fluctuations in the final $n = 0$ magnetic energy and I_{tor}, but the DC value remains insensitive to Φ_{inj}. Physical parameter scans indicate that I_{tor} grows with decreasing η and f_{inj}, and increasing λ_{inj}. The relation between I_{tor}/I_{inj} and $\eta(T_e)$ is found to be $I_{tor} \propto \eta^{-0.65} = T_e$, similar to the $\eta^{-1/2}$ scaling obtained from an analytic helicity balance model, but different from the $\eta^{-0.4}$-scaling observed in the validation simulations. Lowering λ_{inj} slows down the linear growth rates and reduces the current amplification. Under the constraint of fixed I_{inj}, no $n = 0$ amplification occurs for $\lambda_{inj} < 18$. The existence of a critical λ_{inj} where the transition from relaxation to no relaxation occurs is consistent with the helicity balance model. The cutoff in λ_{inj} varies with plasma resistivity and shows sensitivity to toroidal resolution. The relaxation event proceeds unencumbered for slow injector frequencies, i.e. $\tau_A\ f_{inj} \ll 1$. The $n = 1$ to $n = 0$ relaxation occurs increasingly later as $f_{inj}\tau_A$ nears unity. For $f_{inj}\tau_A > 1$, the injector state ($n = 1$) stays dominant and no $n = 0$ amplification takes place.

6.2 Recommendations for Future Work

The work presented here can be improved upon in several ways. A higher mass ratio, $\frac{m_i}{m_e} \geq 200$, should be simulated to check the convergence of the results further, which will require a 2fl-MHD simulation with at least 100×100 poloidal and 86 toroidal degrees of freedom. The calculations show an inward shifting of the magnetic axis with respect to the data, suggesting a more hollow current profile for the simulations. Prescribing the injector current and field profiles at the boundary, thereby fixing λ_{inj}, forces the same λ on the field lines of different length (inductance). This effect represents a worst case scenario for modeling the injectors and is believed to contribute to the hollowness of the current profile.

The full set of extended MHD equations must also be evolved including plasma density and pressure. A dynamic pressure can strongly affect the characteristics of relaxation. The suppressed internal magnetic fields of HIT-SI suggest a diamagnetic effect, likely due to a pressure gradient, which the present models cannot capture as they do not advance plasma pressure. Density boundary conditions matching experimentally-estimated plasma injection with sink and source terms must be formulated. The resulting density can be compared against chord-averaged measurements of electron density as a further validation test. Including radiative effects and neutral particle dynamics will also improve the predictive capability of the models because HIT-SI is possibly radiation- and very likely charge-exchange-dominated at low temperatures. Work is being undertaken by P. Nordgaard and U. Shumlak to incorporate the plasma-neutral fluid model introduced by Meier and Shumlak[71] into NIMROD that can eventually be used in HIT-SI simulations.

6.3 Scaling Study: 'Big HIT' Simulations

This is a proof-of-principle computational study of the relaxation physics of a hotter SIHI-driven spheromak in a geometry that is 2.5 times larger than the current

experiment. The goal is here to determine if SIHI can generate and sustain closed flux surfaces when the plasma is sufficiently hot. $\eta/\mu_0 = 0.71$ m^2/s, equivalent to $T_e = 110$ eV, ten-to-twenty times hotter than the cases simulated up to this point, but not hot enough for plasma ignition, which requires $\approx 5 - 10$ keV. The two-fluid scaling of current amplification yields $I_{tor}/I_{inj} = 10$ for the chosen temperature. Because of the larger geometry, the simulation uses more poloidal mesh points, 40×40 biquartic (4th order polynomial) FE's in the poloidal domain yielding a nodal spacing of less than 1 cm poloidally. To preserve computational resources, which were limited at the launch time of this simulation, only 11 Fourier modes are used. This results in a very coarse toroidal grid with a 2.5 times the toroidal cell size used in the validation simulations, $\Delta_\phi = 15$ cm at the magnetic axis. The coarseness in the toroidal direction may be unimportant since the nonlinear coupling of the $n = 1$ with itself due to the Hall term is the dominant effect in 2fl-MHD until the $n = 0$ becomes the dominant mode. The resistive diffusion time for this case is 88 ms, much longer than the average duration of a plasma shot in HIT-SI (2–10 ms).

The calculation exhibits the characteristic early dominance of the $n = 1$ mode followed by a large transfer of ME from $n = 1$ to $n = 0$ mode as shown in figure 6.1(a), which plots log base 10 of the magnetic energy per toroidal mode as a function of time in ms. The $n = 1$-dominated period ends at $t \approx 0.25$ ms. This is a much smaller fraction of the $\tau_{L/R}$ time than observed in the validation 2fl-MHD simulations. The $n = 0$ ME is greater than the $n = 1$ ME by two orders of magnitude ($\mathcal{O}(2)$), equivalent to a magnetic fluctuation level of 10%. The $n = 1$ ME is larger than the $n = 2$ by $\mathcal{O}(1)$. Because this is a high Lundquist number calculation, there is a notable lag between when relaxation occurs, marked by the large ME exchange between the $n = 1$ and $n = 0$ and when the $n = 0$ ME attains a steady state, which is expected to occur over $\tau_{L/R}/2$ (44 ms). The simulation has been run for 30 ms (nearly $450\tau_{inj}$) and continues to exhibit a gradual rise of the $n = 0$ ME. Figure 6.1(b) shows that I_{tor} grows steadily, tracking ME, but not as steeply since current goes as the square

root of energy (power). $I_{tor} \approx 200$ kA, corresponding to a $I_{tor}/I_{inj} = 10$, exactly as predicted by the two-fluid scaling law.

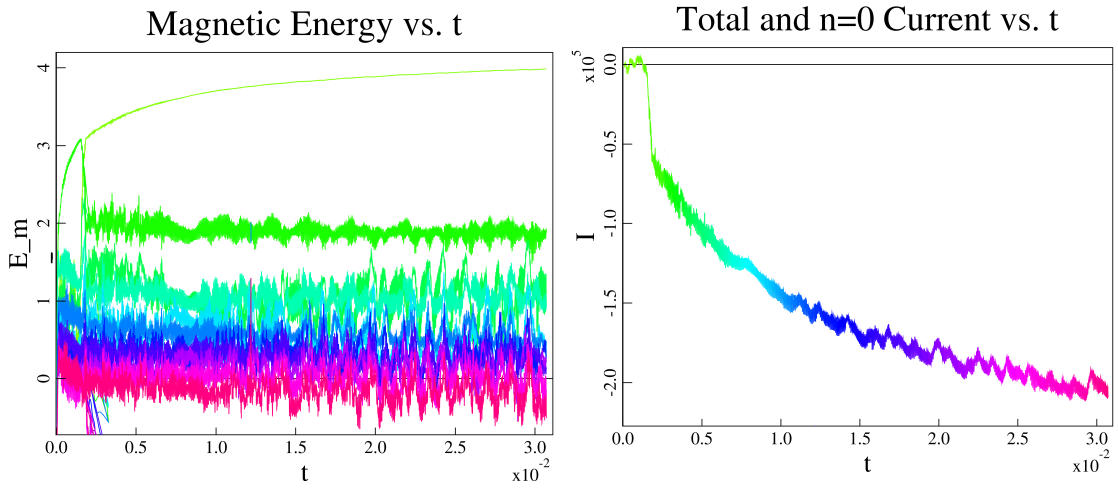

(a) $\log_{10}$ ME per toroidal mode n vs. time (ms)

(b) I_{tor} n vs. time (ms)

Figure 6.1: (a) Log_{10}(ME) per toroidal mode and (b) I_{tor} as a function of time (ms). The ratio of $n = 0$ to $n = 1$ ME is approximately 100, much higher than the ratios observed in the validation 2fl-MHD simulations. I_{tor} undergoes periodic sawtooth oscillations signaling an instability.

Both ME and I_{tor} experience oscillations resembling sawtooth[1, 72] activity, indicative of episodes of instability, signaled by the excursions of the toroidally-averaged rotational transform $\langle q \rangle$ above one. The maximum $\langle q \rangle$ as a function of time during the interval $t = 18 - 26$ ms in the simulation is shown in the lower half of figure 6.2, which displays the episodic behavior. The red line represents $\langle q \rangle = 1$. It is not clear why the instability has persisted up to a time when the profiles have become increasingly spheromak-like and stable. The increased activity in the $n = 2$ is thought to be the precursor for the instability, as it usually precedes the crash in I_{tor}.

The remarkable feature of this calculation is the closed flux surfaces that periodically appear and persist for multiple injector cycles. Figures 6.3(a) and 6.3(b) show Poincaré puncture plots through the $\phi = 0°$ plane at $t \approx 23$ ms in the simulation.

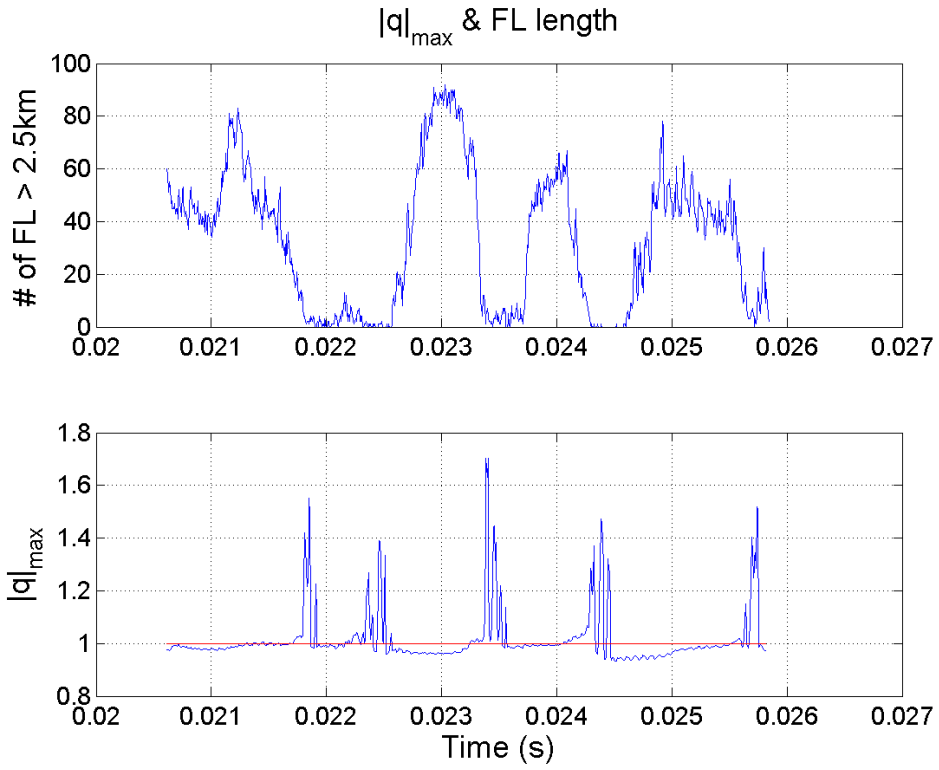

Figure 6.2: Top: history of the number of field lines longer than 2.5 km and bottom: $\langle q \rangle$ as a function of time (ms) during the interval $t = 18 - 26$ ms. Note the periods of long field lines coincide with stable periods, when $\langle q \rangle < 1$.

The maximum allowed field line length is set to 10 km and the maximum allowed number of punctures is set to 600, corresponding to a maximum field line length of about 3 km. A total of 361 field lines are launched from the vicinity of the magnetic axis, $(R, z) = (0.8125, 0.0)$ m. The existence and persistence of closed flux suggests that it is possible to sustain a configuration and generate closed surfaces required for plasma confinement with $\sim 10\%$ fluctuations. This is much greater fluctuation amplitude than previously thought possible for sustaining closed flux. The flux surfaces occur during times of stability when $\langle q \rangle < 1$. They are absent during other times when $\langle q \rangle > 1$. So far, the longest period of sustained closed flux has lasted roughly $20\tau_{inj} \approx 1.5$ ms, much shorter than $\tau_{L/R}$, which does not rule out the possibility that

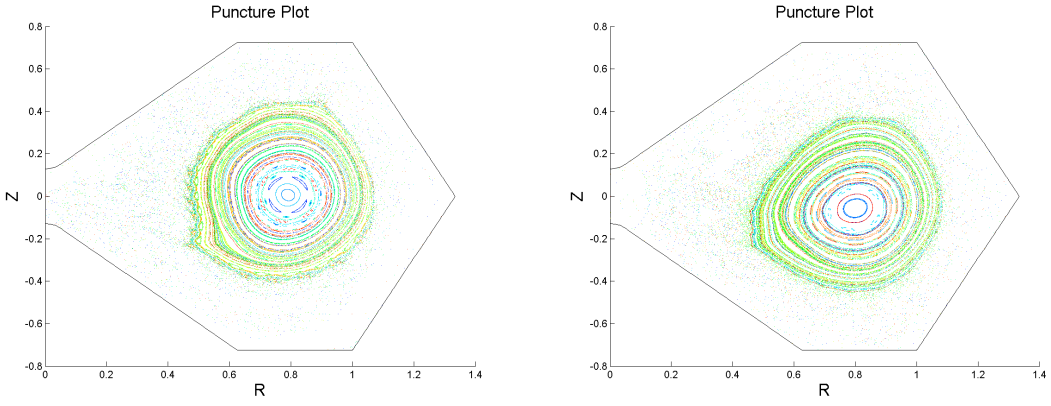

(a) Poincaré puncture plot at $t \approx 23$ ms (b) Poincaré puncture plot at $t \approx 23$ ms

Figure 6.3: Poincaré puncture plots at $t \approx 23$ ms through the $\phi = 0°$ plane, (a) is from time step $3.9{\times}10^5$ and (b) from $3.904{\times}10^5$. The distortions exhibited by the surfaces on the inboard side may be caused by IDCD [31]

this phenomenon could be an outcome of a transient magnetic reconnection event. However, the region of closed flux has grown in volume with I_{tor}, as has the duration of closure. In addition, the λ-profiles inside the flux surfaces look mostly uniform, implying current containment within this region, which is very encouraging. The top half of figure 6.2 shows the number of field lines longer than 2.5 km as a function of time during the interval $t = 18 - 26$ ms. The presence of a significant number of long field lines is synonymous with the existence of flux surfaces. Thus, the periods of long field lines coincide with stable periods. The puncture plots of figure 6.3 correspond to a time when the number of long field lines peaks at nearly 90, 1/4 of the total number of traced field lines. Figure 6.4 shows a 3-D trace of magnetic field lines at a time when $I_{tor}/I_{inj} = 9$. The red short lines are launched from one of the injector mouths. The blue lines are launched from several points near the magnetic axis ($R = 0.825$ m) and clearly trace the flux surfaces. There is a paper in the works by Jarboe *et al.* that is currently investigating the results of this simulation.

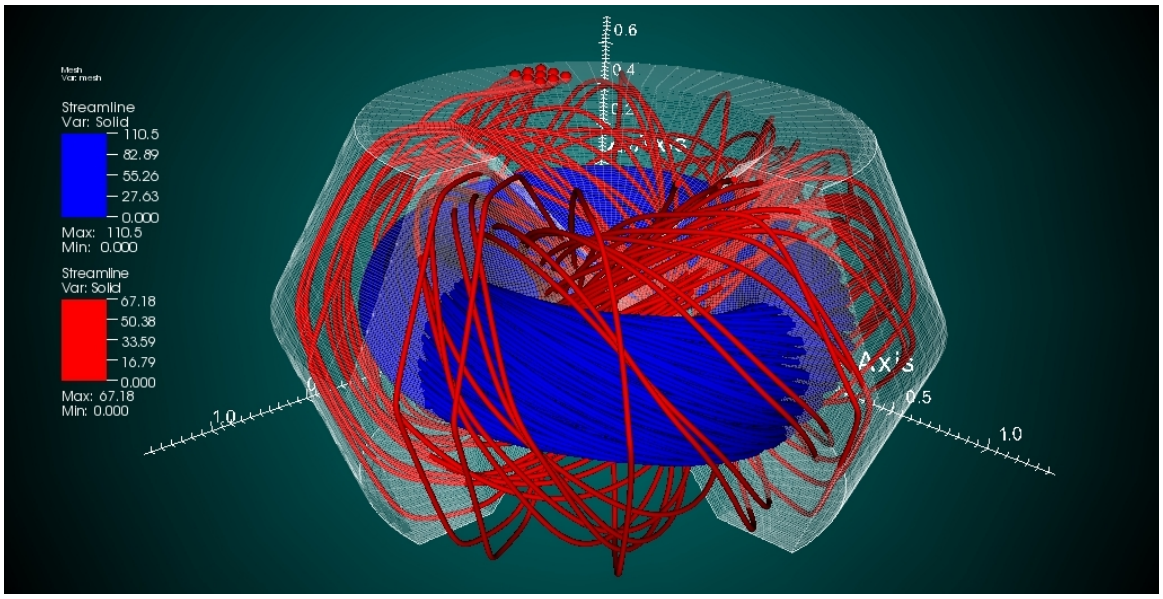

Figure 6.4: 3-D trace of magnetic field lines launched from one of the injector mouths (red lines) and from an array of points near the magnetic axis (blue lines). The blue lines are much longer and clearly isolated from the region directly driven by the injectors, represented by the red lines. This is from a time when $I_{tor}/I_{inj} = 9$.

BIBLIOGRAPHY

[1] J. Wesson. *Tokamaks*. Oxford University Press, 1987.

[2] Jeffrey P Freidberg. *Plasma physics and fusion energy*. Cambridge University Press, 2007.

[3] H. A. B. Bodin and A. A. Newton. Reversed-field-pinch research. *Nucl. Fusion*, 20:1255, 1980.

[4] Loren C. Steinhauer. Review of field-reversed configurations. *Phys. Plasmas*, 18:070501, 2011.

[5] L. Woltjer. A theorem on force-free magnetic fields. *Proceedings of the National Academy of Sciences of the United States of America*, 44(6):489, 1958.

[6] J.B. Taylor. Relaxation of toroidal plasma and generation of reverse magnetic fields. *Phys. Rev. Lett.*, 33:1129–1131, 1974.

[7] J.B. Taylor. Relaxation and magnetic reconnection in plasmas. *Rev. Mod. Phys.*, 58:741, 1986.

[8] T. R. Jarboe, W. T. Hamp, G. J. Marklin, B. A. Nelson, R. G. O'Neill, A. J. Redd, P. E. Sieck, R. J. Smith, and J. S. Wrobel. Spheromak formation by steady inductive helicity injection. *Phys. Rev. Lett.*, 97:115003, Sep 2006.

[9] T. R. Jarboe, A. R. Henins, I.and Sherwood, C. W. Barnes, and H. W. Hoida. Slow formation and sustainment of spheromaks by a coaxial magnetized plasma source. *Phys. Rev. Lett.*, 51:39, 1983.

[10] S. O. Knox, C. W. Barnes, G. J. Marklin, T. R. Jarboe, I. Henins, H. W. Hoida, and B. L. Wright. Observations of spheromak equilibria which differ from the minimum-energy state and have internal kink distortions. *Phys. Rev. Lett.*, 56:842, 1986.

[11] E. B. Hooper, L. D. Pearlstein, and R. H. Bulmer. Mhd equilibria in a spheromak sustained by coaxial helicity injection. *Nucl. Fus.*, 39:863, 1999.

[12] A.J. Redd, B. A. Nelson, T. R. Jarboe, P. Gu, R. Raman, R. J. Smith, and K. J. McCollam. Current drive experiments in the helicity injected torus (hit-ii). *Phys. Plasmas*, 9:2006, 2002.

[13] A. J. Redd, T. R. Jarboe, W. T. Hamp, B. A. Nelson, R. G. ONeill, and R. J. Smith. Flux amplification in helicity injected torus (hitii) coaxial helicity injection discharges. *Phys. Plasmas*, 15:022506, 2008.

[14] R. Raman, D. Mueller, T. R. Jarboe, B. A. Nelson, M. G. Bell, S. Gerhardt, B. LeBlanc, J. Menard, M. Ono, L. Roquemore, et al. Experimental demonstration of tokamak inductive flux saving by transient coaxial helicity injection on national spherical torus experiment. *Physics of Plasmas*, 18:092504, 2011.

[15] KF Schoenberg, JC Ingraham, CP Munson, PG Weber, DA Baker, RF Gribble, RB Howell, G Miller, WA Reass, AE Schofield, et al. Oscillating field current drive experiments in a reversed field pinch. *Physics of Fluids*, 31(8):2285–2291, 1988.

[16] K. J. McCollam, J. K. Anderson, A. P. Blair, D. Craig, D. J. Den Hartog, F. Ebrahimi, R. OConnell, J. A. Reusch, J. S. Sarff, H. D. Stephens, D. R. Stone, D. L. Brower, B. H. Deng, and W. X. Ding. Equilibrium evolution in oscillating-field current-drive experiments. *Phys. Plasmas*, 17:082506, 2010.

[17] T.R. Jarboe, C. Akcay, M.A. Chilenski, D.A. Ennis, C.J. Hansen, N.K. Hicks, R.Z. Aboul Hosn, A.C. Hossack, G.J. Marklin, B.A. Nelson, R.G. O'Neill, P.E. Sieck, R.J. Smith, B.S. Victor, J.S. Wrobel, and M. Nagata. Recent results from the hit-si experiment. *Nuclear Fusion*, 51(6):063029, 2011.

[18] T.R. Jarboe. Review of spheromak research. *Plasma Phys. and Control. Fusion*, 36:945, 1994.

[19] F. Ebrahimi, S. C. Prager, J. S. Sarff, and J. C. Wright. The three-dimensional magnetohydrodynamics of ac helicity injection in the reversed field pinch. *Phys. of Plasmas*, 10:999, 2003.

[20] E. B Hooper, B. I. Cohen, H. S. McLean, R. D. Wood, C. A. Romero-Talamas, and C. R. Sovinec. NIMROD resistive magnetohydrodynamic simulations of spheromak physics. *Phys. Plasmas*, 15:032502, 2008.

[21] R.D. Milroy, C.C. Kim, and C.R. Sovinec. Extended magnetohydrodynamic simulations of field-reversed configurations formation and sustainment with rotating magnetic field current drive. *Phys. Plasmas*, 17:062502, 2010.

[22] JB O'Bryan, CR Sovinec, and TM Bird. Simulation of current-filament dynamics and relaxation in the pegasus spherical tokamak. *Physics of Plasmas*, 19(8):080701, 2012.

[23] T. Gray, VS Lukin, MR Brown, and CD Cothran. Three-dimensional reconnection and relaxation of merging spheromak plasmas. *Physics of plasmas*, 17:102106, 2010.

[24] C. R. Sovinec, J. M. Finn, and D. del Castillo-Negrete. Formation and sustainment of electrostatically driven spheromaks in the resistive magnetohydrodynamic model. *Phys. Plasmas*, 8:475, 2001.

[25] Pablo Luis García-Martínez and Ricardo Farengo. Spheromak formation and sustainment by tangential boundary flows. *Physics of Plasmas*, 17:050701, 2010.

[26] V.A. Izzo. Ph.D. Dissertation, University of Washington, Seattle, WA, 2006.

[27] V.A. Izzo and T.R. Jarboe. Three-dimensional magnetohydrodynamic simulations of the Helicity Injected Torus with steady inductive drive. *Phys. of Plasmas*, 12:056109, 2005.

[28] C. R. Sovinec, A. H. Glasser, T. A. Gianakon, D. C. Barnes, R. A. Nebel, S. E. Kruger, D. D. Schnack, S. J. Plimpton, A. Tarditi, and M. S. Chu. Nonlinear magnetohydrodynamics simulation using high-order finite elements. *J. Comput. Phys.*, 195(1):355–386, March 2004.

[29] C. R. Sovinec, D. D. Schnack, A. Y. Pankin, D. P. Brennan, H. Tian, D. C. Barnes, S. E. Kruger, E. D. Held, C. C. Kim, X. S. Li, D. K. Kaushik, S. C. Jardin, and the NIMROD Team. Nonlinear extended magnetohydrodynamics simulation using high-order finite elements. *Journal of Physics: Conference Series*, 16(1):25, 2005.

[30] C. Sovinec and et al. Nonlinear extended magnetohydrodynamics simulation using high-order finite elements. *J. Phys.: Conf. Series*, 16:25, 2010.

[31] TR Jarboe, BS Victor, BA Nelson, CJ Hansen, C. Akcay, DA Ennis, NK Hicks, AC Hossack, GJ Marklin, and RJ Smith. Imposed-dynamo current drive. *Nuclear Fusion*, 52(8):083017, 2012.

[32] B. S. Victor, T. R. Jarboe, A. C. Hossack, D. A. Ennis, B. A. Nelson, R. J. Smith, C. Akcay, C. J. Hansen, G. J. Marklin, N. K. Hicks, and J. S. Wrobel. Evidence for separatrix formation and sustainment with steady inductive helicity injection. *Phys. Rev. Lett.*, 107:165005, Oct 2011.

[33] F. F. Chen and M. A. Lieberman. *Introduction to plasma physics and controlled fusion/Francis F.* : Plenum Press, New York, 1984.

[34] Paul Murray Bellan. *Fundamentals of plasma physics*. Cambridge University Press, 2006.

[35] M Kruskal and JL Tuck. The instability of a pinched fluid with a longitudinal magnetic field. *Proceedings of the Royal Society of London. Series A. Mathematical and Physical Sciences*, 245(1241):222–237, 1958.

[36] VD Shafranov. The stability of a cylindrical gaseous conductor in a magnetic field. *Atomic Energy*, 1(5):709–713, 1956.

[37] P.M. Bellan. *Spheromaks*. World Scientific Publishing Company, first edition edition, 2000.

[38] G. Bateman. *MHD Instabilities*. MIT Press, 1978.

[39] U. Shumlak and T.R. Jarboe. Stable high beta spheromak equilibria using concave flux conservers. *Phys. of Plasmas*, 7:2959, 2000.

[40] T. R. Jarboe, F. J. Wysocki, J. C. Fernandez, I. Henins, and G. J. Marklin. Progress with energy confinement time in the ctx spheromak. *Physics of Fluids B: Plasma Physics*, 2:1342, 1990.

[41] J.M. Finn and T.M. Antonsen. *Commts on Plasma Phys. and Control. Fusion*, 9:3, 1985.

[42] R C Duck, P K Browning, G Cunningham, S J Gee, A al Karkhy, R Martin, and M G Rusbridge. Structure of the n = 1 mode responsible for relaxation and current drive during sustainment of the sphex spheromak. *Plasma Physics and Controlled Fusion*, 39(5):715, 1997.

[43] D. A. Ennis, B. S. Victor, J. S. Wrobel, C. Akcay, T. R. Jarboe, G. J. Marklin, B. A. Nelson, and R. J. Smith. New understandings and achievements from independent-injector drive experiments on HIT-SI. *Nucl. Fus.*, 50:072001, 2010.

[44] P. Sieck. Ph.D. Dissertation, University of Washington, Seattle, WA, 2006.

[45] R. G. O'Neill, G. J. Marklin, T. R. Jarboe, C. Akcay, W. T. Hamp, B. A. Nelson, A. J. Redd, R. J. Smith, B. T. Stewart, J. S. Wrobel, and P. E. Sieck. A fully relaxed helicity balance model for an inductively driven spheromak. *Phys. Plasmas*, 14:112304, 2007.

[46] J. S. Wrobel, C. J. Hansen, T. R. Jarboe, R. J. Smith, A. C. Hossack, B. A. Nelson, G. J. Marklin, D. A. Ennis, C. Akcay, and B. S. Victor. Relaxation-time measurement via a time-dependent helicity balance model. *Physics of Plasmas*, 20:012503, 2013.

[47] Jonathan Wrobel. Ph.D. Dissertation, University of Washington, Seattle, WA, 2011.

[48] Brian S Victor, Thomas R Jarboe, Aaron C Hossack, David A Ennis, Brian A Nelson, Chris J Hansen, and Jonathan S Wrobel. Advances in steady inductive helicity injection for plasma startup and toroidal current drive. *IEEJ Transactions on Fundamentals and Materials*, 132(7):472–476, 2012.

[49] C. Akcay, C. C. Kim, B. S. Victor, and T. R. Jarboe. Validation of single-fluid and two-fluid magnetohydrodynamic models of the helicity injected torus spheromak experiment with the nimrod code. *Physics of plasmas*, 2013.

[50] Visualize it visualization software. `https://wci.llnl.gov/codes/visit`.

[51] C. R. Sovinec and J. R. King. Analysis of a mixed semi-implicit/implicit algorithm for low-frequency two-fluid plasma modeling. *Journal of Computational Physics*, 229(16):5803 – 5819, 2010.

[52] V. S. Lukin. *Computational Study of Internal Kink Mode Evolution and Associated Magnetic Reconnection Phenomena*. Ph.D. Dissertation, Princeton University, Princeton, NJ, 2008.

[53] B Srinivasan and U Shumlak. Analytical and computational study of the ideal full two-fluid plasma model and asymptotic approximations for hall-magnetohydrodynamics. *Physics of Plasmas*, 18:092113, 2011.

[54] S.I. Braginskii. Transport processes in a plasma. *Reviews of Plasma Physics*, 1:205, 1965. (Consultants Bureau, New York, 1965).

[55] EN Parker. Sweet's mechanism for merging magnetic fields in conducting fluids. *Journal of Geophysical Research*, 62(4):509–520, 1957.

[56] PA Sweet. Electromagnetic phenomena in cosmical physics. In *Symposium (International Astronomical Union) No*, volume 6, page 123, 1958.

[57] D. D. Schnack, D. C. Barnes, Z. Mikic, D. S. Harned, and E. J. Caramana. Semi-implicit magnetohydrodynamic calculations. *Journal of Computational Physics*, 70(2):330 – 354, 1987.

[58] Douglas S Harned and D.D Schnack. Semi-implicit method for long time scale magnetohydrodynamic computations in three dimensions. *Journal of Computational Physics*, 65(1):57 – 70, 1986.

[59] H. Nowacki, M.I.G. Bloor, and B. Oleksiewicz. *Computational geometry for ships*. World Scientific Publishing, 1995.

[60] Matlab software. `http://www.mathworks.com/products/matlab`.

[61] CA Romero-Talamas, EB Hooper, R Jayakumar, HS McLean, RD Wood, and JM Moller. Measurements and phenomenological modeling of magnetic flux buildup in spheromak plasmas. *Physics of Plasmas*, 15:042503, 2008.

[62] B. I. Cohen, A. Romero-Talamas, D. D. Ryutov, E. B. Hooper, L. L. LoDestro, H. S. McLean, T. L. Stewart, and R. D. Wood. The role of the n=1 column mode in spheromak formation. *Phys. Plasmas*, 16:042501, 2009.

[63] T.D. Dudok de Wit, A.L. Pecquet, J.C. Vallet, and R. Lima. The biorthogonal decomposition as a tool for investigating fluctuations in plasmas. *Physics of plasmas*, 1:3288, 1994.

[64] N. Aubry, R. Guyonnet, and R. Lima. Spatiotemporal analysis of complex signals: theory and applications. *Journal of Statistical Physics*, 64(3):683–739, 1991.

[65] T. R. Jarboe. The spheromak confinement device. *Physics of plasmas*, 12:058103, 2005.

[66] V.A. Izzo W.T. Hamp B.A. Nelson R.G. O'Neill A.J. Redd P. Sieck, T.R. Jarboe, R.J. Smith, and et al. Demonstration of steady inductive helicity injection. *Nucl. Fus.*, 46:256, 2006.

[67] Thomas R Jarboe. Steady inductive helicity injection and its application to a high-beta spheromak. *Fusion technology*, 36(1):85–91, 1999.

[68] T. G. Cowling. *Monthly Notices Roy. Astron. Soc.*, 94:39, 1934.

[69] Y.L. Ho and G.G. Craddock. Nonlinear dynamics of field maintenance and quasiperiodic relaxation in reversed-field pinches. *Phys. Fluids B*, 3:721, 1991.

[70] C. R. Sovinec J. M. Reynolds and S. C. Prager. Nonlinear magnetohydrodynamics of pulsed parallel current drive in reversed-field pinches. *Phys. Plasmas*, 15:062512, 2008.

[71] E. T. Meier and U. Shumlak. A general nonlinear fluid model for reacting plasma-neutral mixtures. *Physics of Plasmas*, 19:072508, 2012.

[72] I. T. Chapman. Controlling sawtooth oscillations in tokamak plasmas. *Plasma Physics and Controlled Fusion*, 53(1):013001, 2011.

Appendix A

APPENDICES

A.1 Additional derivations

It is said that assuming the surface potential used in current injection to have the same functional form as the normal magnetic field B_z results in a constant λ_{inj} across the injector mouths. This can be seen by integrating $\lambda(\psi)\mathbf{B} = \mu_0\mathbf{J}$ along $\hat{z}$ inside the resistive layer for a constant λ.

$$\begin{aligned} \lambda \int \mathbf{B}\cdot d\mathbf{z} = \lambda B_z \delta &= \mu_0 \int \mathbf{J}\cdot d\mathbf{z} = \frac{\mu_0}{\eta_{edge}} \int \mathbf{E}\cdot d\mathbf{z} = \frac{\mu_0}{\eta_{edge}} V_{inj}, \\ \lambda &= \frac{\mu_0 V_{inj}}{\eta_{edge} B_z \delta}, \end{aligned} \tag{A.1}$$

where $\delta = 1$ mm is the thickness of the resistive edge, V_{inj} is the applied voltage function to drive the current and η_{edge} is the edge resistivity. Here we use the fact that Ohm's law is completely dominated by $\mathbf{E} = \eta\mathbf{J}$ inside the resistive layer because of high edge resistivity and zero flow BC. Solving eqn. (A.1) for V_{inj} shows that in order to have constant λ_{inj} V_{inj} must indeed have the same spatial form as B_z,

$$V_{inj} = \underbrace{\frac{\lambda_{inj}\eta_{edge}\delta}{\mu_0}}_{\text{constants}} B_z. \tag{A.2}$$

For $\lambda_{inj} = 30$ m^{-1}, $\frac{\mu_0}{\eta_{edge}} \simeq 10^6$ and $\delta = 0.001$ m, the amplitude of V_{inj} comes out $\sim 3 \times 10^5$ greater than that of B_z. This is consistent with the inputs required for B_z and I_{inj} in nimrod.in.

A.2 NIMROD Calibration of the Synthetic Surface Magnetic Diagnostics

HIT-SI achieves surface magnetic measurements by the use of a series of surface magnetic probes (SPs) forming four Amperian arrays surrounding the poloidal plane at the four toroidal locations, $\theta = 0, 45, 180, 225$ degrees. Here a distinction is made between the HIT-SI azimuthal coordinate θ is in a cylindrical coordinate system and the periodic coordinate ϕ in NIMROD's left-handed toroidal coordinate system. This is because $\phi = -\theta$ and this detail matters when one is trying to align synthetic probes from the simulations with the real probes from the experiment. The line along $\theta = 0$ and 180 bisects the X injector mouths. Each Amperian loop comprises 18 SP's, 8 on the small cone labeled S01-08 and 10 on the large cone denoted L10-L01 going clockwise around the poloidal plane. Figure A.1 shows the poloidal and toroidal layout of the Amperian arrays. The probes labeled L06 and L05 are not included in the NIMROD calibration calculations as these probes measure magnetic fields that creep into the diagnostic gap, which is excluded from the simulated geometry.

Three separate NIMROD calculations are performed to carry out the calibration of the synthetic SP's. All three calculations simulate flux-only vacuum shots of the experiment. First simulation only injects normal magnetic field (B_z) through the lower (X injector) boundary, the second simulation through the upper (Y injector) boundary and finally, the third that applies a B_z for both X and Y injectors. The amplitude of B_z is adjusted to produce $\psi_{inj} = 1$ mWb. The normal current is set to zero for all three simulations. To simulate a vacuum environment–NIMROD assumes fully ionized plasmas–the background plasma resistivity is set to a very large number, $\eta/\mu_0 = 4.7{\times}10^5$ m^2/s, yielding a resistive diffusion time of 22 ns, by far the fastest time scale in these injector flux-only, vacuum simulations. The calculations use a 48×48 mesh with bicubic ($pd = 3$) FE's. They are run for about 1.2-1.3 ms, corresponding to approximately 12-14 injector cycles. Figure A.2 shows the locations of the synthetic

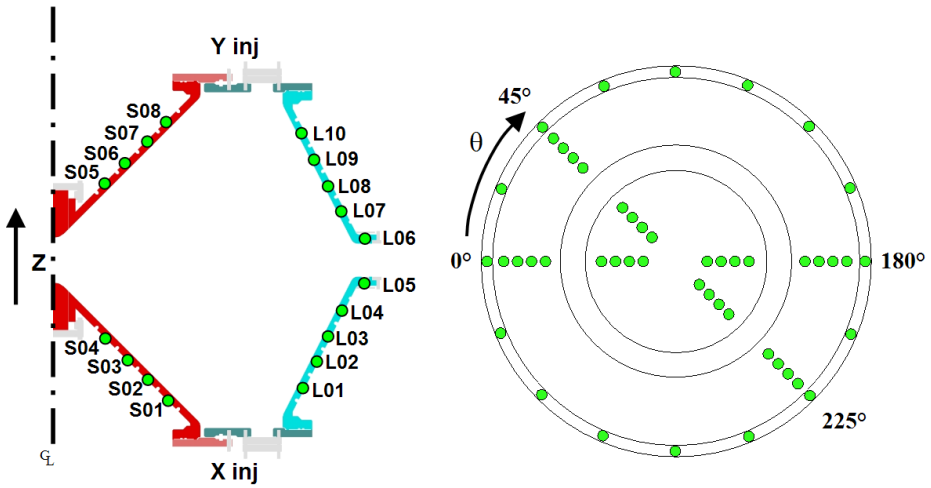

Figure A.1: The poloidal and toroidal layout of the HIT-SI surface magnetic probes. There is an array of 18 SP's at each toroidal location forming an Amperian loop. In addition to making local measurements of **B**, the Amperian arrays make measurements of the toroidally localized plasma current (I_{tor}) enclosed within the SP arrays.

and real SP's. The slight mismatch along the inner cone is due to a difference in the dimensions between the simulated and experimental geometries. But, the difference is small and has no real impact on the results or this current exercise. The mismatch can worsen or improve depending on the poloidal resolution.

Proper comparison of NIMROD and HIT-SI probe signals requires correctly matching the phases of both signals, which in turn requires matching the time bases of the simulation and experiment. The criterion we use for matching the time bases is based on locating a maximum of the HIT-SI injector flux in time and calculating the difference in time between the occurrence of this maximum and a maximum of the simulated injector flux. This offset in time is then added to the time base of HIT-SI SP signals. Figures A.3(a) and A.3(b) indicate the accuracy of the time-base matching for X flux-only and Y flux-only vacuum cases. The slight differences in the amplitude of the actual injector flux and NIMROD-generated flux waveforms are due to the complex nature of the way the flux is generated in the experiment.

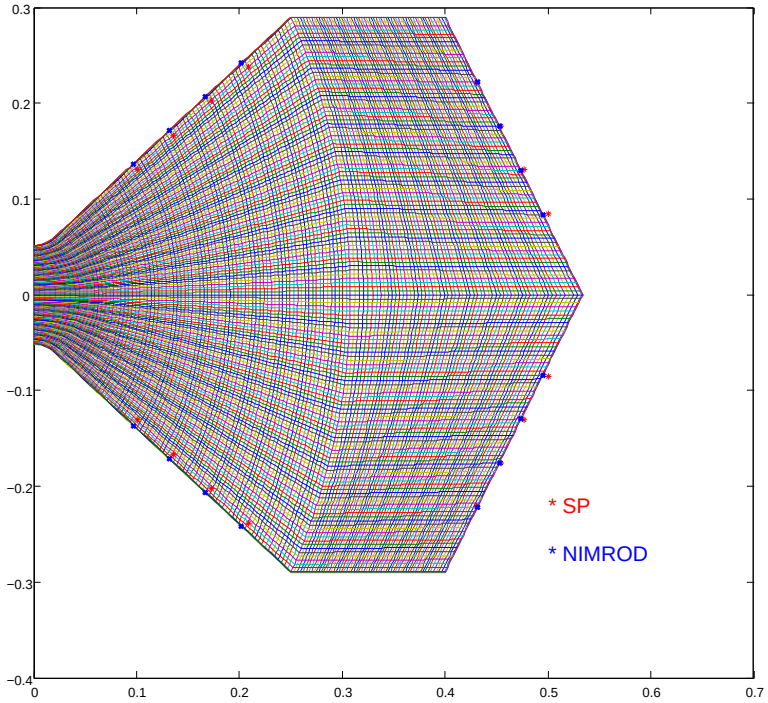

Figure A.2: Locations of the synthetic probes compared to those of the actual HIT-SI SP's

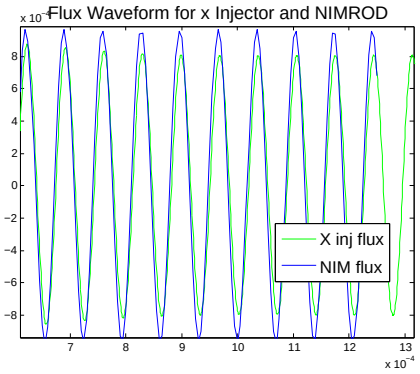

(a) Time base matching for X-only flux simulation

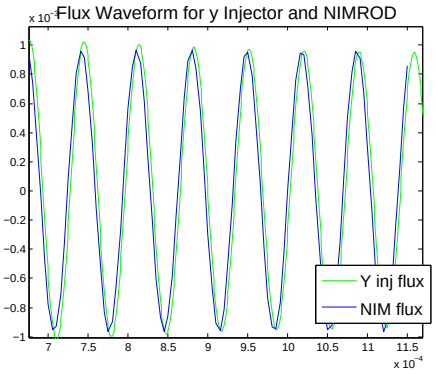

(b) Time base matching for Y-only flux simulation

Figure A.3: Time base matching between the experimental data and simulations using (a) X- and (b) Y-injector flux waveforms.

Each probe signal is plotted in a separate panel beginning with the probe denoted S01, located on the inboard side, right above the midplane (see figure A.1 for a layout of the probes). The panels track the probes in a clockwise direction in the poloidal plane as they go from left to right and top to bottom. Thus, topmost row of panels corresponds to SP's S05-S08, second row to L10-L07, third row to L04-L01 and the final row to S01-S04 respectively. Panels corresponding to 'dead' experimental probes are omitted from the plots. Each panel is named after the SP whose signal is plotted. For example, B_S01P045 means a poloidal field (P) measurement by probe number 01 on the small cone (S) along the Ampérian array located at $\theta = 45°$.

The flux-only calculations by NIMROD capture the symmetry of the vacuum fields very accurately. It is helpful to look at SP signals from $0 - 180°$ and $45 - 225°$ arrays together to see this symmetry. For example, for the X-injector-only simulation, NIMROD shows no toroidal field (B_ϕ) along the 0 and 180-degree Ampérian arrays as these poloidal arrays bisect the X injector mouths and therefore, only register purely poloidal fields (figures A.4 and A.5). Visible in the HIT-SI probe signals in these figures are also some noise pickup due to injector coils and drift effects. The $n = 1$ toroidal symmetry of the injected vacuum magnetic field requires the poloidal fields (B_θ) along $0 - 180°$, and $45 - 225°$ arrays, and B_ϕ along $\theta = 45°$ and $225°$ to be equal and opposite, in other words completely out of phase. Again the NIMROD calculation captures these anti-symmetric features very well as the synthetic probe signals show in figures A.6 through A.8. We see similar symmetries in $\mathbf{B}$ for the Y injector-only simulation. Because the magnetic field in the (R, θ) plane is now rotated 90 degrees, $\mathbf{B}$ should be purely toroidal, and equal and opposite along $0 - 180°$ arrays as confirmed by the synthetic probe traces at $\theta = 0°$ and $180°$ (figures A.9 and A.10). Similarly, B_ϕ and B_θ at $45°$ and $225°$ arrays are equal and opposite as the NIMROD output shows.

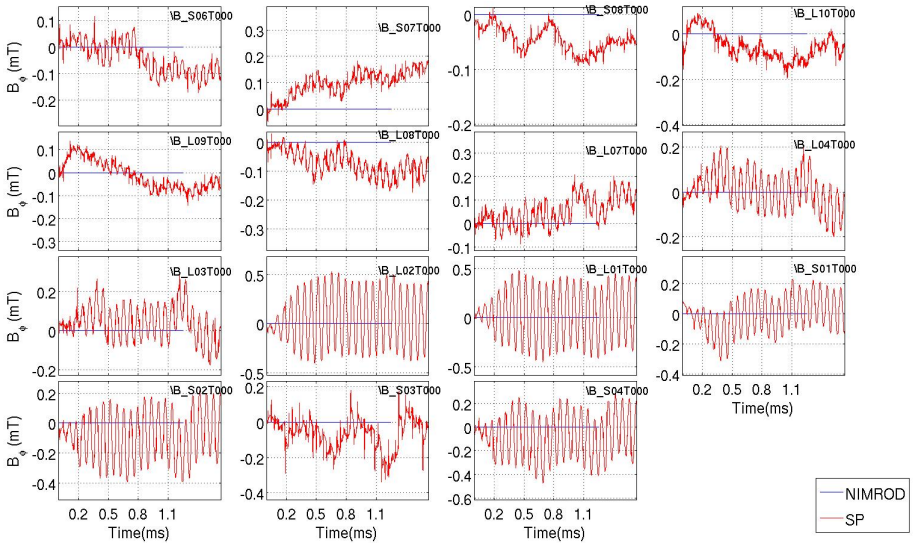

Figure A.4: Comparison of vacuum toroidal magnetic fields for an X injector-only flux shot as measured by the HIT-SI surface probes and simulated by NIMROD at $\theta = 0$ toroidal location (see figure A.1)

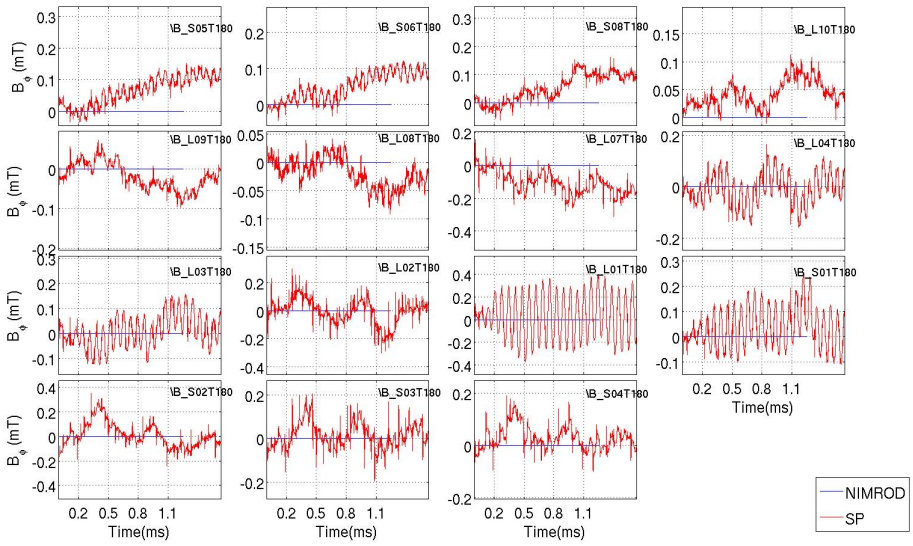

Figure A.5: Comparison of vacuum toroidal magnetic fields for an X injector-only flux shot as measured by the HIT-SI surface probes and simulated by NIMROD at $\theta = 180$ toroidal location (see figure A.1)

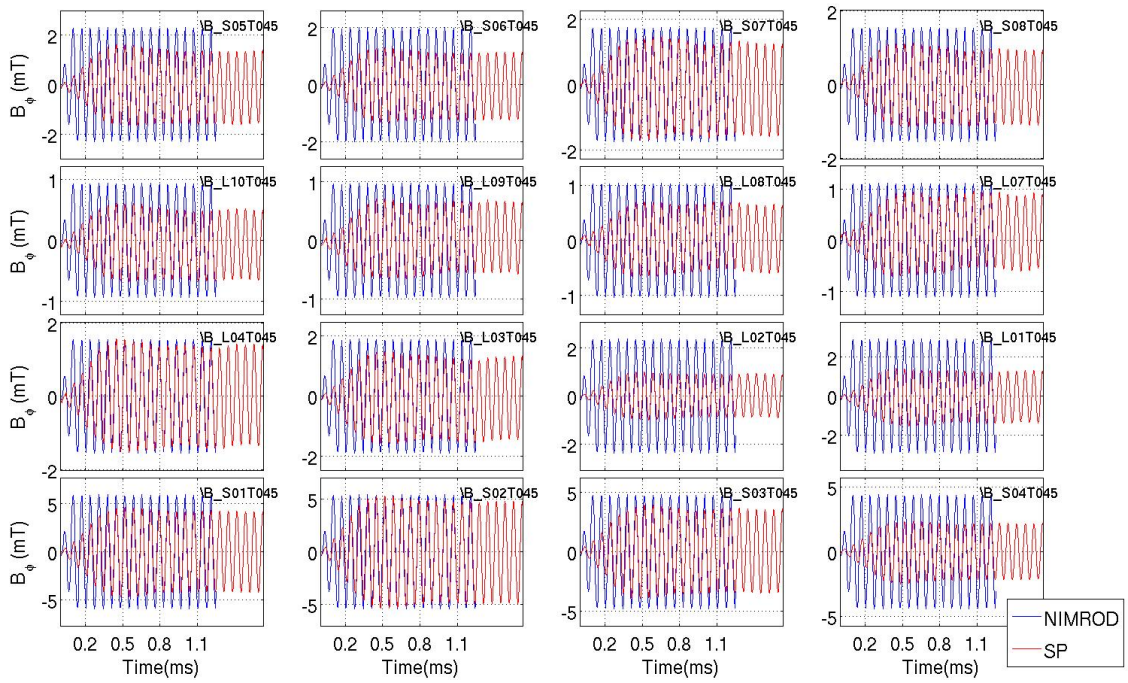

Figure A.6: Comparison of vacuum toroidal magnetic fields for an X injector-only flux shot as measured by the HIT-SI surface probes and simulated by NIMROD at $\theta = 45$ toroidal location (see figure A.1)

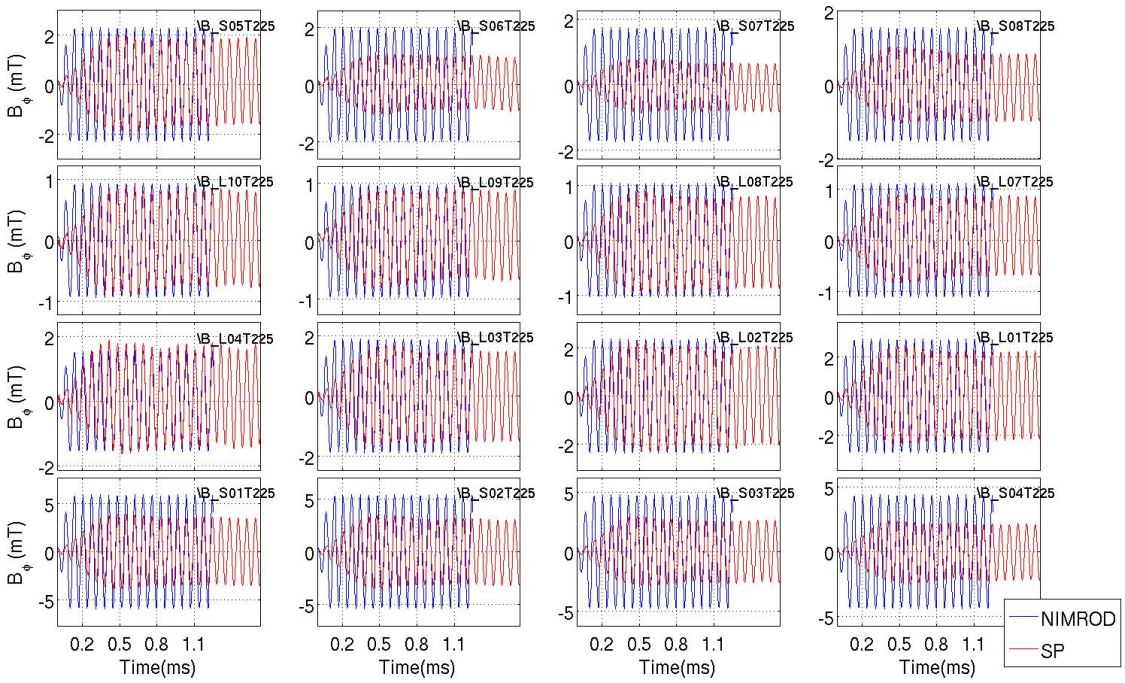

Figure A.7: Comparison of vacuum toroidal magnetic fields for an X injector-only flux shot as measured by the HIT-SI surface probes and simulated by NIMROD at $\theta = 225$ toroidal location (see figure A.1)

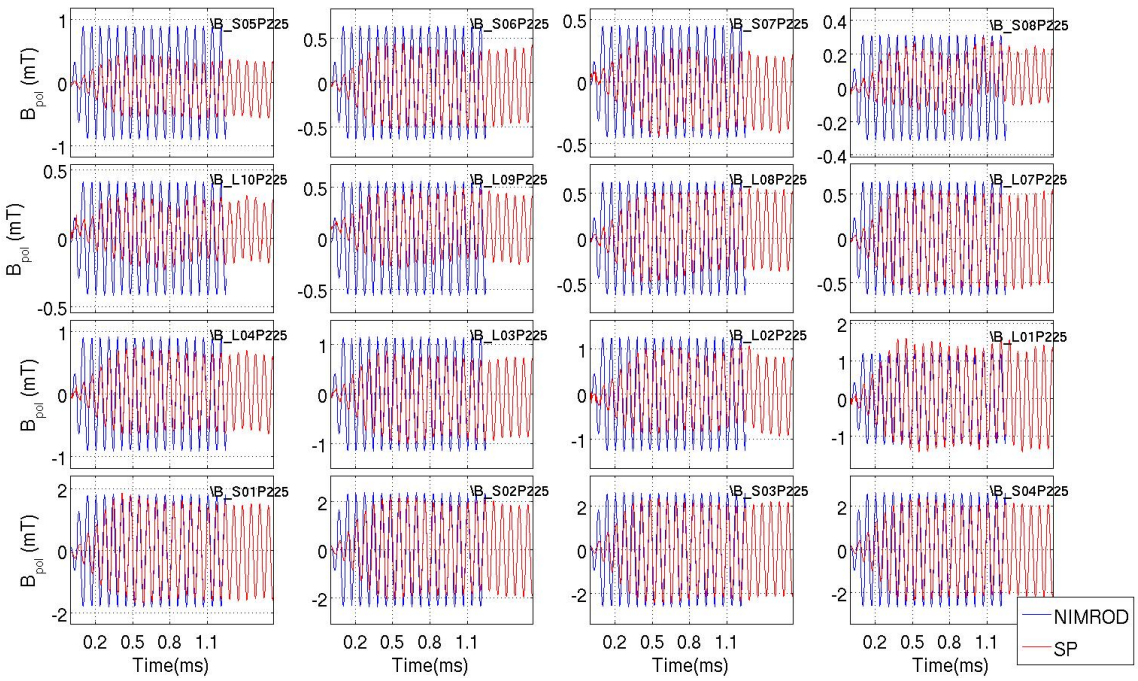

Figure A.8: Comparison of vacuum poloidal magnetic fields for an X injector-only flux shot as measured by the HIT-SI surface probes and simulated by NIMROD at $\theta = 225$ toroidal location (see figure A.1)

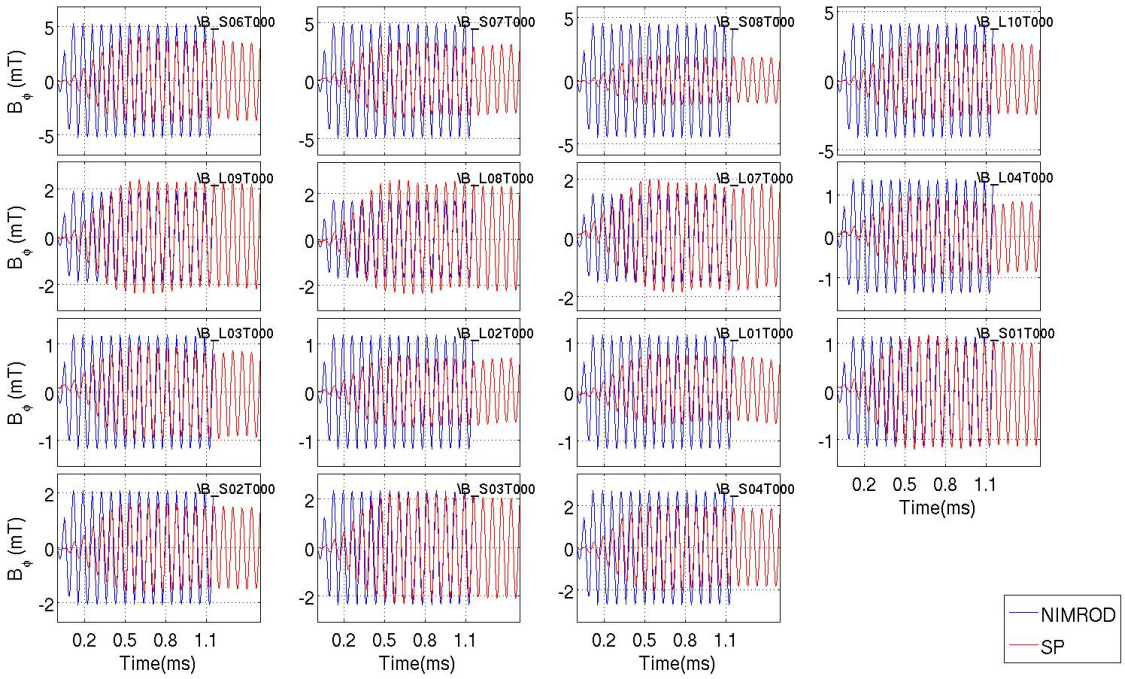

Figure A.9: Comparison of vacuum toroidal magnetic fields for an Y injector-only flux shot as measured by the HIT-SI surface probes and simulated by NIMROD at $\theta = 0$ toroidal location (see figure A.1)

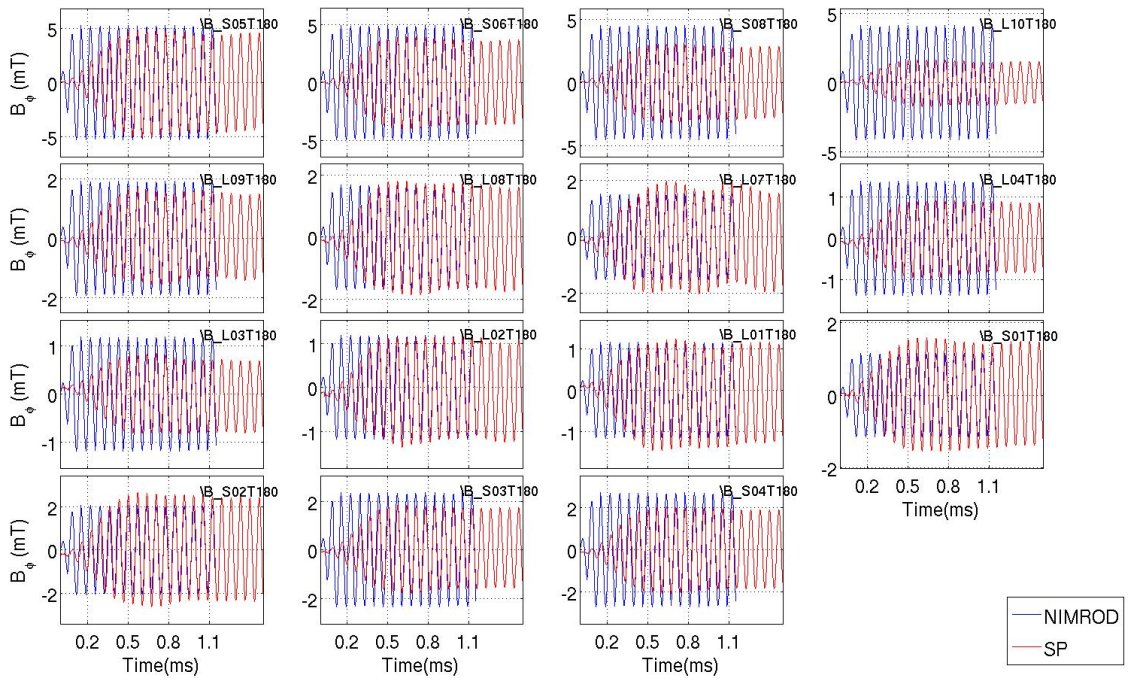

Figure A.10: Comparison of vacuum toroidal magnetic fields for an Y injector-only flux shot as measured by the HIT-SI surface probes and simulated by NIMROD at $\theta = 180$ toroidal location (see figure A.1)

A.3 Obtaining and building NIMROD

A copy of NIMROD can be checked out of the psi-center or Tech-X repository depending on whether you wish to work with NIMPSI (psi-center version) or NIMDEVEL (Tech-X version). HIT-SI subroutines are a part of the main version of NIMPSI (called the trunk). I strongly recommend using the subversion software to obtain a copy of NIMROD, and then to modify, maintain it. Subversion is a very powerful software that allows user to keep track of all their past modifications and activity. To put it bluntly: it will make your life a lot easier. The URL for the Psi-center repo is `https://psicenter.sourcerepo.com/psicenter/NIMPSI/trunk`

NIMROD can be built on any platform as a serial code to be used on a single processor (proc) or as a parallel code to be used in production runs making use of hundreds and thousands of procs (or cores). It is usually helpful to have a local, serial version for development work and debugging. A linux machine is the easiest platform to build NIMROD on. I recommend Ubuntu for OS. The build or compilation requires a mother makefile, `make.inc`, whose contents will contain platform and hardware-dependent information as well as locations of the libraries that NIMROD needs (*e.g.*, SuperLU and METIS). More often then not, it takes some persistence and careful perusal of the error messages to get `make.inc` appropriately modified to build NIMROD. Luckily, NIMROD's /`make_includes` directory contains a bunch of different `make.inc`'s that have been successfully built on various platforms. Always, use one of these as your template and modify it according to your needs. Within each separate NIMROD subdirectories, there are additional makefiles called `Makefile` which are recipes for actually making the F90 object (.o) files from F90 .f files. They also include subroutine dependencies. If you add a new subroutine to NIMROD, you have to include the name of your new subroutine in the `Makefile` corresponding to the correct directory in which you make the modification. You will also have to specify the dependencies for your new file in the `Makefile`.

Both the serial and parallel versions require SuperLU and METIS libraries for direct solves and pre-conditioning of the matrices for iterations. These are both open source and can easily be obtained. However, locally building them could be tricky and unreliable. They are readily available on Hopper and other NERSC machines. Typing `module avail` on Hopper shows you what modules are available for use on Hopper. SuperLU is no longer included as a separate module and takes some digging to get to. You can contact NERSC consultants via phone or email to include your favorite module in the mix or simply ask for their assistance if you have trouble finding what you are looking for.

Assuming you have all the libraries built correctly and have the right `make.inc`, all you have to do is go inside the directory where all your NIMROD directories sit and type `make` then hit return. You will get a series of messages as the code compiles. Pay attention to these although at first they will appear overwhelming. Luckily, the build is only halted by an error, which is the last thing to get displayed.

A.4 Setting up and running a HIT-SI simulation in NIMROD

NIMROD has three main modules located in three separate directories: `nimset`, `nimrod`, and `nimplot`. `nimset` sets up the geometry, initial equilibrium and perturbation. `nimrod` advances the extended (xMHD) equations with the appropriate BC and finally `nimplot` is the post-processor used to analyze the simulation output. An input file `nimrod.in` is needed for specifying the physical, numerical, and boundary parameters. None of the NIMROD executables can be run without `nimrod.in` Currently, two separate subroutines (F90 files) are used for the HIT-SI initialization; one for initialization without the edge layer, `hit_init.f` and the other with the edge layer, `hit_eblock.f`. The details of how the HIT-SI mesh is constructed via Boolean sum interpolation algorithm is covered in appendix B.

The user executes `nimset.f` to invoke one of these subroutines for `gridshape=='newhit'` or 'hit_edge' by typing `./nimset` from a particular run directory that contains the

necessary NIMROD executables. The code outputs the following message:

```
Enter the number of blocks to be stitched
```

Enter 4, then hit return if you are running a SIHI simulation, in other words using a geometry that also includes the edge layer. This is the number of blocks used in the domain decomposition by the gridding subroutine. If you are running a case without the edge layer, then enter 3. The geometry-specific information needed for the meshing algorithms are supplied in additional input files called`input?.txt` or `inputedge?.txt` where ? represents integers from 1 to the number of total blocks used in the construction of the geometry. The current HIT-SI initialization will NOT work without these additional .txt files. They are essentially a series of numbers and strings needed to specify the shape and coordinates of the outline of the geometry. `inputedge?.txt` files contain additional info needed to include the resistive edge layer. These files have to reproduced anytime the geometry has to be modified even if that modification is simply scaling the domain up or down by some factor. IMPORTANT: when you change the poloidal resolution, you have go in all your `input?.txt` (not edge layer ones) and change the integer that appears right at the top of each file. This number sets the relative weight of the number of FE's in each block so that if the number of total cells is increased, each block can adjust the number FE's within. See figure B.4 for an illustration of this feature. I do this in such a way that the weights from all the non-edge-layer blocks add up to the total number of cells (`mx` or `my`) minus 1, where the -1 enters specifically for HIT-SI because the outermost grid point is the resistive edge, to which we always assign only one cell although this method allows more than just one cell inside the resistive layer.

Next `nimset` prompts the user for what type of stitching should be used to join the blocks together, horizontal (side by side tiles) or vertical (stack of tiles):

```
Vertical or horizontal tiling for the stitching?
```

Enter `hor`. This joins the blocks horizontally. Following this, `nimset` should output a few statements and numbers and you should get a `grid.bin` and `dump.00000`. As a

check you should xdraw grid.bin to check the geometry. You should also use `nimplot` to check the initial equilibrium if you are using `nimset` to set it. In the present implementation, `nimset` is only used to construct the geometry and set the initial wave perturbation (which is not really needed for SIHI simulations because we use a low-amplitude Taylor state as a perturbation for $n = 0$ amplification). We use NIMROD's native Grad-Shafranov (GS) solver `nimeq` to set the initial equilibrium explained in the next paragraph.

`nimeq` executable and all the F 90 subroutines associated with `nimeq` are under the /nimset directory. Prior to `nimeq`, a MATLAB GS solver using mimetic quad. elements was employed as part of HIT-SI initialization routines to generate an initial equilibrium. This can still be achieved by setting `new_SI_eq=='true'`. However, we no longer use this option because `nimeq` provides more accurate solutions since it uses the same data structure as the rest of nimrod. `nimeq` requires an input file called `nimeq.in` just `nimrod` requires `nimrod.in`. The magnitude of the initial fields are set in `nimeq.in` via the variable `f1_closed`. Setting it to 10^{-6} approximately results in fields of 10^{-6} T. If `nimeq` ran correctly, it should produce an output called `dump_gs.00000`. You need to set the variable `dump_file= 'dump_gs.00000'` if you want `nimrod` to start from the equilibrium produced by `nimeq`.

You can run NIMROD by typing `./nimrod` inside your local run directory. On the NERSC machines, serial or parallel runs require use of batch scripts. The NERSC web page, NERSC.gov, contains excellent examples of batch scripts for launching jobs on their machines.

GOD SPEED!

Appendix B

APPLICATION OF THE BOOLEAN SUM INTERPOLATION TECHNIQUE AS 2-D MESH GENERATOR FOR NIMROD

An entirely new meshing algorithm has been developed for shaped 2-D geometries in NIMROD. The motivation behind developing the new mesh generator was to have an improved mesh for HIT-SI geometry that also incorporated some of the curvature of the poloidal domain coupled with the desire to have a general mesh generator in NIMROD that could be applicable to a a variety of non-trivial geometries. Though it has not been fully generalized, the mesh generator has successfully created grids for various simple geometries other than the HIT-SI geometry and is still work in progress.

The crux to any meshing algorithm is establishing a one-to-one correspondence between the logical space, which is a unit square and the physical space. The new mesh generator achieves this one-to-one mapping by parameterizing the physical domain in terms of the arc length of the four sides that bound it. Each *side* is mapped to the logical x or y, the line that is bound by [0,1] and comprises mx or my-many cells. A side will often have special vertices of interest along it such as the locations of the injector mouths that need to be accounted for. The additional book-keeping is realized by promoting the special locations to be the vertices of a sub-unit called the *segment*, which is the fundamental unit of operation in this meshing scheme. For example, two special locations along a side require three segments for a geometrical description. The mesh is created by 'blending the four sides' via a technique known as **Boolean sum interpolation** [59], also alluded to as the *blending* algorithm throughout this

document. Splitting the geometry into several smaller 2-D regions called *sectors* and meshing them separately enhances the ability to lay out more uniform elements. The global grid is a union of all the sectors contained within.

In short, a hierarchy of nested structures or objects emerges to address all the necessary features of the meshing technique. This hierarchy is named '3S hierarchy'. These objects, from bottom up, are the segments, sides, and sectors defined as follows:

Segment is the fundamental unit of operation. It is any line or curve that can be described either analytically or numerically. The current working version of the mesh generator only implements an analytical construction for linear and circular segments. Numeric construction requires a line integrator, which has not been yet implemented though the necessary infrastructure is already in place in NIMROD. Segment construction needs the following input from the user:

- RZ coordinates of the vertices, which make the segment ends
- segment shape ('line', 'circle' or 'numeric' etc.)
- other parameters needed for analytic segment construction such as the location of the radius of curvature for a circular segment.
- segment weight, to ensure there is a sufficient number samples along the segment

Side is the composite 1-D object of joined segments. It can contain an arbitrary number of segments that are joined tail-to-head.

Sectors The 2-D object that is a byproduct of the 'blending' of 4 sides. Each sector is isomorphic to a logical unit square. Weights are also assigned to each sector to increase control over the cell distribution throughout the domain.

A geometrical picture containing the entire hierarchy of nested objects is displayed

in fig. B.1. The following sections treat the construction of each nested object and introduce the Boolean Sum interpolation meshing technique.

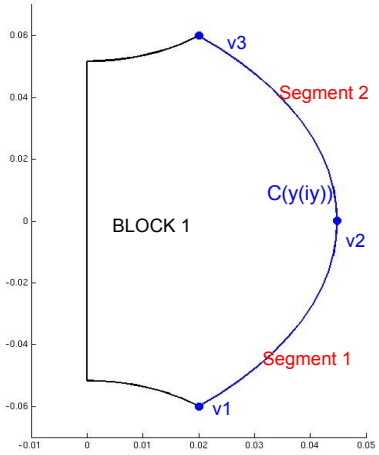

Figure B.1: A single sector showing the inboard side of HIT-SI poloidal plane. Odd numbered sides span the vertical direction and even numbers the horizontal direction. Sides 1 (left), 2 (up) and 4 (bottom) contain no special points, thus are all made of a single segment, which is equivalent to the side. Side 1 is linear, sides 2, 3 and 4 are circular in shape. The outboard edge, side 3 (labeled C) contains one special point, denoted v2. As a result, it contains three vertices v1, v2, v3 and two segments segment 1, segment 2 instead of two vertices and a single segment like the other three sides.

B.1 Segment construction

The segment object is constructed as a derived TYPE in NIMROD. The segment arclength is analytically calculated based on (R, Z) locations of the end points (vertices) and the type of segment `seg_shape`. For non-linear segment shapes, additional parameters such as the physical location of the center of curvature need to be provided. Once the segment arclength is computed a cubic spline, `seg_spl` function is constructed for each segment to parameterize the physical segment in terms of its arclength: $f(\ell) : \ell \rightarrow [R(\ell), Z(\ell)]$ where ℓ is the running arclength and the function $f(\ell)$ is the mapping from arclength ℓ space to physical space (R, Z). Thus, for any

value of $\ell\epsilon[0,l]$ where l is the segment length, a corresponding (R,Z) coordinate can be calculated by evaluating the cubic spline function at the desired arclength.

Each segment is assigned a weight seg%weight that determines the distribution of cells along a side composed of multiple segments. For example, if two neighboring segments have weights 2 and 1 respectively and the same arclength, the segment with weight=2 will have twice as many cells along it as its neighboring segment. The effect of `seg%weight` on cell distribution along a side is discussed further in the following section and an illustration is provided in fig. B.2.

B.2 Side construction

The side is the next higher-level object in the 3S hierarchy. It is a composite 1-D structure consisting of an arbitrary number of segments attached together tail-to-head. Essential in the construction of the object side is the weighted arclength of a side `lw`, which is a sum of all the weighted segment arclengths of contained in the side. The full side arclength `lx` is also calculated by adding the segment (unweighted) arclengths together. `lx` and `lw` are defined as follows:

$$\texttt{lx} = \Sigma_{i=1}^{nv-1} l_i \tag{B.1}$$

$$\texttt{lw} = \Sigma_{i=1}^{nv-1} w_i l_i \tag{B.2}$$

where w_i is the weight, l_i is the arclength of each segment and the sum is carried over segments. nv is the number of total segment vertices along a side and $nv-1$ the number of segments along a side–each segment has two vertices.

At this level (side) of the hierarchy, a one-to-one correspondence is established between the weighted arclength `lw` and logical space (x,y) (the mapping is from `lw` to either x or y). Note that this duality is laid between logical space and `lw` as supposed to `lx` because the grid resolution is controlled by segment weights. Figure B.2 below is an example of how segment weights can affect the cell distribution along a side in a given sector. The `lw` $\leftrightarrow (x,y)$ duality is the second crucial piece to the

meshing technique presented here. The first duality is defined at the segment level (previous section), which connects the arclength space ℓ to physical space (R, Z) for each segment. It is straight forward to generalize the $\ell \leftrightarrow (R, Z)$ duality to the side level so that the weighted arclength `lw` of an entire side is mapped to physical space. Then by the transitive property, any point in logical space can effectively be mapped to physical space via

$$\underbrace{x}_{\text{logical space}} \rightarrow \underbrace{\texttt{lw}}_{\text{side level}} \rightarrow \underbrace{\ell_i}_{\text{segment level}} \rightarrow \underbrace{(R, Z)}_{\text{phys. space}} \tag{B.3}$$

where the last step involves making a function call to the cubic spline evaluation function and using x or y as input for the spline fits constructed at the segment level. Thus, any point in physical space has a logical dual and is actually constructed as a function of logical space as eqn. (B.4) illustrates

$$(R, Z) \equiv \mathbf{R} = \mathbf{R}(\ell) = \mathbf{R}(\texttt{lw}) = [R(\texttt{lw}(x)), Z(\texttt{lw}(y))]. \tag{B.4}$$

This duality is the crux of the whole meshing algorithm. Once a point in logical space is mapped to physical space, creating the final mesh simply becomes a matter of applying the blending algorithm presented in the following section.

B.2.1 Sector construction

The sector (fig. B.1) is the largest of the nested objects in the 3S hierarchy. It is a 2-D construct that contains four *sides*. It is topologically equivalent to a logical square The four sides form the boundary of a sector. Neighboring sectors share a side. Sides of each sector are labeled in a clock-wise direction starting from the left, side 1 and ending at the bottom, side 4. Vertical sides, *i.e.*, odd-numbered (1 and 3) sides are dual to y and horizontal sides (2 and 4) dual to x. Each sector contains a grid `sector%grid`, which is the physical mesh of the sector and a weight `sector%weight` to determine how global cell numbers, mx and my should be divided up amongst sectors.

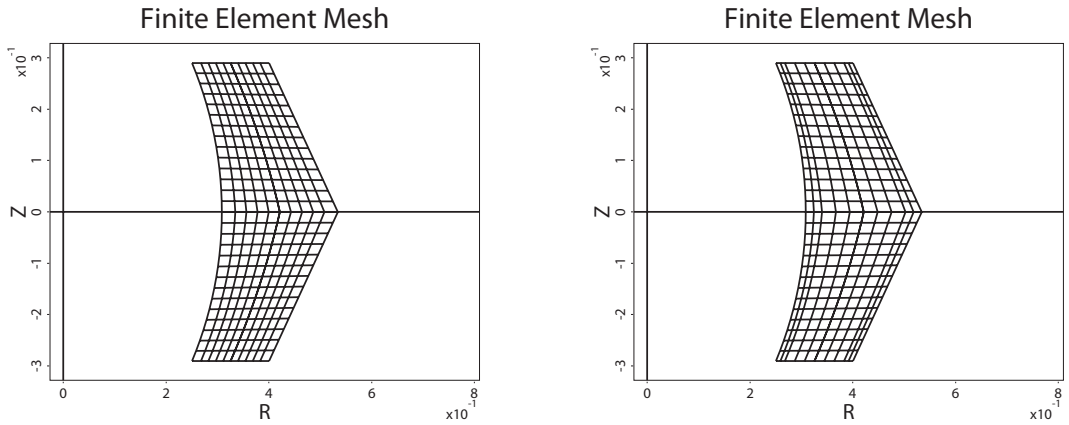

(a) All weights are 1

(b) Shorter segments have a weight of 2

Figure B.2: An example illustrating how weighting segments differently affects the cell distribution along a side and in a sector. In the panel on the right segments 1 and 3 in sides 2 and 4 have a weight of 2 instead of 1. In the left panel all segments are weighted equally. Note that in both cases, the number of cells along sides 2 and 4 (top and bottom) is preserved.

The sector grid is generated by blending the four sides of the sector boundary via the boolean sum interpolation technique covered in the following section. Upon the user's choice, the global domain can be decomposed into multiple sectors. The multi-sector feature increases the versatility of the meshing algorithm by yielding more uniformly shaped cells (fig. B.3) and is proven to be an advantageous and convenient feature for dealing with non-trivial and complex geometries like that of the HIT-SI. Figure B.4 is an example of how different sector weights affect the distribution of grid cells across the entire domain.

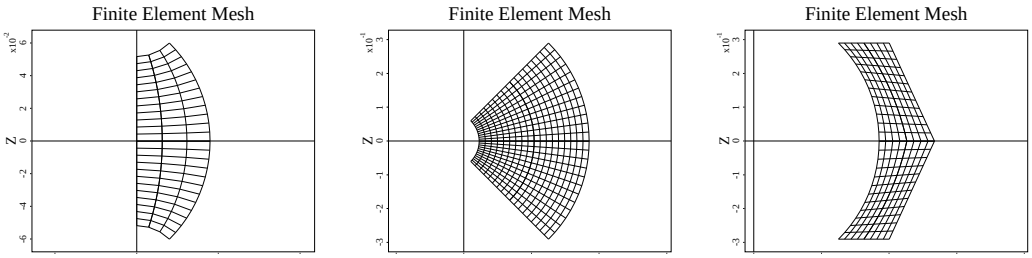

(a) Sector 1: the inboard side (b) Sector 2 (c) Sector 3: outboard side

Figure B.3: An example illustrating multi-sector feature of the algorithm. This is the poloidal geometry of the HIT-SI computational domain. It is split into three separate sectors, which are not shown to correct scale here. Sector 1 (inboard side) is much smaller in area and therefore is only spanned by 3 cells horizontally. Sectors 2 and 3 are comparable in size. For this particular case, the domain decomposition is only implemented in the horizontal direction, hence the global mx has to divided up between sectors whereas the global my is the same for all sectors

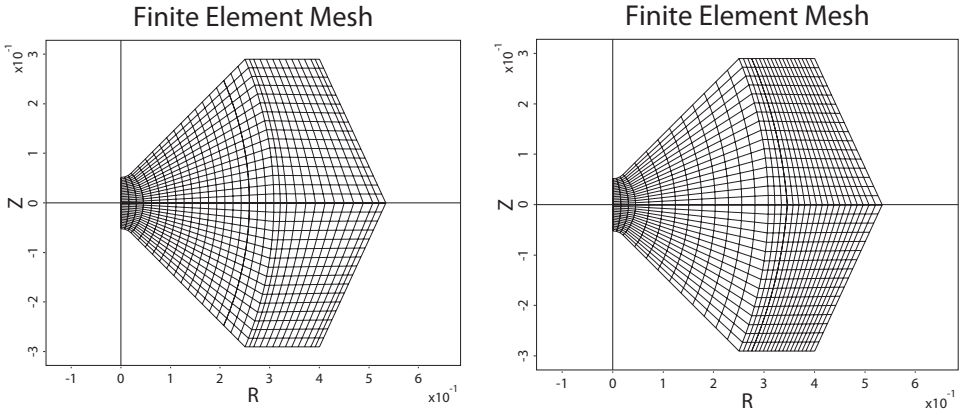

(a) Sectors 2&3 have roughly the same weight (b) Sector 3 has a greater weight than sector 2

Figure B.4: An example of how different sector weights affect the distribution of grid cells across the entire domain. (a) Sectors 2 and 3 of the HIT-SI poloidal plane have equal weights. (b) Sector 3 is weighted more heavily than sector 2, which results in a greater density of cells in sector 3. Note that the global mx is preserved in both cases

B.3 Mesh generation via Boolean Sum Interpolation

The mesh for each sector is generated by 'blending' the 4 sides via **Boolean Sum Interpolation** given by

$$\begin{aligned}\mathbf{R}(x,y) = {} & R_1(\ell(y)) * (1-x) + R_2(\ell(x)) * y + \\ & R_3(\ell(y)) * x + R_4(\ell(x)) * (1-y) \\ & -R_1(\ell(0)) * (1-x) * (1-y) - R_2(\ell(0)) * (1-x) * y \\ & -R_3(\ell(1)) * x * y - R_4(\ell(1) * x * (1-y)\end{aligned} \tag{B.5}$$

where $\mathbf{R}$ is a two-component vector corresponding to a single point in the physical domain. x and y are the usual logical coordinates bound by [0,1]. Eqn. (B.5) is executed inside two-nested `DO` loops that cycle over all the horizontal and vertical coordinates within the sector. In other words, the blending is carried out $(mx + 1) \times (my + 1)$ times for each point inside the sector. R_1, R_2, R_3 and R_4 represent the mapping between logical and physical spaces for each side, defined by eqn. (B.4). Thus, R_1, R_2, R_3, and R_4 map a single point (x^*, y^*) in logical space to four separate physical locations along the sides. For example, (x^*, y^*)=(.5,0) gets mapped to the mid-point of sides 2 and 4 assuming there is no grid packing in the horizontal direction and to the bottom of sides 1 and 3. These four locations along four sides are then blended using $x, (1-x), y, (1-y)$ as multiplicative weighting factors. A physical point (R_o, Z_o) situated close to the left side of the sector has $x_o \sim 0$, and therefore, R_1 has much greater impact than R_3 on the blending that actually generates (R_o, Z_o). The terms in blue correct the over counting due to Boolean Sum generating each corner twice. The mesh for each sector is generated separately in an outer `DO` loop over sectors. Then the final global mesh is obtained by joining all the sectors together.

B.3.1 Resistive layer and mesh packing

The resistive layer is implemented in a fashion identical to the meshing procedure outlined in the preceding sections. The resistive edge regions are promoted to sub-sectors called `eblock`s that have the same underlying structure as regular sectors. This is proven to be an extremely convenient, though laborious, way of adding on the resistive edge layer as there is absolutely no need for developing additional algorithms. `eblocks` are physically joined with the appropriate parent sector along 'external' edges defined by the code. This union results in a new 2-D structure called *super sector*. The final global mesh, in this case is simply a bunch of super sectors stitched together.

Mesh packing feature is easily incorporated into the underlying structure of the 3S hierarchy. By modifying the spacing of grid points in logical space, mesh packing of any type could be accomplished. Packing the cells near the edge as it may be required for the resistive edge can be implemented by changing the uniform distribution of points in logical space to a hyperbolic tangent distribution. For centrally packed grids, the uniform logical space distribution is simply changed to a parabolic or quadratic distribution.

VITA

Cihan Akcay

Bachelor of Science in Physics

The College of William and Mary

May 2002

Doctor of Philosophy

University of Washington

August 2013